Comparing the performance of different catalyst packings for Fischer-Tropsch synthesis

Masana Mhinga

Department of Chemical Engineering
University of Cape Town
30 November 2019

Acknowledgements

I would like to thank my supervisor, Prof. Eric Van Steen for his patient and comprehensive instruction, I would not have accomplished this work without him. I would also like to thank him for encouraging me to work harder and smarter and for challenging my thinking.

Secondly, this work would not have been possible without the financial support of my sponsors, Sasol, I would like to thank them for funding my undergraduate studies and giving me the opportunity and means to continue with my postgraduate studies.

I would like to thank my colleagues in the chemical engineering department at UCT, for giving me assistance when I needed it, and for the healthy distractions. I would like to acknowledge Sandeeran Govender for his helpful advice and for being there to answer questions, repeatedly. I would like to thank Chelsea Tucker for stepping in to provide relief when I was most stuck, for her inspiring enthusiasm and constant readiness to provide me with whatever assistance I needed.

Most importantly, I would like to thank my family for their support and motivation. My mother, for her sacrifices and encouragement and her exemplary show of strength through trying times. My brother, for always making sure that I got to where I needed to be.

Abstract

The increase in global population accompanied by depleting fossil fuel reserves and rising fuel demand is prompting the need to increase and diversify fuel production rates. In addition, increasing global pressure to reduce the contribution of greenhouse gas emissions to global warming and as well as rising oil prices are driving efforts to improve efficiency and environmental sustainability of fuel production. Low-temperature Fischer-Tropsch synthesis is an attractive alternative to crude refining. During Fischer-Tropsch synthesis (FTS), synthesis gas, a mixture of H_2 and CO is converted to a wide range of value-added long chain hydrocarbon products in a polymerisation reaction:

$(2n+1)\ H_2 + n\ CO \rightarrow C_nH_{2n+2} + n\ H_2O$ $\quad -\Delta H = 165 - 214\ \mathrm{kJ \cdot mol^{-1}}$ 0-1

The benefit of Fischer-Tropsch synthesis is that any carbonaceous feedstock can be used to generate synthesis gas, including natural gas, coal and biomass. However, exploitation of biomass requires decentralised, small-scale units, to reduce the complexity of a variable feed supply. To make this feasible, small-scale FT reactors must be simple to operate and achieve high single-pass conversion.

Multi-tubular fixed-bed reactors are ideal for realising this as they are relatively easy to scale-up and operate when compared to other reactor technologies. However, conventional catalyst packings for fixed-bed reactors result in high pressure drop. Structured packings offer an attractive solution as their high porosity (ca. 70%-90%) when compared to that of conventional pellet- or particle packed beds (ca. 40%) results in significant reductions in pressure drop, which lowers gas compression costs. Large pellets are typically used in fixed-bed reactors to reduce pressure drop, resulting in increased internal diffusion limitations which may result in increased CH_4 selectivity and reduced C_{5+} selectivity, the desired product. In contrast, a thin layer of the catalytically active material applied on the surface of the structured substrate results in lower diffusion limitations, and thus maintaining a favourable product distribution. Furthermore, open-cell foams reactors have the potential to enhance external mass in fixed-bed reactors because of their tortuous flow channels and high geometric surface area.

The aim of this study was to compare the performance of catalyst coated on a ceramic open cell foam with that of catalyst powder, pellets and catalyst coated on a ceramic

honeycomb monolith in terms of CO conversion, CH_4 and C_{5+} productivity per gram catalyst using an alumina-supported catalyst containing 22 wt.% Co and 0.05 wt.% Pt. Furthermore, the effect of catalyst layer thickness on catalyst performance was also evaluated.

It was shown that the pellets performed poorly when compared to the catalyst powder due to its much higher CO_2 and CH_4 selectivity, which were attributed to poor temperature control, induced by large diffusion length (i.e., pellet diameter).

The foams and monoliths also performed poorly when compared to the catalyst powder. For monoliths and foams washcoated with ca. 0.5 g of catalyst, it was seen that CO conversion achieved was on average ca. 40% lower than that achieved over the catalyst powder at similar space velocities. The product selectivity was also poor. Furthermore, it was seen that despite the tortuous flow channels of the foams, which were initially thought to produce better mass transfer than the flat-wall channels of the monoliths, the performance of the foams was not better than that of the monoliths. Thus, it is concluded that the use of monoliths and foams does not improve performance in Fischer-Tropsch synthesis. The poor performance may be attributed to poor heat and mass transfer properties in the reactor set-up, and possibly aggravated by catalyst deactivation incurred during reactor startup.

Table of Contents

Table of Figures

List of Tables

Abbreviations

AAS	Atomic adsorption spectroscopy
A-S-F	Anderson-Schulz-Flory
BET	Brunauer-Emmett-Teller
CPSI	Cells per square inch
CTL	Coal-to-liquids
FBR	Fixed-bed reactor
FID	Flame ionisation detector
FTS	Fischer-Tropsch synthesis
GC	Gas Chromatography
GTL	Gas-to-liquids
ICP-OES	Inductively-coupled plasma optical emission spectroscopy
ID	Internal diameter
LT-FTS	Low temperature Fischer-Tropsch synthesis
MFC	Mass flow controller
OD	Outer diameter
PBR	Packed bed reactor
PID	Proportional Integral Derivative
PSD	Particle size distribution
PPI	Pores per inch
SCBR	Slurry bubble column reactor
SEM	Scanning electron microscopy
TCD	Thermal conductivity detector
TEM	Tunnelling electron microscopy
ToS	Time on stream
TPR	Temperature programmed reduction
WGS	Water-gas shift
XTL	X-to liquids, where X refers to a carbon sauce such as gas, coal or biomass

Symbols

$D_{\mathrm{A,B}}$	Diffusion coefficient of compound A in a mixture of A and B [$m^{2}{\cdot}s^{-1}$]
$C_{A,b}$	Concentration of A in the bulk gas [$mol{\cdot}m^{-3}$]
$C_{A,s}$	Concentration of A near the outer surface of the catalyst [$mol{\cdot}m^{-3}$]
d_p	Particle diameter (spherical particles) or pore diameter (foams) [m]
ϵ	Voidage [-]
k_m	External mass transfer coefficient [$cm{\cdot}s^{-1}$]
n	Reaction order
$-r_{CO}{}^{obs}$	Observed CO consumption rate [$mol{\cdot}g^{-1}{\cdot}s^{-1}$]
S_v	Specific volumetric external surface area [?]
t	Cell wall thickness [cm]
Φ	Weisz Modulus
D_{A}^{Eff}	Effective diffusivity of component A [$m^{2}{\cdot}s^{-1}$]
L	Catalyst layer thickness [μm]
η	Effectiveness factor [-]
ϕ	Thiele modulus [-]
ρ_s	Density of a solid [$kg{\cdot}m^{-3}$]
τ	Residence time [s]
β_L	Liquid hold-up based on void volume for square channel monolith [-]
Fr_L	Liquid Froude number [-]
Re_L	Liquid Reynold's number [-]

1. Introduction

1.1. Background and context

It has been predicted that the world population will exceed 9 billion people by 2040, with an associated predicted 45% increase in global fuel demand (BP, 2018). As such, fuel security is a major challenge for world leaders and industry as it is essential for sustaining a good standard of living and to stimulate economic growth. In 2017, fossil fuels constituted 85% of global primary energy production (BP, 2018), although it is generally accepted that this is unsustainable. Furthermore, the domination of fossil fuel production by a handful of countries has been shown to create instability in the market with well-known trickle-down effects.

Diverse fuel sources and technologies are needed to meet the rising demand for liquid fuels. Improving fuel security may help protect the local economy by insulating against disruptions and volatility of supply and oil price that arise due to economic recessions, geopolitical conflicts, natural disasters and epidemics in exporting regions. This is especially important in developing countries where the instability of imported crude oil prices continues to negatively impact long-term planning and economic growth. The diversification of energy production is also driven by changing policies to mitigate climate change, consumer awareness, the instability of oil prices, and technological developments. This has led to the rise of renewables in power generation and fuel production. Among these are solar, wind and biomass. Renewables are facilitating the decentralisation of energy production, which may lead to unprecedented geopolitical transformations (Global Commission on the Geopolitics of Energy Transformation & Van De Graaf, 2019). In addition to designing new processes, improving the efficiency of existing technologies is an important aspect of the innovation that is required to ensure that fuel production becomes more cost-effective while reducing detrimental effects on the environment.

The Fischer-Tropsch synthesis (FT) is one such technology that has the potential to help meet growing fuel demand. The advantage of the Fischer-Tropsch synthesis over conventional fuel production from crude oil is its ability to convert a variety of carbon-containing feedstocks to value-added hydrocarbon products. Some countries rely heavily on oil imports. In addition, the lack of transport infrastructure in remote locations prevents easy access to fuel. Thus, the opportunity to make use of locally accessible

carbon sources may help alleviate the high cost of imported fuel. An increasing number of new natural gas reserves are stranded or found in remote locations, where their size and isolation makes transport and export via pipelines impractical and uneconomical (Wood et al., 2012). In addition, flaring of associated natural gas during oil production is a practice that wastes a potentially valuable resource and is becoming less viable due to stricter environmental restrictions on greenhouse gas emissions. Furthermore, the use of biogas as a feedstock to a small-scale Fischer-Tropsch process is being explored (Tucker and van Steen, 2020). Of fuel consumed in (southern) Africa, it is estimated that approximately 50% is from imports, thus, the case for local production of synthetic fuels is strong in this region (Department of Energy, 2018).

The Fischer-Tropsch process has been largely applied for large-scale production of synthetic liquid fuels in coal-to-liquids (CTL) or gas-to-liquids (GTL) processes, which are collectively abbreviated XTL. Notable existing operations include Sasol's GTL plants (Sasolburg, Oryx and Escavos), PetroSA's Mossel Bay GTL, Shell's GTL Plants (Bintulu and Pearl), The CTL plants in China by China Shenhua Coal Liquefaction Co Ltd and Sasol (in Secunda).

An overview of the Fischer-Tropsch process is given in Figure 1-1. The first step in the Fischer-Tropsch XTL process is synthesis gas generation. Syngas is typically generated by reacting the carbonaceous feedstock, which can be coal, biomass/biogas, or natural gas, with high pressure steam in the presence of oxygen. For coal and biomass, this process is called gasification, and the feedstock is usually crushed and made into a slurry before being fed to the reactor. For natural gas or biogas, the conversion to syngas is called reforming and occurs in the gaseous state (Mohajerani *et al.*, 2018; Tijmensen *et al.*, 2002).The produced syngas is cooled and cleaned to remove H_2S. Water-gas shift reaction may be carried out to increase the amount of H_2 content and reduce CO_2 (Tijmensen *et al.*, 2002). The cooled syngas is transferred to a Fischer-Tropsch reactor, where synthetic crude comprising hydrocarbons of various chain lengths are produced as the main product, as well as water, a by-product. The Fischer-Tropsch synthesis is typically carried out over a cobalt- or iron-based catalyst, at temperatures 200°C to 240°C for low-temperature Fischer-Tropsch synthesis (LT-FTS). High-temperature Fischer-Tropsch synthesis (HT-FTS) is carried out at 300°C to 350°C over Fe-based catalysts (Mohajerani *et al.*, 2018). Reactor pressures between 15 - 40 bar are used. The product of Fischer-Tropsch synthesis is a synthetic crude with a product distribution that depends on the catalyst and reaction conditions used. The FT products are then sent to an upgrading

unit where light gases are removed, different products are separated by fractionation in distillation columns, olefins are hydrogenated, and waxes are cracked to lighter products (Mohajerani *et al.*, 2018). Some products are re-blended to meet market requirements. The desired products from the XTL process are sulphur-free synthetic fuels such as naphtha and diesel, waxes and feedstocks for the production of chemicals and polymers.

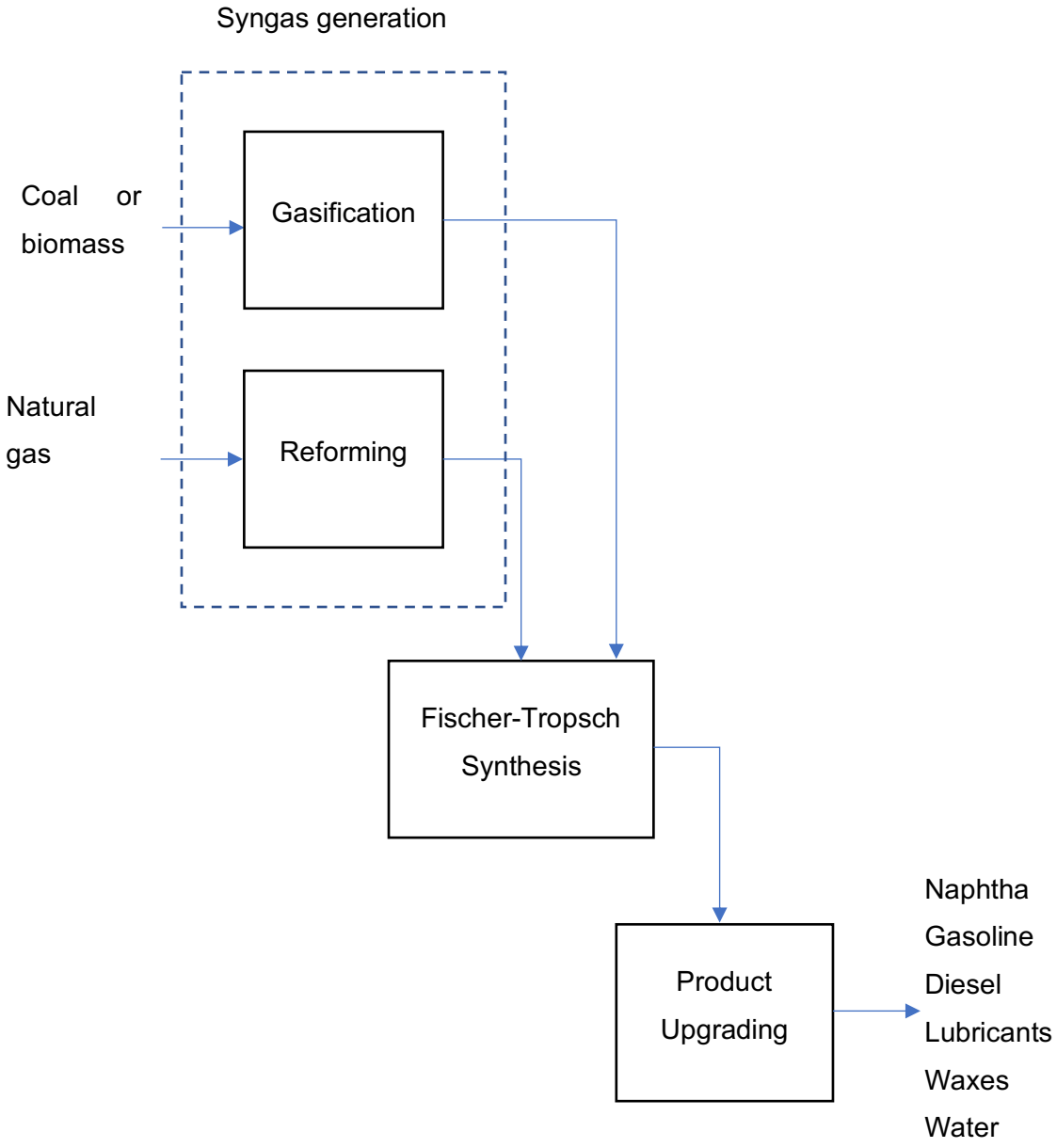

Figure 1-1: Block diagram of the XTL process using Fischer-Tropsch synthesis

A number of studies have investigated the possibilities for small-scale Fischer-Tropsch synthesis to monetise unconventional carbon sources such as biomass, stranded gas and associated gas, that is the gas produced as a by-product of crude oil extraction

(Wood *et al.*, 2012). However, monetisation of these resources requires large capital investments for building processing plants and transport infrastructure, as well as long-term sales contracts to ensure profitability (Wood *et al.*, 2012).

Furthermore, the production of synthesis gas (syngas) has a high contribution to the overall cost of the XTL process, costs of up to 70% of the total cost have been reported (Dry, 2002a). The high cost associated with syngas production implies that the conversion of syngas in the Fischer-Tropsch reactor must be highly efficient to make small-scale FT economically viable. This can be done by achieving high single pass conversion and high selectivity towards desired products. Up to 80% single pass conversion is assumed to be achievable in fixed-bed reactors (Tijmensen *et al.*, 2002). One strategy to accomplish improved performance of compact reactors is the use of intensified reactors, which offer higher surface area-to-volume ratios than conventional fixed-bed reactors, along with reduced pressure drop (Delparish & Avci, 2016). Structured reactors have already been shown to be promising for applications such as hydrogen fuelling stations, onboard reformers, and fuel-based combination heat and power units, where high throughputs are required in small reactor volume (Ciambelli *et al.*, 2010). Hence, this dissertation will investigate the potential to improve the conversion and selectivity of FT using structured reactor packings such as foams and monoliths when compared to pellet-type catalyst packings.

1.2. Overall objectives

The objective of this study is to prepare and test structured catalyst packings, which may have enhanced mass and heat transfer properties, for Fischer-Tropsch synthesis, so to as to improve reactor productivity and product selectivity when compared to randomly packed beds and monolith reactors.

1.3. Scope, limitations and key issues

This study will compare the productivity of a randomly packed bed, monolith and foam reactor. With respect to the development of the foam reactor, the synthesis of foam substrates will not fall within the scope of the project. However, of key interest will be the method and conditions for depositing/coating the catalyst material on to the walls of the substrate. In addition, the morphological effects of the coating method and their impact on reactor productivity will be evaluated.

The dimensions in a laboratory-scale reactor may prevent adequate quantification of temperature gradients as would be seen in large-scale industrial reactors. Nevertheless, the results obtained may be able to establish the relative performance of the different structured catalyst packings that will be tested.

2. Literature review

2.1. Fischer-Tropsch synthesis

The Fischer-Tropsch synthesis converts synthesis gas to a wide range of hydrocarbons and oxygenates. Low-temperature Fischer-Tropsch synthesis (LT-FTS) is typically carried out over a cobalt-base catalyst at temperatures between 200°C and 240°C and high pressures (20 - 40 bars), (Dry, 2002a; Guettel et al., 2008; Merino et al., 2017).

Although there is yet to be consensus on the mechanism of FT, it is widely accepted that FT occurs via a polymerisation reaction for which the sequence is as follows (Adesina, 1996; Shafer et al., 2019):

1. H_2 and CO chemisorb on the catalytic active sites,
2. formation of a monomer
3. carbon chain propagation
4. chain growth termination
5. desorption of the final product from the catalyst surface, with the possibility of re-adsorption of some of the products and their reincorporation into in the chain growth scheme.

Fischer-Tropsch synthesis produces paraffins, olefins, alcohols, aldehydes, ketones, branched compounds (Claeys and van Steen, 2004; Claeys and van Steen, 2005) and even some aromatic compounds (Fletcher, 2009; Grobler et al., 2009). Chain initiation, propagation and termination (steps 2-3) are characterised by primary and secondary reactions involving adsorbed/dissociated/free species. Olefins, and in particular, α-olefins, are the most dominant primary product of Fischer-Tropsch synthesis. The formation of olefins is presented by equation 2-1.

$$n\,CO + 2n\,H_2 \rightarrow C_nH_{2n} + n\,H_2O \qquad -\Delta H_{250°C} = 110 - 149\ \mathrm{kJ \cdot mol_C^{-1}} \qquad 2\text{-}1$$

Equation 2-2 represents the formation of paraffins. The reaction is highly exothermic and depends on chain length, with the heat of reaction is 214 $kJ \cdot mol_C^{-1}$ for methane formation and 165 $kJ \cdot mol_C^{-1}$ if the chain length tends to infinity (Claeys & Van Steen, 2005).

$n\,CO + (2n+1)\,H_2 \rightarrow C_nH_{2n+2} + n\,H_2O$ $\quad -\Delta H_{250°C} = 165 - 214\ \mathrm{kJ \cdot mol_C^{-1}}$ 2-2

Paraffins and other compounds can also be formed in secondary reactions from primarily formed α-olefins.

Oxygenates are formed, sometimes in significant amounts, according to equation 2-3.

$n\,CO + 2n\,H_2 \rightarrow C_nH_{2n+2}O + (n-1)\,H_2O$ $\quad -\Delta H_{250°C} = 98 - 150\ \mathrm{kJ \cdot mol_C^{-1}}$ 2-3

The desired products of LT-FTS reactors are hydrocarbons in the gasoline range (C_5-C_{12}), hydrocarbons in the diesel range (C_{13}-C_{18}) and waxes (C_{19+}) (Yang *et al.*, 2010b). The waxes are typically hydrocracked into liquid fuels such as diesel and gasoline (Dry, 2002b). It should be noted that the selectivity of the transformation of carbon into the desired products is decreased by side reactions, such as the water-gas shift reaction (2-4) and the Boudouard reaction (2-5), which both yield carbon dioxide (Guettel *et al.*, 2008).

$CO + H_2O \rightarrow CO_2 + H_2$ $\quad -\Delta H_{250°C} = 41\ \mathrm{kJ \cdot mol^{-1}}$ 2-4

$2\,CO \leftrightarrow C + CO_2$ $\quad -\Delta H_{170°C} = 172\ \mathrm{kJ \cdot mol^{-1}}$ 2-5

* Heats reaction were obtained from (Claeys & Van Steen, 2005)

2.1.1. Reaction kinetics for Fischer-Tropsch over cobalt-based catalysts

Various mechanistic and empirical models for predicting the reaction rate of Fischer-Tropsch synthesis have been proposed (Botes et al., 2009; Van der Laan & Beenackers, 1999). In the development of the rate expressions, the rate of CO consumption is typically split into the rate for CO_2 formation (e.g., via the water gas shift reaction) and the rate of formation of carbon incorporated into organic compounds (r_{FT}). Fischer-Tropsch synthesis reaction rate laws (i.e., the rate of incorporation of carbon into organic product compounds) have typically been reported with a positive reaction order with respect to H_2 and a negative reaction order with respect to CO. The positive order with respect to H_2 implies that hydrogen accelerates the conversion of CO into organic product compounds and is involved in the rate controlling step. The negative reaction order with respect to CO indicates a high coverage of the surface with CO and/or carbon (Claeys & Van Steen, 2004). A typical example of Langmuir-Hinshelwood type of rate expression describing the rate of the Fischer-Tropsch synthesis is the rate expression given by Yates & Satterfield (1991) shown in equation 2.6, and by Van der Laan & Beenackers (1999) shown in equation 2-7.

$$r_{FT} = A\,\frac{P_{H_2}\cdot P_{CO}}{(1+K_{CO}\cdot P_{CO})^2} \qquad 2\text{-}6$$

Yates & Satterfield (1991).

$$r_{FT} = A\,\frac{P_{H_2}\cdot P_{CO}}{P_{CO}+b\cdot P_{H_2O}} \qquad 2\text{-}7$$

Van der Laan & Beenackers (1999)

The influence of water on Fischer-Tropsch synthesis activity has been unclear with some reporting no significant effect of water on activity (Botes, 2009; Schulz *et al.*, 1997), while some report a negative effect of water (Das *et al.*, 2005), and others have found that water improves catalytic activity (Van Steen & Schulz, 1999).

$$r_{FT} = A\,\frac{P_{H_2}{}^{\frac{3}{2}}\cdot\frac{P_{CO}}{P_{H_2O}}}{\left(1+\frac{b\cdot P_{H_2}\cdot P_{CO}}{P_{H_2O}}\right)^2} \qquad 2\text{-}8$$

Van Steen & Schulz (1999)

2.1.2. Product distribution

A typical cobalt-based low-temperature Fischer-Tropsch synthesis reactor product stream contains 80-95% hydrocarbons (sans water). The array of hydrocarbon products of FT primarily consists of paraffins, 1-olefins, trans-2-olefins, cis-2-olefins, and minor products such as isomerised methyl-branched alkanes (Shafer *et al.*, 2019). Product distribution is a function of conversion as well as operating temperature, mass and heat transfer properties, metal loading, particle size, degree of reduction of the catalyst and catalyst preparation procedure (Blachou et al., 1992; Bukur et al., 2012; Ma et al., 2011; Rytter et al., 2016; Steynberg et al., 2004; van Steen et al., 2018).

2.1.2. (A) **Effect of temperature**

The selectivity in the Fischer-Tropsch synthesis is sensitive to the reaction temperature. Irrespective of the catalyst used, increasing reactor temperature results in increased production of products with shorter chains (i.e., chain growth decreases) (Dry, 2002b). Thus, the formation of the undesired product, methane, which is thermodynamically favoured, increases with increasing temperature, while the selectivity towards high molecular mass products (C_{5+}) decreases. Furthermore,

secondary hydrogenation becomes more important upon increasing the reaction temperature resulting in decreased olefin content in the Fischer-Tropsch product (Dry, 2002b).

2.1.2. (B) **Effect of pressure**

The kinetics of the product formation in the Fischer-Tropsch synthesis is controlled by the partial pressures of the kinetically relevant species. As such the overall pressure may affect the product selectivity. It has been reported that increasing the pressure in the low temperature cobalt-based Fischer-Tropsch synthesis results in a strong increase in the chain growth, but increasing reactor pressure further to beyond 20 bar has little effect on selectivity (van Berge & Everson, 1997). This may be attributed to the decrease in the chain growth termination with increasing CO partial pressure (Schulz *et al.*, 1995; Dry, 2004)

2.1.2. (C) **Effect of the H_2/CO feed ratio**

The H_2/CO ratio is an important variable affecting the amount of hydrocarbon formed, olefin content of reaction products and free carbon formation (Stern *et al*., 1983). High partial pressures of CO increase the likelihood of high surface coverage by adsorbed carbon species on catalytically active sites, which in turn, increases the chain growth probability (Dry, 2004). Conversely, a high H_2 partial pressure leads to early chain termination and increased likelihood for secondary hydrogenation and isomerisation (Dry, 2004). Thus, a high H_2/CO ratio leads to a reduced olefin content and increased presence of branched alkanes (Bukur *et al.*, 2012). It is thought that hydrogen removes oxygen from the catalyst surface, creating more dissociation sites for CO (Moodley, 2008). This effect may be reduced at very low H_2/CO feed ratios, leading to lower catalyst activity than at higher H_2/CO feed ratios.

2.1.2. (D) **Effect of space velocity and conversion**

In a fixed bed reactor, CO conversion increases with decreasing space velocity. A higher residence time (i.e., lower space velocities) also results in increased probability of secondary reactions such as hydrogenation, double bond isomerisation and α-olefin re-incorporation, leading to lower olefin to paraffin (O/P) ratios and increased chain growth probability, while shorter residence times result in higher O/P ratios (Claeys &

Van Steen, 2004). An alternative theory proposed by Iglesia (1997) is that H_2O partial pressure increases with increasing CO conversion, increasing the probability of olefin re-insertion by inhibiting hydrogenation of olefins and chain termination, thus, increasing chain growth. Note that the two theories contradict each other in terms of whether secondary hydrogenation of olefins increases or decreases with CO conversion. Bukur *et al.* (2012) noted that while there is yet to be consensus on the role of H_2O, the effect of residence time on selectivity appeared to be more dominant than that of water.

At low to moderate CO conversion (i.e., < 80%), the selectivity for the formation of methane decreases with increasing conversion, while the selectivity towards the desired product, liquid hydrocarbons (C_{5+}) increases with increasing conversion levels (Bukur *et al.*, 2012; Ma *et al.*, 2011). However, at CO conversions exceeding 80%, CH_4 selectivity increases with conversion, while C_{5+} selectivity decreases or remains stagnant, in which case the difference is made up by C_2 -C_4 hydrocarbons (Bukur et al., 2012; Ma et al., 2011; van Steen et al., 2018).

H_2 and CO may not necessarily be used in the same ratio with which they are fed to the reactor. Dry (2004) stated that the H_2/CO usage ratio for cobalt catalysts is almost independent of the conversion due to low WGS activity, and typically lies in the range between 2.05 and 2.15. However, Ma *et al.* (2011) reported a decrease of the H_2/CO usage ratio with increasing conversion, from 2.26 to 1.9 when increasing the conversion from 12% to 96%. This makes sense when considering the stoichiometric requirements of producing higher molecular mass hydrocarbons which are increased with increasing CO conversion: based on equation 2-2, the H_2/CO usage ratio for the formation of alkanes is $\frac{2n+1}{n}$ for n number of carbons. The formation of CH_4 requires 3 moles of H_2 per mol of CO converted, while the formation of C_{5+}-paraffins has a stochiometric usage ratio of less than 2.2. Thus, a high C_{5+} selectivity will result in a low H_2/CO usage ratio. A high olefin and oxygenate fraction in the product stream may also contribute to bringing the H_2/CO closer to 2. Increased production of CO_2 will reduce the H_2/CO ratio to values below 2. On that basis, the H_2/CO usage ratio can be a rough but useful tool for assessing the efficiency of the Fischer-Tropsch synthesis process in achieving desired selectivity.

2.1.2. (E) **Anderson-Schulz-Flory distribution**

Fischer-Tropsch synthesis is a polymerisation reaction which can be thought of as a repeated sequence comprised of the addition of hydrogen to carbon and oxygen, splitting of the C-O bond and the formation of new C-C bonds (Schulz, 1999). In this sequence, the product distribution is controlled by a chain growth probability. The chain growth probability is a function of the chain growth propagation (R_p) and termination rates (R_t) (Rytter et al., 2016).

$$\alpha = \frac{R_p}{R_p + R_t} \qquad 2\text{-}9$$

The ideal distribution of the organic product compounds as function of carbon number can then be described by the Anderson-Schulz-Flory (A-S-F) model, which assumes that R_p and R_t are independent of chain length (Shafer *et al.*, 2019).

$x_n = (1-\alpha) \cdot \alpha^{n-1}$	2-10
$\frac{W_n}{n} = (1-\alpha)^2 \cdot \alpha^{n-1}$	2-11

Where n is the carbon number, x_n is the mole fraction of products with n carbon atoms in the organic product fraction, W_n is the mass fraction of products with n carbon atoms, and α is the chain growth probability (Yang *et al.*, 2010b).

The chain growth probability can thus be determined from a semi-logarithmic plot of the mole fraction of the products in the organic product stream as a function of the carbon number. Figure 2-1 shows typical ASF plot for 3 different types of Fischer-Tropsch catalysts. The observed trend is primarily linear with some deviations for the C_1 and C_2 fractions. Methane is probably not formed by the insertion of a C_1 species but by the creation of this species (Dry, 2004). It is thought that methane is formed via different pathway or on separate catalytic sites from chain growth (Schulz *et al.*, 1995). A lower amount of C_2 is observed than predicted by the ideal ASF, accompanied by a lower olefin content, which is possibly due to the highly reactive nature of ethylene. Studies have shown that ethylene can easily be incorporated into growing chain lengths (Dry, 2004).

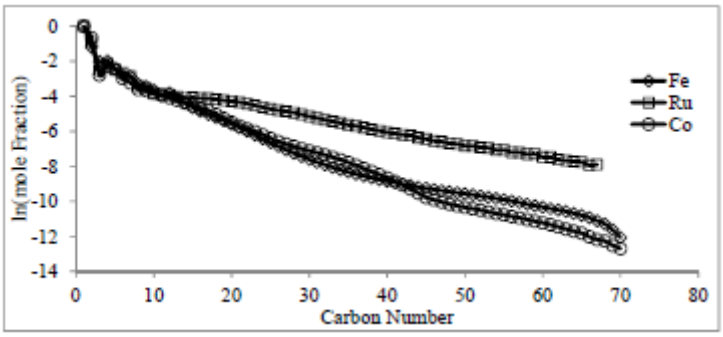

Figure 2-1: Typical ASF plots for iron, ruthenium and cobalt based catalysts (taken from Shafer et al. (2019)

The olefin content decreases with increasing carbon number. This has been linked to higher residence time for high molecular mass olefins than short-chain olefins, due to intraparticle diffusion resistance (Iglesia *et al.*, 1991; Kuipers *et al.*, 1995) as well as increasing solubility with increasing carbon number (Kuipers *et al.*, 1995). Longer residence times may increase the possibility and frequency of re-adsorption and subsequent hydrogenation (Shafer *et al.*, 2019). As carbon number increases, the likelihood for skeletal isomerisation may also increase, as such, the diversity of methyl-branched alkanes increases with an increase in carbon number (Shafer *et al.*, 2019).

The product distribution in Fischer-Tropsch synthesis is governed by the local concentrations of reactants and products and local temperature near catalytically active sites since they govern the rate of chain growth and the rate of desorption. Hence mass limitations may affect the obtained product distribution. Furthermore, the Fischer-Tropsch synthesis reaction is exothermic, (Guettel *et al*., 2008; see eq. 2.1-2.5). Thus, efficient removal of the heat generated by the reaction is key to achieving high selectivity towards long-chain hydrocarbons, since poor heat transfer will result in higher temperatures near the active site. Without effective temperature control, selectivity towards methane, an undesired product increases (Yang *et al.*, 2010b). When optimised, the non-selective nature of Fischer-Tropsch synthesis can be taken advantage of by selecting the catalyst and operating conditions to produce a desired product spectrum (Steynberg *et al.*, 2004). This is advantageous for small-scale Fischer-Tropsch synthesis as plants can be designed to yield certain product spectrums based on local requirements, carbon source availability and trading market demands.

2.2. Catalysts for Fischer-Tropsch synthesis

Four group VIII metals, namely, ruthenium (Ru), nickel (Ni), iron (Fe) and cobalt (Co) exhibit sufficient FT activity for commercial applications (Dry, 2002a). Despite having the highest activity, the high cost and low availability of Ru makes its commercial application infeasible (Dry, 2002a). On the other hand, Ni shows a stronger preference for hydrogenation than chain growth, resulting in very high CH_4 production. Furthermore, the formation of volatile nickel carbonyls at commercially practical pressures and temperatures would result in continuous loss of metal with time (Dry, 2002a). Thus, nickel is not suitable for use in commercial Fischer-Tropsch reactors. Co and Fe have been applied successfully in commercial FT operations (Dry, 2002a). However, CO conversion over Fe-based catalysts is low because they may oxidize to Fe_yO_x at high water partial pressures, which reduces available active sites. Cobalt-based catalysts on the other hand show higher resistance against oxidation due to H_2O (van Berge & Everson, 1997; Van Steen & Claeys, 2008). Thus, cobalt is the preferred metal when high single pass conversion is desired at relatively low space velocities and lower reactor pressures (Van Steen & Claeys, 2008). Cobalt is a suitable metal for LT-FTS with a stoichiometric H_2/CO ratio in the feed and due to its high activity and low intrinsic WGS activity as well as low CO_2 production when compared to Fe-based catalysts, even at high conversion (van Steen *et al.*, 2018).

Cobalt is often supported on highly porous supports such as SiO_2, TiO_2 and Al_2O_3 to achieve high dispersion of active metal, thus maximizing the utilisation of the expensive cobalt (Shafer *et al.*, 2019). Of the three different supports, Al_2O_3 has shown the strongest metal-support interactions (Ma *et al.*, 2011). While sufficiently strong interactions between the active metal and support are required to prevent agglomeration of cobalt nanoparticles, excessively strong support-metal interactions can lead to low reducibility of the catalyst precursor and thus loss in active metal. Thus, promoters such as Pt, Re and Ru are often added to improve the reduction of Co^{2+} to metallic cobalt via hydrogen dissociation and spill-over effect or through a chemical effect (Nabaho *et al.*, 2016; Wang & Chen, 1991). Cobalt loadings of 15-30% are typically applied in industrial catalysts (Lacroix *et al.*, 2011). Due to the high cost of the metal and synthesis gas, the accessibility of active sites to reactants becomes an important consideration to achieve a high conversion.

2.2.1. Deactivation of cobalt FT catalysts

Understanding the deactivation mechanism of a catalyst is important for optimising operating conditions for longevity of the catalyst and to improve catalyst stability. It has been shown that Co-based Fischer-Tropsch catalysts show a 50% decline in activity within a few months (Rytter & Holmen, 2015). Although deactivation can be counteracted by steadily increasing reactor temperature (Rytter & Holmen, 2015), and/or catalyst regeneration, these strategies are limited and eventually become uneconomical.

Deactivation is dependent on the catalyst properties and conditions that the catalyst is exposed to. The deactivation of commercial Co-based low-temperature Fischer-Tropsch catalysts can be thought to occur in two phases: the first is initial sintering that may occur due to exothermic temperature increase at the start of the reaction, the second phase may occur in the long term (Moodley *et al.*, 2009). Proposed mechanisms for the long term deactivation include the formation of stable compounds between cobalt and the support e.g., cobalt aluminate, surface reconstruction, carburisation, carbon deposition, re-oxidation, poisoning and loss of catalyst material via attrition (Rytter & Holmen, 2015).

Sintering and carbon deposition are the primary mechanisms by which industrial Co-based low-temperature Fischer-Tropsch operating at conversions below 60% deactivate (Moodley *et al*., 2009). However, it is also thought that carburisation of cobalt is unlikely in a syngas environment at FT conditions and carbon formed by the Boudouard reaction is likely hydrogenated to a 'CH_2' species (Dry, 2004).

Sintering is the thermally activated coalescence of supported particles. The temperature at which atoms at defects become mobile is called the Hüttig temperature, while the bulk atoms become mobile at the Tamman temperature (Argyle *et al.*, 2014). The Tamman temperature of Co and Pt occur at temperatures significantly higher the operating temperature of low-temperature Fischer-Tropsch reactors and is therefore irrelevant for the deactivation of supported Co catalysts. The Hüttig temperature of Co is higher than the typical operating conditions of low temperature Fischer-Tropsch reactors, see Table 2-1. However, the Hüttig and Tamman temperatures are defined for bulk materials (Argyle *et al.*, 2014). The coalescence temperature could be lower for supported nanoparticles (Argyle *et al.*, 2014). Moreover, axial temperature gradients are typically in the range of 5°C to 20°C in commercial fixed-bed reactors

(Rytter & Holmen, 2015), increasing the likelihood of sintering due to exothermic temperature increase. It has also been shown that the presence of water can encourage agglomeration of cobalt particles (Bartholomew, 2001).

Table 2-1: Hüttig and Tamman temperatures of Co and Pt

Metal	T_{melt} °C	$T_{Hüttig}$ [a] °C	$T_{Tammann}$ [b] °C
Co	1 495	257	611
Pt	1 768	339	747

[a] $T_{Hüttig} = 0.5 \cdot T_{melt}$ (with T in K)

[b] $T_{Tammann} = 0.3 \cdot T_{melt}$ (with T in K)

Re-oxidation of cobalt and formation of Co-support compounds has been reported to be irrelevant under typical Fischer-Tropsch synthesis conditions (Argyle *et al.*, 2014). However, Co-oxide may form at high water partial pressures (Iglesia, 1997). Tsakoumis *et al.* (2010) showed that high partial pressure of H_2O, specifically, CO conversions higher than 65%, can lead to formation of Co-oxides. Furthermore, Van Steen et al. (2005) showed that Co particles with diameters less than 4 nm can oxidise at these levels of conversion.

2.3. Commercial Fischer-Tropsch reactor technology

Current research into Fischer-Tropsch synthesis reactor technology is aimed at improving transport properties for optimised reactor design (Khodakov *et al.*, 2002; Yang *et al.*, 2010; Hooshyar *et al.*, 2012; Liu *et al.*, 2013; Park *et al.*, 2014). Before attempting to optimise transport properties of Fischer-Tropsch synthesis reactors, it is important to understand the technologies in which it is carried out.

Various reactor technologies can be used for Fischer-Tropsch synthesis, however, only a few have found large-scale commercial application. The three leading reactor concepts will be described along with their advantages and disadvantages. However, it is important to note that proprietary modifications have been made to these commercial reactors to improve performance, for example, the use of shaped catalysts to reduce pressure drop in multi-tubular fixed-bed reactors (Steynberg *et al.*, 2004).

2.3.1. Multi-tubular fixed-bed reactors

Figure 2-2 depicts a multi-tubular fixed bed FT reactor. It consists of narrow tubes, in which the FT reaction occurs, and a shell side, through which a cooling medium flows to control the reactor temperature. Multi-tubular fixed-bed reactors are relatively easy to operate and exhibit high liquid product recoveries (Park *et al.*, 2014). They can be scaled-up easily as all the tubes in the reactor are essentially identical. Moreover, the performance of a scaled-up reactor can be predicted with a fair amount of certainty (Steynberg *et al.*, 2004). Examples of commercial multi-tubular fixed-bed reactors are the five ARGE reactors developed by Ruhrchemie and Lurgi in the 1950s for Sasol's Sasolburg plant (South Africa), and the four multi-tubular reactors developed by Lurgi for the Shell Bintulu plant (Malaysia).

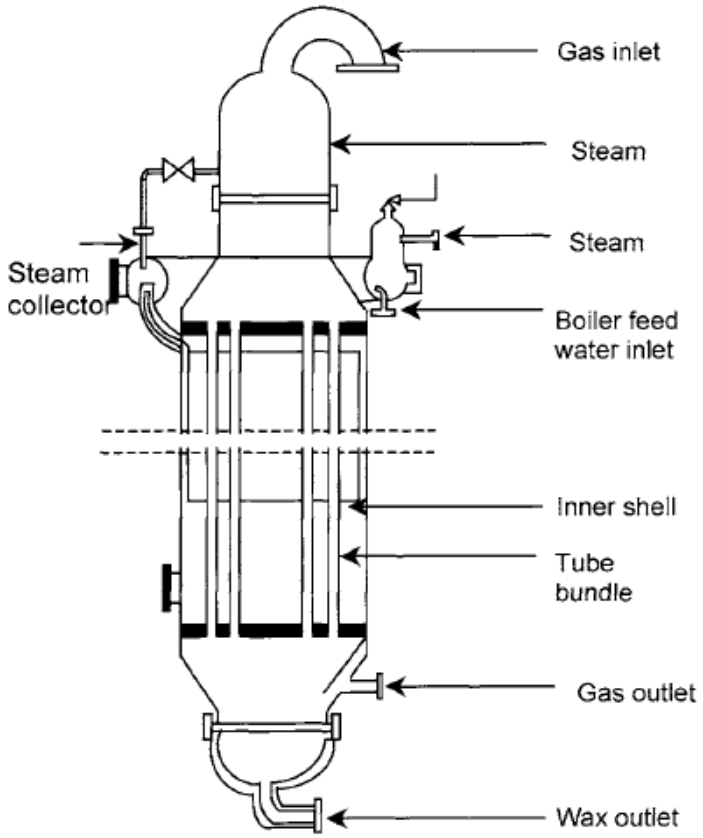

Figure 2-2: Diagram of ARGE reactor (taken from Steynberg et al. (2004)

A portion of the product stream is typically recycled to achieve high overall conversion of fresh feed, increasing space velocity in the reactor tubes (Steynberg *et al.*, 2004). Thus, pressure drop is a major concern for multi-tubular fixed bed reactors (Tijmensen *et al.*, 2002). Gas compression and possible disintegration of weak catalyst pellets can increase FT operating costs (Steynberg *et al.*, 2004). To counteract this, large pellet diameters (~2 mm) are typically used, which may introduce temperature gradients within the catalyst pellets and hotspot formation as well as thermal runaway of the catalyst bed (Liu *et al.*, 2013). This constrains the maximum catalyst activity achievable, as high activity will result in increased heat production per unit mass of catalyst, increased potential for catalyst deactivation, and associated process safety concerns. A common practice to tackle thermal control issues in fixed beds is to dilute the catalyst with a heat conducting inert material to improve the axial and radial heat transfer processes. However, this increases the required reactor volume, a counterproductive solution when attempting to design a compact reactor.

Notwithstanding the disadvantages discussed above, fixed-bed reactors offer the highest catalyst loading per reactor volume and have potential for achieving the highest productivity per reactor volume if temperature control can be improved.

2.3.2. Slurry bubble column reactors

Slurry bubble column reactors (SBCR) are 3-phase reactor systems in which solid catalyst particles are suspended in a continuous liquid, consisting of the FT products, through which the gaseous reactants are bubbled (Adesina, 1996). Heat removal is provided by coils immersed in the reactor vessel. Intense mixing is required to increase heat transfer and ensure a more favourable product distribution. Slurry reactors exhibit lower pressure drops than PBRs (typically 1 atm when compared to 4 atm in PBRs) (Önsan & Avci, 2016). The well-mixed reactor environment allows excellent temperature control, it has been shown that heat transfer coefficients for slurry reactors can be up to five times higher than in packed bed reactors (Steynberg *et al.*, 2004). Thus, uniform temperatures can be maintained throughout the reactor and high single pass conversions can be achieved through high temperature operation (Fratalocchi *et al.*, 2018). SBCRs employ catalyst powders with diameters ranging from 10 μm to 200 μm (Guettel *et al.*, 2008); the combination of good three-phase contact and short diffusion lengths results in good mass transfer. As a result, the reactor product distribution contains low and higher C_{5+} selectivity (Guettel *et al.*, 2008). Furthermore, SBCRs benefit from initial low capital cost due to simple reactor configuration (Adesina, 1996). Slurry bubble column reactors have been demonstrated successfully on an industrial scale by Sasol (Qatar), ExxonMobil, Escravos (Nigeria) and Synfuels China (Steynberg *et al.*, 2004). A diagram representation of a slurry reactor is shown in Figure 2-3.

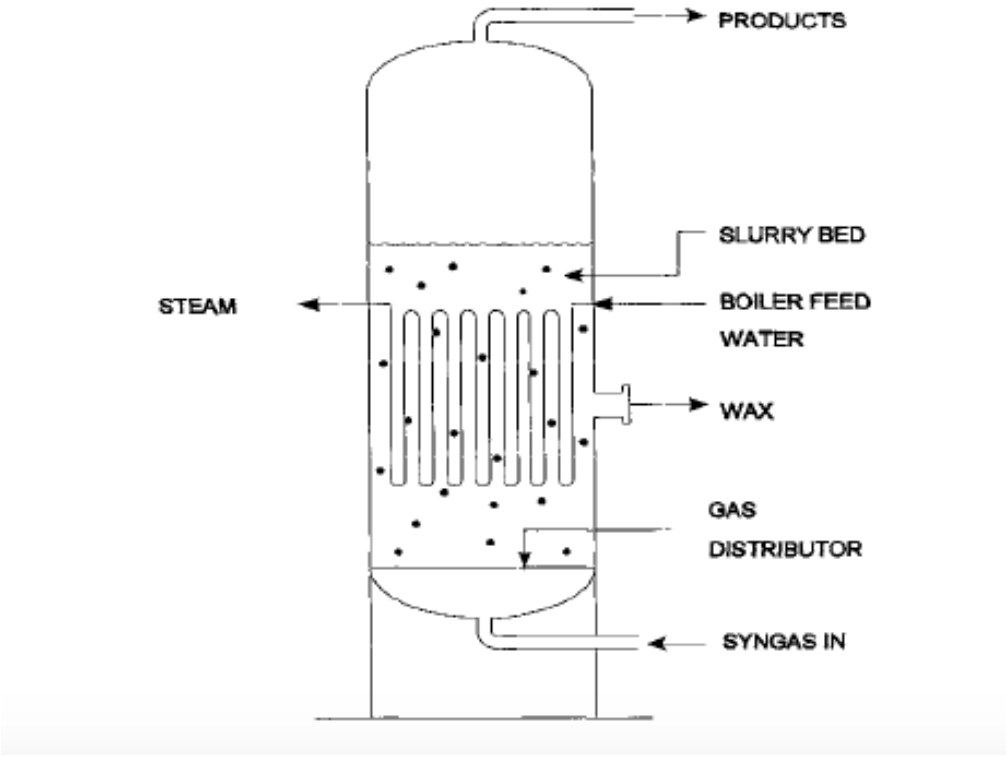

Figure 2-3: Representation of slurry bubble column reactor (taken from Steynberg et al. (2004)

The drawbacks of slurry reactors include severe backmixing and the additional cost of separating the solid catalyst powder from the liquid product (Hooshyar *et al.*, 2012). Moreover, catalyst powders used in SBCRs need to be optimised to withstand mechanical stress, attrition and hydrothermal effects, adding to the cost of the catalyst (Fratalocchi *et al.*, 2018). Unlike fixed bed reactors, which can preserve some of the catalyst when feed gas contains H_2S as the poison is depleted in the anterior end of the catalyst bed, SBCRs experience uniform poisoning of catalyst, and although procedures can be put in place to change the poisoned catalyst relatively quickly, replacing expensive cobalt catalyst due to poisoning still constitutes wasteful expenditure (Steynberg *et al.*, 2004). Regardless, slurry bed reactors are considered to be the most efficient commercial scale reactor for LT-FTS (Schulz, 1999).

2.3.3. Fluidised bed reactors

Fluidised-bed reactors offer excellent heat transfer properties; as a result, they contributed to approximately 90% of FT production in South Africa in 2013 (Liu *et al.*, 2013). However, a major disadvantage for LT-FTS is that the liquid products have been shown to interrupt the fluidisation of the bed by causing particles to agglomerate (Liu

et al., 2013). As a result, they are used primarily for high temperature Fischer-Tropsch synthesis.

2.3.4. Ideal reactor type

Despite their widespread industrial applications, it has been shown that each reactor configuration suffers major drawbacks with respect to productivity, product selectivity or product separation (Hooshyar et al., 2012; Khodakov et al., 2002; Liu et al., 2013; Park et al., 2014; Yang et al., 2010a). An ideal reactor would be one that combines the excellent heat and mass transfer properties of slurry bubble column reactors while maintaining low pressure drop and allowing simple catalyst handling in a fixed bed reactor. To this effect, structured reactor packings have been proposed and studied.

2.4. Structured reactor packings

Structured packings have been used successfully in industrial distillation, absorption columns, combustion, heat exchangers internals and by the automotive industry (Pangarkar et al., 2008; Patcas et al., 2007). To start, different kinds of structured packings can be considered: these include monoliths, corrugated open/closed crossflow packings, knitted packings, and foams (Pangarkar *et al.*, 2008). Although they vary in structure, they all share attractive features, such as low pressure drop, high geometric surface area and enhanced mass and heat transport properties (Pangarkar *et al.*, 2008). A further advantage of structured packings over conventional structured packings is that key parameters such as the shape and size of the packing internals can be designed in detail up to the local surroundings of the catalyst, allowing precision and flexibility (Pangarkar *et al.*, 2008). This means that intrinsic kinetics, mass and heat transfer as well as hydrodynamics can be decoupled and enhanced independently to optimise reactor performance (Pangarkar *et al.*, 2008). In contrast to transport limited pellet-type fixed beds, coating of catalyst and supports onto the walls of structured packings yields shorter diffusion distances, thus reducing mass transfer resistance and increasing catalyst utilisation (Pangarkar *et al.*, 2008). A disadvantage associated with structured packings is that the catalyst loading achieved by coating is usually lower than that in randomly packed fixed beds. However, the loading can be improved by adding multiple layers of coating, and using a structured packing with high geometric area or an integral structured catalyst (Pangarkar *et al.*, 2008). It should however be noted that increasing surface area by increasing pore count has been shown to increase pressure drop (Incera Garrido *et al.*, 2008). Structured packings can be pre-shaped into cartridges for a variety of complicated reactor configurations can simplify reactor loading (Twigg & Richardson, 2007). This makes it possible to purchase pre-formed frames from a commercial supplier. The active catalyst metal can then be loaded onto the foam using various coating techniques.

The high cost of structured packings is a hindrance to their commercialisation. Thus, developing low-cost and efficient structured packings is a critical step towards realising their industrial application for Fischer-Tropsch synthesis.

2.4.1. Monolithic reactors

Monoliths are made up of many identical, parallel channels of about 1 mm in a diameter each (Guettel & Turek, 2009). It is claimed that the geometry of monoliths makes them desirable for gas-to-liquids reactions due to their capacity to achieve high mass transfer coefficients, in addition to offering simple scale-up (Guettel & Turek, 2009). Importantly, pressure drop in monoliths can be three orders of magnitude lower than those observed in packed bed reactors, PBRs (Guettel & Turek, 2009; Önsan & Avci, 2016).The application of monoliths in Fischer-Tropsch synthesis has been studied at laboratory scale (Hilmen et al. (2001); Kapteijn et al. (2005) Liu et al. (2009).

Hilmen *et al.* (2001) compared the performance of washcoated cordierite monoliths with that of fine catalyst powder (38-53 μm) (see Table 2-2). The cordierite monoliths washcoated with Co-Re/γ-Al_2O_3 (catalyst layer thickness = 40 μm) slightly underperform when compared to catalyst powders by 8% in terms of relative catalyst activities. They exhibited similar a product selectivity. Similar results were reported by Liu *et al.* (2009), where the CO conversion achieved over the monoliths was ca. 20% lower than that obtained over the catalyst powder at the same space velocity and temperature. This is likely due to a laminar flow pattern over the flat channels of the monoliths, which would result in higher external mass transfer resistance when compared to packed beds, which have a more tortuosity and thus, better mixing near the external catalyst surface. However, Liu *et al.* (2009) showed that despite the lower conversion in the monoliths, C_{5+} selectivity increased from 69% in the particle bed to 75% in the monoliths. This may be an indication of better internal mass and heat transfer in the monoliths, since being able to keep an H_2/CO ratio similar to that of the bulk gas (H_2/CO =2) inside the catalyst layer may lead to increased chain growth.

Table 2-2: Comparing catalyst performance of powder and washcoated on to monoliths

Study	Morphology	CO conversion	CH_4 selectivity	C_2-C_4 selectivity	C_{5+} selectivity
Hilmen *et al.* (2001) Co-Re/γ-Al_2O_3 210°C, 20 bar H_2/CO = 2	Powder	45.5%	8.3 C-%	9.3 C-%	82.3 C-%
	Monolith	42%	8.9 C-%	8.7 C-%	82.5 C-%
Liu *et al.* (2009) Co-Re/γ-Al_2O_3 220°C, 25 bar H_2/CO = 2	Powder	39%	10 C-%	21 C-%	69 C-%
	Monolith	31%	8 C-%	17 C-%	75 C-%

* The syngas space velocities used to achieve these conversions were not provided in Hilmen *et al.* (2001).

Hilmen *et al.* (2001), Kapteijn *et al.* (2005) and Merino *et al.* (2017) investigated the effect of catalyst layer thickness on reactor performance, i.e., conversion and selectivity. The studies showed that an increase in catalyst layer thickness had no strong effect on conversion or selectivity when the catalyst thickness was less than 50 µm. However, an increase in catalyst layer thickness beyond 50 µm reduced C_{5+} selectivity and increased methane production (Hilmen *et al*., 2001; Kapteijn *et al*., 2005; Merino *et al*., 2017). Hilmen *et al.* (2001) and Merino *et al.* (2017) also reported thermal runaway when catalyst layer thickness was greater than 50 µm, with CH_4 being the main product in these cases. In the study by Merino *et al.* (2017) a 230 CPSI FeCralloy® monoliths coated with 70 µm of 20%Co-0.5%Re/Al_2O_3 catalyst exhibited thermal runaway, with reactor temperature rising above the set temperature of 220°C to 300°C. At this runway temperature, CO conversion reached 100%, with C_{5+} selectivity of 0 C-%, CH_4 selectivity of 75 C-%, and the balance being CO_2 (Merino *et al*., 2017). This is a dramatic shift compared to same monolith when catalyst layer thickness was 44 µm. At this thickness, temperature was controlled at 220°C, C_{5+} selectivity was 65% while CH_4 selectivity was limited at 20 C-%. The effects on temperature control and selectivity were attributed to an increase in internal diffusion limitations with increasing catalyst layer thickness (Hilmen *et al*., 2001; Kapteijn *et al*., 2005; Merino *et al*., 2017). Indeed, the results obtained over the catalysts with washcoat thickness greater than 50 µm are consistent with internal heat and mass transfer resistance, which result in enrichment of H_2 with increasing catalyst layer depth, accelerating the reaction rate. The increased amount of heat being released and accumulated leads to thermal runaway. Under these conditions, CO_2 production increases due to greater extent of the water-gas shift reaction, i.e., $X_{CO} > 80\%$ (Ma *et al.*, 2011), CH_4 production increases due to an increase in availability of H_2 (WGS product) as well as the high reactor temperatures.

Hilmen *et al.* (2005) tried to reduce the temperature runaway experienced with thick catalyst layers coated on a monolith by oil circulation. The oil/product recirculation improved heat transfer, but no improvements in selectivity are realised. Furthermore, the obtained CO conversion was lower (36.4%) and the catalyst was more prone to catalyst deactivation, making this an ineffective method for heat removal (Hilmen *et al.*, 2005). Furthermore, heat management through external heating or cooling is less effective in monoliths than in PBRs due to lack of radial heat transfer by convection, it is suggested that materials with high thermal conductivity can be used to compensate for lacking convective heat transfer (Önsan & Avci, 2016). Attempts have been made to improve temperature control by using monolith materials with high thermal

conductivity. Merino *et al.* (2017) compared the performance of FeCralloy® monoliths with that of aluminium monoliths, FeCralloy® is reported to have an intrinsic thermal conductivity of 16 $W \cdot m^{-1} \cdot K^{-1}$, whereas that of aluminium is 200 $W \cdot m^{-1} \cdot K^{-1}$ (Visconti *et al.*, 2011). Compared to the FeCralloy®, for which C_{5+} production was already negligible at 70 µm, it was shown that a conversion of 11% could be obtained even at a catalyst layer thickness of 90 µm (Pore density = 280 CPSI, SV = 6 $L_N \cdot g_{Cat} \cdot h^{-1}$) when aluminium monoliths were used, with a CH_4 selectivity was 27%, and C_{5+} selectivity was 61%, and no thermal runaway being reported. However, metallic monoliths have been shown to have poor washcoat adherence as well as uneven catalyst coating (Hilmen *et al.*, 2001; Nijhuis *et al.*, 2001).

A key to achieving good reactor performance is to limit catalyst layer thickness, however, it is desired to have high catalyst holdup to ensure high reactor productivity by volume in addition to catalyst mass. Merino *et al.* (2017) pointed out that catalyst loading can be increased by using structures with high geometric surface area, which can also be seen as increasing the cell density.

2.4.2. Open-cell foam reactors

Open-cell foams have a sponge-like structure with tortuous channels. The cells, which are the empty cavities, make up the flow area and are surrounded by interconnected solid material (struts). The openings connecting the cells are called windows (Twigg & Richardson, 2007). Images of a foam structure are shown in Figure 2-4, a & b. They are typically made with pore densities between 10 and 100 pores per inch (PPI). Foams consist of meso- and macro-pores which result in open porosity values between 90% to 92% (Twigg & Richardson, 2007).

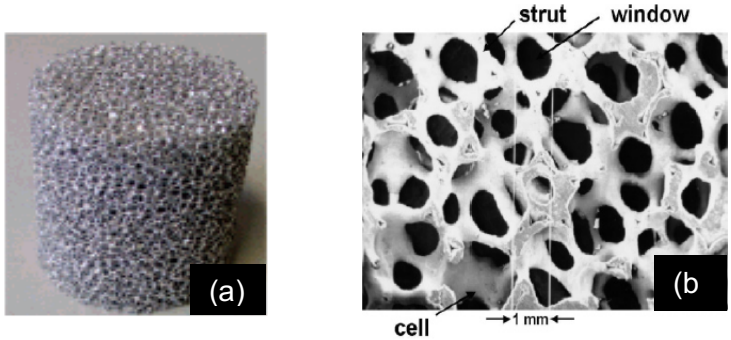

Figure 2-4: Foam structures (a) external structure of aluminium foam (Pangarkar *et al.*, 2008) and (b) internal ceramic foam structure (Twigg & Richardson, 2007).

Different processes for the manufacture of foams exist. The three most common methods are the reticulated sponge method (also known as the replica method), gel casting and hollow beads method. The reticulated sponge method is the most popular method for producing commercial foams and was first patented by Schwartzwalder and Somers (Twigg & Richardson, 2007). The frame of the foam structure is provided by a sponge-like organic polymer, polyurethane being the most popular and readily available in a variety of cell sizes and cell densities (Twigg & Richardson, 2007). An aqueous slurry containing ceramic particles with diameters between 0.1 to 10 μm, wetting agents, dispersion stabilisers and viscosity modifiers is poured into the walls of the polymeric foam. After drying the polymeric material is burnt off in a carefully controlled calcination process, leaving behind a ceramic replica of polymer foam (Twigg & Richardson, 2007). Alternatively, a slurry with a higher viscosity is poured into the cells of the polymeric foam, such that a ceramic foam that is a negative replica of the polymeric material is formed (Twigg & Richardson, 2007). Suspensions with a low viscosity result in foams with low mechanical strength, high porosity and large pores; whereas highly viscous slurries result in foams with high mechanical strength, lower porosity and smaller pore sizes (Twigg & Richardson, 2007). In the second method, a foaming agent is added to a ceramic suspension, the mixture is foamed by "mechanical action", it is then dried, calcined and sintered. The third method involves the coating of different organic/polymeric with a slurry containing ceramic material, the coated beads are then dried and calcined (Binner, 2005). Coated beads are joined together by second slurry coating, dried, calcined and sintered (Binner, 2005). The third method can result in predominantly open-celled or closed-cell foams depending on the relative amount of slurry and beads used (Binner, 2005). The choice of preparation method has an effect on the structure's mechanical strength, pore size and porosity (Twigg & Richardson, 2007). Ultimately, the cell density, strut thickness and cell size are primarily dictated by the porosity of the starting [polymeric] material.

As with monoliths, foams have a low BET surface area, thus a highly porous secondary support must be coated onto the commercial substrate. The secondary supports also forms an adherent layer that prevents the loss of the catalyst due to flaking that would otherwise occur because of the differences in the thermal expansion coefficients of the catalyst layer and the substrate (Giani *et al.*, 2006).

Foams offer low pressure-drop due to the high porosity, they have large geometric surface area and good transport properties, making them attractive for exothermic or endothermic reactions in long, narrow reactor tubes where pressure drop is prevalent.

The benefits of foams have already been demonstrated in several applications, such as reforming of carbon monoxide (Richardson *et al.*, 2003a), catalytic oxidation of CO (Giani *et al.*, 2005; Garrida *et al.*, 2008), and Fischer-Tropsch synthesis (Chin *et al.*, 2005). Existing work regarding foams is focused on highlighting intensified catalytic performance due to enhanced heat and mass transfer properties, a few of those studies are summarised and discussed in this section.

Loading a heat conducting diluent mixed in with the catalyst, such as SiC may promote isothermal conditions and prevent thermal runaway in the catalyst bed. As a proposed improvement to this, Lacroix *et al.* (2011) and Fratalocchi *et al.* (2018) have shown that foams made from highly conductive materials can be used as a heat sink for removing heat generated during the Fischer-Tropsch synthesis. Lacroix *et al.* (2011) compared the performance of a Co-based catalyst supported on a SiC foam with that supported on an Al_2O_3 foam for Fischer-Tropsch synthesis in a fixed bed reactor. The C_{5+} selectivity of the two catalysts was similar (~ 83-84%) at low space velocity, however, the CO conversion achieved over the Al_2O_3-based foam was lower at 42% when compared to the SiC foam, which was 64%. However, when operating at higher conversions, the C_{5+} selectivity obtained over the SiC supported catalyst (80%) was higher than the Al_2O_3 catalyst (54%), at CO conversions of 71% and 77% for Co/SiC and Co/Al_2O_3 respectively (Lacroix *et al.*, 2011). The study further showed that SiC foams have the potential to be reused without compromising reactor performance, as the SiC material is inert and can be recovered by an acid wash (Lacroix *et al.*, 2011). Fratalocchi *et al.* (2018), filled the cells of a 40 PPI aluminium foam structure with 23%Co-0.1%Pt/Al_2O_3 catalyst. The Fischer-Tropsch synthesis performance of this packing was compared with that of a randomly packed bed of the same catalyst diluted with α-Al_2O_3 of the same particle diameter as the catalyst (300 µm). The results of the experiment showed superior thermal control in the presence of a packed foam than in the randomly-packed bed as the packed foam reactor could be operated isothermally at temperatures up to 240°C, while thermal runaway occurred in the randomly-packed bed at a temperature as low as 195°C (Fratalocchi *et al.*, 2018). CO conversion of 45% and 68% were obtained at 220°C and 240°C respectively. However, it is worth noting that the enhanced performance of the packed-foam reactor when compared to that of the randomly-packed bed could be due to the difference in the thermal conductivity of the different diluents used, the aluminium of the foam structure vs the Al_2O_3 particles to dilute the powder catalyst. The authors argue that filling the pores of the catalyst increases catalyst hold-up in the bed volume. Park *et al.* (2014) designed a shell-and-tube reactor concept that featured a foam with high thermal conductivity in the tube-

side, and hot oil circulation in the shell-side to control reaction temperature. The 10 PPI nickel foam was washcoated with an 8 wt.% Co catalyst supported on γ-Al_2O_3. The foam showed higher C_{5+} production at 98.7 $ml \cdot kg_{Cat}^{-1} \cdot h^{-1}$ than Co/ γ-Al_2O_3 pellets with a diameter of 50 mm, which only produced 33.2, the foam showed higher at 98.7 $ml \cdot kg_{Cat}^{-1} \cdot h^{-1}$ at similar space velocity. When tested in a normal fixed bed (i.e., without oil circulation for temperature control, the foam still produced more C_{5+} than the pellet at 86.7 $ml \cdot kg_{Cat}^{-1} \cdot h^{-1}$. The improved performance was attributed to enhanced heat and mass transfer process.

While typical flow patterns in the uniform channels of honeycomb monoliths and micro-structured reactors are laminar, it is often claimed that the extensive tortuosity of open-cell foam structures results in turbulent flow, leading to enhanced radial mixing, and thus, better mass transfer (Richardson *et al.*, 2003; Patcas *et al.*, 2007). To support this claim Patcas *et al.* (2007) reported that the mass transfer coefficients of foams during CO oxidation over Pt/SnO_2 catalyst lie between those of honeycomb monoliths and packed beds. Furthermore, foams outperformed monoliths in terms of radial temperature gradients.

Randomly packed beds experience large temperature gradients due to few contacts points for heat conduction between catalyst pellets, thus, gas phase convection is the primary mechanism for heat transfer to the reactor wall (Merino *et al.*, 2017). In contrast, the networks created by the walls of structured reactors allow for both conduction and convection to facilitate heat removal (Merino *et al.*, 2017). Therefore, the effective thermal conductivity of the structured packing substrate plays a significant role in ensuring that the expected heat transfer enhancement is realised.

Substrate materials were compared with respect to thermal conductivity. The thermal conductivities of different materials were obtained from literature and are shown in Table 2-3. It is known that metals usually have superior heat transfer characteristics than ceramics, for example, metallic foams have been used as compact heat sinks in microelectronic devices such as computer chips (Pangarkar *et al.*, 2008). However, long term durability is compromised for metallic substrates due to weaker adherence of the catalyst layer to the walls when compared to ceramic substrates (Pangarkar *et al.*, 2008). Silicon carbide has high thermal conductivity, high mechanical strength, low thermal expansion coefficient, high chemical inertness and oxidative resistance and has high thermal stability (Lacroix *et al.*, 2011; Liu *et al.*, 2013), therefore, open cell silicon carbide foams satisfy the requirements of an industrial catalyst support.

Table 2-3: Thermal conductivities of substrate materials (taken from Wallard *et al.*, 2017)

Material	Thermal conductivity at 373.2 K [$W \cdot m^{-1} \cdot K^{-1}$]	Thermal conductivity at 573.2 K [$W \cdot m^{-1} \cdot K^{-1}$]
Pure metals		
Cobalt	89	69
Aluminium	240	233
Nickel	83	67
Iron	72	56
Refractory materials		
Alumina (Al_2O_3)	35	
Zirconia (ZrO_2)	1.8	
Silicon carbide (SiC)	90	

Park *et al.* (2014) coated a metallic foam ready-made Co/ γ-Al_2O_3 catalyst. The cobalt catalyst powder was made into a slurry by mixing it with 10-11 wt.% alumina solution and isopropyl alcohol. After dipping and removal of excess liquid, the foam was dried at 120°C for 4 h and then calcined at 400°C for 8 h. Similarly, Hilmen *et al.* (2001) coated Co-Re/ γs-Al_2O_3 catalyst on a cordierite monolith. Both groups reported good dispersion of cobalt metal on the walls of the structured support.

An important consideration is that the thickness of layers added to the foam frame may alter pore density and size distribution, as washcoats can fill or even block smaller pores, as well as decrease the pore size of larger pores (Richardson et al., 2000). The challenge with commercial foams is that the quoted pore density often reflects the pore density of the polymeric precursor used to manufacture the foam, and gives a range of pore sizes which have been shown to vary widely from the measured mean pore diameter (Sweeting *et al.*, 1994). This is a concern because a wide pore distribution already exists in commercial foams and may have an effect on the expected pressure drop reduction (Richardson *et al.*, 2000). Caution must be used when using commercial foams in reactor testing and pore sizes should be re-evaluated after coating.

2.5. Hydrodynamics and transport phenomena

Transport phenomena play an important role in the performance of a catalyst during a chemical reaction. As seen in Sasol's commercial fixed bed reactors, diffusion resistances may lead to decreased reactor productivity and reduced selectivity towards high chain hydrocarbons and olefins (Steynberg *et al.*, 2004). The extent of these resistances can be quantified using the effectiveness factor, a measure of the deviation of the observed reaction rate from the intrinsic surface reaction rate.

2.5.1. External mass transfer limitations

The diffusion of reactants from the bulk gas phase through the fluid film surrounding the catalyst surface to the external surface of the catalyst particle may be hindered by external mass transfer resistance. External mass transfer resistance is affected by the extent of mixing of the fluid phase near the outer surface and the effective diffusivities of individual components in the fluid.

Evidence has shown that at the reactor operating conditions, 20 bar and 220°C, liquid products may form in the pores and on the external surface of the catalyst (Liu *et al.*, 2009; Biquiza *et al.*, 2010). Trickling of the liquid due to gravity and convection results in a steady-state thickness of the liquid layer. Reactants and some of the volatile products will dissolve in this liquid. Thus, diffusion of reactants and products between the bulk gas phase and catalyst surface through this liquid boundary is likely to result in external mass transfer resistance. The majority of industrial co-current fixed-bed reactors operate in the film or trickle flow regime (Pangarkar *et al.*, 2008). In monoliths, two distinct flow patterns are encountered in monoliths, viz. film flow and Taylor or slug flow. Film flow occurs at low liquid velocities and intermediate gas velocities. It consists of a film covering the channel wall surface with gas flow in the open void space (see Figure 2-5). This flow pattern is associated with low mass transfer rates (Pangarkar *et al.*, 2008). At higher liquid velocities, flow in monolith channels transitions into the Taylor flow regime, which is characterised by elongated capsule-shaped gas bubbles separated from the channel wall by a thin film and from each other by liquid slugs (Pangarkar *et al.*, 2008). Channel diameters of less than 2mm are required for Taylor flow (Pangarkar *et al.*, 2008). This flow pattern is associated with enhanced mass transfer due to greater interaction between the gas and liquid phases (Pangarkar *et al.*, 2008). Similar to particle-bed reactors, foams are likely to operate in the trickle flow regime at low liquid velocities and pulse flow at high liquid patterns (Pangarkar *et al.*, 2008).

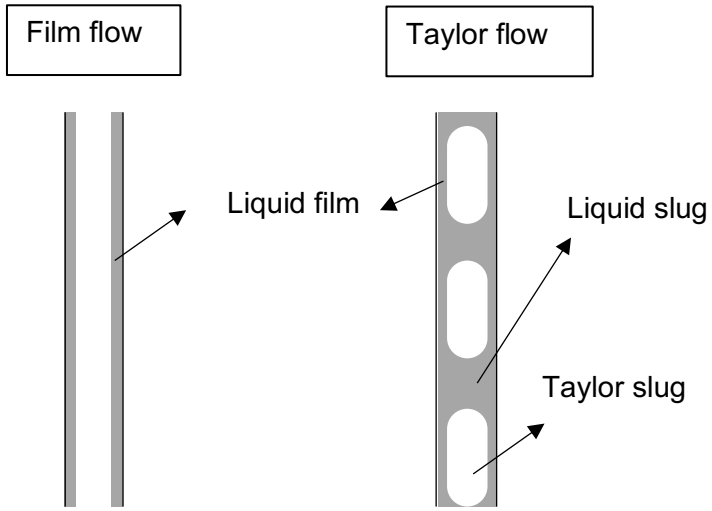

Figure 2-5: Film flow and Taylor/slug flow pattern in monolith channel

In film flow, mass transfer rates are related to the catalyst wetting efficiency, which increases with increasing gas velocity and pressure. An increase in superficial gas velocity causes the fluid film to be thinner, such that the reactant concentration on the surface of the catalyst surface is closer to that in the bulk phase. This was demonstrated by Yang *et al.* (2010b) who performed catalytic tests over Co/γ-Al_2O_3 catalyst and reported an increase in CO conversion with an increase in superficial syngas velocity. This was also accompanied by improved temperature control. On the other hand, Taylor flow is dominated by surface tension. Thus, increasing gas velocity increases the thickness of the liquid film, thus decreasing the rate of mass transfer (Pangarkar *et al.*, 2008).

2.5.1. (A) **Mass transfer correlations**

Mass transfer properties can be quantified in the form of the dimensionless Sherwood number, which is a ratio between the total mass transfer and mass transfer due to film diffusion. It can be related to the hydrodynamic properties of the catalyst system (Reynolds number), and the fluid properties (Schmidt number) (Groppi *et al.*, 2008). Various studies have developed mass transfer correlations for particle-beds, monoliths and foams (see e.g., the review paper by Pangarkar *et al.*, 2008). In equations 2-12 to 2-15, *Sh* is the Sherwood number, *Re* is the Reynold's number, *Sc* is the Schmidt number, k_g is the gas mass transfer film coefficient (convection), d_p is particle diameter, $D_{A,m}$ is mass diffusivity, U_o is superficial gas velocity and *v* is the kinematic viscosity.

$$Sh = 2 + 1.1 \cdot Re^{0.6} \cdot Sc^{\frac{1}{3}} \quad \text{2-12}$$

$$Sh = \frac{k_g \cdot d_p}{D_{A.m}} \quad \text{2-13}$$

$$Re = \frac{U_o \cdot D_p}{v} \quad \text{2-14}$$

$$Sc = \frac{v}{D_{A,B}} \quad \text{2-15}$$

Knowing the external mass transfer coefficient, the extent of external mass transfer limitations can be estimated using the Carberry number (Ca). External mass transfer resistance is negligible if the Carberry number is less than 0.05 for a first order reaction (Mears, 1971).

$$Ca = \frac{-{r_A}^{obs}}{k_m \cdot S_v \cdot C_{A,b}} = \frac{C_{A,b} - C_{A,s}}{C_{A,b}} < \frac{0.05}{n} \quad \text{2-16}$$

where ${-r_A}^{obs}$ is the reaction rate based on conversion of A, $k_m$is the film diffusion coefficient, S_v is the specific volumetric external surface area of a catalyst particle (taken as $\frac{6}{d_p}$ for spherical particles), n is the reaction order and $C_{A,b}$ and $C_{A,s}$ are the bulk and surface concentrations of A respectively.

2.5.1. (B) **Monoliths**

Mass transfer coefficients in film flow in a monolith are a strong function of the liquid hold up (β_L) and the hydraulic diameter (d_h) which are variable across different monoliths and applications (Pangarkar *et al.*, 2008). The liquid hold-up for co-current downflow in film flow can be correlated with (Heibel *et al.*, 2003):

$$\beta_L = \left(\frac{{Fr_L}^2}{Re_L}\right)^{0.46} \quad \text{2-17}$$

with Fr_L as the Froude number for the liquid film, i.e., the ratio of inertial and gravitational forces, and Re_L is the Reynolds number for the liquid flow. The Froude number can be obtained from:

$$Fr_L = \frac{u_L}{\sqrt{g \cdot d_h}} \quad \text{2-18}$$

with u_L and g as the superficial liquid velocity and gravitational acceleration, and d_h the hydraulic diameter

Lebens *et al.* (1999) proposed a theoretical correlation to describe gas-liquid mass transfer in film flow (equation 2-19 and 2-20) for counter-current flow systems. However, it is uncertain whether this correlation is valid for co-current downflow systems.

$$Sh = 1.04 + 0.35 \cdot Gz^{0.63} \quad \text{2-19}$$

$$Sh = \frac{\delta^2 \cdot u_L}{Z \cdot D_L} \quad \text{2-20}$$

with Gz is the Graetz number

$$Gz = \frac{Re_L \cdot Sc_L \cdot \delta}{H} \quad \text{2-21}$$

with δ the film thickness, Z the column height (or length of the monolith), and H is flow distance.

A mass transfer correlation suitable for co-current downflow in monoliths under Taylor flow conditions was developed by Bercic & Pintar (1997):

$$k_L a_e = \frac{0.133 \cdot {u_{TP}}^{1.2}}{{L_{Slug}}^{0.57}} \quad \text{2-22}$$

with k_L the liquid-side mass transfer coefficient, a_e is the gas-liquid mass transfer area, L_{Slug} is the slug length while u_{TP} is the total linear velocity through a channel and consists if the liquid velocity (u_L) and the gas velocity (u_g).

This correlation (equation 2-21) cannot be used to determine the mass transfer coefficient in a film flow system at low flow rates as it has been shown that mass transfer correlations developed at high flow rates (Taylor flow) do not adequately describe mass transfer at low flow rates (film flow) (Heiszwolf *et al.*, 2001)

It should be realized that most mass transfer correlations have been developed using water as a liquid under non-reacting conditions. The liquid products produced in the Fischer-Tropsch synthesis are more viscous than water. Thus, flow transition from film

flow to Taylor flow may occur at lower linear gas and liquid velocities than those predicted using water-based correlations (Pangarkar *et al.*, 2008). Furthermore, the liquid flow rate slows down at the corners of the channels, resulting in lower than predicted gas-liquid interactions (Pangarkar *et al.*, 2008). Thus, mass transfer correlations for square channel monoliths have a large error.

2.5.1. (C) **Open-cell foams**

Mass transfer properties of foams can be predicted with correlations based on dimensionless numbers and foam geometry (Richardson *et al.*, 2000; Richardson *et al.*, 2003; Groppi *et al.*, 2007; Incera Garrido *et al.*, 2008). Incera Garrido *et al.* (2008) developed a correlation to describe the mass transfer properties in foams. In addition to the dimensionless Reynolds and Schmidt numbers, they proposed a dimensionless factor F_g, that accounts for the contribution of the non-uniform geometry of the foams cellular structure:

$$Sh = 1 \cdot Re^{0.47} Sc^{\frac{1}{3}} F_g \quad \text{2-23}$$

$$F_g = \left(\frac{D_p}{0.001 \cdot m}\right)^m \cdot \epsilon_h^n \quad \text{2-24}$$

where is ϵ_h is the hydrodynamically relevant porosity of the foam. m and n are fitting parameters, which Incera Garrido et al. (2008) determined to 0.58 and 0.44 respectively.

The correlation was developed for cordierite foam. However, the authors also tested the correlation on experimental data for metallic foams and found that the predicted values were accurate within a 6% error (Incera Garrido *et al.*, 2008).

2.5.2. Internal mass transfer limitations

In LT-FTS, a large amount of the reaction products are liquids, causing the pores to fill with liquid (Steynberg *et al.*, 2004). The diffusion coefficients of H_2 and CO can be three to five orders magnitudes lower in a liquid medium than in gas (Hilmen *et al.*, 2001; Liu *et al.*, 2009). However, the diffusivity of CO is lower than that of H_2, resulting in an enrichment of H_2 towards the centre of the catalyst particle in comparison to the external surface of the catalyst particle (Stern *et al.*, 1983). As a result, the reaction rate at the centre of the catalyst may be faster than the reaction on the external catalyst surface, resulting in concentration and temperature gradients through the pellets. Furthermore, since a high H_2/CO ratio causes increased hydrogenation and chain

termination, low C_{5+} selectivity and low olefin content are expected in the presence of internal mass transfer limitations (Stern *et al.*, 1983; Bukur *et al.*, 2012). On the other hand, the α-olefin re-adsorption model posits that C_{5+} selectivity is increased by internal mass transfer resistance slowing the removal of reactive molecules such as α-olefins (Iglesia *et al.*, 1991). Other studies have disputed this model and suggested that the decline in O/P ratio with increasing carbon number is an effect of strong physisorption rather than re-adsorption, supported by kinetic modelling studies which show that O/P ratios are independent of re-adsorption (Kuipers *et al.*, 1995; Rytter *et al.*, 2016).

The extent of internal mass transfer resistance is closely linked to the particle size which serves as an equivalent to diffusion distance. Rytter *et al.* (2016), showed that C_{5+} selectivity decreases with an increase in particle size. The decrease in C_{5+} selectivity was ascribed to the difference in the diffusion rates of CO and H_2 in liquid filled pores. Similarly, Post *et al.* (1989) investigated effect of particle size (220 μm – 2.6 mm) on internal mass transfer limitations over a Fe- and Co-based LT-FTS catalyst and found that the conversion of CO decreased with an increase in particle size. Since diffusion distance increases with particle size, mass transfer resistance also increases with increasing particle size, negatively affecting conversion and selectivity.

Iglesia (1997) developed a structural parameter χ, which accounts for the effect of the catalyst structure on product selectivity. As seen in (equation 2-25), χ is proportional to the square of the diffusion length, L. C_{5+} selectivity increases with an increase in χ, however, it is also shown that going to very large values of χ results in decreases the C_{5+} selectivity (Claeys & van Steen, 2004). This is attributed to increased formation of methane due to H_2 enrichment. L is the diffusion distance, ε is the porosity, θ_{me} is the active metal density, and r_p is the pore radius.

$$\chi = \frac{L^2 \cdot \varepsilon \cdot \theta_{me}}{r_p} \qquad 2\text{-}25$$

Increase in particle size increases the residence time, increasing the likelihood of secondary hydrogenation, such that the formation of alkanes is favoured over that of olefins.

Regardless of the mechanism, it is reasonable that residence time in the catalyst pores plays a role in product selectivity, i.e., some degree of internal mass transfer is required to ensure chain growth, while also leading to lower olefin to paraffin ratio. However,

since the shortage of CO will result in hydrogenation being favoured over chain propagation, excessive internal mass transfer resistance can result in a product distribution characterised by short-chain hydrocarbons and a decreased reaction rate.

The degree of internal mass transfer resistance can be quantified using the Weisz-Prater criterion (Froment, 2011):

$$\Phi = \frac{-r_A{}^{obs}}{D_{\mathrm{A}}^{Eff} \cdot C_{CO,s}} L^2 \quad \text{2-26}$$

$$\Phi = \eta\phi \quad \text{2-27}$$

$$\phi = L\sqrt{\frac{k \cdot \rho_s}{D_A^{Eff}}} \quad \text{2-28}$$

$$\eta = \frac{3}{\phi}\left(\frac{1}{tanh\ \phi} - \frac{1}{\phi}\right) \quad \text{2-29}$$

$$D_{\mathrm{A}}^{Eff} = \frac{\varepsilon}{\tau} D_{\mathrm{A,B}} \quad \text{2-30}$$

In equation 2-27 and 2-26, Φ is the Weisz modulus, η is the effectiveness factor, ϕ is the Thiele modulus, $C_{A,s}$ is the concentration of reactant A on the catalyst surface and D_{A}^{Eff} is the effective diffusivity of reactant A in the catalyst particle. L is the ratio of catalyst volume to external surface area (Froment, 2011).

2.5.3. Heat transfer limitations

During exothermic chemical reactions, heat is generated by the chemical reaction occurring in the catalyst particles, leading to an increase in reactor temperature.

High temperatures lead to increase methane and CO_2 production (Adesina, 1996) as these products are thermodynamically favoured at high temperatures, with a heat of reaction of -214 kJ·mol^{-1} at 250°C for CH_4 formation (Claeys & van Steen, 2005). High rates of heat removal are desired to prevent temperature elevations that can negatively impact selectivity, and even cause thermal decomposition of the catalyst as well as carbon deposition (Adesina, 1996; Önsan & Avci, 2016). Inefficient removal of heat due to heat transfer limitations causes internal temperature of the particles to become higher than that of the surrounding fluid. Because of their higher density, liquid products on the catalyst surface and within catalyst pores can aid in the removal of heat generated by the reaction. However, at the elevated temperatures, the production

of liquid hydrocarbons decreases in favour of gaseous products, which are not as effective at removing heat (Lacroix *et al.*, 2011). Further accumulation of heat in the catalyst particle can cause hotspots, accelerating the reaction rate. Note that while this may present as an increased effectiveness factor, the rate of transfer of reactants from the bulk gas to the external catalyst surface remains sluggish in comparison to the surface reactions, causing external mass transfer to become rate limiting (Levenspiel, 1993).

The external heat transfer limitation can be expressed by the Mears criterion as shown in equation 2-30. The effect of external heat transfer limitations can be said to be negligible if the effectiveness factor is decreased less than 5% for a first order reaction.

$$\Delta T_{film} = \frac{r_A^{obs} \cdot |\Delta H_{rxn}| \cdot d_p}{6 \cdot \alpha_p} < \frac{0.05 \cdot R \cdot T_g}{E_a} \quad \text{2-30}$$

where ΔH_{rxn} is the molar heat of reaction based on the conversion of A, α_p is the heat transfer coefficient between the particle and the bulk fluid, R is the ideal gas constant, T_g is the bulk gas temperature, and E_a is the experimental activation energy. α_p can be estimated by a correlation by Wakao *et al.* (1979) which has been validated for Reynold's numbers between 0.1 and 100.

$$Nu = 2 + 1.1 \cdot R_e^{0.06} \cdot Pr^{\frac{1}{3}} \quad \text{with} \quad Re = \frac{U_o \cdot D_p}{v} \quad \text{2-31}$$

$$\mathrm{Pr} = \frac{C_{p,g} \cdot \mu_g}{\lambda_g} \quad \text{2-32}$$

$$Nu = \frac{\alpha_p \cdot d_p}{\lambda_g} \quad \text{2-33}$$

Nu is the Nusselt number, Pr is the Prandtl number, $C_{p,g}$ is the gas heat capacity and λ_g is the thermal conductivity of the gas mixture.

Internal heat transfer limitation can be neglected if the following criterion is satisfied.

$$\Delta T_{int} = \frac{r_A^{obs} \cdot |\Delta H_{rxn}| \cdot {d_p}^2}{60 \cdot \lambda_p} < \frac{0.05 \cdot R \cdot T^2}{E_a} \quad \text{2-34}$$

with ΔT_{int} as the difference between the surface and average internal temperature of the catalyst particle, $|\Delta H_{rxn}|$ as the absolute value of the reaction enthalpy, R as the

ideal gas constant, and T as the temperature of the bulk fluid. E_a is the apparent activation energy. The thermal conductivity of the catalyst particle (λ_p) can be estimated from the volume-weighted average of thermal conductivity resistances of the catalyst particles (λ_{cat}) and the dilution particles (λ_{dil}).

$$\frac{1}{\lambda_p} = \frac{1-x}{\lambda_{cat}} + \frac{x}{\lambda_{dil}} \quad \text{2-35}$$

2.5.4. Pressure drop and geometric properties of ceramic foams

Richardson *et al.* (2000) reported that the pressure drop over ceramic foams can be approximated by Forscheimer equation with Ergun expression for the Forscheimer coefficient, the equation is shown below:

$$\frac{\Delta P}{L} = a_0 u + a_1 u^2 \quad \text{2-36}$$

where $\frac{\Delta P}{L}$ is the pressure drop per unit length, u is the superficial velocity and a_0 and a_1 are constants which represent viscosity and turbulence contributions to flow resistance respectively, as defined by Ergun & Orning (Richardson *et al.*, 2000; Pangarkar *et al.*, 2008). The values of a_0 and a_1 are dictated by the characteristics of the foam and fluid properties, see equations 2-37 and 2-38. The factor 'α' depends on the geometry and packing of the particles, Ergun and Orning recommended a universal value of $\alpha = 4.17$. S_v is the geometric surface area per unit volume of solid, μ is viscosity and ρ is the density of the fluid (Richardson *et al.*, 2000). ε is the voidage. Thus, the pressure drop predicted by this correlation can be compared to the pressure drop obtained experimentally in order to validate the flow characteristics.

$$a_0 = \frac{\alpha S_v^2 \mu (1-\varepsilon)}{\varepsilon^3} \quad \text{2-37}$$

$$a_1 = \frac{\alpha S_v \rho (1-\varepsilon)}{\varepsilon^3} \quad \text{2-38}$$

Specific geometric surface area, defined as the total external surface area of the substrate, is easily determined for the straight channels of the monoliths. In contrast, the wide distribution in strut thickness, cell size and shape, as well as the uneven distribution of pore density along the length and cross section of the foam result in an irregular geometry, making the estimation of foam S_v more difficult. In addition, burning

of the polymeric template during the manufacturing process of these reticulated structures may result in the formation of hydrodynamically irrelevant internal pores in addition to the void space surrounding the struts, such that ordinary methods like N_2-adsorption cannot be used to measure the surface area (Incera Garrido *et al.*, 2008). However, they showed that Hg Intrusion and MRI can be used to measure S_v. S_v can also be estimated from theoretical models that assume regular unit cells. One of these models was proposed by Gibson & Ashby (1988) and is based on tightly packed tetrakaidekahedra (TTKD). The tetrakaidekahedral unit cell contains 14 faces (windows), 6 of which are square and 8 are hexagonal, the windows are bordered by triangular struts (Richardson *et al.*, 2000). However, the model has been shown to overestimate the geometric surface area as it does not account for the variation in strut thickness and the accumulation of solids along the cross-section of the foam (Incera Garrido *et al.*, 2008; Lacroix *et al.*, 2011).

$$S_{geo,TTKD} = \frac{4.82}{D_p}\sqrt{\frac{\rho_{bulk}}{\rho_{solid}}} = \frac{4.82}{D_p}\sqrt{1-\epsilon} \qquad \text{2-39}$$

where D_p is the characterising length used for foams and is the sum of the average inner pore diameter d_p and the strut size d_t.

2.6. Washcoating of structured catalysts

The bare monoliths and foams are not suitable for deposition of active metal because they have low specific area (Nijhuis *et al.*, 2001; Pangarkar *et al.*, 2008; Lacroix *et al.*, 2011). Thus, the active metal must be deposited in a secondary support with a high specific area. This can be done by impregnating the secondary support with the catalyst precursor and washcoating the calcined catalyst on the substrate. Alternatively, the secondary support can be coated onto the structured substrate first, followed by deposition of the active metal (Nijhuis *et al.*, 2001). The benefit of the former method is that it established and tested catalyst characterisation methods can be used. Furthermore, more uniform distribution of the precursor can be achieved.

The deposition of prepared catalyst on the surface of monoliths is has been widely studied (Blachou *et al.*, 1992; Agrafiotis & Tsetsekou, 2000; Nijhuis *et al.*, 2001; Valentini *et al.*, 2001). The coating of foams with secondary support and active metal can be accomplished using similar techniques as those used commonly for monoliths (Richardson *et al.*, 2000; Giani *et al.*, 2006). However, achieving a homogeneous coat on foams can be more difficult due to their tortuous structure (Giani *et al.*, 2006).

Coating methods can be classified into two basic groups: the first is pore filling, where the catalyst partially fills the macropores of the substrate. The other is a deposition method, where a layer of the support and active metal is formed on the channel walls (Nijhuis *et al.*, 2001). A schematic representation of the two groups of coating methods is shown in Figure 2-6. The pore filling method offers stronger adherence of catalyst to the structured substrate. However, since the available macropore volume is limited, the amount of catalyst that can be loaded within those macropores is also limited. The pore filling method also introduces longer diffusion paths (Nijhuis *et al.*, 2001), which may retard internal heat and mass transfer. In contrast to the pore filling method, the amount of catalyst that can be coated on the structured substrate using the deposition method is only limited by the geometric surface area and the flow channel volume (or diameter), thus, significantly more catalyst can be applied using deposition, albeit with difficulty in ensuring good adherence of the layer with the substrate. Furthermore, coating by deposition on the walls of the of the structured substrate results in shorter diffusion lengths since a thin layer of catalyst can be coated on the substrate instead of being distributed through the macropores of the relatively thick channel walls or struts (in the case of foams). (Nijhuis *et al.*, 2001). Ultimately, the choice of coating method used depends on the application.

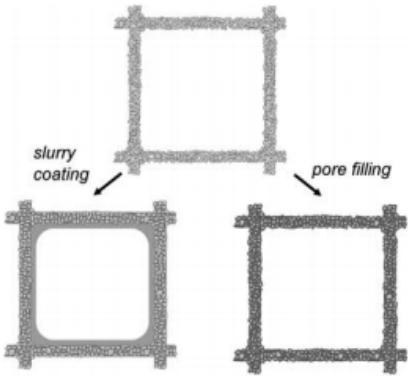

Figure 2-6: Resulting catalyst layer following slurry coating and pore filling method (taken from Nijhuis *et al.*, 2007)

2.6.1. Pore-filling: Sol-gel method

Giani *et al.* (2006) and Nijhuis *et al.* (2007) used pseudo-boehmite (AlOOH) as a precursor for Al_2O_3. The sol is usually a mixture of pseudo-boehemite, water and a dispersing agent(s) such as HNO_3, HCl and Urea, prepared with stirring to disperse solid particles uniformly through the sol.

The rheological properties of the sol depends on the solid content, acid content and ageing conditions (Giani *et al.*, 2006). To perform the washcoating, the monoliths or foams are immersed in the sol. The pores of the substrate walls/struts are filled with the sol-gel via percolation. Excess liquid is removed with a jet of compressed air. The active metal can be applied using wet impregnation.

2.6.2. Deposition: Slurry coating

Slurry coating is a deposition technique. This method involves immersing the substrate (monolith or foam) in a slurry containing catalyst powder with a particle size distribution similar to the larger macropores in the substrate for a short time. The pores of the substrate absorb the liquid in the slurry, depositing a layer of particles on the walls as they cannot enter the pores (Nijhuis *et al.*, 2001). The excess liquid is then removed by blowing with compressed air (Park *et al.*, 2014). This is followed by drying in a horizontal position under continuous gentle rotation to ensure an even washcoat thickness (Nijhuis *et al.*, 2001).

Preparation of a stable slurry is imperative for ensuring effective washcoating. The stability of the slurry, the catalyst loading and the number of washcoats required depends on the viscosity of the slurry (Agrafiotis & Tsetsekou, 2000; Almeida *et al.*, 2011). Low viscosity slurries result in high adhesion to the substrate and homogenous coating, however, the catalyst load per coating obtained is low (Agrafiotis & Tsetsekou, 2000; Almeida *et al.*, 2011). Conversely, highly viscous slurries allow for high catalyst loadings with fewer coating steps, albeit with less homogeneity, lower adherence and increased risk of channel/pore congestion (Almeida *et al.*, 2011).

The viscosity of the slurry is a function of pH, solids content and particle size distribution of the solid (Blachou *et al.*, 1992; Agrafiotis & Tsetsekou, 2000; Hilmen *et al.*, 2001). The control of pH is important for ensuring high repulsion between particles, so as to prevent settling. It has been shown that a pH widely different from the point of zero charge (PZC) will result in a high surface charge which may increase the stability of the slurry (Almeida *et al.*, 2011). Blachou *et al.* (1992) and Agrafiotis & Tsetsekou (2000) found that optimum viscosity of a γ -Al_2O_3 slurry is achieved at a pH between 3 and 4, while pH values that are higher, i.e., closer to PZC of alumina (at pH=7.5), lead to increased viscosity. pH values lower than 3 also increase the viscosity, causing the particles to settle and making it more difficult to handle (Agrafiotis & Tsetsekou, 2000). Acids such as HCl or HNO_3 can be used to control the pH of the slurry.

The solids content should lie between 35 wt.% and 45 wt.% to ensure a high catalyst loading with minimum number of washcoat (Blachou *et al.*, 1992; Agrafiotis & Tsetsekou, 2000; Hilmen *et al.*, 2001). Lastly, stable slurries are created by balancing the gravitational and drag forces acting on the particles (Almeida *et al.*, 2011). A balance of these two forces is obtained at low terminal velocities, which is directly proportional to the square of the particle size and inversely proportional to viscosity (Almeida *et al.*, 2011). Hence, small particle diameters result in more stable slurries. The limitation to how small particle sizes can be selected is due to the increase in viscosity with decrease in particle size. It has been shown that slurries with particles below 10 μm are stable (Nijhuis *et al.*, 2001; González-Velasco *et al.*, 2003) whereas large particles settle fast and require vigorous stirring of the slurry to remain homogenous during slurry preparation and dip-coating process (Agrafiotis & Tsetsekou, 2000). Tarì *et al.* (1998) investigated the effect of particle size distribution on slurry properties. They indicated that a bimodal particle size consisting of a high fraction of coarse particles results in relatively low viscosity, a more stable slurry and more effective packing of the particles.

A single washcoat is often not sufficient to achieve the desired catalyst loading, and thus multiple coating steps must be performed (Merino *et al.*, 2017). The foam can be dried and calcined after each addition of a washcoat or it can be dried and dipped again, with only one calcination after the final washcoat (Nijhuis *et al.*, 2001). The disadvantage of the former is that it is more time consuming. However, it allows the catalyst loading to increase more rapidly because catalyst is not resuspended in the slurry as would be the case without intermediate calcination between washcoats.

Another consideration when washcoating is the placement of the active metal with respect to the secondary support and the foam or monolith substrate. The substrate can be coated with a slurry containing a support that is already loaded with active metal (Nijhuis *et al.*, 2001). Alternatively, the substrate can be coated with the secondary support with subsequent deposition of the active metal. The advantage of the former method is that conventional catalyst preparation methods can be used (Nijhuis *et al.*, 2001). In addition, it can be argued that this method makes it easier to deposit a predetermined amount of active metal on the structured substrate. However, the second method ensures that the active metal does not become inaccessible behind multiple layers of secondary support. For the latter method, active metal deposition using incipient wetness impregnation and supercritical reactive deposition have been shown to be effective.

2.7. Objectives

The aim of this study is to compare the catalytic performance a catalyst powder, pellets, monoliths and foams in Fischer-Tropsch synthesis. Thus, the objectives of this study are to:

- Washcoat a ceramic foam and honeycomb monolith with Co-Pt/γ-Al_2O_3
- Run reactor tests for four different catalyst packings for the LT-FTS reactors with cobalt catalysts: powder, pellets, monolith and a foam reactor
- Compare the productivity and selectivity obtained for the different catalyst packings

2.8. Hypothesis

Following from the literature, the following was hypothesised: The productivity per mass of cobalt and C_{5+} selectivity obtained over a washcoated ceramic (SiC) foam reactor will be higher than that over a monolith reactor and pellets in a fixed-bed reactor due to reduced heat and mass transfer resistances in foam reactors.

2.9. Key questions

- How does the productivity, and product selectivity of the foam reactor compare with that of a monolith and pellets in a fixed-bed reactor?
- Can the transport resistances present in the catalyst powder, pellet, monolith and foam be quantified and qualified from the experimental data obtained?
- What transport resistances are present in the performance of the catalyst powder, the pellet, monoliths and foams?

3. Experimental Methodology

3.1. Catalyst preparation

3.1.1. Preparation of Co-Pt/γ-Al_2O_3 catalyst

A Co-Pt/γ-Al_2O_3 catalyst containing 22 wt.% Co and 0.05 wt% Pt was prepared by vacuum evaporation (van Berge *et al.*, 2005). Puralox SCCa 5/150 supplied by Sasol was used as a catalyst support. Puralox was calcined in a static oven for 3 hours at 200°C to remove any trapped moisture. An aqueous solution was made by dissolving 40 g $Co(NO_3)_2 \cdot 6H_2O$ in 50 ml of distilled water, which is then added to 50 g of Puralox to create a slurry. The suspension was then vacuum treated for 2.5 hours in a rotary evaporator at 75°C and 45 mbar at a rotation speed of 70 rpm. This is followed by batch-wise (8g) calcination at 230°C (ramping up at 2°C·min^{-1} and down at 4°C·min^{-1}) in air (37.5 ml·min^{-1}·$g^{-1}_{Cat\text{-}carrier}$). The calcined impregnated carrier is re-slurried in a solution containing 35 g $Co(NO_3)_2 \cdot 6H_2O$ and 67.2 mg chloroplatinic acid and 50 ml distilled water. The catalyst precursor is vacuum dried and calcined as described above.

A portion of the calcined catalyst precursor, Co_3O_4-Pt/γ-Al_2O_3, was wet-milled using a McCrone Micronising mill for 60 minutes (two repeats of 30 minutes each). The milling was done in batches of 4 ml of catalyst (~ 3.35 g) using 7 ml of ethanol as a dispersant. The ethanol was evaporated in ambient conditions in a fumehood over a period of approximately 12 hours. The wet catalyst was then dried in an oven at 60°C for 6 hrs. The particle size distribution of the wet-milled catalyst was determined using the Mastersizer 2000. The Mastersizer uses the Mie theory to estimate particle size distribution from the light scattering behaviour of a material based on its refractive index and density (Callesen *et al.*, 2018). The refractive index was taken as the weighted average of the refractive index of cobalt and alumina (Polyanskiy, 2018), resulting in a weighted average of 1.63. The McCrone micronizing mill can reportedly grind materials from 125 µm to less than 5 µm within 30 minutes, however longer grinding time was required for this catalyst. The particle size distributions of the catalyst after wet-milling for 30 and 60 minutes are given in Figure 3-1 and Table 3-1.

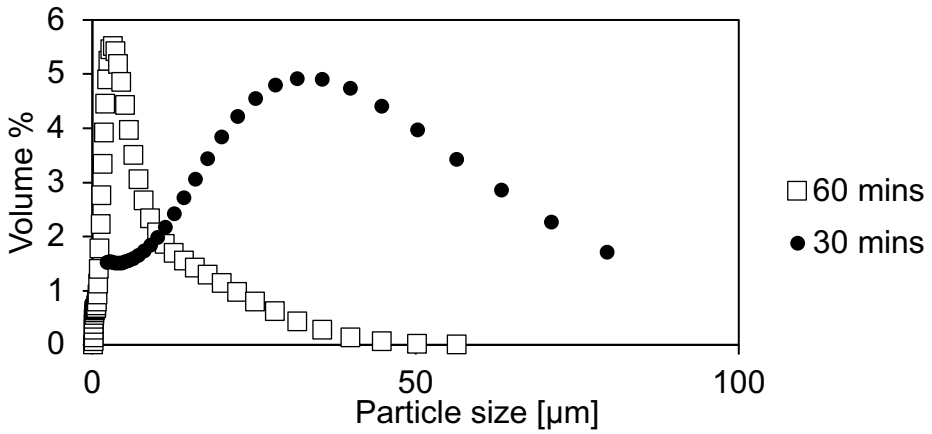

Figure 3-1: Particle size distribution of catalyst wet-milled for 30 and 60 minutes

Table 3-1: Average particle size distribution of catalyst wet-milled for 30 and 60 minutes

Duration of milling	d_{50} [µm]	d_{90} [µm]
30 minutes	19.6	55.3
60 minutes	3.15	11.5

3.1.2. Geometric and material properties of 230 CPSI honeycomb monoliths

A 150 × 150 × 150 mm block of cordierite honeycomb monolith with a cell density of 230 cells per square inch (CPSI) was supplied by Applied Ceramics Inc (Atlanta, Georgia/USA). The geometric features of structured catalysts are required for determining washcoat layer thickness and have an influence on hydrodynamics under reactions conditions (e.g., pressure drop and mass transfer limitations). The geometric features of the monolith as provided by the supplier are shown in Table 3-2. The pitch, the distance of each cell measured from centreline to centreline of opposite cell walls, is 1.67 mm. The hydraulic diameter (d_h) is 1.47 ± 0.05 mm (the width of a cell). The geometric surface area (S_v) is 2.10 $mm^2 \cdot mm^{-3}$ and is defined as the total external surface area of the monolith walls, i.e., excludes the surface area contribution of pores within the cell walls, the geometric surface area. The open frontal area (OFA) is the percentage of cross-sectional area available for flow. d_h, S_v, and OFA were defined as follows:

$$d_h = pitch - t \quad \text{3-1}$$

$$S_v = \frac{4 \cdot (pitch - t)}{pitch^2} \quad \text{3-2}$$

$$OFA = \left(1 - \frac{t}{pitch}\right)^2 \cdot 100 \qquad 3\text{-}3$$

with t as cell wall thickness.

Dimensions reported as nominal values were calculated as the average of the minimum and maximum value measured/calculated.

Table 3-2: Supplier specified geometric and material properties of cordierite honeycombs

Cell density [CPSI]	230
Cell wall thickness [mm]	0.203 ± 0.051
Pitch [mm]	1.67
Nominal hydraulic diameter [mm]	1.47 ± 0.05
Nominal geometric surface area [$mm \cdot mm^{-2}$]	2.10 ± 0.072
Nominal open frontal area [%]	77
Cell wall pore volume	0.20 – 0.22 $cm^3 \cdot g^{-1}$
Cell wall porosity	32 – 36%
Median pore diameter	4 – 7 µm
Cordierite composition	13.8 wt.% MgO 34 wt.% Al_2O_3 50 wt.% SiO_2
Specific heat at 100°C	0.837 $J \cdot g^{-1} \cdot K^{-1}$
Thermal conductivity	2.5 $W \cdot m^{-1} \cdot K^{-1}$
Heat capacity	1.92 $J \cdot cm^{-3} \cdot K^{-1}$

3.1.2. (A) **Cutting monolith pieces**

A 150 × 150 × 150 mm block of cordierite monolith was cut perpendicular to the direction of the flow channels into slabs, of 25 mm in thickness using a sintered diamond saw. To obtain monolith pieces that can fit in the reactor tube which has an internal diameter of 10 mm, square pieces with 16 channels were obtained. The cut pieces were filed to remove protruding cell walls to minimise errors in estimating total geometric surface area.

3.1.3. Geometric and material properties of 30 PPI β-SiC open-cell foams

Cylindrical β-SiC open-cell foams with a diameter of 15 mm and height of 25 mm were supplied by SICAT (Strasbourg, France) and manufactured in ACM GmBH laboratories (Willstätt, Germany). The foams obtained had a pore density of 30 pores per inch (PPI). The foams were custom-made for this study, thus no supplier data for the geometric properties of the 30 PPI foams was available. However, data for 8 & 20 PPI foams, which the supplier was able to provide, were extrapolated to estimate pore diameter of the 30 PPI foams (see Figure 3-2); an average pore diameter of 1.5 mm was found. This is consistent with geometric properties for identical 30 PPI β-SiC (Ou *et al.*, 2017), obtained using mercury (Hg) intrusion porosimetry and X-ray micro computed tomography (see Table 3-3). However, the irregular structure of the foams makes it difficult to ascertain whether pore sizes and strut diameters are similar from foam to foam; in fact, Incera Garrido *et al.* (2008) showed that pore sizes can vary axially in a foam.

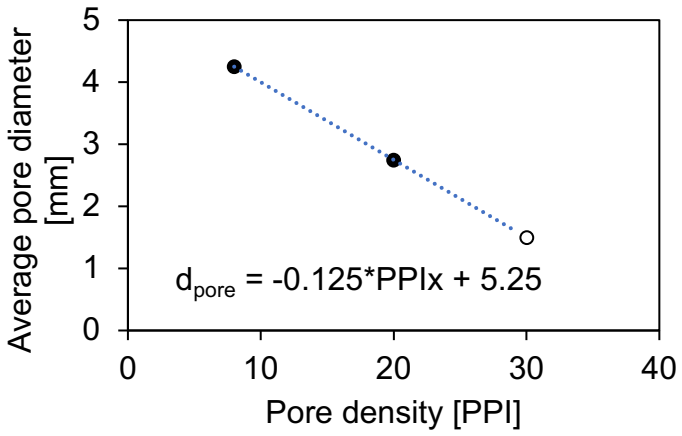

Figure 3-2: Estimation of average pore diameter of 30 PPI β-SiC foams by extrapolation

Table 3-3: Geometric properties of 30 PPI β-SiC foams as reported by Ou *et al.* (2017),

Property	Value
Average pore diameter (d_p)	1.48 ± 0.12 mm
Open porosity (i.e., the hydrodynamically relevant porosity) $(\in_o)$	78.9 ± 3.34%
Strut diameter (t_s)	0.42 ± 0.019 mm

3.1.3. (A) **Resizing of foams**

In order to fit the foams in a reactor tube with an internal diameter of 10 mm, they were reduced to 8.5-9 mm by wet-grinding on the Struers Knuth Rotor 3 polishing machine (600 rpm), SiC grinding paper with P600 grit size was used. Although the material of the grinding paper and the foam are the same, filing was made possible due to the coarse surface of the grinding paper in relation to the smooth surface of the foam.

3.1.4. Washcoating

The procedure described by Nijhuis *et al.* (2001) was used to washcoat the monoliths and the foams. A slurry containing 21.4 g of the milled catalyst in 50 ml of deionised water was prepared in a beaker. HNO_3 was added dropwise to adjust the pH of the slurry to 3.5. The substrates (foams or monoliths) were immersed in the slurry for 15 minutes and then slowly removed. Compressed air was blown through the pores/channels to remove excess liquid. The remaining moisture was removed by. Photographs of uncoated and washcoated substrates taken with a 16 MP dual lens camera are shown in Figure 3-3 and Figure 3-4.

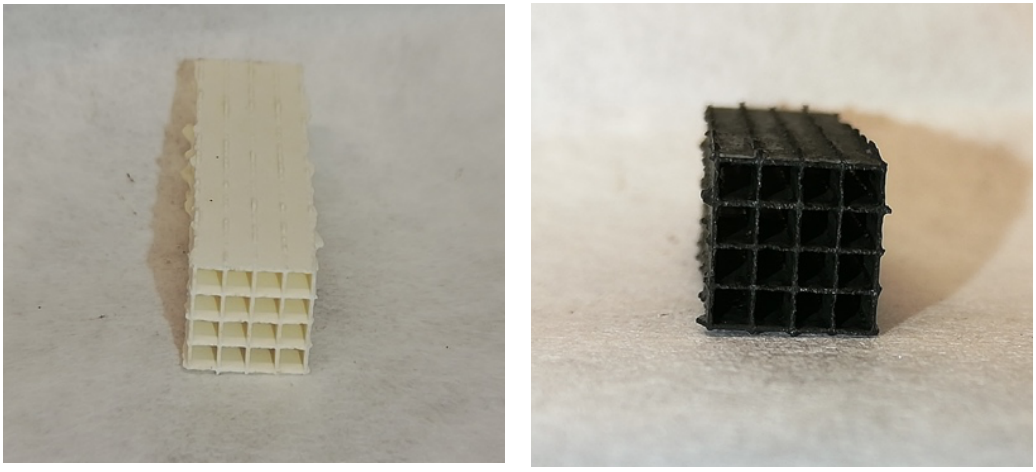

Figure 3-3: Uncoated cordierite monolith (left) and washcoated monolith (right)

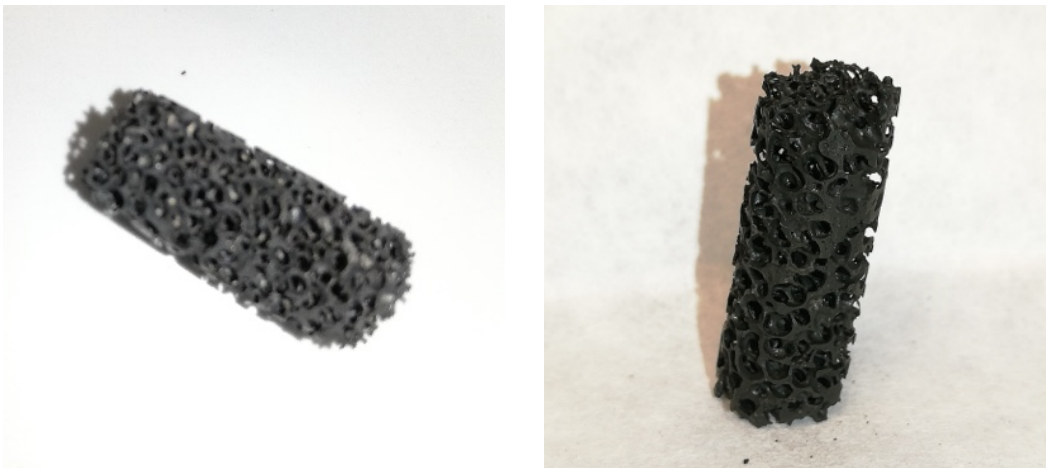

Figure 3-4: Uncoated foam (left) and washcoated foam (right)

Adherence tests were carried out on one foam/monolith per batch. The coated foam/monolith was weighed and then submerged in ca. 30 ml of n-hexane, which was then placed in an ultrasonic bath for 30 minutes. The foam/monolith was removed from the hexane and dried in a 60°C oven for one hour. The dried foam/monolith was reweighed to obtain the retention of catalyst mass by difference. Minor particles of catalyst could be observed floating in the hexane after sonication,

3.1.5. Catalyst moulding

Catalyst pellets were formed by moulding the milled catalyst on a plate with holes with a diameter of 5 mm and height of 5 mm. A mass of 2.61g of the milled catalyst was mixed with 0.7 ml of deionised water. A drop of 6.3 wt.% HNO_3 was added to act as a dispersing agent. The mixture was transferred to a pellet mould and allowed to dry at room temperature for 1 hour, followed by drying in a 120°C oven for 12 hours.

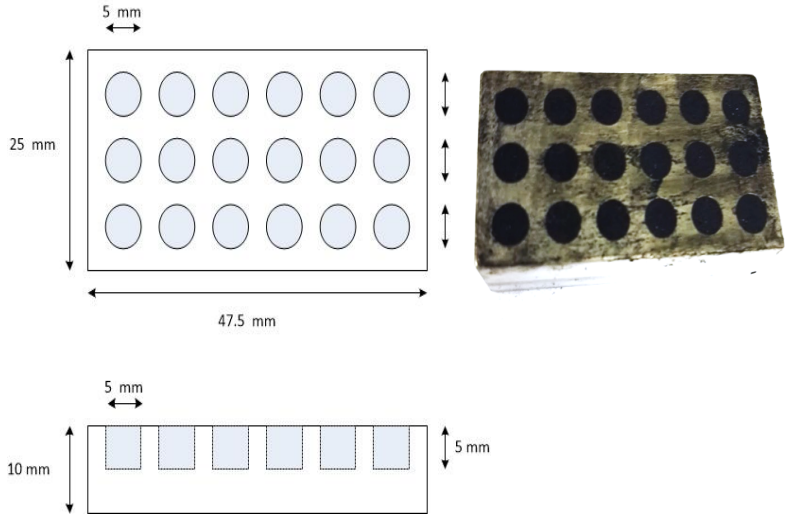

Figure 3-5: Pelletising mould schematic (left) and mould filled with Co-Pt/Al_2O_3 catalyst slurry (right)

3.2. Catalyst characterisation

3.2.1. Metal loading

Inductively-coupled plasma optical emission spectroscopy (ICP-OES) was used to confirm the cobalt and platinum loadings. The calcined catalyst (50 mg) was first dissolved in 10 ml of aqua regia (3 HCl: 1 HNO_3), the dissolved samples were then digested in a Mars 5 Microwave digester at 180°C for 30 minutes, at a ramp rate of 3°C./min. The digested samples were transferred to volumetric flasks with type-1 deionised water (S > 18 MΩ·cm) added to each flask to make up the volume to 25 ml (standard specifications of type 1 deionised water are shown in Table 0-7 in Appendix F). Diluted HNO_3 (2 wt.-%) was then used to dilute 0.5 ml of each sample.

3.2.2. SEM imaging

The morphology of the catalysts was imaged using scanning electron microscopy (FEI Nova NanoSEM 230). Prior to imaging, the monoliths and foams were broken into fragments to obtain cross-sectional view of channel walls and struts. The images were used to determine the average particle size of the fresh catalyst and the wet-milled catalyst powder, to confirm the catalyst layer thickness on the foams and monoliths, and to evaluate homogeneity of the washcoat layer.

3.2.3. Nitrogen physisorption

The BET surface area of the catalyst support (Puralox-SCCa 5/150), the calcined catalyst powder, the uncoated structured substrates, the coated substrates and uncalcined washcoating powder was determined using nitrogen on a Tristar II 3020 Micrometrics analyser. Samples were degassed at 150°C under vacuum for over 12 hours prior to the analysis. Equilibrium N_2 isotherms were measured at -196°C (77K). Specific surface area was calculated based on Brunauer-Emmett-Teller (BET) method, while micropore volume and size were estimated using the Barret-Joyner-Halenda (BJH) method applied to the desorption branch.

3.2.4. Washcoat layer thickness

The average washcoating thickness (L) was determined estimated using equation 3-4, where w_{cat} is the catalyst loading, S_v is the structures specific geometric surface area and $V_{structure}$ is the volume of the coated substrate. The density of the washcoat layer

($\rho_{coatings}$) was estimated by adding BJH pore volume to the density of the reciprocal of the catalyst solid density (pore free) as shown in equation 3-5.

$$L = \frac{w_{cat}}{\rho_{coatings} \cdot S_v \cdot V_{substrate}} \quad \text{3-4}$$

$$\rho_{coatings} = \frac{1}{1/\rho_{catalyst(pore\ free)} + V_{pore}} \quad \text{3-5}$$

3.2.5. Energy filtered transmission electron microscopy (EFTEM)

EFTEM was performed on the calcined unreacted catalyst powder and the spent pellets, monoliths and foams to determine whether particle growth had taken place during the reaction. Catalyst was scraped off mechanically from the spent monoliths and foams. The samples, including the powder and the pellets, were crushed separately using a mortar and pestle into a fine powder and were suspended in ethanol. Drops of each sampled were transferred onto a carbon-coated copper grid. The samples were imaged using FEI T20 TEM with a 200 kV accelerator for energy filtered microscopy.

3.3. Fischer-Tropsch synthesis activity tests

3.3.1. Reactor set-up

The activity tests were carried out in a fixed-bed reactor set up shown in Figure 3-7. Hydrogen (H_2), carbon monoxide (CO), nitrogen (N_2) and argon (Ar) were supplied to the rig at a pressure of 60 bar via separate gas lines. Pressure regulators were used to reduce the pressure to ca. 25 bar. The flowrate of each gas was controlled individually using Brooks mass flow controllers (MFCs). H_2 and CO were blended prior to being fed to the reactor. An argon gas line was connected to the synthesis gas line and was primarily used to pressurise the reactor. A four-way valve was available to either direct gas flow through the reactor or to by-pass the reactor. The reactor was a steel tube with an internal diameter of 10 mm. It was heated electrically using a three-zone heating system, i.e., three steel heating coils on the outer walls of the reactor tube, each with its own PID* controller but all collecting temperature recordings from the same stationary thermocouple". The temperature was controlled by a stationary thermocouple located in a ¼ inch (OD) thermowell. Power output to the heating coils is controlled via a stationary thermocouple, inserted in a thermowell. The thermowell was located within the catalyst bed when testing powder and above the catalyst bed when testing pellets, monoliths or foams. In the latter case, the position of the stationary thermocouple was maintained at 145 mm above the reactor outlet. The reactor's axial temperature profile was determined under argon gas flow, with a flowrate of 240 $ml \cdot min^{-1}$ while the reactor tube was packed with 300 µm SiC particles: the reactor temperature was set at 220°C, and temperature measurements were taken by moving the mobile thermocouple at 10 mm intervals along the length of the reactor tube. The temperature profiles obtained for testing the catalyst powder or pellets/monoliths/foams are shown in Figure 3-6. It can be seen that an isothermal zone of ~50 mm is obtained when the reactor is packed with catalyst powder. The catalytic material is located within the isothermal zone. Since the temperature profile of the catalyst bed (isothermal zone) could not be measured when the reactor contained pellets/monoliths/foams, the similarity between the temperature profiles above the catalyst bed of both configurations may be taken as an indication that the isothermal zones were also similar.

*PID: Proportional Integral Derivative

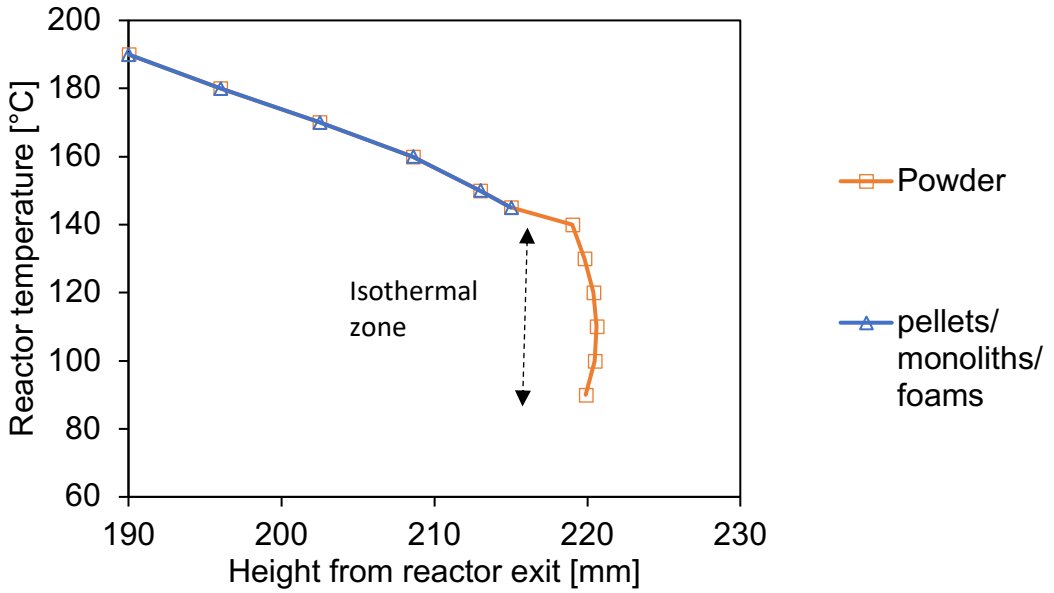

Figure 3-6: Temperature profile in the reactor

Downstream of the reactor, two heating zones with separate thermocouples and heating tape were heated electrically. Power supply to the reactor tube heating coils and the product pipeline heating tapes was varied using PID controllers written in LabVIEW software.

Liquid products were removed from the gas products in a hot trap operating at 180°C and 20 bar to remove liquid products. Argon was added through the bypass line to maintain reactor pressure at 20 bar. A needle valve in the reactor effluent line was used to reduce the reactor product pressure to ca. 1 bar. A bonnet-cap needle valve was placed after the bypass line, which is used together with the pressure reducing needle valve to control the flowrate of the pressure regulating argon to prevent excessive dilution of the product stream. Two subsequent cold traps operating at ambient temperature were used to remove water and remaining liquid hydrocarbons from the product stream. The reactor products stream could be sent to the vent or to the online GC-TCD.

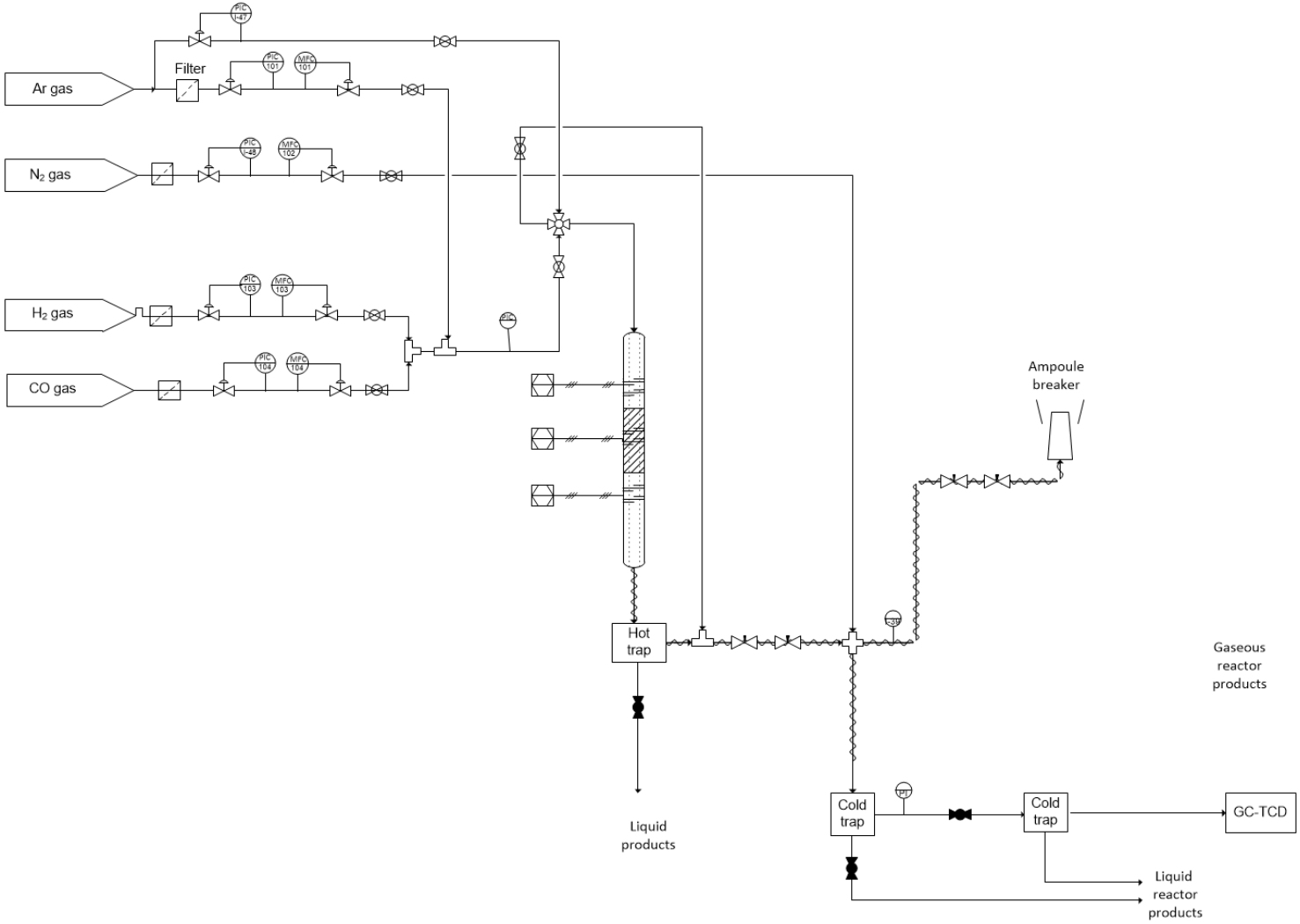

Figure 3-7: Schematic of the fixed-bed reactor set-up

3.3.2. Reactor loading

Figure 3-8 shows the typical packing of the reactor tube. For all catalyst packings, silicon carbide (SiC, 300 μm) particles were placed above the catalyst bed to allow pre-heating of the reactant gas prior to entering the catalyst bed. The catalyst was loaded within the 50 mm isothermal zone (see Figure 3-6).

For the catalyst powder and the pellets, 0.5 g of catalyst was loaded. The catalyst powder and the pellets were diluted with ca. 4 g and 6.2 g of 300 μm SiC particles, respectively. The SiC particles act as a heat sink to reduce thermal runaway and to reduce wall effects by decreasing open volume that would otherwise occur between the catalyst pellets and the reactor tube wall.

The mass loading of the structured catalysts was varied, details for each mass loading are provided in the relevant results section for that catalyst (Chapter 4.4). The structured reactor packings were not diluted with SiC particles. The structured packing was wrapped in glass wool to fill the gaps between the reactor tube wall and the packing to minimize by-passing of the flow.

For all the catalyst packings, glass wool occupying a height of about 5 to 8 mm was placed at the top and bottom of the catalyst bed. In the case of the powder, this was done to prevent migration of the catalyst particles from the isothermal zone due to gravity and gas flow, whereas the glass wool prevented SiC particles from entering the void spaces of the catalyst particles. For the pellets, the same was done for consistency.

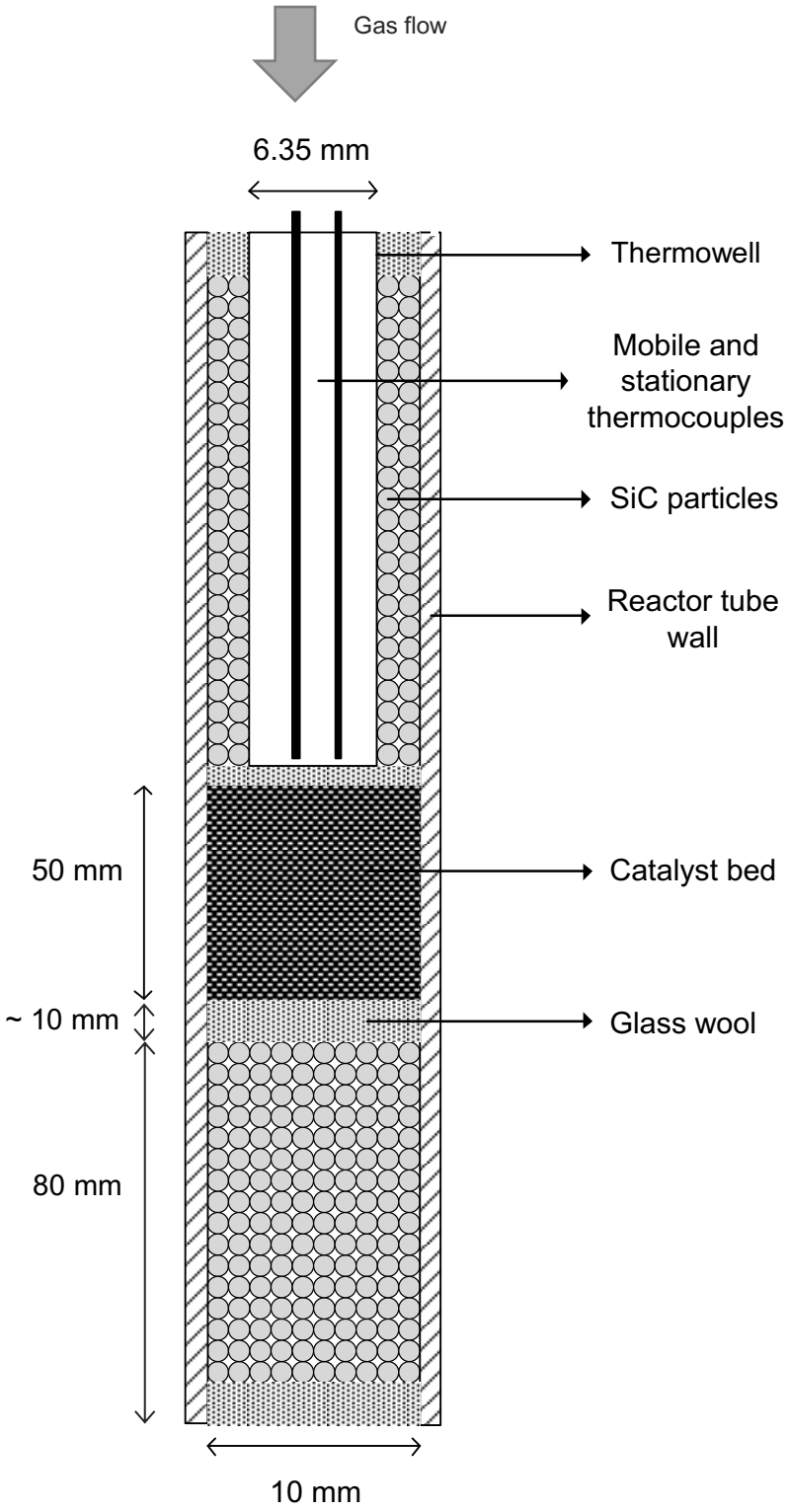

Figure 3-8: Schematic representation of the loaded reactor tube

3.3.3. Catalyst testing

Before Fischer-Tropsch synthesis was carried out, the catalyst was reduced in a pure hydrogen flow (240 ml·min^{-1}·g$^{-1}_{cat}$) at 350°C for 16 hrs (ramping up at 5 °/min from 50°C to and cooling back down to 50°C in 60 minutes). The reduction results in the formation of metallic cobalt (Sun *et al.*, 2000):

$$Co_3O_4 + H_2 \rightarrow 3CoO + H_2O \quad \text{3-6}$$

$$3CoO + 3H_2 \rightarrow 3Co° + 3H_2O \quad \text{3-7}$$

For the startup of the Fischer-Tropsch synthesis, a stoichiometric mixture of H_2 and CO (H_2/CO = 2) at a total flowrate of 240 ml·min^{-1} was passed through the catalyst bed at 200°C and atmospheric pressure, and conversion at atmospheric pressure was obtained. Then, the reactor was pressurised to 20 bars. Reactor pressure was maintained by pressure regulating gas (Ar), flowing through a by-pass line and mixing with the reactor product as shown in Figure 3-7. The total flowrate of reactor products was controlled by adjusting a needle valve downstream from the by-pass line to prevent excessive dilution of the product stream. Once at pressure and with the reactor temperature still at 200°C, synthesis gas at 240 ml·min^{-1} was re-introduced into the reactor. An exotherm already occurs at this relatively low temperature, extent of the exothermic temperature increase will be given for each catalyst test in Chapter 7.3. Once the reactor temperature returned the setpoint value of 200°C, the reactor temperature was steadily increased at a set ramp rate of 1°C/min to 220°C. Reactor products were directed to the online GC-TCD. When changing space velocity, the flowrate of reactant gases and nitrogen were adjusted manually using mass flow controller boxes. Space velocity was typically reduced (i.e., decreasing the flowrate). Hydrogen flowrate was typically reduced first, which may have led to a brief enrichment of CO in the feed.

Ampoule samples of the tail gas were taken periodically at each space velocity for offline GC-FID analysis. Evacuated glass ampoules were prepared by remoulding commercially available glass Pasteur pipettes (Lasec) under a LPG-O_2 torch as displayed in Figure 3-9. The evacuated ampoule, ‘E’, is used to collect the rail gas through the ampoule breaker. Before taking a sample, flow to the GC-TCD was stopped to direct all the reactor products to the ampoule sampling port. The flow was stabilised for at least two minutes before a sample was taken, ensuring that the sampled was representative of the average product distribution. To take a sample, the

thin capillary of an evacuated glass ampoule was inserted inside the ampoule sampling port. The ampoule breaking for was turned to break the tip of the capillary, allowing gas products to be rapidly drawn into the evacuated ampoule. The bulb of the evacuated ampoule, now filled with reactor products, was quickly sealed using a portable butane torch.

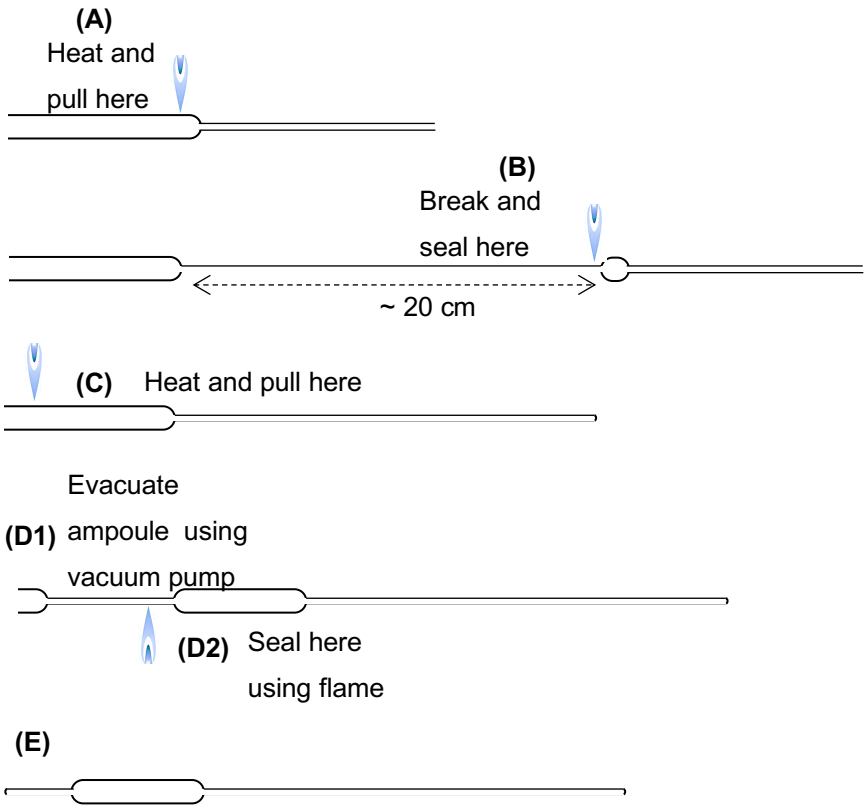

Figure 3-9: Preparation procedure of evacuated ampoules for sampling product stream

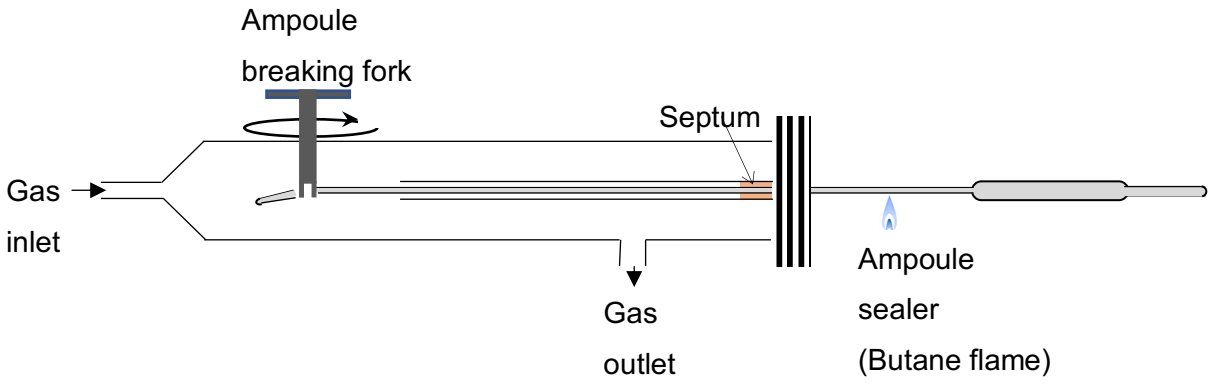

Figure 3-10: Schematic of ampoule sampling port

3.3.4. Analysis of inorganic gases using GC-TCD

The reactor effluent is mixed with a known quantity nitrogen gas (10 vol.%), which acts as an internal standard. A wax trap operating at 180°C removes liquid hydrocarbons from the product stream, while a subsequent cold trap operating at room temperature removes most of the water, which is a by-product of Fischer-Tropsch synthesis. The permanent gases (H_2, CO, CO_2, CH_4 and N_2) are separated and analysed on an online Varian 7820 gas chromatogram equipped with a thermal conductivity detector (GC-TCD), with the operating conditions shown in Table 3-4.

Table 3-4: Operating conditions of the on-line GC-TCD

Columns	20 m MolSieve 5A	10m PoraPlot Q 5A
Column pressure	10 psi	35 psi
Oven temperature	70°C	
Run time	14 mins	
Equilibrating time	1 minute	
Detector temperature	250°C	
Flows	Reference flow	15 ml·min^{-1}
	Make-up flow (N_2)	3 ml·min^{-1}

An example of a typical GC-TCD trace obtained for during the catalyst testing is shown in Figure 3-11. The peaks are identified based on retention time and elution order. Hydrogen (H_2), carbon dioxide (CO_2), nitrogen (N_2), methane (CH_4) and carbon monoxide (CO) are detected in that order.

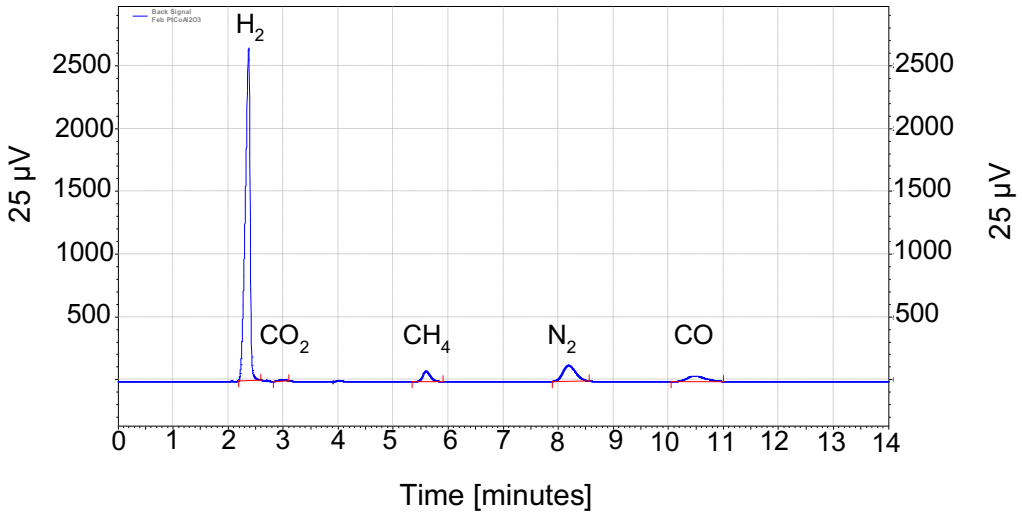

Figure 3-11: Example of GC-TCD trace

Since the volumetric flowrate (NTP) of nitrogen was known, the molar flowrate of nitrogen could be determined using the ideal gas law:

$$F_{N_2} = \frac{P \cdot V_{N_2}}{R \cdot T} \quad \text{3-8}$$

The peak areas obtained from the GC-TCD data were converted to molar flowrates (F_i) by comparing the obtained peak areas to the peak area of nitrogen (see equation 3-9). A_i and A_{N_2} are the peak areas of the analyte and nitrogen (the internal standard) respectively. $RR_{f,i}$ is the response factor of component '*i*' relative to the internal standard, N_2. The $RR_{f,i}$ values were determined by calibrating the GC-TCD by flowing gas from a cylinder with a known concentration of the analytes (H_2, CO_2, N_2, CH_4 and CO), the details of the calibration are shown in Appendix A.3.

$$F_i = F_{N_2}\left(\frac{A_i}{A_{N_2}}\right) \Big/ RR_{f,i} \quad \text{3-9}$$

The conversion of CO was calculated based on the difference between the flowrate of CO in the gas feed and the CO in the reactor product as measured by the GC-TCD. Note that before Fischer-Tropsch synthesis was carried out, syngas was passed through the reactor bypass at flowrates to be considered in this study. It was found that the measured flowrates showed consistent deviation from the set values, H_2 flowrates were at most 4% higher than the set flowrates, while CO flowrates were typically 5% lower than the set flowrates, see Appendix A.5. Thus, conversion and selectivity were calculated from the measured rather than the set flow rates to account for this error.

$$X_{CO} = \frac{F_{CO_{in}} - F_{CO_{out}}}{F_{CO_{in}}} \cdot 100\% \quad \text{3-10}$$

Selectivity to compound *i* was taken as the amount of carbon in reacted CO that has been converted to compound *i* as seen in equation 3-11 below. 'n_c' is the number of carbon atoms in a single molecule of compound i. For CH_4 and CO_2, 'n_c' is 1, thus the selectivity for these two compounds was calculated as shown in equations 3-12 and 3-13.

$$S_i = \frac{F_{i_{out}} \cdot n_{C_i}}{F_{CO_{in}} - F_{CO_{out}}} \cdot 100\ \mathrm{C} - \% \quad \text{3-11}$$

$$S_{CH_4} = \frac{F_{CH_4}}{F_{CO_{in}} - F_{CO_{out}}} \cdot 100\ \mathrm{C} - \% \quad \text{3-12}$$

$$S_{CO_2} = \frac{F_{CO_2}}{F_{CO_{in}} - F_{CO_{out}}} \cdot 100\mathrm{C} - \% \quad \text{3-13}$$

The hydrogen to CO usage ratio was also of interest and was calculated as:

$$R_{H_2:CO} = \frac{F_{H_2 in} - F_{H_2 out}}{F_{CO_{in}} - F_{CO_{out}}} \quad \text{3-14}$$

3.3.5. Analysis of volatile reactor products using GC-FID

Volatile components of the product stream are collected at the ampoule sampling point and analysed using an offline GC equipped with a flame ionisation detector (Varian 3900). To transfer the hydrocarbon products from the glass ampoule to the GC, the ampoule was broken using a grip pliers, and then the gas was drawn from the ampoule using a gas-tight syringe.

The temperature programme and operating conditions are given in Figure 3-12 and Table 3-5 below.

Table 3-5: Operating conditions of GC-FID

Column	Type: Cp-Sil 5 CB
	Length × diameter: 50 m × 0.25 mm
	Stationary phase: 50 µm dimethylpolysiloxane
Injection temperature	200°C
Head pressure	25 psi
Detector temperature	200°C
Detector Flows	Introduction gas: 25 ml·min^{-1} N_2
	Carrier gas: 30 ml·min^{-1} H_2
	300 ml·min^{-1} Air
Split ratio	3:7

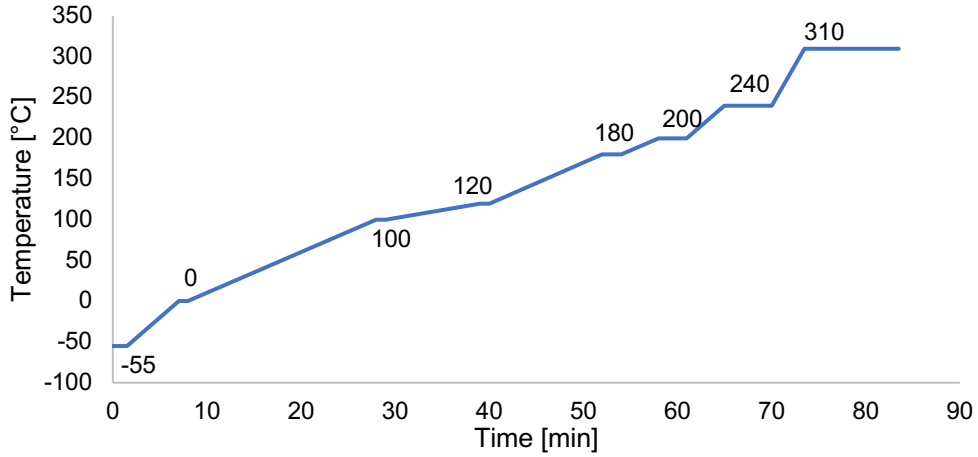

Figure 3-12: GC-FID column oven temperature profile

Peaks on the GC-FID trace of the product distribution from the Fischer-Tropsch synthesis can be identified easily owing to the highly logical sequence; peaks generally appear in order of increasing carbon number with retention time. At low carbon numbers the products are highly olefinic while the paraffins are more dominant at higher carbon numbers. 1-olefins are the major olefin product compounds, while trans- and cis-2-olefins constitute the remainder. Methyl-branched paraffins are also identified in the product spectrum. An example of typical chromatogram that was obtained using GC-FID and the corresponding peak identification are shown Figure 3-13 and Table 3-6 respectively.

Since CH_4 can be detected by both GC-TCD and CG-FID, the peak areas obtained using GC-FID were converted to molar flowrates using CH_4 as a reference:

$$F_i = \frac{A_i \cdot F_{CH_4}}{A_{CH_4} \cdot n_{C_i}} \quad \text{3-15}$$

The selectivity for the formation of the C_1-C_4 product fraction was calculated on a carbon basis as shown in 3-16. As only products up to C_{13} were detected by the GC-FID, the C_{5+} selectivity was taken as the fraction of all products not including C_1-C_4 products assuming closure of the carbon balance.

$$S_{C,i} = \frac{F_i \cdot n_{C_i}}{\sum_i F_i \cdot n_{C_i}} \cdot 100 \quad \text{3-16}$$

$$S_{C_{2-4}} = S_{C_2} + S_{C_3} + S_{C_4} \quad \text{3-17}$$

$$S_{C_{5+}} = 100 - S_{C_1} - S_{C_{2-4}} \quad \text{3-18}$$

where S_{C_1} refers to the selectivity of CH_4, CO_2 and methanol.

Furthermore, the olefin content was determined for each carbon number.

$$O/P = \frac{F_{n_{olefin,i}}}{F_{n_{paraffin,i}}} \quad \text{3-19}$$

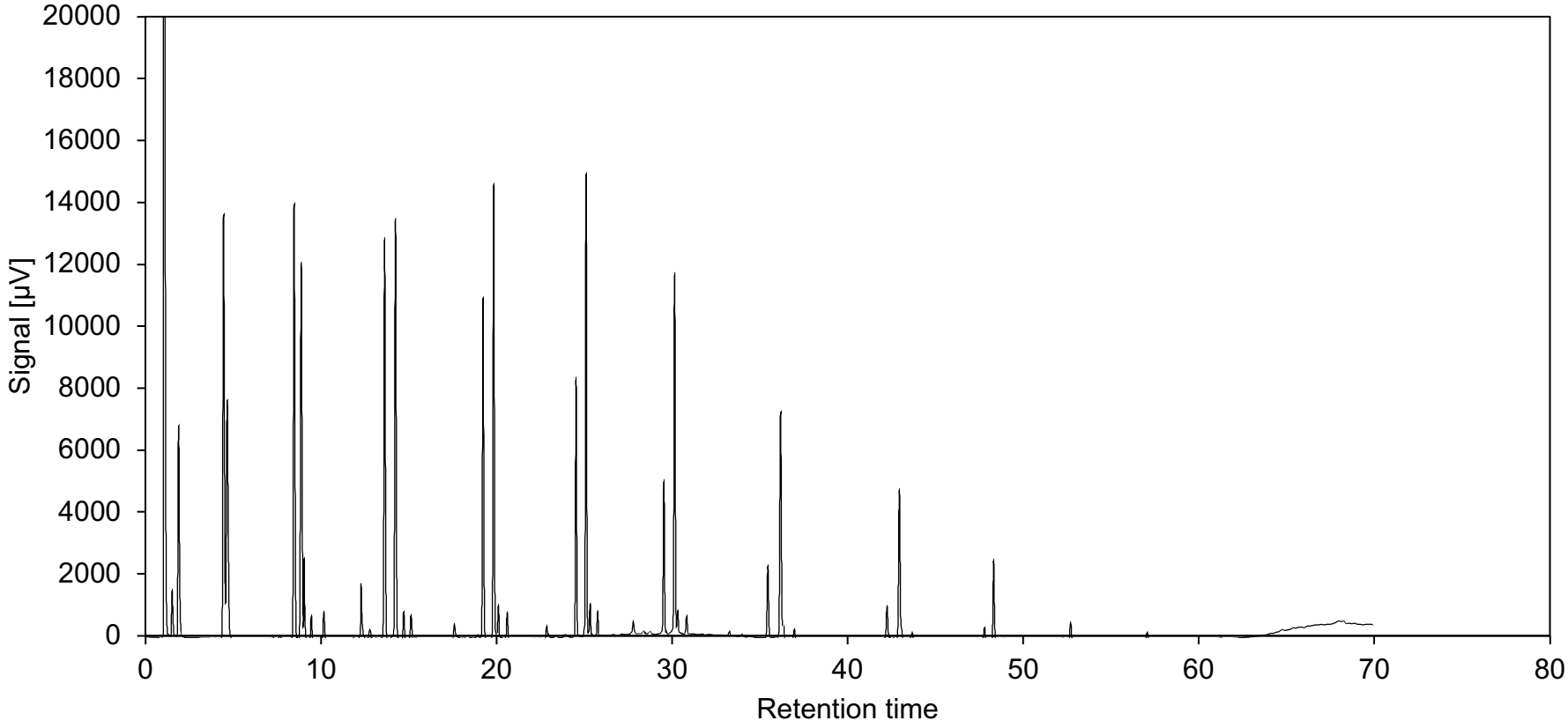

Figure 3-13: Sample of an FID-trace of the product distribution from Fischer-Tropsch synthesis

Table 3-6: Peak identification

Retention time [min]	Peak Name	Retention time [min]	Peak Name
1.08	methane	24.69	1-heptene
1.55	ethylene	25.26	n-heptane
1.93	ethane	25.49	trans-2-heptene
4.51	propene	25.93	cis-2-heptene
4.73	propane	27.96	4-methyl-heptane
7.36	2-methyl-1-propane	28.54	2-methyl-heptane
7.66	methanol	28.97	3-methyl-heptane
8.56	1-butene+2-methyl-propene	29.73	1-octene
8.97	n-butane	30.35	n-octane
9.55	trans-2-butene	30.52	trans-2-octene
10.27	cis-2-butene	31.05	cis-2-octene
11.97	3-methyl-1-butene	33.33	4-methyl-octane
12.46	ethanol	34.24	2-methyl-octane
12.92	2-methyl-butane	34.68	3-methyl-octane
13.76	1-pentene	35.71	1-nonene
14.15	2-methyl-1-butene	36.45	n-nonane
14.38	n-pentane	36.6	trans-2-nonene
14.85	trans-2-pentene	37.24	cis-2-nonene
15.27	cis-2-pentene	40.2	methyl-nonane
15.54	2-methyl-2-butene	42.52	1-decene
17.58	2-methyl-pentane	43.21	n-decane
18.29	3-methyl-pentane	43.94	cis-2-decene
19.39	1-hexene	46.29	methyl-decane
19.99	n-hexane	48.03	1-Undecene
20.25	trans-2-hexene	48.55	undecane
20.76	cis-2-hexene	49.13	cis-2-undecene
23.02	n-Butanol	52.48	1-dodecene
23.6	2-methyl-hexane	52.95	n-dodecane
24.05	3-methyl-hexane	57.3	n-tridecane

4. Results

4.1. Catalyst preparation results

4.1.1. Metal loading

The targeted metal loading was 22 wt.-% Co and 0.05 wt.-% Pt on a fully reduced catalyst. It is known that the cobalt nitrate catalyst precursor decomposes to the oxidic form of cobalt (Co_3O_4) during calcination (Chu *et al.*, 2007). The cobalt metal loading in the freshly calcined catalyst was expected to be 20.4 wt.-% due to the additional mass of the oxygen before the catalyst is reduced.

The calcined catalyst powder, the wet-milled, the pellet and dried washcoating slurry powder were analysed with ICP-OES. The different catalysts were expected to have identical metal loading since they were all prepared from one batch of catalyst. The Co loading obtained was higher than the targeted value, as can be seen in Table 4-1. A more usual result is for metal loadings to be lower than targeted because cobalt(II) nitrate typically absorbs moisture from the air and attains a slightly inflated mass, such that less than the required mass is weighed during preparation. it was observed that while some catalyst had stuck to the walls of the rotavap flask, the mass recovered after calcination was still higher than expected, suggesting that the catalyst wasn't fully calcined. Thus, the second loading of cobalt was probably based on an incorrect estimation of the support mass. Moreover, the metal loadings between different catalysts differed even though they were all taken from the same batch of catalyst: the Co and Pt loadings of the washcoating slurry powder, as well as the Pt loading of the calcined catalyst powder were higher than expected, while the metal loadings of the wet-milled powder and the pellet were lower, implying that impregnation was not homogenous. Errors in weighing the samples for ICP-OES analysis could have also contributed.

Table 4-1: Metal loading of tested calcined catalyst powder, milled catalyst, pellet and washcoating

Element	Expected	Calcined catalyst powder	Milled catalyst powder	Pellet	Washcoating slurry
Co [wt.%]	20.4	21.4	22.1	21.1	23.3
Pt [wt.%]	0.05	0.08	0.03	0.03	0.06
Al [wt.%]	38.2	37.2	36.9	37.3	35.1

4.2. Washcoating

The foams and monoliths were washcoated as described in chapter 3.1.4.

4.2.1. Honeycomb monoliths

Figure 4-1 shows SEM images of the cordierite monoliths before and after washcoating. The SEM image of the cross-section of an uncoated monolith (a) was used to confirm the wall thickness and cell size. The nominal wall thickness (t) and hydraulic diameter (d_h) specified by the supplier are 0.203 ± 0.051 mm and 1.47 mm respectively. The values of t and d_h measured using SEM were found to fall within the range specified by the supplier. The nominal wall thickness, t, was measured at 0.24 ± 0.002 mm and d_h was 1.45 ± 0.02 mm. Note that hydraulic diameter is estimated for square ducts as four times the available flow area divided by the perimeter of the channel as shown in equation 4-1.

$$d_h = \frac{4a^2}{4a} = a \qquad \square \; a \qquad \text{4-1}$$

The catalyst layer thickness was measured using SEM. Images ‘e’ and ‘f’ show the washcoat layer thickness for the monoliths coated with 0.50 g and 0.24 g of catalyst (HcM 3 and 4 respectively). The catalyst layer thicknesses measured using SEM were found to be 44.9 ± 4.7 µm and 22.3 ± 1.6 µm for respectively, for an average of 15 measurements. Furthermore, image ‘b’ is the cross-section of the HcM 4. When comparing image ‘b’ and ‘a', it can be seen that washcoating yields in slight rounding at the corners. Thus, the catalyst layer is likely to be thicker at the corners than on the flat channel walls. This was also reported by Nijhuis *et al.* (2001). Images ‘c’ and ‘d’ show the surface of the washcoat layer for HcM 4. The washcoat exhibits small cracks, pits and bumps. The cracks are generally less than 1 µm in size. The pits can be as large as 25 µm, while the bumps can be up to 12 µm in height. The cracks may reduce catalyst adherence over time on stream. They may also improve internal mass transfer by decreasing diffusion distance, while the surface roughness provided by the pits and bumps could result in increased disturbance of the flow pattern over the catalyst layer.

To confirm that the catalyst layer thicknesses observed using SEM are representative of the whole sample, the catalyst layer thickness was also estimated by assuming homogeneous distribution of the washcoat over the entire surface area of the monolith channel walls. The estimates are shown in Table 4-2. Minimum and maximum layer thicknesses were estimated from the maximum and minimum geometric surface areas provided by the supplier respectively, sample calculations are shown in Appendix C.1.

Note that the catalyst loading of HcM 1 is similar to that of HcM 3, and that of HcM 2 is similar to that of HcM 4. Thus, it was assumed that the catalyst layer thicknesses would be identical for monoliths with similar catalyst loadings. The estimated values fall within the range of the measured washcoat layer thicknesses. The similarity between the measured and estimated washcoat layer thicknesses for monoliths with similar catalyst loadings indicates that the assumption of uniform catalyst layer thickness may be used despite local variations of up to 10% in washcoat thickness.

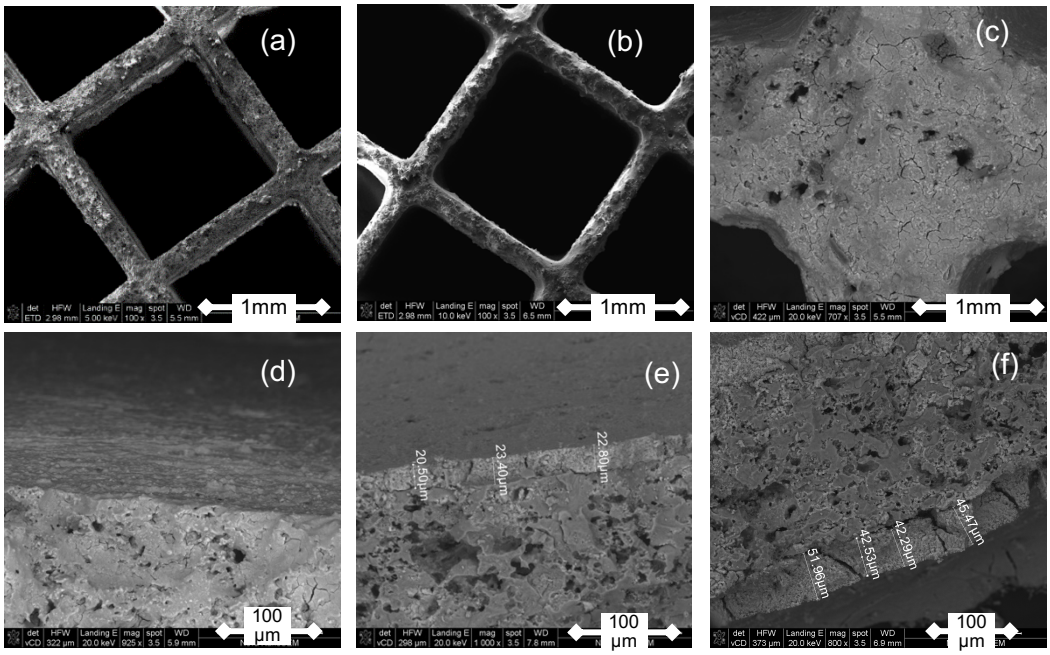

Figure 4-1: SEM images of the cordierite monoliths (a) uncoated cross-section (b) coated cross-section (c) coated corner (d) coated channel wall (e & f) layer thickness of HcM 4 (0.25 g) and HcM 3 (0.50 g) respectively

Adherence tests were carried out on monoliths coated with ca. 33 wt.-% of catalyst and 19 wt.-% of catalyst, which are identical to the loadings of HcM 1 and 2 respectively. The adherence test involved sonicating the washcoated monoliths at ambient conditions in hexane for 30 minutes and measuring the change in mass of the washcoated monolith. The results of the adherence test show that that both monoliths retained their mass well, 98.7% and 98.9% for the monoliths coated with 0.24 g and 0.50 g of catalyst, respectively.

Table 4-2: Summary of washcoating characteristics of prepared monoliths

	HcM 1			HcM 2		
Uncoated mass [g]	1.03			1.05		
Catalyst loading [g]	0.51			0.25		
Catalyst wt.-%	33%			19%		
Number of coatings required	3			1		
	min.	nom.	max.	min	nom.	max.
Layer thickness [μm]	42.3	44.9	47.6	20.7	22.3	23.8

4.2.2. SiC open-cell foams

Uncoated foams of 25 mm in height and 15 mm in diameter were filed to a diameter of 8-8.5 mm. Since the filing was done manually, it was not possible to ensure a uniform diameter along the height of the filed foams. In addition, since the isothermal zone is 50 mm in height, the foams were coated in pairs. To vary catalyst layer thickness, the mass of catalyst coated on each pair of foams was varied. The washcoating procedure described in Chapter 6.1.6 was followed.

Due to the irregular structure of the foams and the small size of the pores, it is difficult to provide evidence that pore blockage did not occur during washcoating. However, visual inspection of the pores near the outside of the foams suggested that the washcoating was achieved without pore blockages as the pores remained open, see Figure 3-4.

As with the monoliths, the catalyst layer thickness was estimated based on the assumption that the catalyst was coated uniformly on the entire geometric surface area foam struts. Geometric surface area was estimated using the model based on tetrakaidekahedral (TTKD) unit cells for open cell foams, this model is discussed in more detail in Chapter 2.5.4. Sample calculations are shown in Appendix D.1.

Figure 4-2 shows SEM images of fragments of an uncoated foam strut (a) and a foam coated with 0.25 g of catalyst (c). It is clear that there is significant disparity in the catalyst layer thickness estimated based on geometric surface area and the catalyst layer thickness measured using SEM. It is possible that the TTKD model greatly underestimates the geometric surface area of the foams, resulting on inflated catalyst layer thickness estimates. More importantly, the disparity is a strong indication that the catalyst is not deposited uniformly on the catalyst surface. This is confirmed in Figure 4-3, which shows SEM images of a spent SiC

foam coated with 0.66 g of catalyst. The image clearly shows that the catalyst is not coated homogenously on foam. Unsurprisingly, the catalyst layer is thickest around corners and curvatures of the struts. The extent of the variation in catalyst layer thickness on a single foam is worrying; for this foam, the measured catalyst layer thickness varied widely from a minimum of 9.5 μm to a maximum of 109.3 μm, while the estimated catalyst layer thickness was 77.0 μm, meaning that there is as much as a 67.5 μm difference between the estimated catalyst layer thickness and the measured thickness. Since reactants and products will experience a variety of diffusion distances in a single foam due to the wide variation in catalyst layer thickness, the assessment of internal mass transfer limitations based on diffusion distance may be distorted.

Table 4-3: Summary of washcoating characteristics of prepared foams

Mass of catalyst washcoated (wt.%)	Uncoated mass [g]	Catalyst loading [g]	Required number of washcoats	Estimated layer thickness [mm]	Adherence [%]
OcF 1 (22.6 wt.%)	1.01	0.18	3	21.0	98.1
OcF 2 (30.1 wt.%)	1.09	0.47	6	54.8	93.9
OcF 3 (15 wt.%)	0.82	0.24	3	28.0	95.3

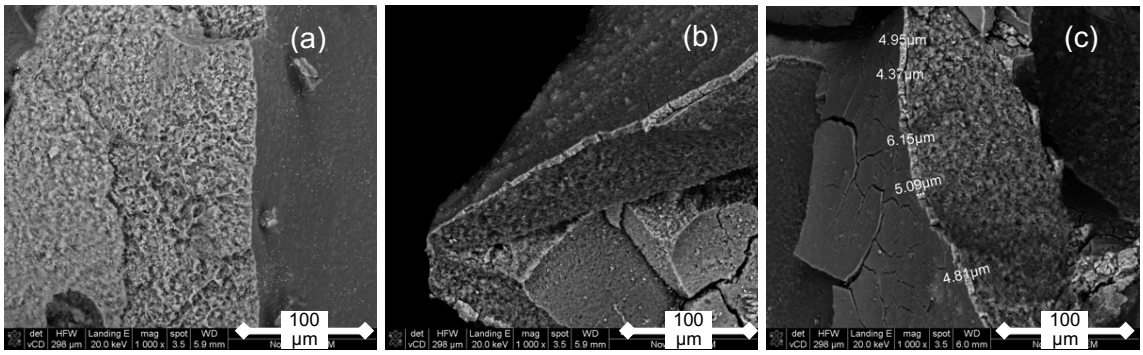

Figure 4-2: Images of the SiC open-cell foams (a) cross section of uncoated strut (b) uncoated 30 PPI foam c) coated 30 PPI foam

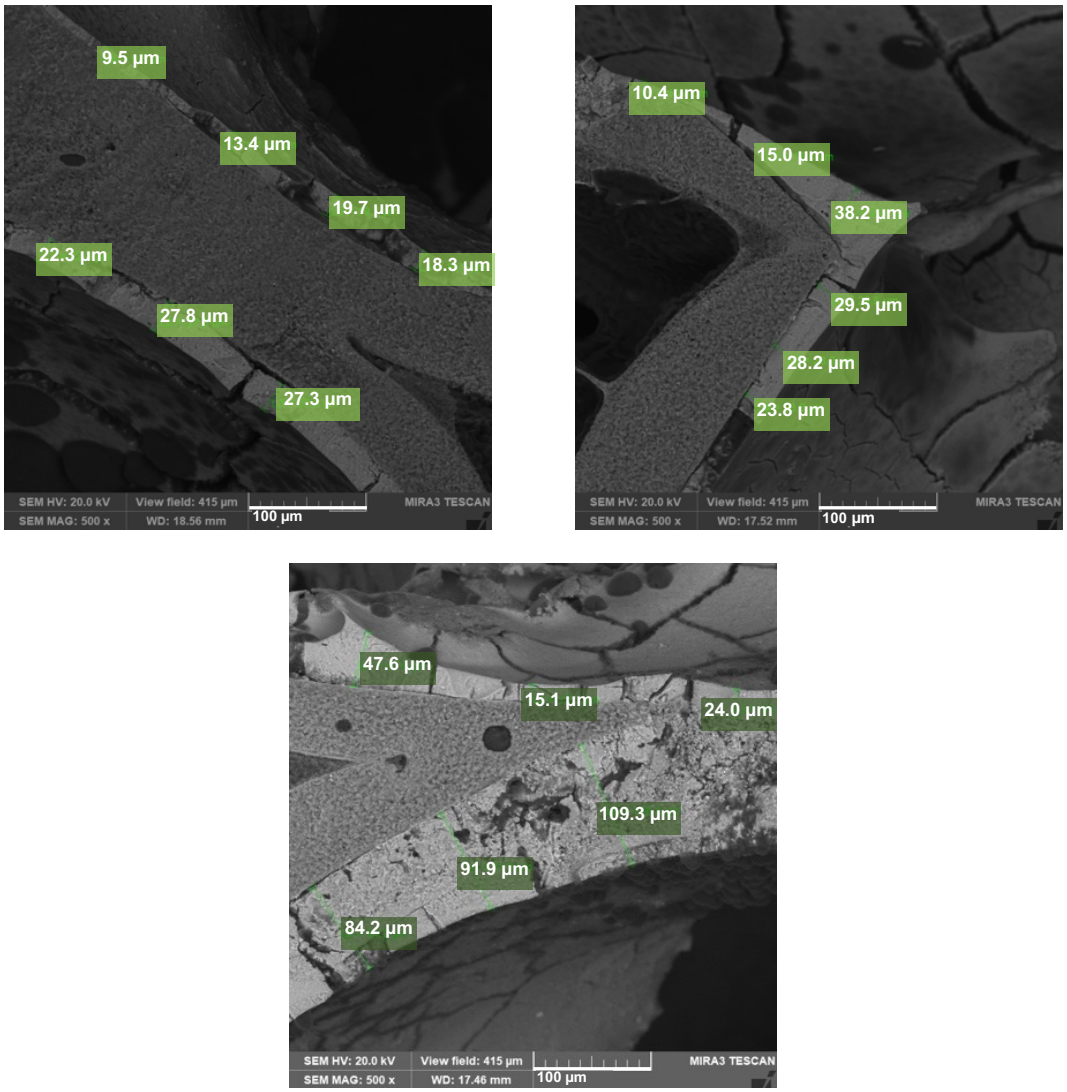

Figure 4-3: Images of SiC foam washcoated with 0.66 g of catalyst

Foams coated with similar mass of catalyst were sonicated in hexane for 30 minutes to evaluate washcoat adherence, which is taken as the percentage of total coated foam mass remaining after sonication and drying. The adherence results, shown in Table 4-3, indicate that the catalyst adheres well to the foam struts. Since catalyst sitting in the pores would be removed easily by sonication when the foam is placed in a liquid (and sonicated), the strong adherence can be viewed as evidence that no significant blockage of pores occurred. Furthermore, multiple washcoating steps were required to achieve the desired catalyst mass loading.

4.3. Nitrogen physisorption

The BET surface area, pore volume and average pore size of different samples were analysed using N_2-physisorption. The results are summarised in Table 4-4.

Puralox SCCa 5/150 has a BET surface area and 150 $m^2 \cdot g^{-1}$ and pore volume of 0.5 $cm^3 \cdot g^{-1}$ (Rytter & Holmen, 2016). After impregnation and two calcination steps, the BET surface area and the pore volume of catalyst powder were 29% and 44% lower than those of the support respectively. This will also be achieved by physical mixing of the catalyst precursor and the support. Since the catalyst pellets were prepared using fine (wet-milled) catalyst powder that coalesced together after drying and calcination, it is not surprising that they showed a lower BET surface area and pore volume than the catalyst powder.

It is known that cordierite has a low specific surface area (< 1 $m^2 \cdot g^{-1}$) and pore volume (Nijhuis *et al.*, 2001), which is corroborated by the N_2 physisorption results. The uncoated SiC foam also has a low BET surface area. This is the reason why the active metal is deposited on a secondary support with high BET surface area (Puralox). The washcoating slurry, which was dried and calcined in the same conditions used to washcoat the monoliths and foams, has a BET surface area, which is similar to that of the catalyst powder, while the pore volume has decreased. The latter may be attributed to a partial collapse of the pore structure during drying, resulting in smaller pores overall.

Table 4-4: BET surface area (S_{BET}), pore volume (V_{pore}) as determined from desorption branch and average pore size for powder, pellet and structured catalysts

Sample	S_{BET} [$m^2 \cdot g^{-1}$]	V_{pore} [$cm^3 \cdot g^{-1}$]	d_{pore} [Å]
Co-Pt/Al_2O_3 powder	107	0.28	85
Co-Pt/Al_2O_3 pellet	98	0.19	74
Washcoat layer	109	0.17	-
Cordierite monolith (uncoated)	0.38	0.05	-
Washcoated monolith (HcM 1)	25	0.05	-
SiC Foam (uncoated)	26	0.14	-
Washcoated SiC foam (OcF 2)	78	0.19	-

4.4. Catalyst performance of randomly packed beds

Fischer-Tropsch synthesis was carried out at a temperature of 220°C, pressure of 20 bar and an H_2/CO feed ratio of 2. The different catalyst packings were tested in a stainless steel, tubular reactor with an internal diameter of 10 mm. The catalysts were placed in a 50 mm long isothermal zone to reduce the effect of axial temperature difference along the catalyst bed. Any temperature increase occurring during catalyst tests due to the exothermic nature of Fischer-Tropsch synthesis was recorded. Comparison of the different reactor packings is based on the assumption that the same intrinsic kinetics occur because the same batch of catalyst was used for testing the catalyst powder, making pellets, and washcoating of the substrates.

During the reactor tests, the flowrate of synthesis gas was changed such that catalyst performance could be evaluated as a function of space velocity. As already stated in Chapter 3.3.3, the flowrate of H_2 was usually reduced first, potentially resulting in brief decrease in the H_2/CO ratio of the feed.

4.4.1. Catalyst powder

The catalyst powder, Co-Pt/Al_2O_3 (0.5 g) with a particle size distribution of 125 ± 3.0 µm was diluted with ca. 4 g of 300 um SiC, enough to fill a catalyst bed volume of 2.35 ml. Figure 4-4 is a schematic showing the position of the catalyst bed and thermowell, note that the figure is not drawn to scale. Within the thermowell, the stationary (controlling) thermocouple was placed just above the catalyst bed (145 mm from the reactor outlet) to maintain the isothermal zone at 220°C. The mobile thermocouple could be moved up and down to measure the temperature profile of the catalyst bed without significantly affecting the isothermal zone. Prior to the Fischer-Tropsch synthesis, the catalyst was reduced in pure at 350°C for 16 hours at atmospheric pressure and a hydrogen flowrate of 240 $ml \cdot min^{-1} \cdot g^{-1}_{cat}$

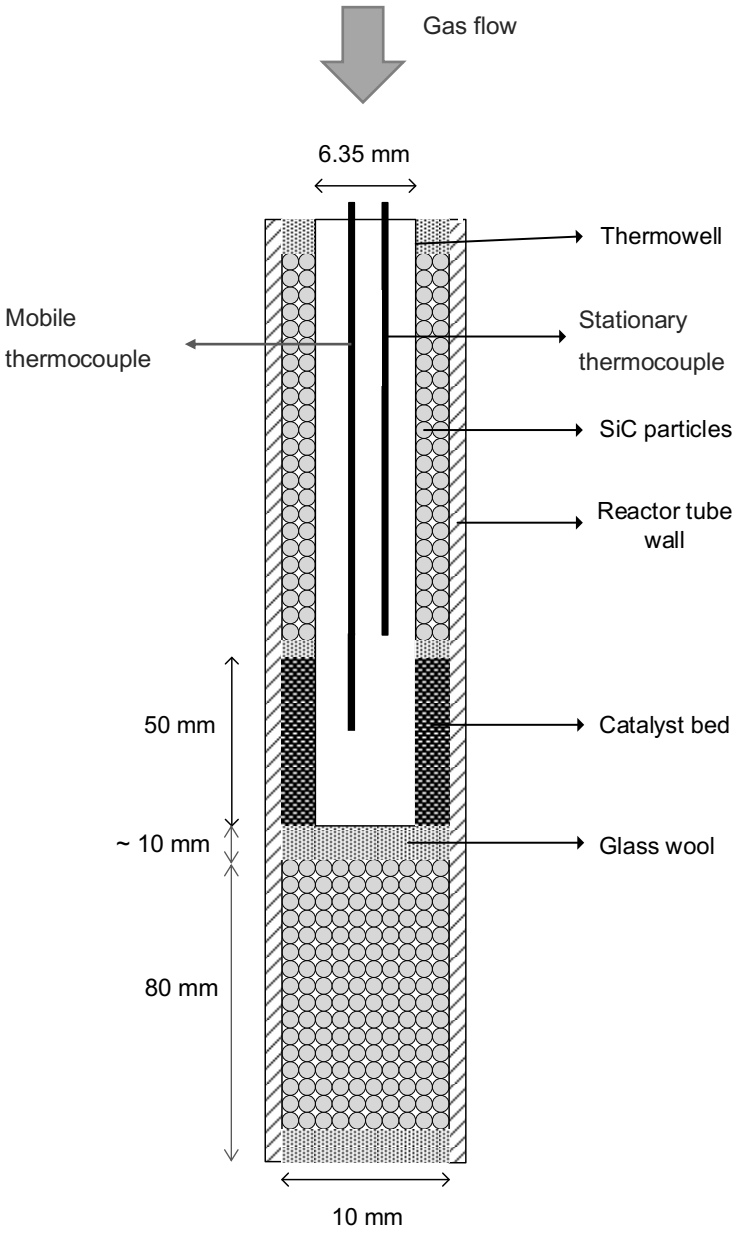

Figure 4-4: Schematic drawing of catalyst bed for testing of the catalyst powder

4.4.1. (A) **Catalyst activity**

The reaction was started at 200°C and 20 bar using a space velocity of 0.11 $mmol_{CO} \cdot s^{-1} \cdot g^{-1}_{Cat}$. Initially, the temperature of the catalyst bed during the startup rose by 5°C but returned to the setpoint temperature of 200°C within 30 minutes. The temperature was then increased to 220°C slowly using a ramp rate 1°C/min - a temperature overshoot to 225°C was observed but decreased within 22 minutes to the set temperature of 220°C. Analysis of the reactor products using GC-TCD was started once the reactor temperature returned to 220°C. The time elapsed (after startup) before reactor products were analysed by GC-TCD was ca. 1 hour and 20 minutes. Upon reaching steady-state, the conversion was increased by decreasing the space velocity. No further temperature rise was observed upon changing the space velocity.

Figure 4-5 shows CO conversion as a function of time on stream at four different space velocities (i.e., 0.11, 0.083, 0.058, and 0.028 $mmol_{CO} \cdot s^{-1} \cdot g^{-1}_{Cat}$). Generally, the CO conversion appeared to be stable with time on stream. However, at the lowest space velocity, the CO conversion dropped from an initial high of 77% to an average of 69%. It is possible that the CO flowrate was decreased first, resulting in an increase in the H_2/CO ratio, and a spike in the reaction rate. In this case, the increased partial pressure of H_2 relative to CO may have also led to increased reduction of the catalyst surface, thus improving catalyst activity.

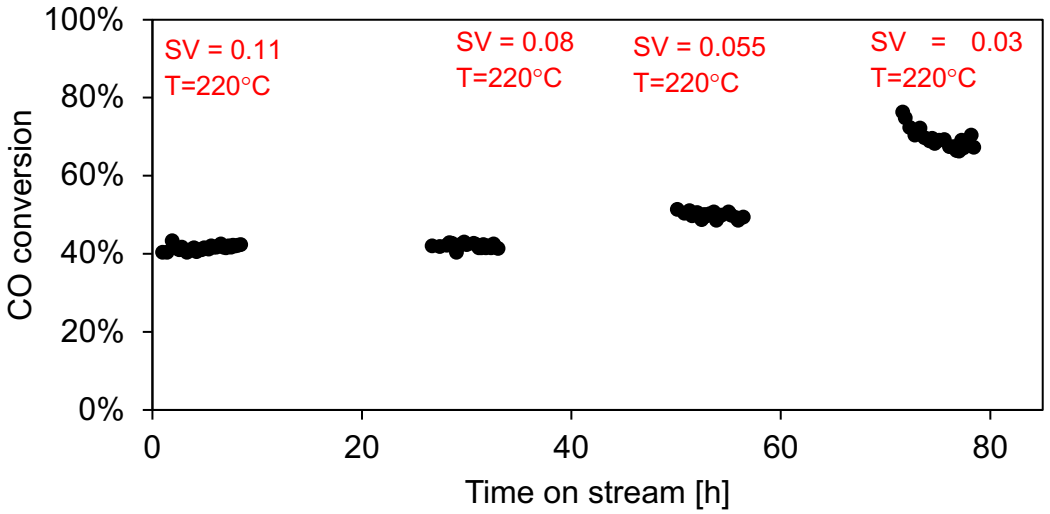

Figure 4-5: CO conversion as a function of time on stream over Co-Pt/Al_2O_3 powder at 220°C and 20 bar at different space velocities [SV in $mmol_{CO} \cdot s^{-1} \cdot g^{-1}_{Cat}$]

Decreasing the space velocity from 0.11 $mmol_{CO} \cdot s^{-1} \cdot g^{-1}_{Cat}$ to 0.083 $mmol_{CO} \cdot s^{-1} \cdot g^{-1}_{Cat}$, did not result in a significant change in the conversion, which remained at 42%. This may be an indication of catalyst deactivation during testing at 0.11 $mmol_{CO} \cdot s^{-1} \cdot g^{-1}_{Cat}$ or during the

transition to 0.083 $mmol_{CO} \cdot s^{-1} \cdot g^{-1}_{Cat}$: While the CO conversion appeared to be stable for the duration of the test at 0.11 $mmol_{CO} \cdot s^{-1} \cdot g^{-1}_{Cat}$, the H_2/CO usage ratio was abnormally low for Fischer-Tropsch synthesis, at an average of 1.80, whereas an H_2/CO usage ratio of 2.05 to 2.15 is typically observed (Dry, 2004). Low H_2/CO usage ratios have been linked to water-gas shift activity, which is associated with catalyst deactivation due to oxidation of Co to CoO, which also facilitates particle growth in the reducing Fischer-Tropsch environment (Ma *et al.*, 2011). Carbon deposition on the catalyst surface may have been another contributing factor: Moodley (2008) reported the formation of inactive carbon species on the catalyst surface, due to a sudden decrease in H_2/CO feed ratio on the catalyst. Since the flowrate of H_2 was typically decreased first when decreasing space velocity, resulting in a momentary decrease in the H_2/CO ratio, the possibility of carbon deposition cannot be eliminated.

The CO conversion over a non-deactivated catalyst should increase with a decrease in space velocity. A fixed-bed design equation for Fischer-Tropsch synthesis (Fogler, 2016) can be derived by assuming pseudo-first order rate kinetics in terms of H_2 (Van der Laan & Beenackers, 1999). For a constant H_2/CO feed ratio of 2, a similar expression can be derived in terms of CO.

$$-r_{CO} = k' \cdot P_{H_2} = k' \cdot (2 \cdot P_{CO}) = k \cdot P_{CO} \qquad 4\text{-}2$$

The space velocity is inversely proportional to residence time, and thus, inversely proportional to conversion as can be shown for a simple first order reaction, including volume contraction.

$$\frac{W}{F_{CO,0}} = \tau = \int_0^X \frac{1}{-r_{CO}}\, dX \qquad 4\text{-}3$$

$$\frac{W}{F_{CO,0}} = \int_0^X \frac{\left(3 - \left(2 - \frac{1}{n}\right) \cdot X\right)}{k \cdot P_{total} \cdot (1 - X)}\, dX = \frac{1}{k \cdot P_{total}} \left(\left(2 - \frac{1}{n}\right) \cdot X + \left(\left(2 - \frac{1}{n}\right) - 3 \right) \cdot \ln(1 - X) \right) \qquad 4\text{-}4$$

(with n the average carbon number in the product – typically taken as 2)

The pseudo first order rate constant (k) was calculated by rearranging Equation 4-4. Figure 4-6 shows that the pseudo first order rate constant decreases with an increase in conversion. Ideally, the rate constant should only be a function of temperature. The decline in the pseudo first order rate constant may be caused by catalyst deactivation induced by the exposure to CO-rich gas upon changing space velocity. The observed catalyst activity may be lowered than it would have been without deactivation, possibly due to carbon deposition.

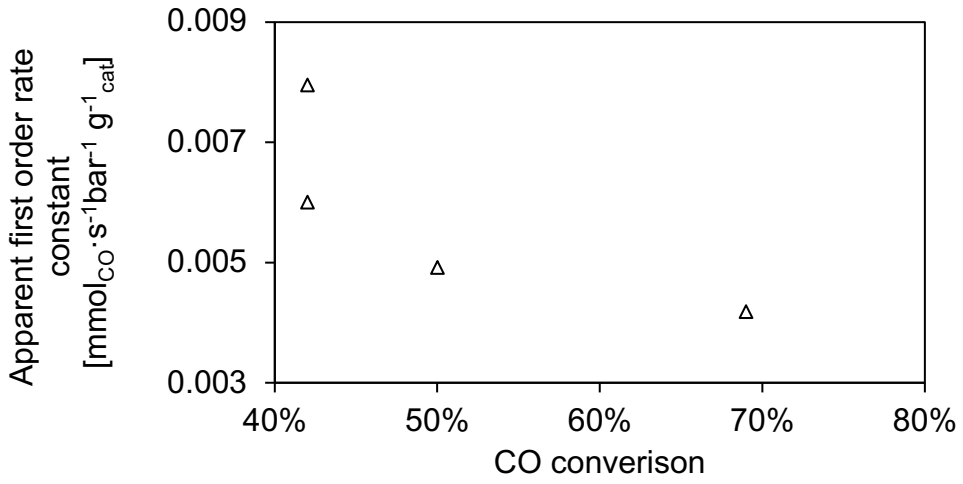

Figure 4-6: Pseudo first order reaction rate constant as a function of average CO conversion in the Fischer-Tropsch synthesis over catalyst powder at 220°C and 20 bar

4.4.1. (B) **CO_2 selectivity**

Figure 4-7 shows CO_2 selectivity as a function of time on stream at different space velocities. In general, the CO_2 selectivity is low and did not exceed 2 C-% for all the space velocities tested, which is expected for cobalt-based LT-FTS catalysts (Steynberg *et al.*, 2004). The CO_2-selectivity appears to be stable with time on stream. However, the CO_2 selectivity seems to increase with decreasing space velocity, and thus with an increase in CO conversion. The increasing CO_2 selectivity with increasing CO conversion may be attributed to an increase in the secondary water-gas shift reaction (Ma *et al.*, 2011). The Boudouard reaction may also be responsible for increased CO_2 production and concomitant catalyst deactivation (Moodley *et al.*, 2009).

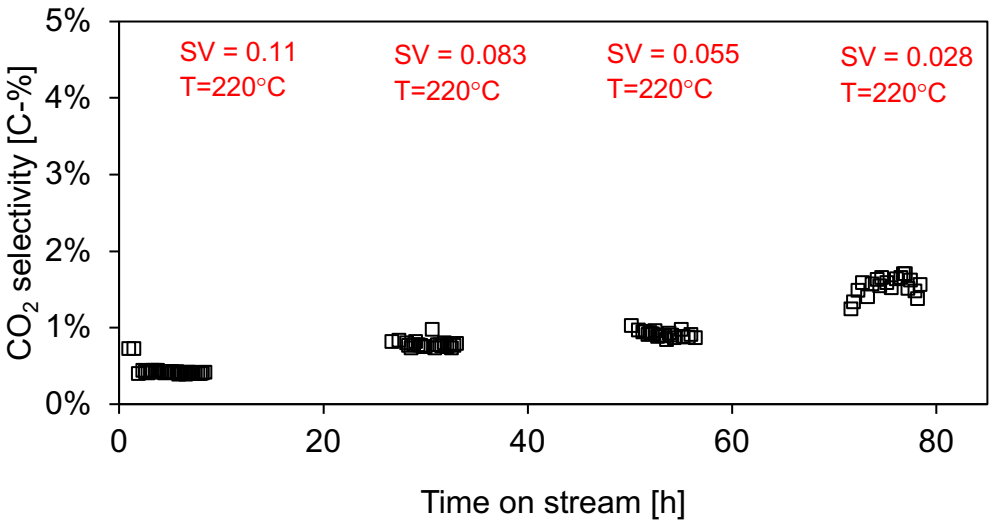

Figure 4-7: CO_2 selectivity as a function of time on stream over Co-Pt/Al_2O_3 powder at 220°C and 20 bar at different space velocities [SV in mmol$_{CO}$·s^{-1}·g$^{-1}_{Cat}$]

4.4.1. (C) **Product distribution**

Methane is an undesired product of the Fischer-Tropsch synthesis. The observed methane selectivity over the catalyst powder ranged from 16 C-% and 21 C-%. They are higher than those typically reported for similar conversion levels in cobalt-based Fischer-Tropsch synthesis in laboratory scale fixed-bed reactors operating at 220°C and 20 bar, which are typically in the range of 5 - 12% (Bukur *et al.*, 2012; Rytter *et al.*, 2016). Figure 4-8 shows CH_4 selectivity as a function of time-on stream at different space velocities. The CH_4 selectivity decreases only slightly with decreasing space velocity which correlates with the increasing CO conversion. However, while the CO conversion at a space velocity of 0.11 and 0.083 $mmol_{CO} \cdot s^{-1} \cdot g^{-1}_{Cat}$ were similar, the methane selectivity at the latter space velocity is ca. 4% higher. The difference in this methane selectivity at similar conversions could be a further indication of catalyst deactivation.

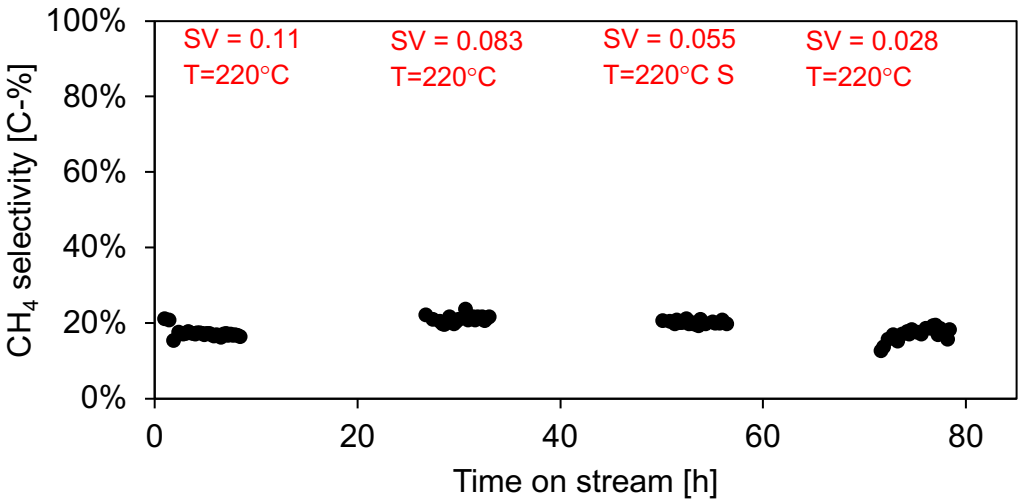

Figure 4-8: CH_4 selectivity as a function of time on stream over Co-Pt/Al_2O_3 powder at 220°C and 20 bar at different space velocities [SV in $mmol_{CO} \cdot s^{-1} \cdot g^{-1}_{Cat}$]

The average CH_4 selectivity obtained from the time on stream data was used together with the peak areas obtained via GC-FID analysis to estimate the product distribution (see Chapter 3.3.5). The product distributions, namely, the selectivity for CH_4, CO_2, C_2 -C_4 and C_{5+} along with the associated average CO conversion are summarized in Figure 4-9 as a function of space velocity. The C_2 -C_4 fraction at 0.11 $mmol_{CO} \cdot s^{-1} \cdot g^{-1}_{Cat}$, which was estimated to be 11.4%. Upon decreasing the space velocity to 0.083 $mmol_{CO} \cdot s^{-1} \cdot g^{-1}_{Cat}$, the C_2 -C_4 selectivity increased to an average of ca. 14%. At lower space velocities, the C_2 -C_4 product fraction appears to be largely independent of space velocity and remained at approximately 14% at all conversion levels. The C_{5+} selectivity is expected to increase with decreasing space velocity (i.e.,

increasing CO conversion) (Rytter *et al.*, 2016). However, upon decreasing the space velocity from 0.11 $mmol_{CO} \cdot s^{-1} \cdot g^{-1}_{Cat}$ to 0.083 $mmol_{CO} \cdot s^{-1} \cdot g^{-1}_{Cat}$, the C_{5+} selectivity decreased from an average of 72% to 65%, despite the unaltered conversion. This is likely a consequence of the catalyst deactivation suggested to have occurred upon switching space velocity. Subsequent reductions in space velocity let to a slight increase in the C_{5+} selectivity with decreasing space velocity (i.e., increasing CO conversion). However, the response was still significantly muted as C_{5+} selectivity increased by 1% and 2% for gains of 8% and 19% in CO conversion. This was attributed to catalyst deactivation.

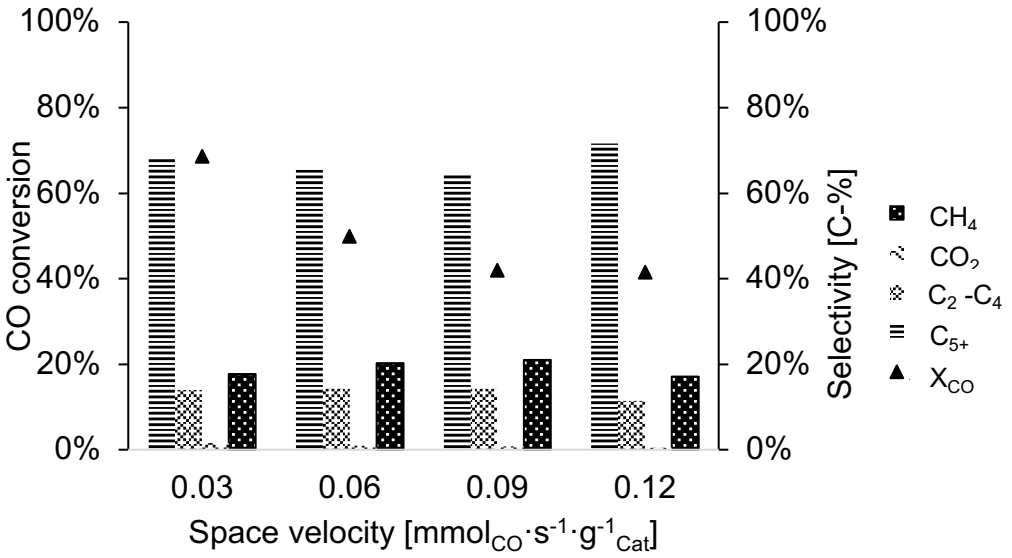

Figure 4-9: Product distribution and average CO conversion of Fischer-Tropsch synthesis over Co-Pt/Al_2O_3 powder catalyst

Figure 4-10 shows the O/P ratio for carbon numbers up to C_{13} at the different space velocities. At all the space velocities, the expected low value for the O/P ratio in the C_2 product fraction was observed as a result of high reactivity of ethylene (Dry, 2004). Furthermore, the O/P ratio decreases with an increase in carbon number from C_3 onwards. This is attributed to an increase in secondary hydrogenation of olefins with an increase in carbon number (Bukur *et al.*, 2012). The olefin content for the C_9 product fraction at 0.11 $mmol_{CO} \cdot s^{-1} \cdot g^{-1}_{Cat}$ was lower than expected, possibly due to an error in detection.

It is expected that the extent of secondary reactions increase with a decrease in space velocity (i.e., increasing residence time), since this would increase the likelihood for secondary hydrogenation of olefins (Bukur *et al.*, 2012). However, the observed trend is contradictory to this, with the highest space velocity (0.11 $mol_{CO} \cdot s^{-1} \cdot g^{-1}_{Cat}$) yielded the lowest tO/P ratio, while the O/P ratio in the various carbon number fractions did not differ much upon decreasing the space velocity from 0.083 to 0.029 $mmol_{CO} \cdot s^{-1} \cdot g^{-1}_{Cat}$. It is noted that while the CO conversion

increased with decreasing space velocity, the product distributions at the space velocities from 0.083 to 0.029 $mmol_{CO} \cdot s^{-1} \cdot g^{-1}_{Cat}$ were similar. This was earlier attributed to catalyst deactivation when decreasing the space velocity from 0.11 to 0.83 $mmol_{CO} \cdot s^{-1} \cdot g^{-1}_{Cat}$. The unexpected trend of increasing olefin content with decreasing space velocity is more evidence suggesting the strong influence of catalyst deactivation on the product distribution.

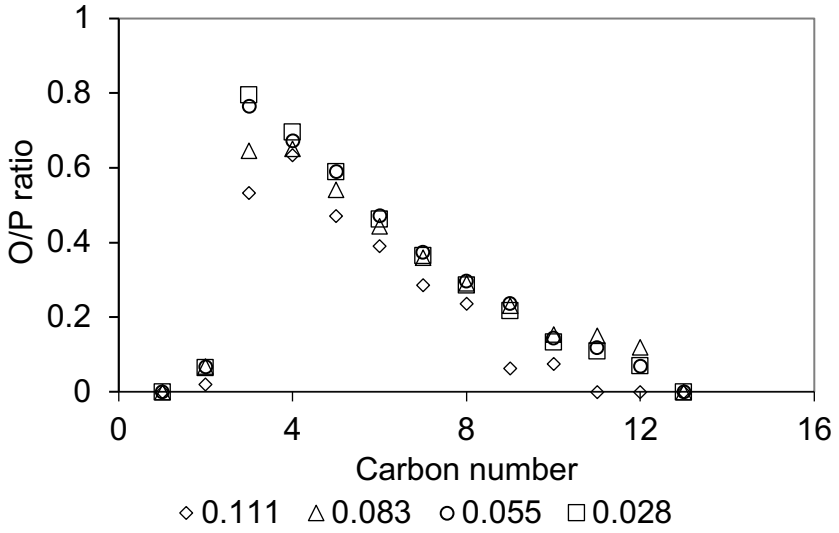

Figure 4-10: Olefin-to-Paraffin ratio as a function of carbon number obtained over the catalyst powder at 200°C and 20 bar at different space velocities [SV in $mmol_{CO} \cdot s^{-1} \cdot g^{-1}_{Cat}$]

4.4.1. (D) **Summary and insights**

The catalyst powder performance data is summarised in Table 4-5. It was seen that the performance of the catalyst may have been affected by deactivation, as evidenced by the unchanging CO conversion when decreasing space velocity from 0.11 $mmol_{CO} \cdot s^{-1} \cdot g^{-1}_{Cat}$ to 0.083 $mmol_{CO} \cdot s^{-1} \cdot g^{-1}_{Cat}$ and low H_2/CO usage ratio at 0.11 $mmol_{CO} \cdot s^{-1} \cdot g^{-1}_{Cat}$. This was potentially due to oxidation of Co to CoO under high H_2O partial pressure and the Fischer-Tropsch reducing environment (Ma et al., 2011). It is also suspected that the momentary decrease in the H_2/CO ratio when decreasing space velocity may have facilitated carbon deposition (Moodley, 2008). Between 0.083 and 0.028 $mmol_{CO} \cdot s^{-1} \cdot g^{-1}_{Cat}$, the CO conversion behaved more predictably, increasing with decreasing space velocity, while the C_{5+} selectivity only increased slightly with increasing conversion due to the deactivation.

Table 4-5: Summary of the performance of the catalyst powder

Syngas Flowrate [ml·min^{-1}]	240	180	120	60
Space velocity [mmol$_{CO}$·g$^{-1}_{Cat}$·s^{-1}]	0.11	0.083	0.055	0.03
Temperature [˚C]	220	220	220	220
H_2/CO usage ratio	1.80	2.15	2.12	2.12
Average X_{CO}	42 ± 0.5%	42 ± 0.6%	50 ± 0.8%	69 ± 1.6%
Average S_{CH_4} [C-%]	17 ± 0.3%	21 ± 0.9%	20 ±0.5%	18 ± 1.2%
Average S_{CO_2} [C-%]	0%	1 ± 0.1%	1%	2 ± 0.1%
$S_{C_2-C_4}$ [C-%]	11%	14%	14%	14%
$S_{C_{5+}}$[C-%]	72%	65%	66%	68%

4.4.2. Pellets

Cylindrical pellets weighing 0.51 g were loaded into the fixed-bed reactor as shown in Figure 3-8 in Chapter 3.3.2. Each pellet was 5 mm in diameter with an average catalyst mass of 0.140 g. The pellets were loaded ensuring equal distance from the reactor tube wall; and equal amounts of 300 µm SiC particles were placed around each pellet to counteract wall effects and provide a diluent to reduce thermal runaway. The catalyst bed was diluted with a total of 6.2 g of SiC particles. Catalyst reduction and reactor startup were carried out as described in Chapter 3.3.3. The Fischer-Tropsch synthesis was started at 0.11 $mmol_{CO} \cdot s^{-1} \cdot g^{-1}_{Cat}$ at 200°C and 20 bar. The catalyst was subsequently tested at 0.083, 0.055, 0.14 and 0.028 $mmol_{CO} \cdot s^{-1} \cdot g^{-1}_{Cat}$ by decreasing the flowrate of syngas. The flowrate of H_2 was usually changed first, resulting in a momentary change in the H_2/CO feed ratio. Reactor products were analysed using GC-TCD immediately after startup.

4.4.2. (A) **Catalyst activity**

Figure 4-11 shows the CO conversion as a function of time on stream at different space velocities. After startup, the intention was to increase the temperature of the reactor from 200°C to 220°C, at $1°C \cdot min^{-1}$. However, before the temperature ramping programme was started, the temperature measured ca. 5 mm above the catalyst bed increased rapidly and had reached 250°C within 30 minutes after startup. It can thus be deduced that the temperature within the catalyst bed was significantly higher. The catalyst activity in the first hour after startup was high, due to the elevated reactor temperature. The first CO conversion measurement (45 minutes after startup) was 84.8%. Both the temperature and CO conversion gradually decreased over a period of 24 hours such that the temperature measured above the catalyst bed read 238°C and an average CO conversion of 66.6%. This initial decline in catalyst activity is expected while the catalyst reaches steady state. This is a consequence of a reduction in temperature, possibly aggravated by catalyst deactivation.

Upon decreasing the space velocity to 0.083 $mmol_{CO} \cdot s^{-1} \cdot g^{-1}_{Cat,}$ the temperature above the catalyst bed rose to 248°C and decreased to the setpoint of 220°C after one hour. In this case, the CO flow rate was decreased first, leading to temporary enrichment of the H_2 in the catalyst. It is possible that the higher partial pressure of H_2 when compared to CO led to increased reduction of the catalyst, changing the structure of the catalyst surface. This may have led to an increased reaction rate and the observed increased in temperature. Note that as the H_2/CO ratio returned to normal, the environment in the CO conversion continued to decline with time to about 55%. It is worth noting that it was later realised that the space velocity was decreased

from 0.083 to 0.055 $mmol_{CO} \cdot s^{-1} \cdot g^{-1}_{Cat}$ before a stable CO conversion had been achieved. Thus, the test was repeated at the same space velocity and a stable CO conversion averaging at 57% was observed. Since the flowrates of the gases were changed in the same order, i.e., increasing the H_2 flowrate and then the CO flowrate, it is possible that the resulting momentary enrichment of H_2 in the gas feed led to increased reduction of the catalyst. This may be the reason for a higher CO conversion for the second run at 0.083 $mmol_{CO} \cdot s^{-1} \cdot g^{-1}_{Cat}$.

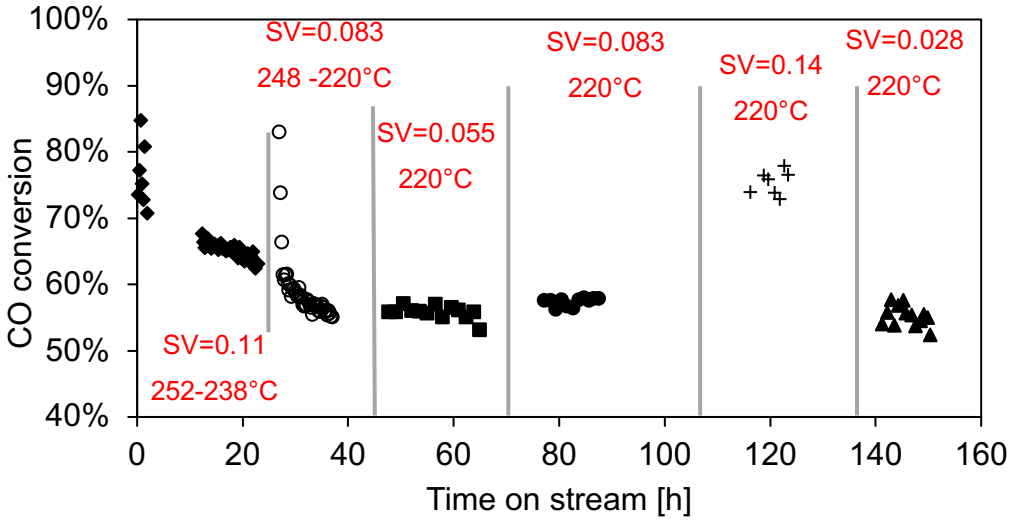

Figure 4-11: CO conversion as a function of time on stream over Co-Pt/Al_2O_3 pellets at 220°C and 20 bar at different space velocities [SV in $mmol_{CO} \cdot s^{-1} \cdot g^{-1}_{Cat}$]

The CO conversion generally decreases with a decrease in space velocity. This is contrary to the expected trend for a kinetically controlled reaction with a positive overall reaction order. For a first order reaction, conversion (X) is expected to increase with decreasing space velocity see equation 4-4 obtained by integrating equation 4-2; see Chapter 4.4.1. Thus, the observed trend may indicate that the reaction may be dominated by transport resistances rather than intrinsic rate kinetics. The space velocity was increased to 0.14 $mmol_{CO} \cdot s^{-1} \cdot g^{-1}_{Cat}$ with the expectation that this would improve mixing at the boundary layer to the extent of reversing external mass transfer limitations, however, the CO conversion increased further. This may be attributed to the occurrence of internal mass and heat transport limitations contributing substantially to the observed catalyst activity.

At space velocities lower than 0.083 $mmol_{CO} \cdot s^{-1} \cdot g^{-1}_{Cat}$, the catalyst activity showed a flat response to changes in flowrate (i.e., the difference in conversion is less than 1.5%), but when the space velocity was increased to 0.011 and 0.14 $mmol_{CO} \cdot s^{-1} \cdot g^{-1}_{Cat}$, a larger increase in CO conversion was observed. Note that when changing space velocity from 0.083 $mmol_{CO} \cdot s^{-1} \cdot g^{-}$

$^{1}_{Cat}$ (180 ml·min^{-1}) to 0.14 mmol$_{CO}$·s^{-1}·g$^{-1}_{Cat}$ (300 ml·min^{-1}), caution was taken to increase the flowrates of H_2 and CO gradually to avoid 'shocking' the catalyst.

Returning to the issue of poor transport properties, the maximum temperature gradient inside the catalyst pellet was estimated using the Mears Criterion (see Chapter 2.5.3). For an average heat of reaction of 165 kJ·mol^{-1}, the temperature difference between the bulk gas and the centre of the pellet could be as high as 16.6°C at 0.11 mmol$_{CO}$·s^{-1}·g$^{-1}_{Cat}$. The resulting acceleration of the reaction rate on the catalyst surface could have caused the diffusion of reactants from the bulk gas to the catalyst surface to become the rate limiting step.

If the reaction over the catalyst pellets is dominated by external mass transfer limitations, the reaction rate can be modelled as shown by equation 4-5:

$$r'_{CO} = k_m \cdot a_m \cdot ([CO]_b - [CO]_s) \qquad 4\text{-}5$$

where k_m is a mass transfer coefficient and a_m the mass transfer area, which was estimated at:

$$a_m = \frac{A_{pellet}}{m_{pellet}} = \frac{2 \cdot \frac{\pi}{4} \cdot d_{pellet}^2 + \pi \cdot d_{pellet} \cdot h_{pellet}}{m_{pellet}} \qquad 4\text{-}6$$

$$= \frac{2 \cdot \frac{\pi}{4} \cdot 0.5^2 + \pi \cdot 0.5 \cdot 0.5}{0.14} \cdot 10^{-4} = 8.41 \cdot 10^{-4} \cdot \frac{m^2}{g}$$

Assuming a very fast reaction rate over the exothermically heated surface of the pellet, the concentration of CO at the external surface $[CO]_s$ can be assumed to be significantly lower than the concentration of CO in the bulk $[CO]_b$. Thus, the mass transfer coefficient can be estimated from a first order approach (see equation 4-4). It is recognized that the temperature profile in the catalyst pellet is not uniform, but the external mass transfer coefficient is not a strong function of temperature, and this analysis will give some indication on possible mass transfer limitations in the reactor set-up. The obtained, modified mass transfer coefficient is shown in Figure 4-12 as a function of space velocity. It appears that the mass transfer coefficient increases with an increase in space velocity. The increase in the mass transfer coefficient with increasing space velocity (and thus in this type of experiments with increasing linear velocity) is expected. However, the increase in the mass transfer coefficient is stronger than expected.

The corresponding Sherwood numbers (based on the molecular gas phase diffusion of CO into H_2) was estimated to be in the range between 1.4 and 0.2. The reduction in the mass

transfer coefficient may be related to a change in the medium through which diffusion takes place as well.

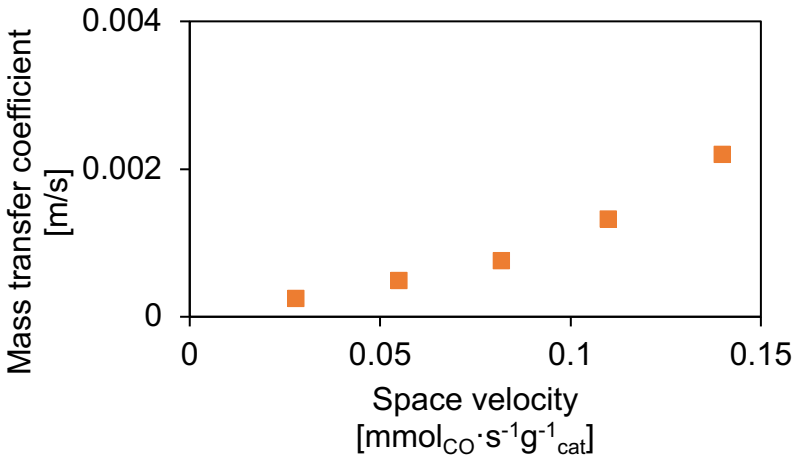

Figure 4-12: Observed mass transfer coefficients over the catalyst pellets assuming external mass transfer limited operation

4.4.2. (B) **CO_2 selectivity**

The obtained CO_2 selectivity as a function of time on stream over the pellets is shown in Figure 4-13. The CO_2 selectivity correlates with the trends exhibited by the CO conversion. High CO_2 selectivity can be seen during the unsteady-state (elevated temperature and high CO conversion) phases at 0.11 and 0.083 $mmol_{CO}·s^{-1}·g^{-1}_{Cat}$ possibly due to the high reactor temperature. In general, the CO_2 selectivity decreased with a decrease in space velocity, apart from that at 0.14 $mmol_{CO}·s^{-1}·g^{-1}_{Cat}$, where CO_2 selectivity was significantly lower than observed at lower space velocities. Here the average CO_2 selectivity was 1.5% while the average CO_2 selectivity at lower space velocities was higher than 3.6%. It is important that the CO_2 selectivities obtained over the catalyst pellets were high, as this is not typical for cobalt-based LT-FTS catalysts operating at mild reactor conditions (van Steen *et al.*, 2018). This further supports the assertion that the conditions in the local surroundings of the catalyst particles were quite severe (very high catalyst temperature and significant external mass transfer resistance). It is possible that carbon deposition, linked to the high CO_2 production could have contributed to gradual decline in catalyst activity, possibly due to an increase in the Boudouard reaction (Moodley et al., 2009). Increased CO_2 production has also been suggested to result from increased water-gas shift activity, caused by oxidation of Co to CoO in the presence of high H_2O partial pressures (Ma *et al.*, 2011).

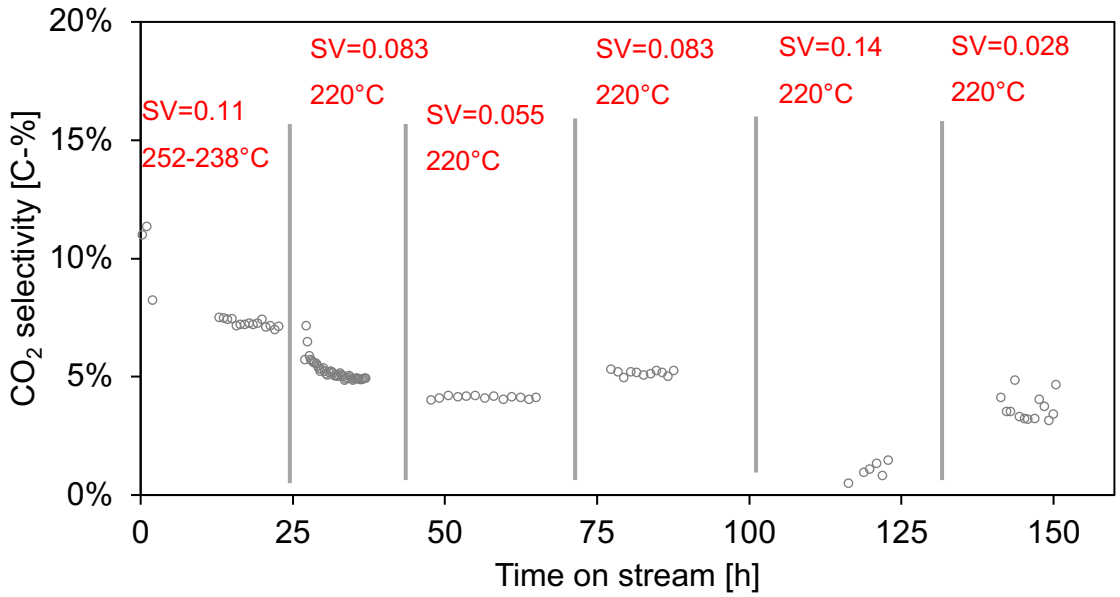

Figure 4-13: CO_2 selectivity as a function of time on stream over Co-Pt/Al_2O_3 pellets at 220°C and 20 bar at different space velocities [SV in $mmol_{CO} \cdot s^{-1} \cdot g^{-1}_{Cat}$]

4.4.2. (C) **Product distribution**

The selectivity of the Fischer-Tropsch synthesis for the undesired product (S_{CH_4}) obtained over the pellets as a function of time on stream at different space velocities is shown in Figure 4-14. The CH_4 selectivity between 5 and 12 C-% are typically reported for Fischer-Tropsch synthesis carried out in laboratory scale reactors such as the one used in this study (Bukur *et al.*, 2012; Rytter *et al.*, 2016). However, the CH_4 selectivity obtained over the pellets appear to be rather high, with values exceeding 33 C-% for all space velocities except 0.14 $mmol_{CO} \cdot s^{-1} \cdot g^{-1}_{Cat}$. The high CH_4 selectivity is likely to be a result of hotspot formation. Interestingly, the CH_4 selectivity appears to start low during the unstable phases of the catalyst performance tests and gradually increased, refer to the circled areas on the graph. This is not surprising, as heat released by the chemical reaction is likely to accumulate with increasing time on stream in the presence of heat transfer limitations.

Furthermore, the CH_4 selectivity primarily shows a low response to changes in space velocity. Between 0.11 and 0.055 $mmol_{CO} \cdot s^{-1} \cdot g^{-1}_{Cat,}$ the average CH_4 selectivity lies between 41% and 42% (note that the CO conversion at these space velocities was similarly independent of changes in space velocity). The CH_4 selectivity at 0.14 $mmol_{CO} \cdot s^{-1} \cdot g^{-1}_{Cat}$ is remarkably low. This can be attributed to increased cooling of the pellets by convection as a result of the increased gas flowrate, bringing the internal temperature of the catalyst pellet closer to the setpoint of 220°C. Since CH_4 is a thermodynamically favoured product, reduced catalyst

temperature can greatly diminish its production. However, it should also be noted that the repeated though brief exposure to high H_2/CO ratios when increasing the space velocity from 0.083 to 0.14 $mmol_{CO} \cdot s^{-1} \cdot g^{-1}_{Cat}$ could have 'cleaned' the catalyst surface of adsorbed carbon. It can be seen that upon decreasing the space velocity down to 0.028 $mmol_{CO} \cdot s^{-1} \cdot g^{-1}_{Cat,}$ the CH_4 selectivity increased again, to an average value of 3 C-%, which is more similar to the one obtained at the space velocities from 0.055 to 0.11 $mmol_{CO} \cdot s^{-1} \cdot g^{-1}_{Cat}$.

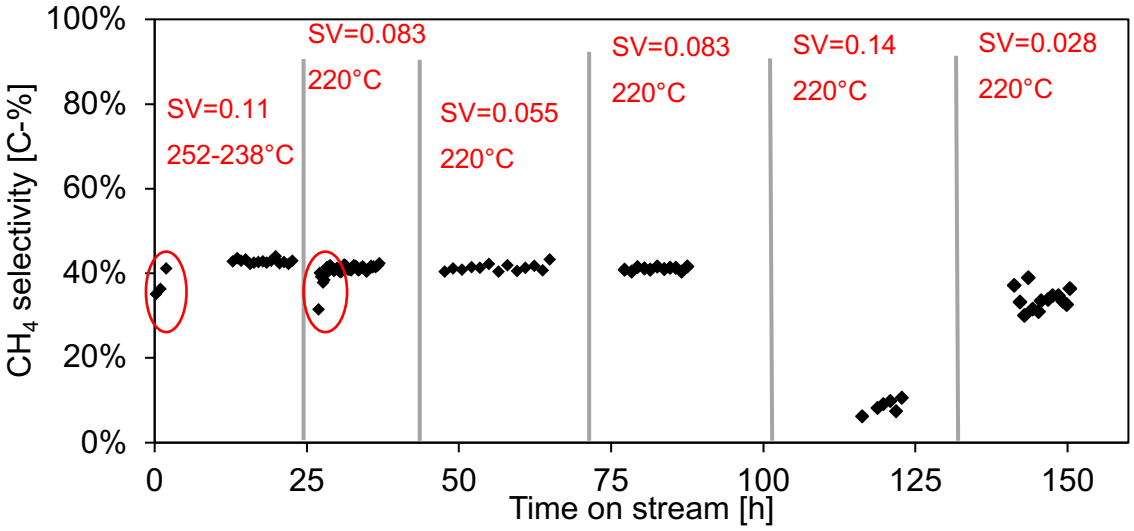

Figure 4-14: CH_4 selectivity as a function of time on stream over Co-Pt/Al_2O_3 pellets at 220°C and 20 bar at different space velocities [SV in $mmol_{CO} \cdot s^{-1} \cdot g^{-1}_{Cat}$]

The steady-state CO conversion, CH_4 selectivity and CO_2 selectivity were averaged for a duration of over 7 hours at each space velocity. These, along with the C_2 - C_4 and C_{5+} selectivity, which were obtained via GC-FID analysis, are shown in Figure 4-15. The C_2 – C_4 selectivity increases with an increase in space velocity, while the C_{5+} selectivity increased with a decrease in space velocity. This trend is expected, since decreasing space velocity increases residence time, providing more time for chain propagation to occur (Kuipers *et al.*, 1995; Ma *et al.*, 2011). Note that the C_{5+} fraction predominantly constitutes less than 50% of the hydrocarbon products. This is not surprising given that the large pellet diameter is likely to have led to severe heat and mass transfer resistance. This could have led to high internal temperatures of the catalyst, for which the contrary trend of CO conversion with changing space velocity, as well as the high CH_4 and CO_2 selectivity have already been presented as evidence. However, when the space velocity was increased to 0.14 $mmol_{CO} \cdot s^{-1} \cdot g^{-1}_{Cat}$, very high C_{5+} selectivity (84%) as well as low CH_4 (9%) and CO_2 (<1%) selectivity were obtained. In addition to the 'cleaned' catalyst surface, it is possible that the increased linear gas velocity greatly enhanced mass transfer, thus increasing the rate of heat removal by convection, such

that the temperature gradient within the catalyst pellet became more suitable for C_{5+} production.

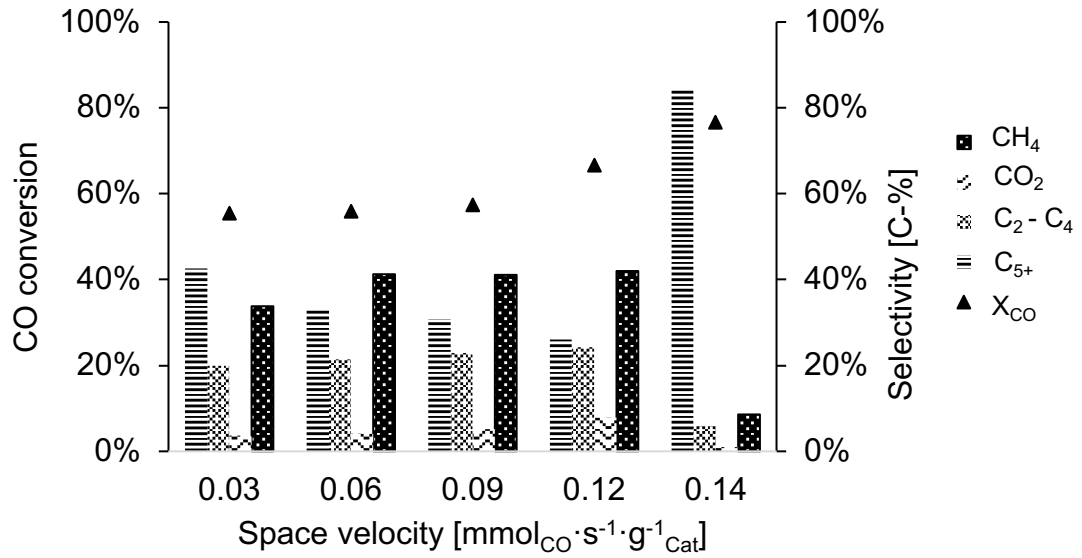

Figure 4-15: Average CO conversion and product distribution of Fischer-Tropsch synthesis over Co-Pt/Al_2O_3 pellets at 220°C and 20 bar

Figure 4-16 shows the olefin content as a function of the carbon number at different space velocities. With the exception of the data at 0.14 $mmol_{CO}·s^{-1}·g^{-1}_{Cat.}$, the olefin ratios increase with carbon number up to C_4 but decrease with carbon number thereafter. This is expected as C_2 olefins are likely to be re-inserted while an increase in secondary hydrogenation occurs at higher chain lengths to decrease the olefin content. Olefin content typically show a maximum in C_3 fraction (Shafer *et al.*, 2019). However, the olefin content obtained over the pellets show a maximum in the C_4 product fraction. This can be attributed to enhanced double bond isomerisation activity, since internal olefins are less reactive for secondary hydrogenation than α-olefins (Claeys and van Steen, 2004). This may be a result of increased residence time of products in the pores of the catalyst due to internal mass transfer limitations.

The O/P-ratio mostly increases with a decrease in space velocity. It should be noted that O/P ratios are expected to decrease with decreasing space velocity due to increasing residence time and increased opportunity for secondary reactions of olefins to occur (Bukur *et al.*, 2012). This is thought to be a result of catalyst deactivation, which may have reduced the number of sites available for olefin reinsertion. The exception is the data at 0.14 $mmol_{CO}·s^{-1}·g^{-1}_{Cat}$, which has a higher O/P ratio than the lower space velocities. This is the expected result as per the trend presented in Bukur *et al.* (2012). However, catalyst deactivation may have increased the O/P ratios even further by diminishing the available number of active sites.

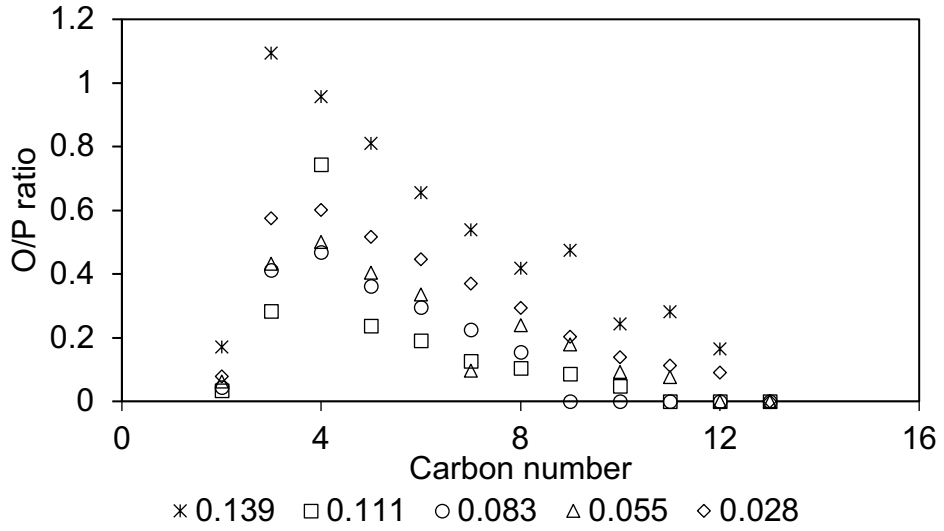

Figure 4-16: Olefin/paraffin ratio as function of carbon number obtained over Co-Pt/A_2O_3 pellets at 220°C and 20 bar at different space velocities [SV in $mmol_{CO} \cdot s^{-1} \cdot g^{-1}_{Cat}$]

4.4.2. (D) **Summary and insights**

The results of the performance of the catalyst pellets are summarised in Table 4-6. While the catalyst pellets achieved high CO conversion during Fischer-Tropsch synthesis, they performed poorly in terms of selectivity (high CH_4 selectivity and low C_{5+} selectivity). A very significant observation was that the CO conversion increased with an increase in space velocity, which is indicative of severe external mass transfer resistance. Furthermore, during startup and at high space velocities, high reaction rates resulted in sustained high temperatures. This resulted in high CO_2 and CH_4 selectivity, with between 3.6 C-% and 7.8 C-% carbon converted to CO_2 and between 33 C-% to 42 C-% of carbon converted to methane. This is undesirable. C_{5+} selectivity were generally low (<50 C-%). Better catalyst performance was observed at the highest space velocity 0.14 $mmol_{CO} \cdot s^{-1} \cdot g^{-1}_{Cat}$. While the CO conversion followed the general trend, the hydrocarbon product distribution was drastically improved when compared to the other space velocities, which was attributed to enhanced transport phenomena at the high linear gas velocity. In addition, the catalyst activity could have been improved during the gradual increase of space velocity from 0.083 $mmol_{CO} \cdot s^{-1} \cdot g^{-1}_{Cat}$. Lastly, H_2/CO usage ratios were higher than the typical range of 2.05 to 2.15 given by Dry (2004), this is likely linked to the high CH_4 selectivity. However, the H_2/CO usage ratio obtained at 0.14 $mmol_{CO} \cdot s^{-1} \cdot g^{-1}_{Cat}$ fell within the expected range, supporting the assertion that the catalyst pellet behaved most ideally when operating the highest space velocity where mixing near the

external catalyst surface was likely enhanced, and cooling of the catalyst surface by the increase gas flow rate may have been increased.

Table 4-6: Summary of the performance Co-Pt/Al_2O_3 pellets

Space velocity [$mmol_{CO} \cdot s^{-1} \cdot g^{-1}_{Cat}$]	0.14	0.11	0.083	0.055	0.028
Syngas Flowrate [$ml \cdot min^{-1}$]	300	240	180	120	60
Temperature [˚C]	238	238	238	238	238
Integral reaction rate [$mmol_{CO} \cdot min^{-1} \cdot g^{-1}_{Cat}$]	0.56	0.39	0.25	0.16	0.081
H_2/CO usage ratio	2.06	2.32	2.38	2.45	2.28
Average X_{CO}	77 ± 3%	67 ± 4%	57 ± 2%	56 ± 2%	56 ± 3%
Average S_{CH_4}[C-%]	9 ± 3%	42 ± 3%	41 ± 1%	41 ± 1%	34 ± 4%
Average S_{CO_2}[C-%]	1 ± 1%	8 ± 1%	5 ± 0.3%	4 ± 0.2%	4 ± 1%
$S_{C_2-C_4}$ [C-%]	6%	24%	23%	21%	20%
$S_{C_{5+}}$ [C-%]	84%	26%	31%	33%	43%

4.5. Catalyst performance of honeycomb monoliths

Two pairs of honeycomb monoliths were washcoated with different masses of catalysts to evaluate the effect of catalyst layer thickness. When loading the square monolith pieces into the reactor tube, the pieces were wrapped in glass wool before loading into the reactor to minimise gas bypassing. Furthermore, the pieces were wrapped so as to align flow channels and reduce disturbing the distribution of gas. The wrapped monolith pieces were loaded into the reactor tube as shown Figure 4-17. For both sets of monoliths, the catalyst reduction and reactor startup procedure described in Chapter 3.3.3 was followed.

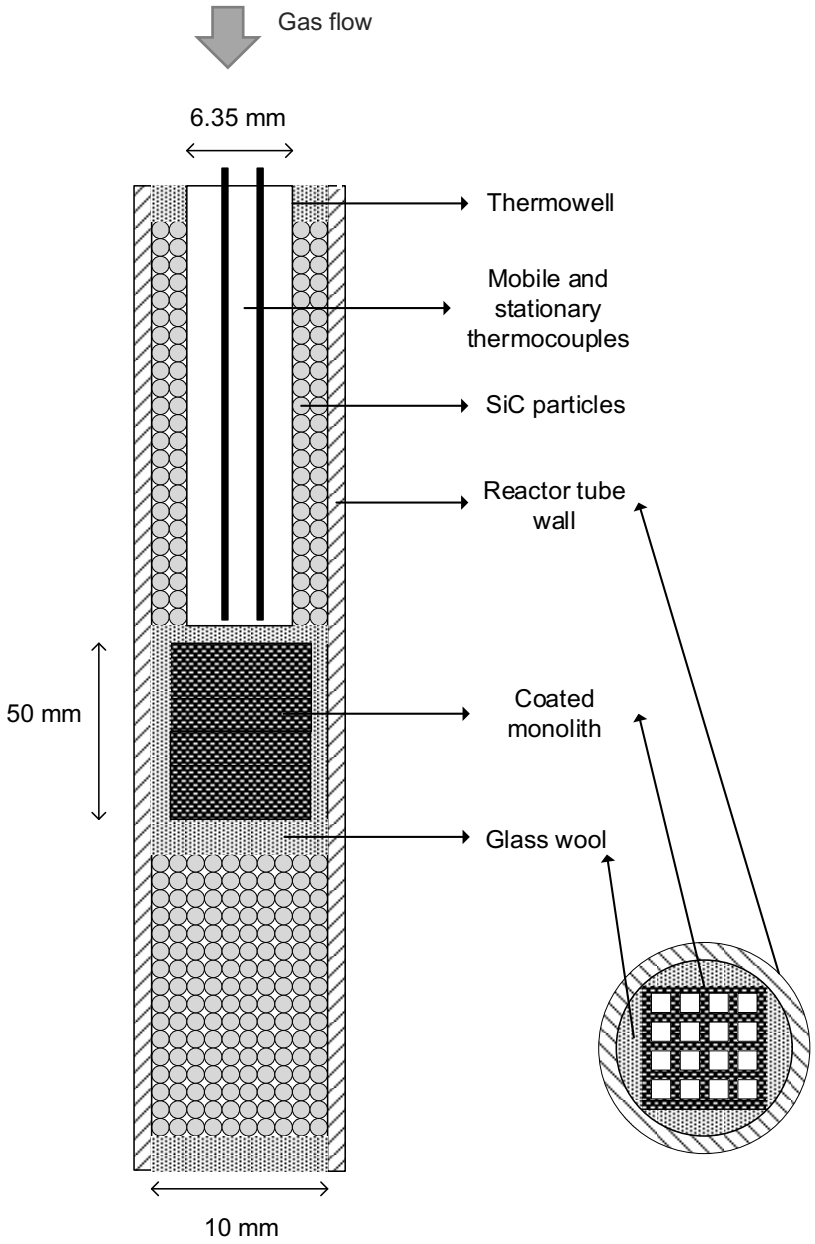

Figure 4-17: Schematic drawing of the reactor loading with monolith catalyst

4.5.1. Honeycomb monolith 1 (HcM 1)

For the first pair of the monoliths, the individual pieces were washcoated so that 0.25 g and 0.26 g of the Co-Pt/Al_2O_3 catalyst was coated on either piece, resulting in a total of 0.51 g. The average coating thickness was 45 µm. Catalyst performance tests were carried out in the order of 0.11, 0.080, 0.054 and 0.028 $mmol_{CO} \cdot s^{-1} \cdot g^{-1}_{Cat}$.

4.5.1. (A) **Catalyst activity**

Figure 4-18 shows conversion as a function of time on stream at different space velocities which are given in $mmol_{CO} \cdot s^{-1} \cdot g^{-1}_{Cat}$ and indicated on the graph in red along with the reactor temperature during the catalyst during the catalyst performance test. The catalyst test was started at 0.11 $mmol_{CO} \cdot s^{-1} \cdot g^{-1}_{Cat}$ at 200°C. However, it was seen that even at this relatively low starting temperature, the temperature measured 5 mm above the catalyst bed increased to 250°C shortly after startup, which implies that the temperature within the catalyst bed was significantly higher. The corresponding catalyst activity was high. Although the time for the reactor temperature to return the setpoint was not observed, it can be deduced from the decline of CO conversion with time on stream that the reactor temperature took ca. 17 hours to return to the setpoint. Note that as the catalyst spent a considerable amount of time at a temperature near or higher than the Hüttig temperature of Co (257°C), it is possible that deactivation due to sintering may have reduced catalyst activity. The CO conversion at this space velocity settled at a steady-state value of ca. 9.8 ± 1%. Conversion was stable with time on stream for the lower space velocities.

As expected, the CO conversion increased with a decrease in space velocity. The average CO conversion at 0.080, 0.050 and 0.027 $mmol_{CO} \cdot s^{-1} \cdot g^{-1}_{Cat}$ was 13.3%, 16.4% and 33.0% respectively. This is in line with the fixed-bed reactor performance equation for a simple first order reaction. The increase in CO conversion is 'nearly' linear with a decrease in space velocity. The reaction rate constant was estimated as described in section 4.4.1. (A) and is plotted as a function of CO conversion in Figure 4-19. The rate constant at a conversion of 16.4% (i.e., 0.080 $mmol_{CO} \cdot s^{-1} \cdot g^{-1}_{Cat}$) was much lower than the rate constants estimated at the other space velocities. Once again, it is possible that momentary exposure to a reduced H_2/CO ratio when decreasing the space velocity from 0.080 to 0.050 $mmol_{CO} \cdot s^{-1} \cdot g^{-1}_{Cat}$ could have led to some catalyst deactivation. The catalyst activity appears to recover during subsequent runs. The first order rate constant appears to fluctuate around an average of $1.50 \cdot 10^{-3} \pm 0.13 \cdot 10^{-3}$ $mmol_{CO} \cdot s^{-1} bar^{-1}\ g^{-1}_{cat}$.

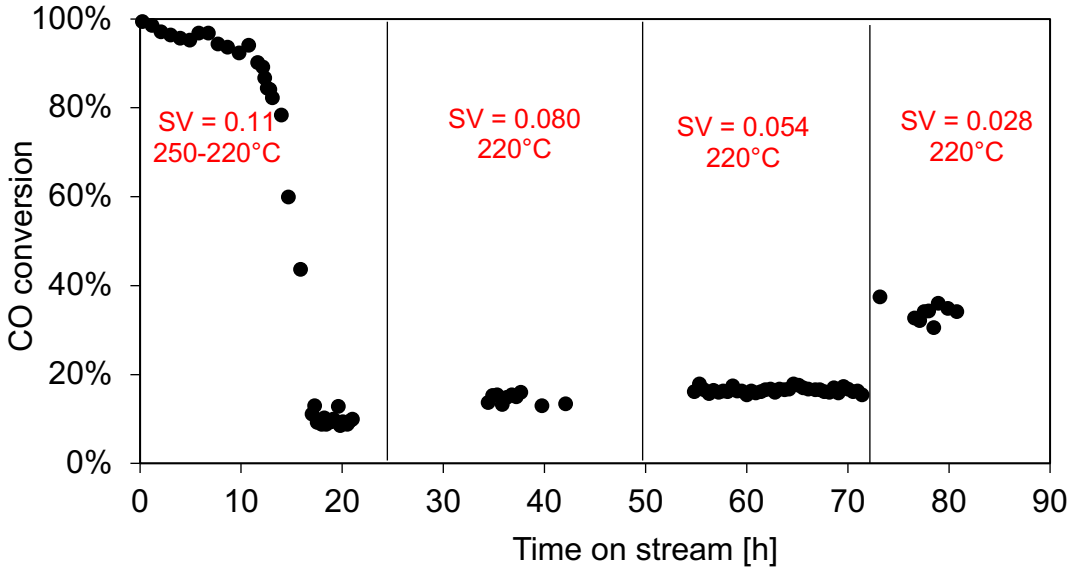

Figure 4-18: CO conversion as a function of time on stream over a Co-Pt/Al_2O_3 coated monolith at different space velocities at 220°C and 20 bar

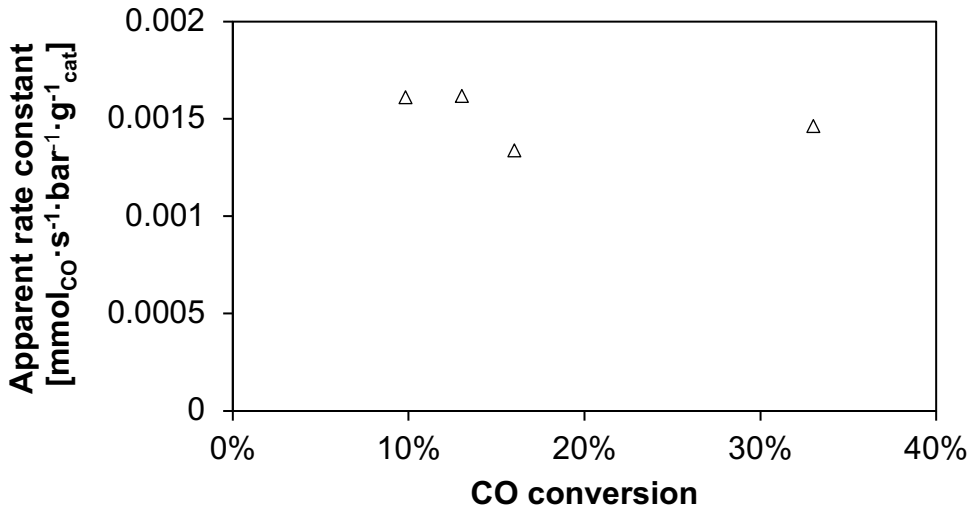

Figure 4-19: Apparent first order rate constant as a function of CO conversion over HcM 1 at 220°C and 20 bar

4.5.1. (B) **CO_2 selectivity**

The CO_2 selectivity as a function of time on stream at different space velocities is shown in Figure 4-20. Initially, the CO_2 selectivity is high after startup, between 26% and 16%, correlating with the high reactor temperature and CO conversion. CO_2 selectivities of less than 2% are typically expected in cobalt-based LT-FTS catalysts (Steynberg *et al.*, 2004). The high CO_2 production points to the water-gas shift reaction (Ma *et al.*, 2011), although the Boudouard

reaction may also have been occurring to a greater extent than expected (Moodley *et al.*, 2009), which would result in carbon deposition and possible deactivation. However, the CO_2 selectivity settles at values close to zero once steady-state operation was achieved. Virtually no CO_2 was detected for subsequent runs, an average CO_2 selectivity of 0.6% was measured at the lowest space velocity.

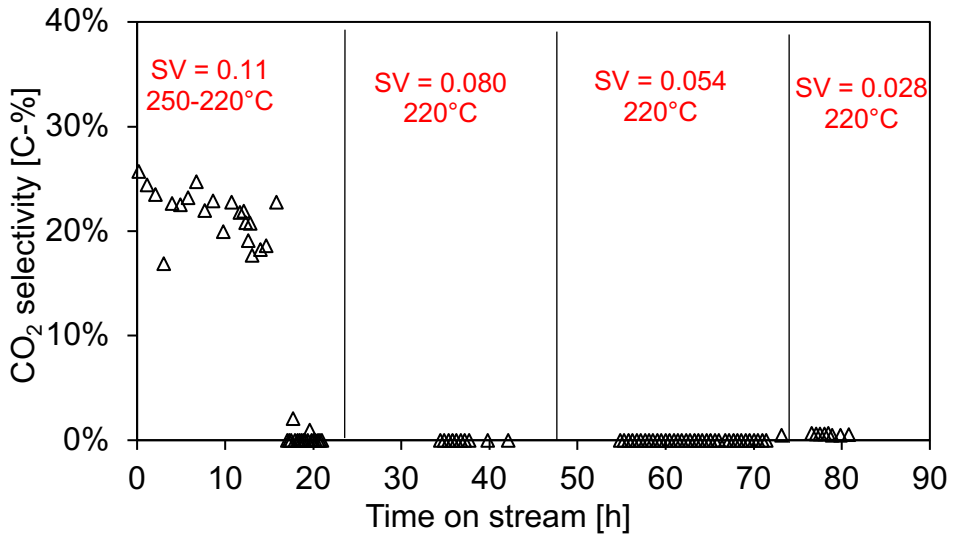

Figure 4-20: CO_2 selectivity as a function of time on stream over a Co-Pt/Al_2O_3 coated monolith at different space velocities at 220°C and 20 bar [SV in $mmol_{CO} \cdot s^{-1} \cdot g^{-1}_{Cat}$]

4.5.1. (C) **Product distribution**

Figure 4-21 shows the CH_4 selectivity as function of time on stream at different space velocities. Predictably, CH_4 production is highest at startup due to the high reactor temperature. The CH_4 selectivity decreases gradually along with the reactor temperature. An average steady-state CH_4 selectivity of 23 ± 3 C-% was observed. The CH_4 selectivity appears to be stable with time on stream for the other space velocities.

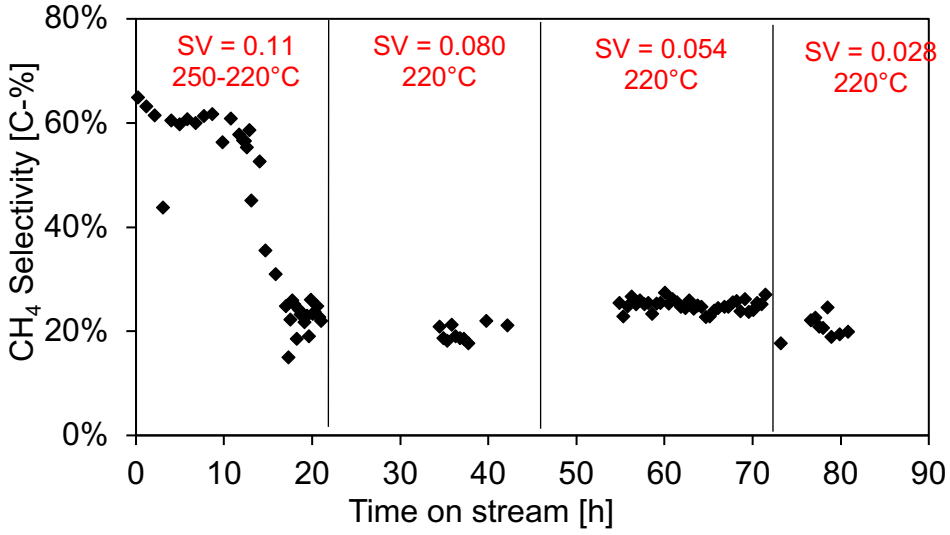

Figure 4-21: CH_4 selectivity as a function of time on stream over a Co-Pt/Al_2O_3 coated monolith at different space velocities at 220°C and 20 bar [SV in $mmol_{CO} \cdot s^{-1} \cdot g^{-1}_{Cat}$]

The steady-state performance data (CH_4 and CO_2 selectivities) averaged for over 7 hours-on-stream and the hydrocarbon product composition obtained via GC-FID analysis, is shown in Figure 4-22, along with the correlating average CO conversion. Note that while CH_4 selectivity is typically expected to decrease with a decrease in space velocity possibly related to the increase in CO conversion (Bukur *et al.*, 2012), no obvious trend is visible in the obtained trend. In fact, the CH_4 selectivities appear to be remarkably similar in magnitude. If the 1 percentage point decrease in CH_4 selectivity when decreasing space velocity from 0.11 to 0.080 $mmol_{CO} \cdot s^{-1} \cdot g^{-1}_{Cat}$ can attributed to the monolith showing an expected trend, then the slight increase in CH_4 selectivity from 22 ± 1 C-% to 25 ± 3 C-% upon further decreasing space velocity to 0.050 $mmol_{CO} \cdot s^{-1} \cdot g^{-1}_{Cat}$ is off-trend. It may have resulted from the catalyst deactivation that is suggested to have occurred due to a momentary decrease in the H_2/CO ratio upon changing space velocity. Furthermore, although the CO conversion doubled upon decreasing space velocity to 0.028 $mmol_{CO} \cdot s^{-1} \cdot g^{-1}_{Cat}$, the CH_4 selectivity only decreased by 3 percentage points. Thus, it can be said that catalyst deactivation may have substantially retarded chain growth, resulting in increased preference for CH_4 production

The C_2 – C_4 and C_{5+} selectivities do not exhibit a clear response to changes in space velocity (or conversion). When looking at Figure 4-22, it is puzzling that the product composition at a conversion level of 13 ± 0.5% (0.080 $mmol_{CO} \cdot s^{-1} \cdot g^{-1}_{Cat}$) and 33 ± 1% (0.028 $mmol_{CO} \cdot s^{-1} \cdot g^{-1}_{Cat}$) are nearly identical. Again, minor changes in catalyst structure could be partly responsible for these observations. It is also possible that higher syngas flowrates may result in more rapid

removal of products, leading to low chain growth probability, whereas the increased residence time at a lower space velocity could provide a better chance for α-olefin re-adsorption and improve chain growth probability.

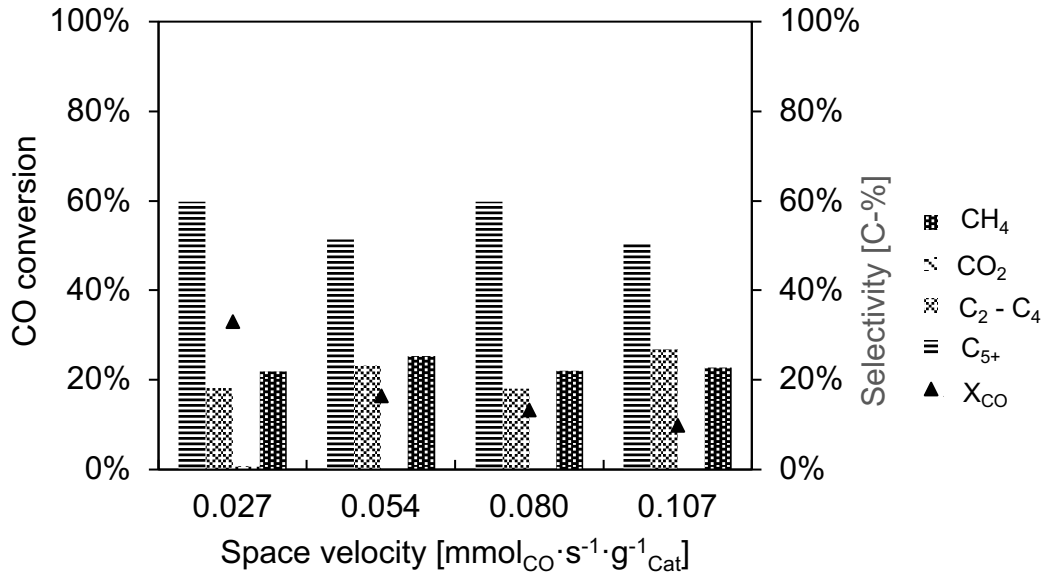

Figure 4-22: Average CO conversion and product distribution of Fischer-Tropsch synthesis products over Co-Pt/Al_2O_3 coated cordierite monolith (HcM 1)

The O/P ratios at different space velocities are shown in Figure 4-23 as a function of carbon number. For all the space velocities, the O/P ratios generally decrease with an increase in carbon number. However, some expected deviations are observed for all the space velocities: the O/P ratio at the C_2 product fraction is lower than the trend presented by the data, this is due to the high reactivity of ethylene; there is a maximum at C_3 and a subsequent dip in the O/P ratio at C_4.

The O/P ratio also decreases with a decrease in space velocity. This supports the previous suggestion that increased residence time due to decreased space velocity may lead to increased α-olefin readsorption and chain growth probability (Ma et al., 2011).

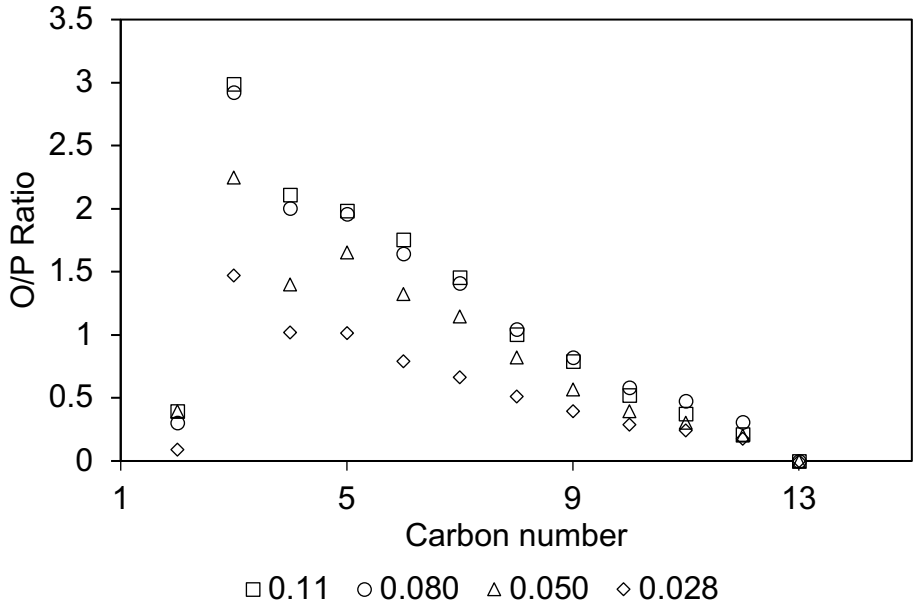

Figure 4-23: Olefin/Paraffin ratio obtained at different space velocities over HcM 1 at 220°C and 20 bar

4.5.1. (D) **Summary and insights**

The catalyst performance data for HcM 1 are summarised in Table 4-7. Exothermic temperature increase of up to 250°C was observed after startup and could have lasted for ca. 17 hours. Thus, catalyst deactivation due to sintering may have occurred during the initial stages of catalyst testing. The catalyst exhibited stable CO conversion as well as CO_2 and CH_4 selectivity with time on stream after steady-state was achieved. It should be noted that despite achieving lower CO conversion levels, the CH_4 selectivities obtained over HcM 1 are not much lower than those obtained over the catalyst powder. At 0.11 $mmol_{CO} \cdot min^{-1} \cdot g^{-1}_{Cat}$, where the most significant deactivation of the catalyst is thought to have occurred in HcM 1, the C_{5+} selectivity is 22 percentage points lower than that achieved over the catalyst powder. While it is not advisable to compare selectivities at different conversion levels because of the complex interplay between primary and secondary reactions (Claeys & Van Steen, 2004), the data obtained over HcM 1 shows that catalyst stability plays an important role in catalyst performance. Lastly, heat and mass transfer limitations may have prevented effected removal of heat generated by the reaction, resulting in the exothermic temperature increase thought to have caused deactivation.

Table 4-7: Summary of catalyst performance parameters for a Co-Pt/Al_2O_3 coated monolith with a catalyst layer thickness of 45 µm (HcM 1)

Syngas Flowrate [ml·min^{-1}]	240	180	120	60
Space velocity [mmol$_{CO}$·min^{-1}·g$^{-1}_{Cat}$]	0.11	0.080	0.050	0.028
Temperature [˚C]	250 - 220	220	220	220
Integral reaction rate [mmol$_{CO}$·min^{-1}·g$^{-1}_{Cat}$]	0.057	0.057	0.047	0.047
H_2/CO usage ratio	2.35	2.13	2.25	2.25
Average X_{CO}	9.8 ± 1%	13 ± 0.5%	16 ± 1%	33 ± 1%
Average S_{CH_4}[C-%]	23 ± 3%	22 ± 1%	25 ± 3%	22 ± 1%
Average S_{CO_2}[C-%]	0%	0%	0%	0.6 ± 0.05%
$S_{C_2-C_4}$[C-%]	27%	18%	23%	18%
$S_{C_{5+}}$[C-%]	50%	60%	51%	60%

4.5.2. Honeycomb monolith 2 (HcM 2)

A pair of 25 mm long honeycomb monoliths was coated with a total catalyst loading of 0.25 g, corresponding to a catalyst layer thickness of 22.3 µm. The monoliths were tested at 4 different space velocities, that is 0.22, 0.17, 0.11 and 0.055 $mmol_{CO} \cdot s^{-1} \cdot g^{-1}_{Cat}$. The Fischer-Tropsch synthesis testing was started at 0.22 $mmol_{CO} \cdot s^{-1} \cdot g^{-1}_{Cat}$, at 200°C and 20 bar.

4.5.2. (A) **Catalyst activity**

The CO conversion over time on stream with changing space velocity is presented in Figure 4-24. After startup, exothermic temperature increase up to 251°C was observed, which decreased gradually after 2 hours-on-stream, eventually stabilising at 230°C, where it remained for a further 20 hours. Note that the reactor temperature was measured ca. 5 mm above the catalyst bed, thus, the temperature within the bed would likely have been higher. Due to the high temperatures, the initial activity of the catalyst was high, with an average CO conversion of 85 ± 3%. It is noted that the 2-hour long operation at temperatures near the Hüttig temperature of cobalt (257°C) may have contributed to catalyst deactivation through sintering of the active metal. This could possibly be worsened by high H_2O partial pressure that may arise at high CO conversion levels. High H_2O partial pressures are thought to cause catalyst deactivation through oxidation and by increasing the rate of sintering (Ma et al., 2011). The CO conversion seems be more stable with time on stream at lower different space velocities.

Upon reducing the space velocity from 0.22 $mmol_{CO} \cdot s^{-1} \cdot g^{-1}_{Cat}$ to 0.17 $mmol_{CO} \cdot s^{-1} \cdot g^{-1}_{Cat}$, the reactor temperature rapidly dropped to the setpoint within an hour. This was accompanied by a decrease in CO conversion to an average value of 26 ± 1%. The H_2/CO usage ratio also dropped from 2.2 to 2.1. However, no significant change in CO conversion was observed when further decreasing the space velocity from 0.17 to 0.11 $mmol_{CO} \cdot s^{-1} \cdot g^{-1}_{Cat}$, whereas, an increase in CO conversion is expected with decreasing space velocity (Biquiza *et al.*, 2010). Moreover, the H_2/CO usage ratio increased to an average value of 2.4. Withstanding the complex relationship between secondary and primary reactions, as well as the simultaneous occurrence of multiple reactions in the Fischer-Tropsch synthesis, an increase in the H_2/CO usage ratio may be seen as an increased preference for the production of light hydrocarbons (i.e., a decrease in chain growth probability. Despite the CO conversion appearing to be stable with time on stream for the ca. 10-hour duration of the Fischer-Tropsch synthesis at 0.17 $mmol_{CO} \cdot s^{-1} \cdot g^{-1}_{Cat}$, the unexpected increase in the H_2/CO usage ratio and the lack of response

of the CO conversion to decreasing the space velocity may indicate catalyst deactivation via a decrease in the number of site available for CO dissociation. It is also possible that the momentary decrease in the H_2/CO ratio in the feed when decreasing space velocity from 0.17 to 0.11 may have resulted in carbon deposition, increased carbon deposition due to sudden decrease in the H_2/CO has been reported by Moodley (2008). Upon decreasing the space velocity to 0.055 $mmol_{CO} \cdot s^{-1} \cdot g^{-1}_{Cat}$, the CO conversion nearly doubles to an average of 46 ± 3%. This result is closer to the ideal behaviour as predicted by the fixed-bed design equation with simple pseudo-first order rate law (see equation 4-4 in chapter 4.4.1. (A)). It may be argued that despite the presumed deactivation (i.e., loss in the number of active sites), enough sites remained to dissociate a limited number of reactant atoms. Thus, the increase in conversion at the lowest space velocity may be linked to the presence of fewer atoms in the feed to the reactor.

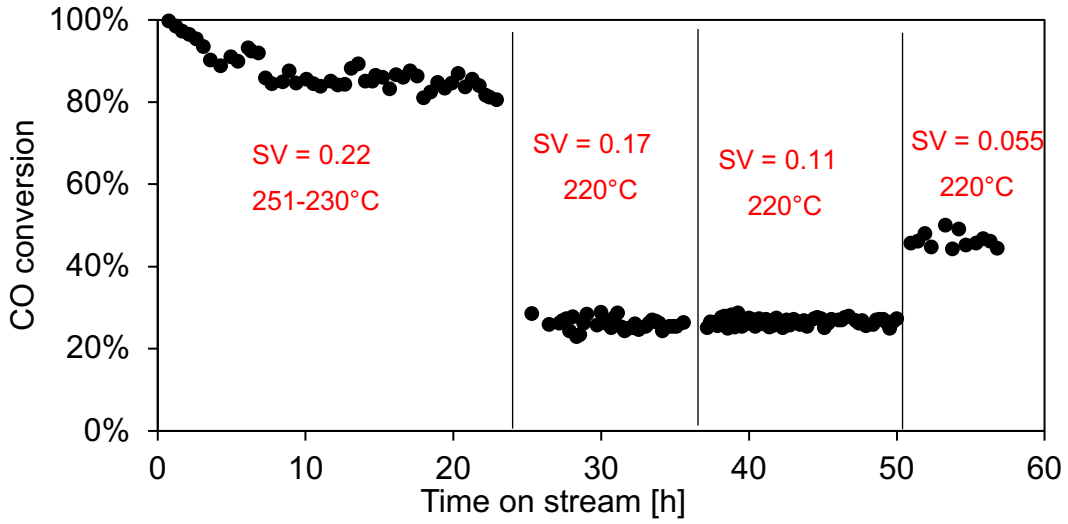

Figure 4-24: CO conversion as a function of time on stream over a Co-Pt/Al_2O_3 coated monolith (HcM 2) at different space velocities at 220°C and 20 bar [SV in $mmol_{CO} \cdot s^{-1} \cdot g^{-1}_{Cat}$]

4.5.2. (B) **CO_2 selectivity**

The high temperature after startup (at 0.22 $mmol_{CO} \cdot s^{-1} \cdot g^{-1}_{Cat}$) resulted in high CO_2 selectivity of 19 ± 1%. Note that cobalt-based catalysts do not typically exhibit CO_2 selectivities greater than 2% (Shafer *et al.*, 2019). The sustained high production of CO_2 at high CO conversion (>80%) is consistent with an increased extent of the water-gas shift (WGS) reaction. This may be an indication of catalyst deactivation by oxidation of metallic cobalt to CoO under high H_2O partial pressures (Ma *et al.*, 2011; Rytter & Holmen, 2015). Carbon deposition, caused by increased extent of the Boudouard reaction has also been proposed as a mechanism for

deactivation of Co-Pt/Al_2O_3 catalysts (Moodley *et al.*, 2009). CO_2 production dropped drastically when the space velocity was decreased to 0.17 $mmol_{CO} \cdot s^{-1} \cdot g^{-1}_{Cat}$, with virtually no CO_2 selectivity being detected. For the space velocities of 0.11 and 0.055 $mmol_{CO} \cdot s^{-1} \cdot g^{-1}_{Cat}$, the CO_2 selectivity decreased slightly but stayed at ca. 1 C-%. This may indicate a slowing in the rate of catalyst deactivation.

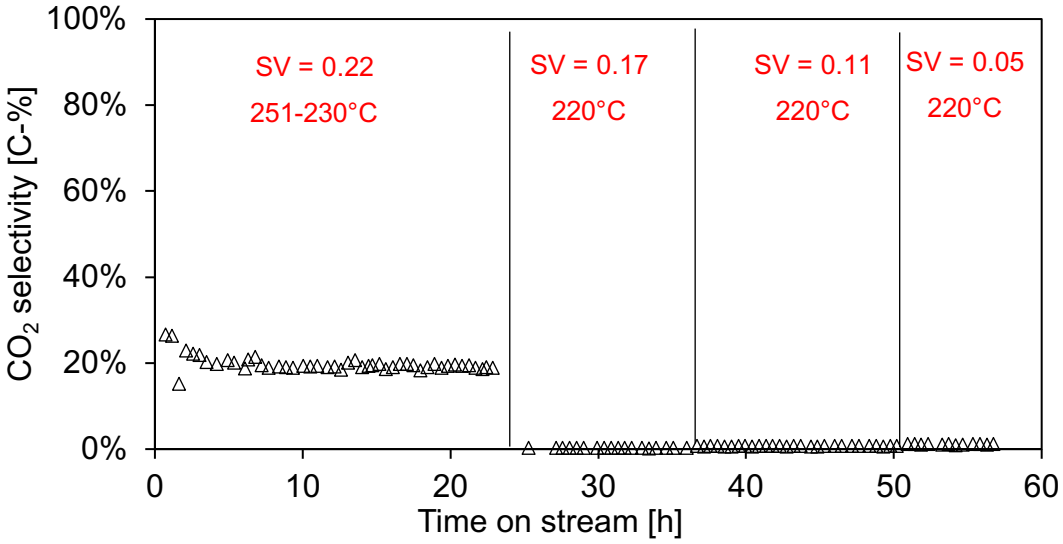

Figure 4-25: CO_2 selectivity as a function of time on stream at different space velocities over HcM 2 at 220°C and 20 bar [SV in $mmol_{CO} \cdot s^{-1} \cdot g^{-1}_{Cat}$]

4.5.2. (C) **Product distribution**

Figure 4-26 shows the CH_4 selectivity as a function of time on stream on stream at different space velocities. It can be seen that methane production after startup was high, with a methane selectivity of ca. 72 C-%. Even after the reactor temperature stabilised at about 230°C, the methane selectivity was sustained at an average value of 67 ± 1 C-%. Compared to selectivities of 5-12% reported in literature (Bukur *et al.*, 2012; Rytter *et al.*, 2016). This is an alarming production of an undesired product with a high greenhouse potential. As with the CO conversion and CO_2 selectivity, a sharp decrease in CH_4 selectivity was seen when the space velocity was decreased to 0.17 $mmol_{CO} \cdot s^{-1} \cdot g^{-1}_{Cat}$. This is attributed to rapid cooling of the catalyst as less heat was released at a lower reaction rate. When further decreasing the space velocity to 0.11 $mmol_{CO} \cdot s^{-1} \cdot g^{-1}_{Cat}$, the CO conversion increased slightly from 26 ± 1 C-% to 27 ± 1 C-%. However, instead of exhibiting similar CH_4 selectivities or a slight decrease in CH_4 selectivity as expected, the CH_4 selectivity increased from an average value of 20 ± 1 C-% to 25 ± 1 C-%. This can be seen as more evidence of catalyst deactivation to favour early termination of chain growth by hydrogenation of adsorbed single carbon species.

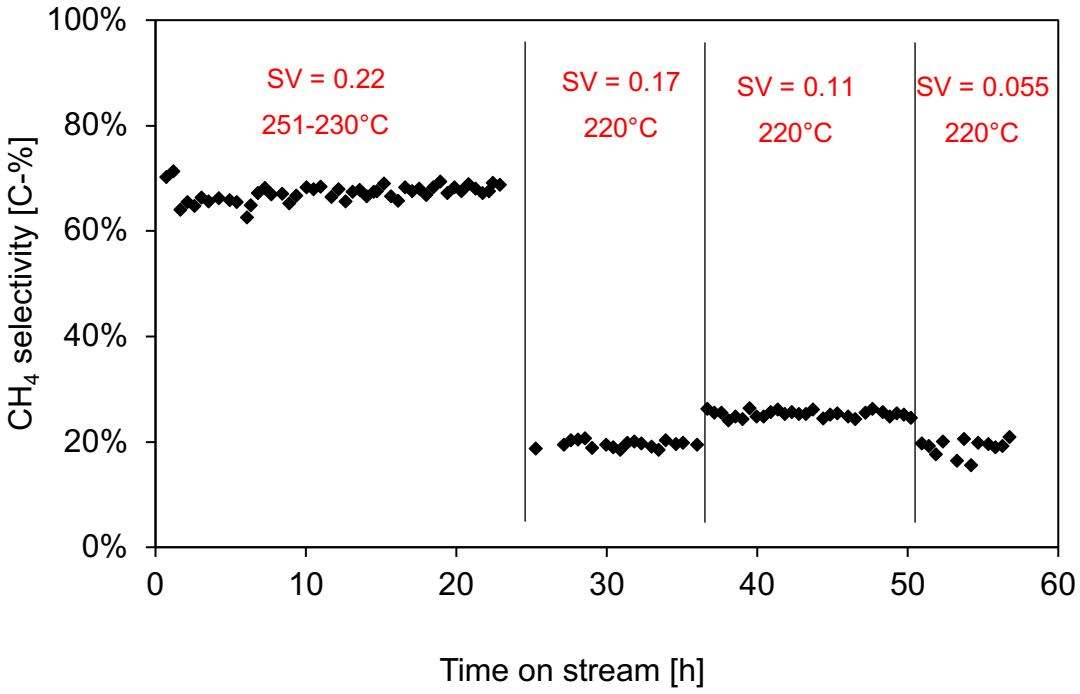

Figure 4-26:CH_4 selectivity as a function of time on stream at different space velocities over HcM 2 at 220°C and 20 bar [SV in $mmol_{CO} \cdot s^{-1} \cdot g^{-1}_{Cat}$]

Figure 4-27 shows the full product distribution (CO_2, CH_4, C_2 - C_4 and C_{5+} selectivities in C-%) at each space velocity, along with the associated CO conversions. The product distribution at 0.22 $mmol_{CO} \cdot s^{-1} \cdot g^{-1}_{Cat}$ was expected to be poor due to the high reaction temperature (230°C) and high CO_2 and CH_4 selectivities obtained by GC-TCD analysis. However, the C_{5+} selectivity of 0.5% obtained via GC-FID is shockingly low. It can be seen that the majority of carbonaceous products were light gases, with CO_2 and CH_4 constituting the majority of the product compounds. This strongly supports the assertion that the catalyst was exposed to very high temperatures, presumably due to severe transport limitations, and possibly causing significant catalyst deactivation. The product distribution at the subsequent space velocity of 0.17 $mmol_{CO} \cdot s^{-1} \cdot g^{-1}_{Cat}$ is much improved, with a C_{5+} selectivity of 66%. Arguably, such a large gain in C_{5+} selectivity (ca. 55 percentage points, carbon) may suggest that the internal temperature of the catalyst played a larger role than the suspected deactivation. However, the C_{5+} selectivity at 0.11 $mmol_{CO} \cdot s^{-1} \cdot g^{-1}_{Cat}$ decreased by 11 percentage points despite a slight increase in CO conversion of ca 0.5 percentage points. As previously stated, the low increase in CO conversion may be indication of catalyst deactivation, whereas the CO conversion is expected to increase proportionally with the decrease in space velocity, see chapter 4.4.1. (A). Thus, the decline in C_{5+} selectivity may have resulted from the reduced availability of CO dissociation sites required to facilitate chain growth. The catalyst performance and product selectivities reported at 0.055 $mmol_{CO} \cdot s^{-1} \cdot g^{-1}_{Cat}$ are more promising, with a C_2 – C_4 selectivity

decreasing from ca. 20 C-% to ca. 11 C-%, while C_{5+} selectivity increased from 55 C-% to 70 C-%

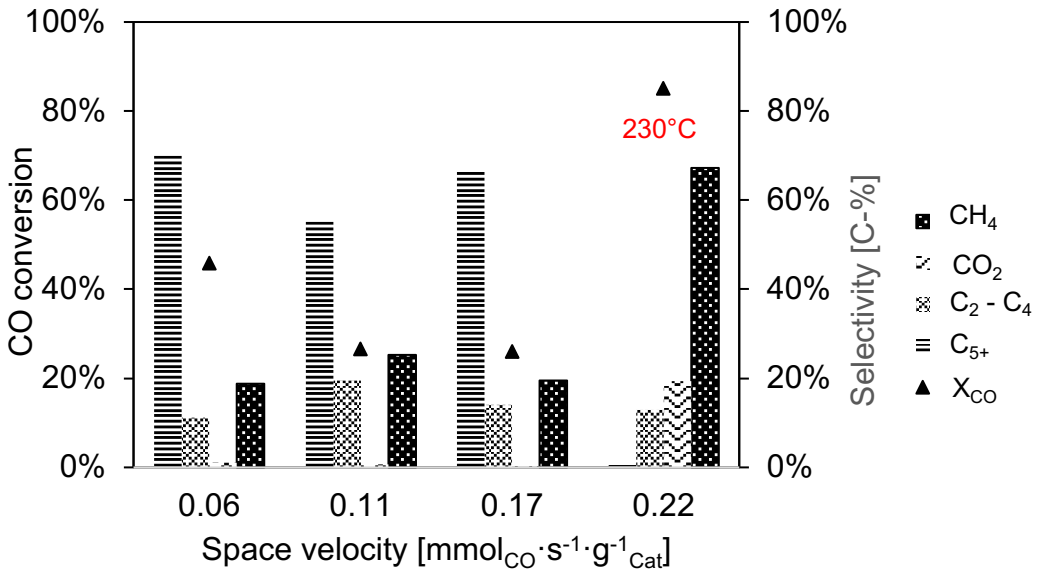

Figure 4-27: Average CO conversion and product distribution of Fischer-Tropsch synthesis products over Co-Pt/Al_2O_3 coated cordierite monolith (HcM 2)

The O/P ratios at the different space velocities are plotted as a function of carbon number in Figure 4-28. The O/P ratios generally decrease with an increase in carbon number and exhibit the expected low O/P ratio at the C_2 product fraction as well as s maximum at the C_3 product fraction (Förtsch *et al.*, 2015). Furthermore, the O/P ratios decreased with a decrease in space velocity, thus is attributed to a longer residence time, leading to increased opportunity of olefin re-insertion and chain growth (Bukur *et al.*, 2012). At 0.22 $mmol_{CO} \cdot s^{-1} \cdot g^{-1}_{Cat}$, no olefins were detected via GC-FID for carbon numbers greater than 8. This is not surprising due to the low chain growth (i.e., low C_{5+} selectivity); 87% carbon fed to the reactor was converted to single-carbon molecules (CO_2 and CH_4), drastically decreasing the probability for the formation of double bonds. Conversely, due to the high gas flowrate, less residence time in the catalyst pores results in a reduced chance for olefin readsorption/re-insertion, thus the O/P ratio would still be higher than that at lower space velocities.

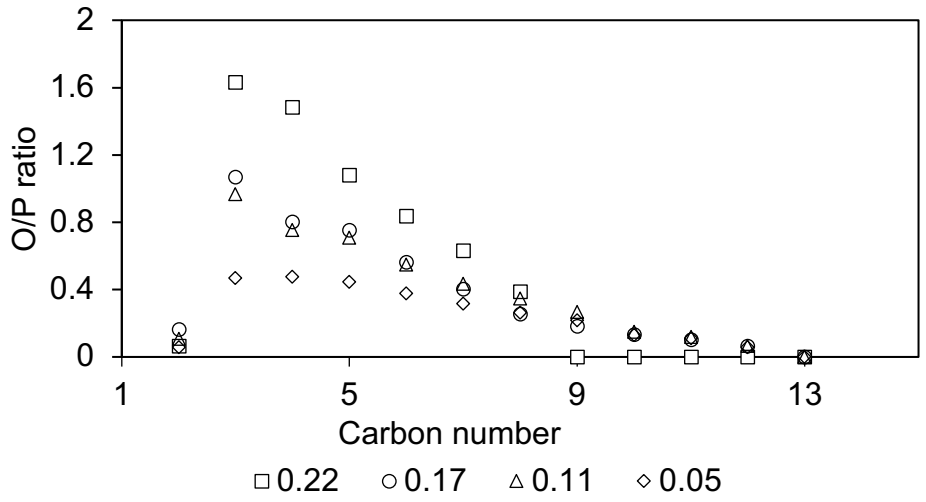

Figure 4-28: O/P ratios as a function of carbon number obtained over HcM 2 at 220°C and 20 bar at different space velocities [SV in $mmol_{CO} \cdot s^{-1} \cdot g^{-1}_{Cat}$]

.

4.5.2. (D) **Summary and insights**

Table 4-8 provides a summary of the reactor performance data for HcM 2, the honeycomb monoliths coated with 0.25g of Co-Pt/Al_2O_3 catalyst, which is equivalent to a washcoat layer thickness of 22.2 ± 1.6 µm. Initial phase of testing at 0.22 $mmol_{CO} \cdot s^{-1} \cdot g^{-1}_{Cat}$ showed that the catalyst sustained high temperatures (230°C), as well as high CO_2 and CH_4 selectivities. It is thought that poor heat and mass transfer properties of the coated monolith may have prevented effective temperature control, and thus may be responsible for catalyst deactivation via either or a combination of sintering, oxidation and carbon deposition (Hilmen *et al.*, 2001; Moodley *et al.*, 2009; Ma *et al.*, 2011). It is also considered that deactivation may have occurred due to transitory decrease in the H_2/CO ratio when decreasing the space velocity from 0.17 to 0.11 $mmol_{CO} \cdot s^{-1} \cdot g^{-1}_{Cat}$. Lastly, the catalyst is deemed to have performed best at the lowest space velocity (0.055 $mmol_{CO} \cdot s^{-1} \cdot g^{-1}_{Cat}$) on the basis of highest CO conversion coupled with low CH_4 and high C_{5+} selectivity.

Table 4-8: Summary of catalyst performance for a Co-Pt/Al_2O_3 coated monolith with a catalyst layer thickness of 22.3 µm (HcM 2)

Syngas flowrate [$ml \cdot min^{-1}$]	240	180	120	60
Space velocity [$mmol_{CO} \cdot s^{-1} \cdot g^{-1}_{Cat}$]	0.22	0.17	0.11	0.055
Temperature [°C]	250 - 230	220	220	220
H_2/CO usage ratio	2.2	2.1	2.4	2.1
Average X_{CO}	85 ± 3%	26 ± 1%	27 ± 1%	46 ± 3%
Average S_{CH_4}[C-%]	67 ± 1%	20 ± 1%	25 ± 1%	19 ± 2%
Average S_{CO_2}[C-%]	19 ± 1%	0%	1%	1 ± 0.1%
$S_{C_2-C_4}$[C-%]	13%	14%	20%	11%
$S_{C_{5+}}$[C-%]	0.5%	66%	55%	70%

4.6. Catalyst performance of washcoated open-cell foams

As with the honeycomb monoliths, the washcoated foams were wrapped in a thin layer of glass wool to prevent gas bypass. Figure 4-29 shows how the foams were loaded in the reactor tube. The stationary and mobile thermocouples were situated ca. 5 mm above the catalyst bed. Catalyst reduction and reactor startup were carried out as described in chapter 3.3.3.

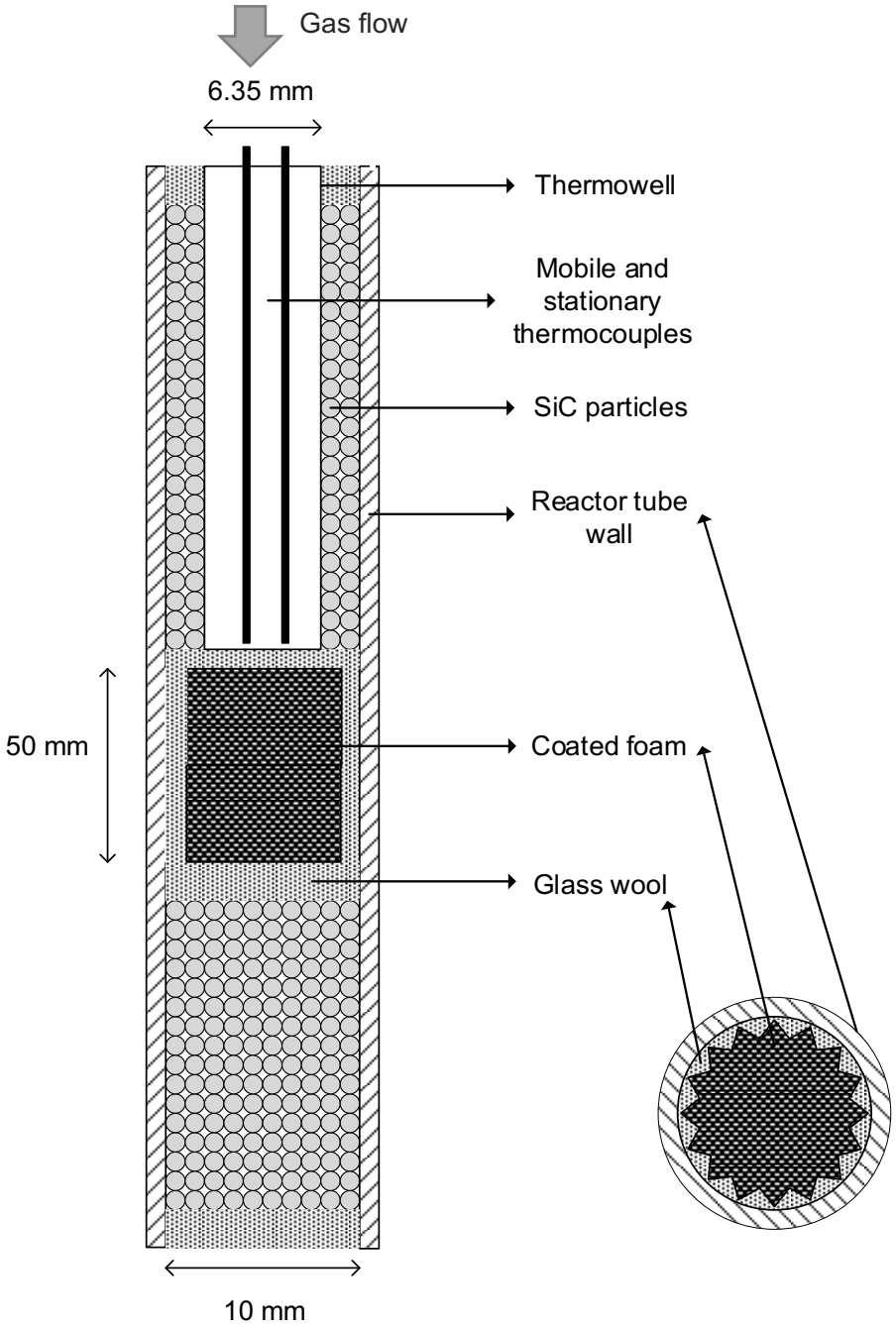

Figure 4-29: Schematic drawing of reactor loading with foam packing

4.6.1. SiC open-cell foam 1 (OcF 1)

0.18 g of catalyst was washcoated on 30 PPI open-cell foams. This resulted in an estimated catalyst layer thickness of ca. 21 µm. However, SEM images revealed that the washcoating of the foams was not homogenous, resulting in catalyst layer thicknesses that varied widely. The Fischer Tropsch synthesis was started at 200°C and 20 bar, at a space velocity of 0.31 $mmol_{CO} \cdot s^{-1} \cdot g^{-1}_{Cat}$. Performance data of the catalyst was also collected at 0.23, 0.15 and 0.077 $mmol_{CO} \cdot s^{-1} \cdot g^{-1}_{Cat}$.

4.6.1. (A) **Catalyst activity**

The CO conversion as a function of time on stream at the different space velocities is shown in Figure 4-30, and appears to be stable with time on stream. Unlike the pellet and the monoliths, the temperature measured ca. 5 mm above the catalyst bed did not increase noticeably after startup. The low mass of the catalyst and the reduced reaction rate relative to the mass of SiC foam may have improved the rate of heat removal through conduction. Thus, the foam could more effectively act as a heat sink for the heat generated by the reaction. The ability of SiC foams to act as heat sinks has previously been demonstrated by Fratalocchi *et al.* (2018). Furthermore, space velocity at startup was higher than that for the pellets and monolith, which were started up at space velocities between 0.11 and 0.22 $mmol_{CO} \cdot s^{-1} \cdot g^{-1}_{Cat}$. Thus, the increased gas flowrate may have increased the rate of heat removal by convection (Merino *et al.*, 2017).

A linear increase in CO conversion with a decrease in space velocity is expected if the reaction can be modelled using the fixed-bed reactor design equation with simple pseudo-first order rate law (see equation 4-44.4.1. (A)). However, when decreasing the space velocity from 0.31 to 0.23 $mmol_{CO} \cdot s^{-1} \cdot g^{-1}_{Cat,}$ no significant change in CO conversion was observed, with the average CO conversion being ca. 13%. When the space velocity was further decreased to 0.15 $mmol_{CO} \cdot s^{-1} \cdot g^{-1}_{Cat}$, the CO conversion decreased to an average of 11 ± 1%. Thus far, it can be seen that the catalyst maintained low CO conversion despite the decrease in CO space velocity and decreased with increasing space velocity. This contrary behaviour of the catalyst may be an indication of catalyst deactivation. As with the previous catalyst tests, the H_2 flowrate was typically decreased first when decreasing space velocity. It is hypothesized that a momentary decrease in the H_2/CO ratio in the feed may have led to carbon deposition.

The low CO conversion may also be attributed to the low catalyst loading in the reactor, necessitating significantly lower space velocities to achieve higher CO conversion. This is

consistent with the observation that upon further decreasing the space velocity from 0.15 to 0.077 $mmol_{CO} \cdot s^{-1} \cdot g^{-1}_{Cat}$, the CO conversion increased significantly, yielding an average value of 24 ± 2%. The doubling of CO conversion when the space velocity was halved is consistent with the assumption that the reaction can be described using a pseudo-first order rate law.

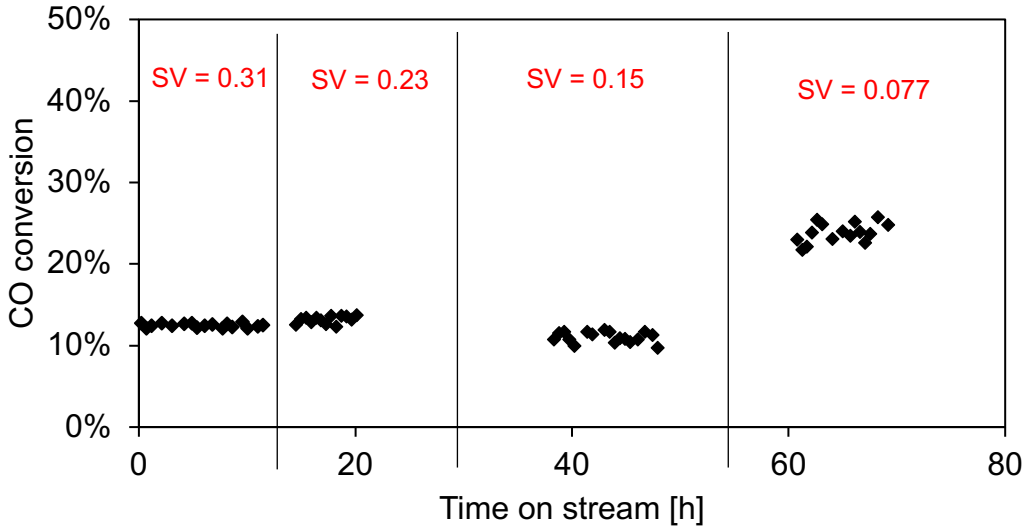

Figure 4-30: CO conversion as a function of time on stream over a Co-Pt/Al_2O_3 coated SiC foam (OcF 1) at different space velocities at 220°C and 20 bar [SV in $mmol_{CO} \cdot s^{-1} \cdot g^{-1}_{Cat}$]

4.6.1. (B) **CO_2 selectivity**

The CO_2 selectivity at different space velocities is shown as a function of time on stream in Figure 4-31. Since no exothermic temperature increase was observed after startup, it is not surprising that CO_2 production after startup was negligible. Additionally, the CO_2 selectivity was stable with time on stream and remained close to 0 C-% at the space velocities from 0.31 to 0.15 $mmol_{CO} \cdot s^{-1} \cdot g^{-1}_{Cat}$. The CO_2 selectivity increased slightly upon decreasing the space velocity to 0.077 $mmol_{CO} \cdot s^{-1} \cdot g^{-1}_{Cat}$. However, the CO_2 selectivity was still very low with a maximum at ca. 0.23 C-%. This falls comfortably close to the lower limit of CO_2 selectivities of 1 – 2 typically observed over cobalt-based low temperature Fischer Tropsch catalysts (Rytter et al., 2016). In addition, an increase in CO_2 selectivity with increasing CO conversion is expected (Ma *et al.*, 2011).

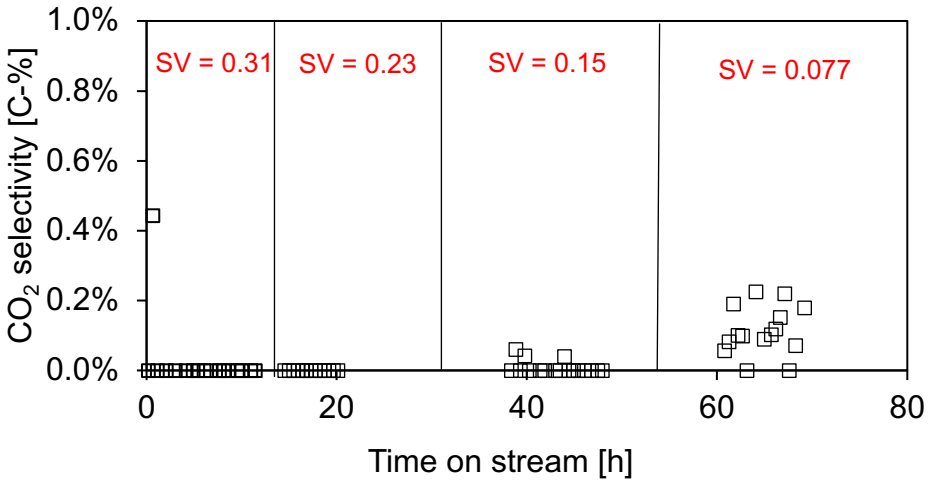

Figure 4-31: CO_2 selectivity as a function of time on stream over a Co-Pt/Al_2O_3 coated SiC foam (OcF 1) at different space velocities at 220°C and 20 bar [SV in $mmol_{CO} \cdot s^{-1} \cdot g^{-1}_{Cat}$]

4.6.1. (C) **Product distribution**

Figure 4-32 shows the CH_4 selectivity at different space velocities as a function of time on stream. The CH_4 selectivity generally seems stable with time on stream but is more scattered at the two lowest space velocities. However, the standard deviations were 2 C-% and 1 C-% at 0.15 and 0.077 $mmol_{CO} \cdot s^{-1} \cdot g^{-1}_{Cat}$ respectively, which is deemed acceptable for the level of accuracy that can be reasonably expected from the experimental setup. It has been shown that CH_4 selectivity typically decreases with increasing CO conversion up to a conversion of 80% (Ma *et al.*, 2011). That appears to be the case from the space velocities of 0.31 to 0.15 $mmol_{CO} \cdot s^{-1} \cdot g^{-1}_{Cat}$, the CH_4 selectivity increased with decreasing CO conversion. However, it is noted that the CH_4 selectivity at 0.077 $mmol_{CO} \cdot s^{-1} \cdot g^{-1}_{Cat}$ (X_{CO} = 24 ± 2%) is higher than that at 0.31 and 0.23 $mmol_{CO} \cdot s^{-1} \cdot g^{-1}_{Cat}$ (X_{CO} = 13 ± 1%), contrary to the expected trend. It is thought that the cause of the discrepancy may be deactivation caused by upsets in the H_2/CO ratio in the feed as well as deactivation with time on stream. These could have reduced the number of sites available for CO dissociation, thus, reducing the chance for chain propagation. It is also noted that the CH_4 selectivities obtained over OcF 1 are generally lower than those obtained over the catalyst powder, pellets and monoliths, which were had values generally greater than 18 C-%, even at higher conversions. This may be a result of the better temperature control over this foam.

The distribution of the carbon-containing product compounds (S_{CH_4}, S_{CO_2}, $S_{C_2-C_4}$ and $S_{C_{5+}}$) in the tail gas are shown for each space velocity in Figure 4-33. It can be seen that the trends shown by the C_2 - C_4 selectivity mirror that of the CH_4 selectivity. The C_{5+} selectivity decreased

with decreasing space velocity, whereas C_{5+} selectivity is expected to increase with decreasing space velocity (van Steen *et al.*, 2018). However, this discrepancy was generally consistent with the observed CO conversions as C_{5+} selectivity decreased with decreasing CO conversion (Ma *et al.*, 2011). It is noted that the C_{5+} selectivity at a conversion of 24% (0.077 $mmol_{CO} \cdot s^{-1} \cdot g^{-1}_{Cat}$) was 77 C-%, which is lower than that the selectivities achieved at a conversion of 13% (0.31 and 0.23 $mmol_{CO} \cdot s^{-1} \cdot g^{-1}_{Cat}$), which were greater than 81 C-%. The observed trends in C_{5+} selectivity are attributed to the catalyst deactivation thought to have occurred. Overall, OcF 1 appears to achieve high C_{5+} selectivities, with the lowest being greater than 66 C-% and the highest at 84 C-%.

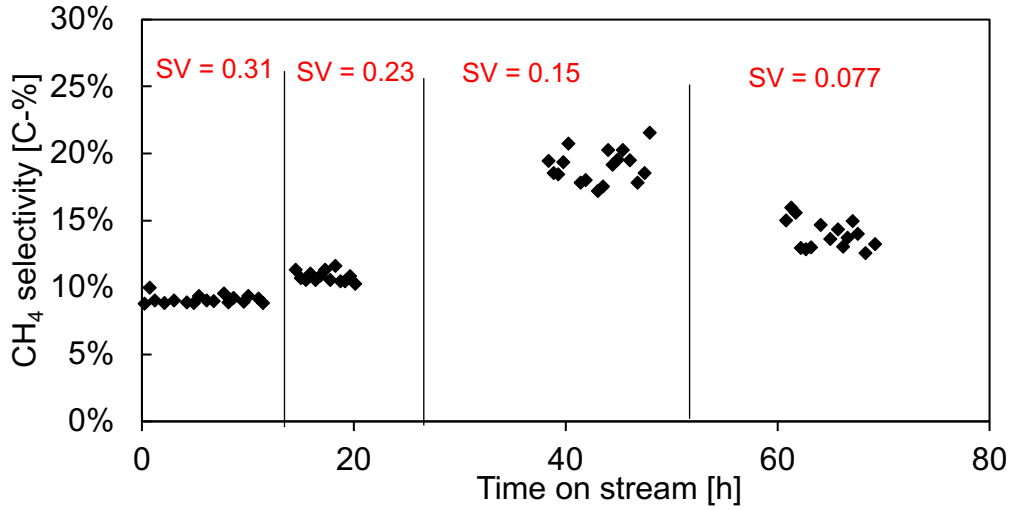

Figure 4-32: CH_4 selectivity as a function of time on stream over a Co-Pt/Al_2O_3 coated SiC foam (OcF 1) at different space velocities at 220°C and 20 bar [SV in $mmol_{CO} \cdot s^{-1} \cdot g^{-1}_{Cat}$]

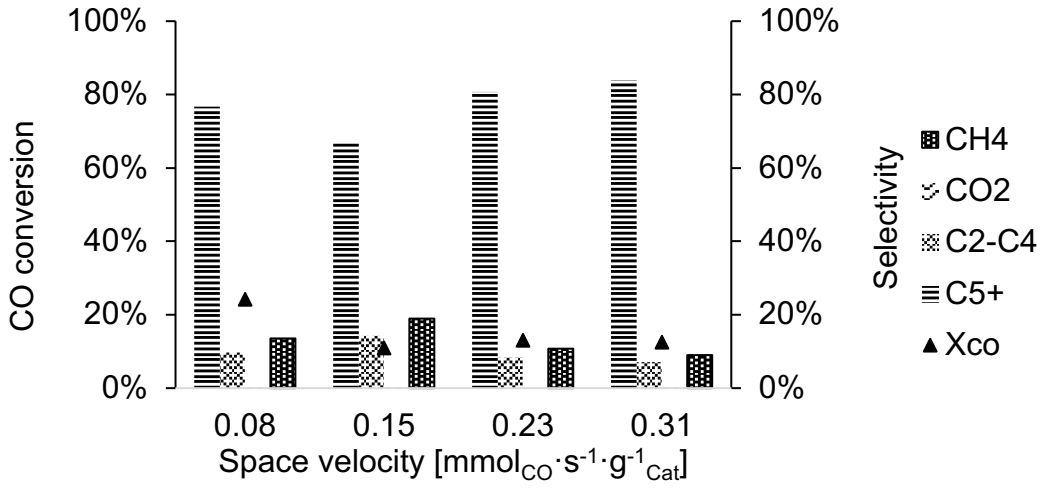

Figure 4-33: Average CO conversion and product distribution of Fischer-Tropsch synthesis products over Co-Pt/Al_2O_3 coated SiC foam (OcF 1)

Figure 4-34 shows the olefin/paraffin ratio as a function of carbon number obtained at different space velocities in the Fischer-Tropsch synthesis performed over a foam catalyst (OcF 1). Predictably, the olefin/paraffin ratios decrease with an increase in carbon number. This can be attributed to the increased extent of secondary reactions involving olefins such as hydrogenation and re-adsorption as a result of chain length dependent diffusivity and solubility in the liquid products that accumulate in the pores and on the external surface of the catalyst (Iglesia *et al.*, 1991; Claeys & Van Steen, 2004). The O/P ratios decrease with a decrease in space velocity. This is also attributed to the increased extent of secondary reactions with decreasing residence time.

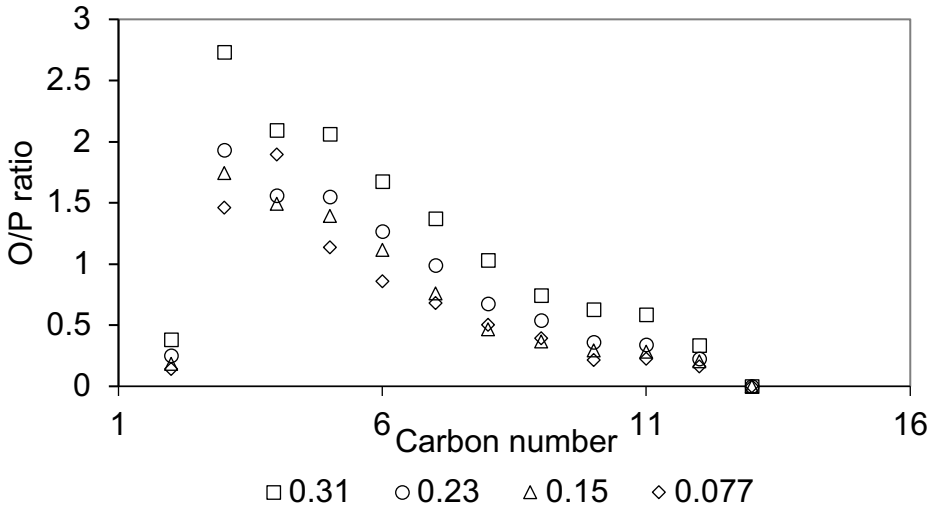

Figure 4-34: Olefin/Paraffin ratios as a function of carbon number obtained at different space velocities in the Fischer-Tropsch synthesis at 220°C and 20 bar over a Co-Pt/Al_2O_3 coated foam (OcF 1) [SV in $mmol_{CO} \cdot s^{-1} \cdot g^{-1}_{Cat}$]

4.6.1. (D) **Summary and insights**

The performance of the foam washcoated with 0.18 g of catalyst is summarised in Table 4-9. Unlike the catalyst powder, the catalyst pellets and the washcoated monoliths, no temperature rise above the catalyst bed was observed after startup. This suggests good thermal control over the catalyst. While a decrease in space velocity is typically accompanied by an increase in CO conversion, the CO conversion did not change significantly between the space velocities of 0.31 and 0.15 $mmol_{CO} \cdot s^{-1} \cdot g^{-1}_{Cat}$. In fact, a decrease in CO conversion of ca. 2 percentage points was observed upon decreasing space velocity from 0.23 to 0.15 $mmol_{CO} \cdot s^{-1} \cdot g^{-1}_{Cat}$. This was attributed to a low availability of catalytically active sites, possibly due to the low mass of catalyst in the reactor and significant contribution of catalyst deactivation. CH_4 selectivity generally increased with an decrease in space velocity, while C_{5+} selectivity decreased with

decreasing space velocity. A transitory decrease in the H_2/CO ratio may have occurred when decreasing space velocity, as the H_2 flowrate was typically decreased first. This may have caused carbon deposition (Moodley, 2008) and resulted in a continual decline in sites available for CO dissociation, and thus, reduced chain growth.

Table 4-9: Summary of catalyst performance data for Fischer-Tropsch synthesis over SiC foams with a catalyst loading of 0.18 g (OcF 1)

Syngas Flowrate [ml·min^{-1}]	240	180	120	60
Space velocity [mmol$_{CO}$·g$^{-1}_{Cat}$·s^{-1}]	0.31	0.23	0.15	0.077
Temperature [˚C]	220	220	220	220
H_2/CO usage ratio	2.0	2.1	2.4	2.0
Average X_{CO}	13 ± 1%	13 ± 1%	11 ± 1%	24 ± 2%
Average S_{CH_4}[C-%]	9 ± 1%	11 ± 1%	19 ± 2%	14 ± 1%
Average S_{CO_2}[C-%]	0%	0%	0%	0.2%
$S_{C_2-C_4}$[C-%]	7%	8%	14%	10%
$S_{C_{5+}}$[C-%]	84%	81%	67%	77%

4.6.2. Open-cell foam 2 (OcF 2)

Two cylindrical SiC foam pieces with a total catalyst loading of 0.47 g were loaded into the reactor tube. This catalyst loading corresponds with an estimated catalyst layer thickness of ca. 55 µm. The catalyst reduction and reactor startup procedure was carried out as described in Chapter 3.3.3. The Fischer-Tropsch synthesis was started at 200°C and 20 bar, at a space velocity of 0.12 $mmol_{CO} \cdot s^{-1} \cdot g^{-1}_{Cat}$. The syngas flowrate was also decreased to obtain catalyst performance data at space velocities of 0.088, 0.059 and 0.029 $mmol_{CO} \cdot s^{-1} \cdot g^{-1}_{Cat}$.

4.6.2. (A) **Catalyst activity**

CO conversion is shown as a function of time on stream with changing space velocity in Figure 4-35. Note that the intention is to ramp the reactor temperature from 200°C to the reactor operating temperature of 220°C at a rate of 1°C/min after startup. However, after reactor startup the temperature measured ca. 5 mm above the catalyst bed rose from 200°C to 331°C before the temperature ramping was initiated. The temperature remained at ca. 331°C for about 9 hours. The poor temperature control was probably a result of internal heat transfer resistance associated with the thick washcoat layer on this foam. At this temperature, the CO conversion was ca. 100%. The Hüttig temperature of metallic cobalt is ca. 257°C (Argyle *et al.*, 2014). Thus, the prolonged Fischer-Tropsch synthesis at a significantly higher temperature may have led to catalyst deactivation due to sintering. Furthermore, considerable oxidation of cobalt to oxidic forms is thought to occur at CO conversions of more than 80%, driven by the high H_2O partial pressures (Tsakoumis *et al.*, 2010; Ma *et al*., 2011; Argyle *et al.*, 2014). Thus, there is reasonable concern that catalyst performance observed may not be representative of the true activity of the catalyst. The temperature began to decrease after 9 hours on stream, with concomitant decrease in CO conversion. A variety of factors may have assisted the decrease in reactor temperature. Sintering and oxidation of the catalyst could have decreased active surface area, thus reducing the reaction rate and the amount of heat generated. Cooling of the reactor through convection could then occur faster and more efficacy. Strongly adsorbed species and heavy waxes may build-up on the catalyst with time on stream, restricting access to the catalyst surface. Whereas, the accumulation of liquid/wax products in the pores and on external surface of the catalyst may increase diffusion limitations (Liu *et al.*, 2009). This may further decrease the reaction rate and heat released.

The reactor temperature eventually cooled to 220°C after ca. 24 hours on stream, resulting in an average steady-state CO conversion of 11 ± 1%. The CO conversion at subsequent space velocities appears to be stable with time on stream. As space velocity was decreased, the

average CO conversion increased by a factor roughly equal to the reciprocal of the factor by which the space velocity was increased, i.e., $X_{CO,2} \sim X_{CO,1} \cdot \left({}^{1}/_{(SV_2/SV_1)}\right)$. This is the trend predicted by packed bed reactor model with pseudo-first order rate law for the Fischer-Tropsch synthesis (see equation 4-4 in section 4.4.1. (A)) (van der Laan & Beenackers, 1999). This might suggest that little or no further catalyst deactivation occurred with time on stream or the changing of space velocity.

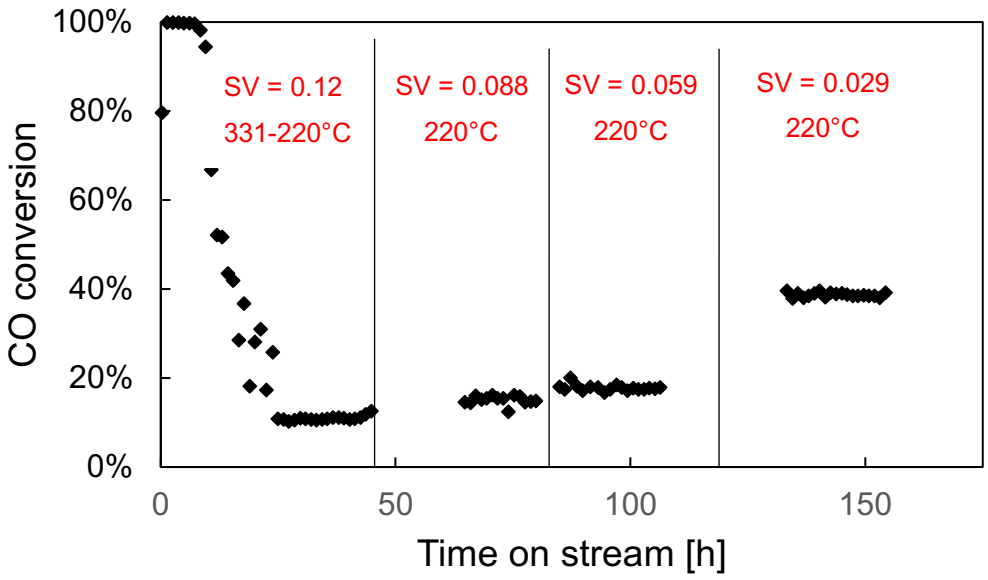

Figure 4-35: CO conversion as a function of time on stream over a Co-Pt/Al_2O_3 coated SiC foam (OcF 2) at different space velocities at 220°C and 20 bar [SV in $mmol_{CO} \cdot s^{-1} \cdot g^{-1}_{Cat}$]

4.6.2. (B) **CO_2 selectivity**

Figure 4-36 shows the CO_2 selectivity obtained in the Fischer-Tropsch synthesis over the washcoated foam at different space velocities as a function of time on stream. The CO_2 selectivity after startup very high, starting at ca. 25 C-%. This is considerably higher than the CO_2 selectivity of 1 – 2 C-% typically observed over cobalt catalysts (Rytter *et al.*, 2016). However, the high CO_2 selectivity is not surprising given the high reactor temperature and high CO conversion after startup. Ma *et al.* (2011) showed that the increase in CO_2 selectivity with increasing CO conversion is accelerated at CO conversions greater than 70%. It is noted that even during the 9-hour period when CO conversion was ca. 100%, CO_2 selectivity gradually decreased to ca. 0 C-% once steady state was achieved. The H_2/CO usage ratio started at a value 1.9 and increased with the decreasing CO_2 selectivity. At the stable CO_2 selectivity of close to 0 C-%, the H_2/CO ratio was at an average of 2.8. Thus, the high CO_2 selectivity was

likely caused by an increased extent of the water-gas shift reaction, which decreases the H_2/CO usage ratio by consuming CO and producing H_2. Since the rate of the WGS reaction is increased by the presence of oxidic cobalt species, this supports the previous suspicion that the catalyst deactivated by oxidation due to high H_2O partial pressure (van Steen et al., 2005; Tsakoumis *et al.*, 2010; Ma *et al.*, 2011).

As space velocity was decreased and the CO conversion increased, the CO_2 selectivity increased to an average of 0.9% at the lowest space velocity.

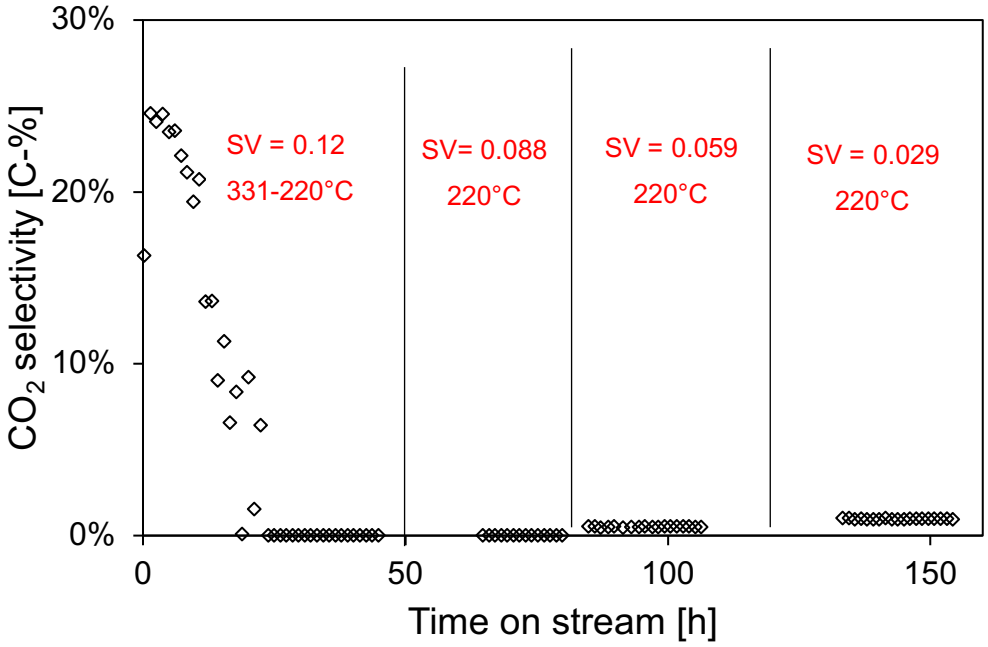

Figure 4-36: CO_2 selectivity as a function of time on stream obtained in the Fischer-Tropsch synthesis over a Co-Pt/Al_2O_3 coated SiC foam (OcF 2) at different space velocities at 220°C and 20 bar [SV in $mmol_{CO} \cdot s^{-1} \cdot g^{-1}_{Cat}$]

4.6.2. (C) **Product distribution**

Figure 4-37 below shows the CH_4 selectivity as a function of time on stream. Given the large temperature increase after startup at the space velocity of 0.12 $mmol_{CO} \cdot s^{-1} \cdot g^{-1}_{Cat}$, it is not surprising that methane selectivity was initially high because CH_4 is thermodynamically favoured (Claeys & van Steen, 2005). Furthermore, CH_4 selectivity may be related to the increase in CO_2 selectivity which increases the H_2/CO ratio because CO_2 production consumes CO and possibly increasing H_2 in the case of the WGS reaction (Tucker & van Steen, 2020). The CH_4 selectivity gradually decreased from a maximum of 55% to a steady-state average of 26.5% as the reactor temperature dropped to 220°C. The H_2/CO usage ratio

at steady state was at an average of 2.8, which is expected since a high extent of methanation during Fischer-Tropsch synthesis brings the H_2/CO usage ratio closer to 3 (see equation 2-2). In the last hour of the Fischer-Tropsch synthesis at the space velocity of 0.12 $mmol_{CO} \cdot s^{-1} \cdot g^{-1}_{Cat}$, the CH_4 selectivity appeared to be decreasing with increasing time on stream. At the same time, CO conversion was increasing slightly with time on stream (see Figure 4-35). Water co-feeding experiments over a Pt promoted cobalt catalyst have shown that negative water effect has limited reversibility at low H_2O partial pressures (Das *et al.*, 2005; Jacobs *et al.*, 2014). Thus, it is possible that the increase in CO conversion and decrease in CH_4 selectivity were a result of the reversal of catalyst oxidation.

The CH_4 selectivity was quite high even at lower space velocities, where the reactor temperature was supposedly at its set point of 220°C. Furthermore, the CH_4 selectivity increased with a decrease in space velocity (i.e., increase in CO conversion) between the space velocities of 0.12 to 0.059 $mmol_{CO} \cdot s^{-1} \cdot g^{-1}_{Cat}$. This is contradictory to the expected trend as CH_4 selectivity typically decreases with decreasing space velocity and increasing CO conversion (Bukur *et al.*, 2012). This behaviour is attributed to catalyst deactivation that has already been detailed. More positively, the CH_4 selectivity decreased from 32 ± 4 C-% to 22 ± 2 C-% when the space velocity was decreased from 0.059 to 0.029 $mmol_{CO} \cdot s^{-1} \cdot g^{-1}_{Cat}$. More comprehensive product selectivities are presented in Figure 4-38, which shows the product distributions at the different space velocities along with average CO conversions achieved. As with the CH_4 selectivity, the C_2 - C_4 selectivity appears to be increasing with an increase in conversion. C_{5+} selectivity decreased with decreasing space velocity up to the space velocity of 0.059 $mmol_{CO} \cdot s^{-1} \cdot g^{-1}_{Cat}$. This contradicts the expected trend as the yield of C_{5+} products typically increases with decreasing space velocity (van Steen *et al.*, 2018). Once again, the data at the space velocity of 0.029 $mmol_{CO} \cdot s^{-1} \cdot g^{-1}_{Cat}$ deviated from the trend presented by the preceding space velocity, with C_{5+} selectivity increasing to 58 C-%. It is unlikely that the catalyst suddenly improved after decreasing the space velocity from 0.059 to 0.029 $mmol_{CO} \cdot s^{-1} \cdot g^{-1}_{Cat}$. Residence time in the catalyst increases with decreasing space velocity. This may have increased the probability of re-adsorption and hydrogenation of α-olefins. A decrease in space velocity may increase external mass transfer limitations, resulting in the build-up of liquid/wax products surrounding the catalyst. This may improve C_{5+} selectivity through transport resistance enhanced α-olefin readsorption (Iglesia *et al.*, 1991) and by dampening against increase in the temperature of the catalyst, which prevents high CH_4 selectivity.

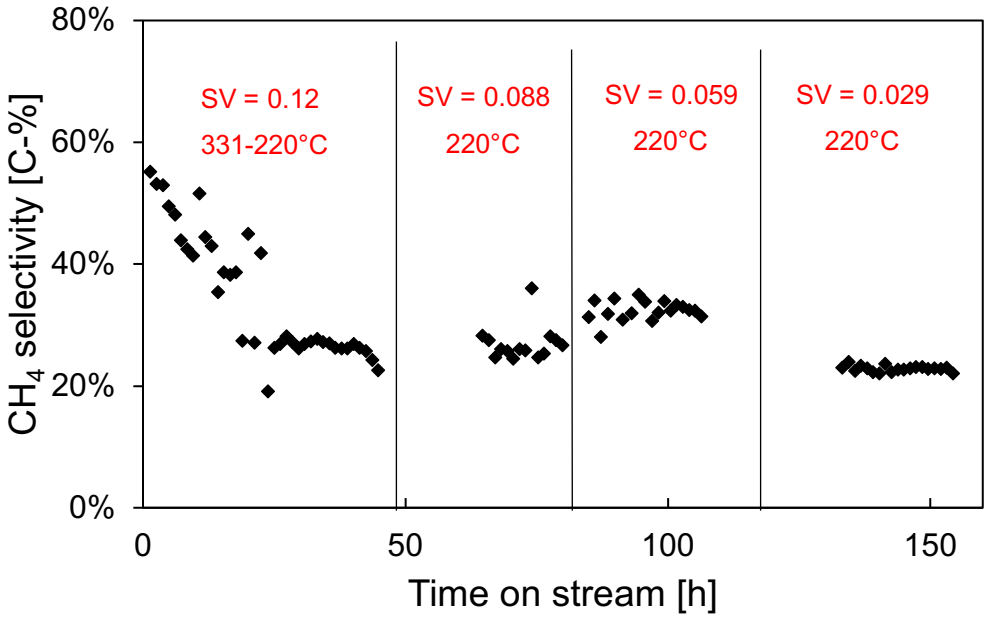

Figure 4-37: CH_4 selectivity as a function of time on stream over a Co-Pt/Al_2O_3 coated SiC foam (OcF 2) at different space velocities at 220°C and 20 bar [SV in $mmol_{CO} \cdot s^{-1} \cdot g^{-1}_{Cat}$]

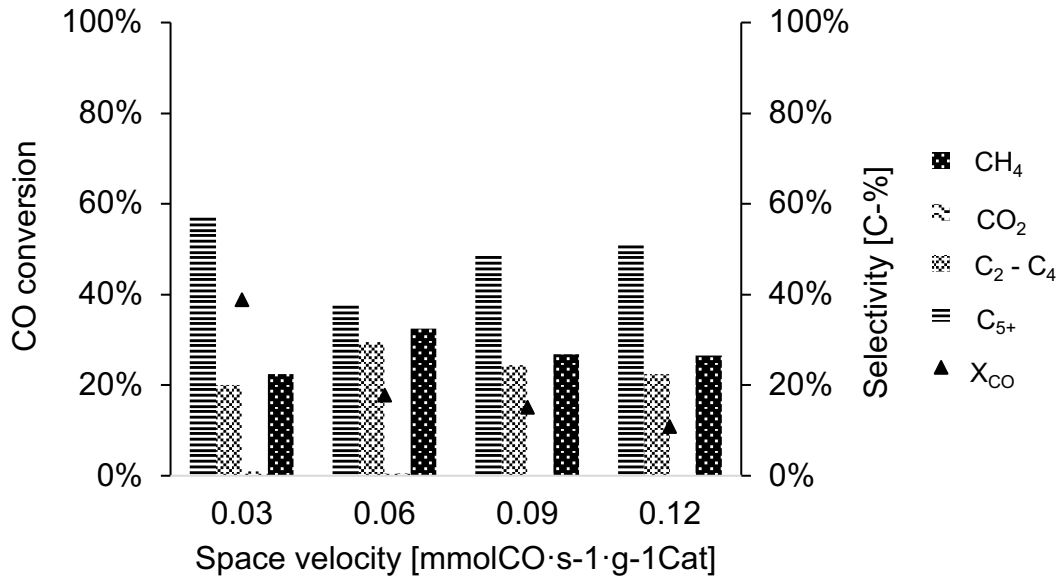

Figure 4-38: Average CO conversion and product distribution of Fischer-Tropsch synthesis over a Co-Pt/Al_2O_3 coated foam (OcF 2) at 220°C and 20 bar

O/P ratios obtained at the different space velocities were plotted as a function of carbon number in Figure 4-39. Predictably, the O/P ratios decrease with increasing number. This is attributed to increased residence time and chain length dependent solubility of higher molecular mass compounds (Kuipers *et al.*, 1995). O/P ratios were very low within the C_2 product fraction and showed a maximum at C_3, this is generally attributed to the high tendency

of ethylene to be re-incorporated into growing carbon chains (Förtsch *et al.*, 2015; Shafer *et al.*, 2019). The O/P ratio generally decreased with a decrease in space velocity. This is the expected trend with an increase in residence time, which increases the chance for secondary reactions of olefins (Rytter *et al.*, 2016; Shafer *et al.*, 2019).

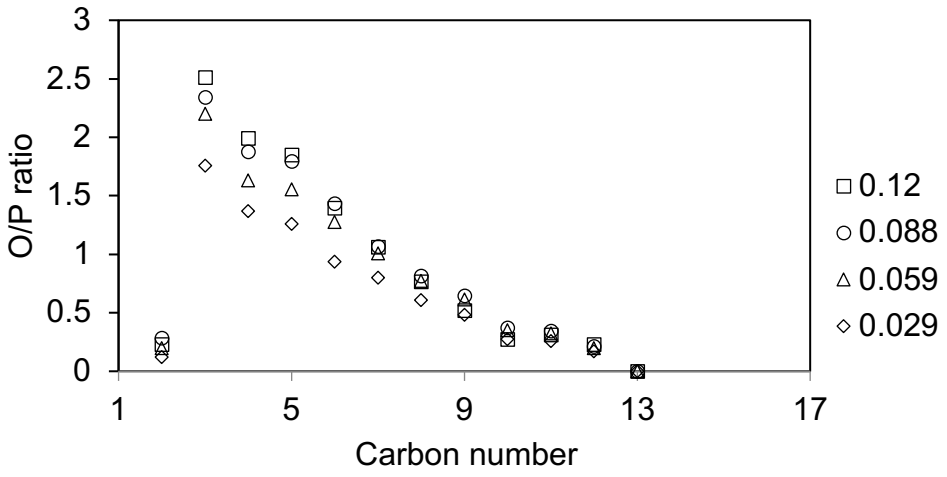

Figure 4-39: Olefin/Paraffin ratio as a function of carbon number in the Fischer-Tropsch synthesis at 220°C and 20 bar over a foam catalyst (OcF 2) at different space velocities [SV in $mmol_{CO} \cdot s^{-1} \cdot g^{-1}_{Cat}$]

4.6.2. (D) **Summary and insights**

The catalyst performance data of the foam washcoated with 0.47 g of Co-Pt/Al_2O_3 catalyst is summarised in Table 4-10. Severe thermal runaway was observed, with the catalyst bed temperature exceeding 331°C for approximately 9 hours. This, along with the high CO_2 selectivities imply that it is highly probably that this catalyst suffered significant catalyst deactivation due to sintering and oxidation. Furthermore, this catalyst can be said to have performed poorly as the CH_4 selectivities were high and C_{5+} selectivities were low. The poorest performance was observed at the space velocity of 0.059 $mmol_{CO} \cdot s^{-1} \cdot g^{-1}_{Cat}$, with a CH_4 selectivity of 32 ± 4 C-% and C_{5+} selectivity of 38 C-%. It is thought that the relatively thick washcoat layer on this catalyst may have led to internal mass transfer limitations, which may, in addition to deactivation of the catalyst with time on stream, be responsible for the disparity between the expected and the observed trends on product selectivities.

Table 4-10: Summary of catalyst performance data for Fischer-Tropsch synthesis over SiC foams with a catalyst loading of 0.47 g (OcF 2)

Syngas flow rate [ml·min^{-1}]	240	180	120	60
Space velocity [mmol$_{CO}$·g$^{-1}_{Cat}$·s^{-1}]	0.12	0.088	0.059	0.029
Temperature [°C]	331 - 220	220	220	220
H_2/CO usage ratio	1.8 - 2.8	2.5	2.5	2.3
Average X_{CO}	11 ± 1%	15 ± 1%	18 ± 2%	39 ± 2%
Average S_{CH_4}[C-%]	26 ± 2%	27 ± 4%	32 ± 4%	22 ± 2%
Average S_{CO_2}[C-%]	25% → 0%	0%	0 ± 0.1%	1 ± 0.1%
$S_{C_2-C_4}$[C-%]	22%	24%	30%	20%
$S_{C_{5+}}$[C-%]	51%	49%	38%	58%

4.6.3. Open-cell foam 3 (OcF 3)

OCF 3, which is a pair of 30 PPI β −SiC foams, was coated with 0.24 g of Co-Pt/Al_2O_3 catalyst, this correlates with an estimated washcoat layer thickness of ca. 28 µm. In Chapter 4.2.2, SEM imaging of the washcoated foams showed that the catalyst layer thickness on the surface of the foam varied widely, i.e., the coating was not homogenous, which may have implications on catalyst performance. The performance of this coated foam in Fischer-Tropsch synthesis was tested at space velocities of 0.23, 0.17, 0.12 and 0.058 $mmol_{CO} \cdot s^{-1} \cdot g^{-1}_{Cat}$. The Fischer-Tropsch synthesis was started at a reactor temperature of 200°C and total pressure of 20 bar, with the intention of ramping up the temperature to 220°C at a rate of 1°C/min.

4.6.3. (A) **Catalyst activity**

Figure 4-40 shows the CO conversion as a function of time on stream at different space velocities. After reactor startup at the space velocity of 0.23 $mmol_{CO} \cdot s^{-1} \cdot g^{-1}_{Cat}$, the temperature measured ca. 5mm above the catalyst bed rose to 246°C within 10 minutes and without the temperature ramping programme being initiated. Regardless, the reactor temperature decreased to the desired temperature of 220°C after approximately half an hour and was set to remain there for the duration of the catalyst test. However, it can be seen in Figure 4-40 that the CO conversion, which started at ca. 100% at the highest reactor temperature, decreased more gradually and only reached an average steady-state CO conversion of 6% after 3.75 hours-on-stream. The time lag between the stabilisation of CO conversion and the reactor temperature implies that a considerable axial temperature gradient exists (Jess & Kern, 2012). Thus, the temperature within the catalyst bed may have been higher than what could be measured by the thermocouple placed ca. 5 mm above the catalyst bed. Although the measured temperature was 11°C lower than the Hüttig temperature of metallic cobalt, which is 257°C (Argyle *et al.*, 2014), the rapid rise in temperature could have had detrimental effects on catalyst activity. After the reactor temperature stabilised, CO conversion appeared to be stable with time on stream at all space velocities tested thereafter. Note that the gap in the data at the space velocity of 0.23 $mmol_{CO} \cdot s^{-1} \cdot g^{-1}_{Cat}$ was due to an accidental disconnection of the GC-TCD computer from its power supply.

When space velocity was decreased, the CO conversion increased proportionally, i.e., $X_{CO,2} \sim X_{CO,1} \cdot \left({}^{1}/_{(SV_2/SV_1)}\right)$. CO conversion was 9 ± 1%, 12 ± 1% and 24 ± 2% at the space velocities of 0.17, 0.12 and 0.058 $mmol_{CO} \cdot s^{-1} \cdot g^{-1}_{Cat}$ respectively. This is close to the expected trend according to the packed bed reactor design equation assuming simple 1st order rate

kinetics (van der Laan & Beenackers, 1999). Regardless, the CO conversion achieved over this catalyst was low. This is benchmarked against HcM 2, which showed CO conversions between 26% and 46% at similar catalyst loading. The low CO conversion may indicate that the initial catalyst deactivation after startup had a strong influence on activity.

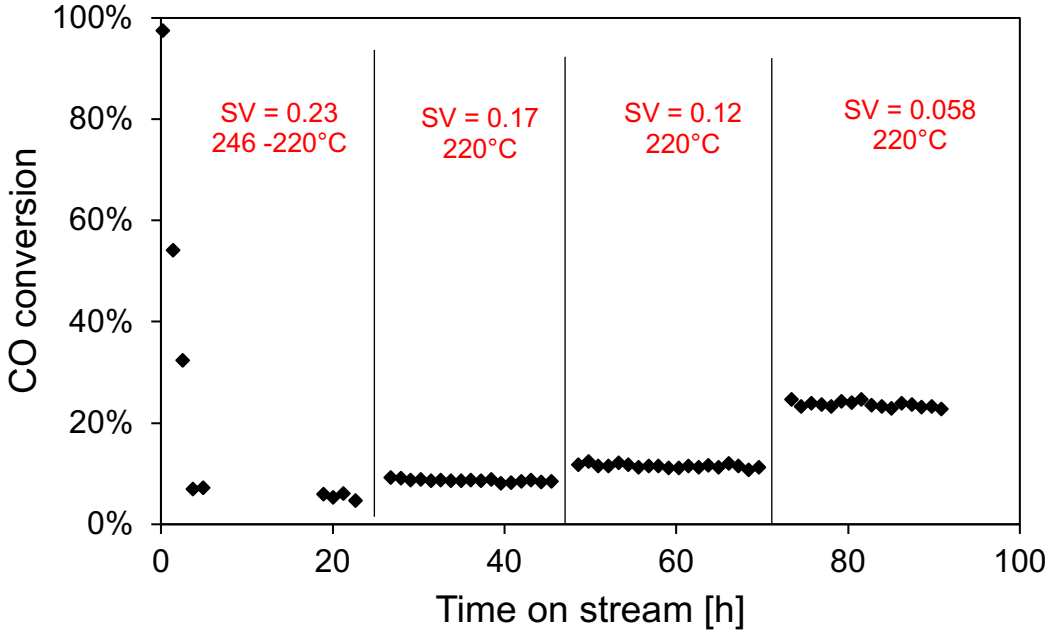

Figure 4-40: CO conversion as a function of time on stream over a Co-Pt/Al_2O_3 coated SiC foam (OcF 3) at different space velocities at 220°C and 20 bar [SV in $mmol_{CO} \cdot s^{-1} \cdot g^{-1}_{Cat}$]

4.6.3. (B) **CO_2 selectivity**

Figure 4-41 shows the CO_2 selectivity as a function of time on stream obtained at different space velocities over the washcoated foam (OcF 3). A high rate of CO_2 production was observed after startup, with initial CO_2 selectivity of ca. 18 C-%. It should be noted that the expected CO_2 selectivity in a fixed bed reactor is typically 1-2% (Rytter *et al.*, 2016). However, the CO_2 selectivity decreased as CO conversion decreased during the first 3.75 hours on stream, such that virtually no CO_2 was detected by the GC-TCD thereafter. Furthermore, as CO conversion decreased, the H_2/CO usage ratio steadily increased from an initial low of 2 to 2.9. This strongly suggests that the high CO_2 selectivity shortly after startup was likely due to an increase in the extent of the water-gas shift (WGS) reaction. High WGS activity during low-temperature Fischer-Tropsch synthesis over cobalt typically arises due to the presence of oxidised cobalt species (Rytter & Holmen, 2015). Note that the same conditions that promote the oxidation of cobalt, that is high reactor temperature and high H_2O partial pressure, also promote sintering of the cobalt particles (Ma *et al.*, 2011). High H_2O partial pressure can be inferred from the high CO conversion, as H_2O is the major by-product of the Fischer-Tropsch

synthesis reaction (Adesina, 1996). Thus, oxidation and sintering were likely mechanisms by which the washcoated foam (OcF 3) deactivated.

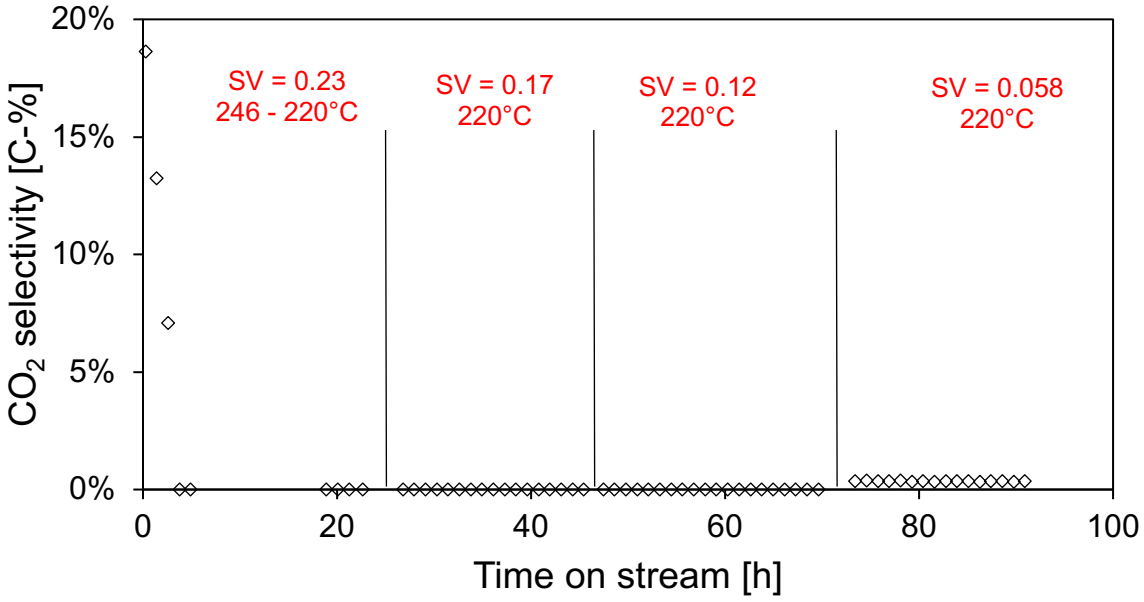

Figure 4-41: CO_2 selectivity as a function of time on stream over a Co-Pt/Al_2O_3 coated SiC foam (OcF 3) at different space velocities 220°C and 20 bar [SV in $mmol_{CO} \cdot s^{-1} \cdot g^{-1}_{Cat}$]

4.6.3. (C) **Product distributions**

The CH_4 selectivity at different space velocities is shown in Figure 4-42 as a function of time on stream. It can be seen that the initial CH_4 selectivity after reactor startup is high, starting at approximately 40 C-%. The CH_4 selectivity decreased to ca. 21 C-% with time on stream until the point where data recording was interrupted on the GC-TCD. As expected for CO conversion greater than 80%, the CH_4 selectivity decreased with decreasing CO conversion and decreasing reactor temperature prior to the interruption (Dry, 1982; Ma *et al.*, 2011; Bukur *et al.*, 2012). The initially high selectivity for methanation is attributed to high reactor temperature (Adesina, 1996). However, the CH_4 selectivity at the space velocity of 0.23 $mmol_{CO} \cdot s^{-1} \cdot g^{-1}_{Cat}$ increased with time on stream after data recording was resumed. Since neither reactor temperature, the CO conversion nor the CO_2 selectivity showed a corresponding trend, this might be an artefact of the equilibrating of the GC-TCD.

Overall, the CH_4 selectivities generally decreased with decreasing space velocity (i.e., with increasing CO conversion). The exception was that the CH_4 selectivity remained at an average of ca. 20 C-% upon decreasing space velocity from 0.17 to 0.12 $mmol_{CO} \cdot s^{-1} \cdot g^{-1}_{Cat}$ despite the CO conversion having increased by a factor of ~1.33 from 9 ± 1% to 12 ± 1%. Since CH_4

selectivity is expected to decrease with increasing CO conversion or decreasing space velocity (Bukur *et al.*, 2012), this may signal that catalyst deactivation occurred, resulting in the increase in catalyst sites with a preference for CH_4. CH_4 is likely formed on different catalyst sites through the creation of the C_1 species rather than through the termination of C_1 monomers that would have otherwise been incorporated into growing hydrocarbon chains (Dry, 2004). The CH_4 subsequently decreased to an average of 16 ± 2% when the space velocity was decreased to 0.058 $mmol_{CO} \cdot s^{-1} \cdot g^{-1}_{Cat}$. Furthermore, the average H_2/CO usage ratios decreased with decreasing CH_4 selectivity, from 2.9 at the CH_4 selectivity of 26 ± 4 C-% to 2.2 at the CH_4 selectivity of 16 ± 2 C-%. This is consistent with the expectation that an increase in the extent of the methanation reaction will increase the H_2/CO usage ratio since methanation consumes 3 H_2 molecules per molecule of CO converted. On the other hand, higher hydrocarbons result in lower H_2/CO usage ratios (see equation 2-2).

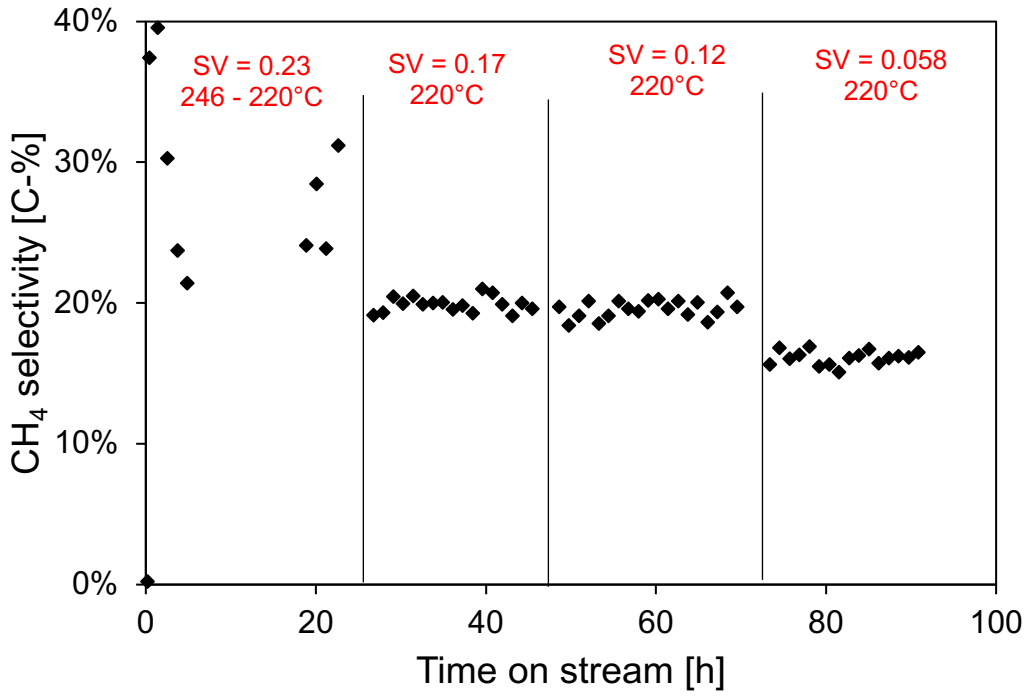

Figure 4-42: CH_4 selectivity as a function of time on stream over a Co-Pt/Al_2O_3 coated SiC foam (OcF 3) at different space velocities 220°C and 20 bar [SV in $mmol_{CO} \cdot s^{-1} \cdot g^{-1}_{Cat}$]

The product selectivities at different space velocities and the associated average CO conversion levels are shown in Figure 4-43. The C_2 – C_4 and the C_{5+} selectivities correspond with the trends shown by the CH_4 selectivities. C_2 -C_4 selectivity generally decreased with decreasing space velocity while C_{5+} selectivity increased with decreasing space velocity (i.e., increasing CO conversion). This is the expected trend as increasing residence time with decreasing space velocity increases the chance for secondary reactions of olefins such as hydrogenation and re-insertion to occur (Bukur et al., 2012; van Steen et al., 2018). Similar to

the CH_4 selectivity, some deviation from this trend was observed and is suspected to be a result of catalyst deactivation: the C_2 – C_4 selectivity did not decrease when the space velocity was decreased to from 0.17 to 0.12 $mmol_{CO} \cdot s^{-1} \cdot g^{-1}_{Cat}$ but stayed at ca.16 C-%. The same was true of C_{5+} selectivity, which did not increase from ca. 64 C-%.

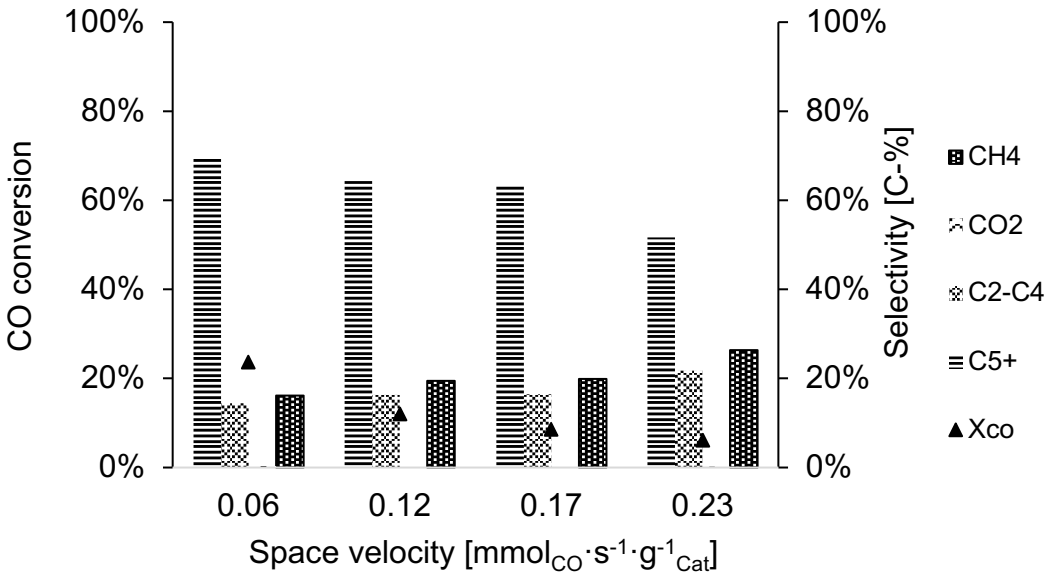

Figure 4-43: Average CO conversion and product distribution of Fischer-Tropsch synthesis over a SiC foam coated with 0.24g of Co-Pt/Al_2O_3 (OcF 3)

The O/P ratios as a function of carbon number obtained over the washcoated foam at different space velocities are displayed in Figure 4-44. The O/P ratios generally follow the expected trends and deviations. The O/P ratios generally decrease with increasing carbon number, this is typically attributed to the increase in solubility and residence time with increasing chain length within the presumably liquid filled pores of the catalyst (Kuipers *et al.*, 1995). The O/P ratios in the C_2 product fraction are very low due to the high probability of C_2 olefins to be incorporated into growing chains. The O/P ratios decrease with decreasing space velocity, due to increased residence time increasing the chance for the occurrence of secondary reactions involving olefins (Bukur *et al.*, 2012).

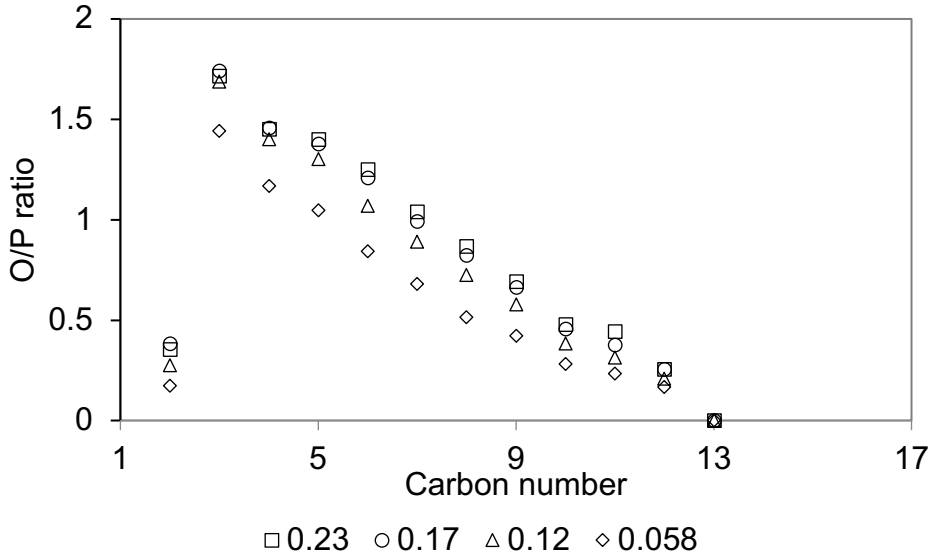

Figure 4-44: O/P ratio as a function of carbon number obtained over a SiC foam coated with 0.24g of Co-Pt/Al_2O_3 catalyst at different conversion levels [SV in $mmol_{CO} \cdot s^{-1} \cdot g^{-1}_{Cat}$]

.

4.6.3. (D) **Summary and insights**

The catalyst performance of OcF 3, the foam washcoated with 0.24 g of catalyst is summarised in Table 4-11. The exothermic increase in reactor temperature up to 246°C, the gradual decline in CO conversion to a low value of 6 ± 1%, the high CO_2 selectivity and the low H_2/CO usage ratio during the first 3.75 hours after startup suggest catalyst deactivation via sintering and oxidation. Withstanding the deactivation, the CO conversions behave ideally by increasing proportionally with the decrease in space velocity. Stagnant product distribution when decreasing space velocity from 0.17 to 0.12 $mmol_{CO} \cdot s^{-1} \cdot g^{-1}_{Cat}$ is thought to indicate catalyst deactivation via an increase in methanation catalyst sites.

Table 4-11: Summary of performance data for FTS over a washcoated SiC foam (OcF 3)

Space velocity [$mmol_{CO} \cdot s^{-1} \cdot g^{-1}_{Cat}$]	0.23	0.17	0.12	0.058
Temperature [°C]	220	220	220	220
H_2/CO usage ratio	2.9	2.6	2.7	2.2
Average X_{CO}	6 ± 1%	9 ± 1%	12 ± 1%	24 ± 2%
Average S_{CH_4}[C-%]	26 ± 4%	20 ± 1%	20 ± 2%	16 ± 2%
Average S_{CO_2}[C-%]	0%	0%	0%	0%
$S_{C_2-C_4}$[C-%]	22%	16%	16%	14%
$S_{C_{5+}}$[C-%]	52%	64%	64%	70%

5. Discussion

5.1. Comparing the different catalyst packings

5.1.1. Apparent catalyst activity

Since approximately 0.5 g of catalyst was loaded for the catalyst powder and the catalyst pellets, a comparison is made with monoliths and foams coated with similar amount of catalyst. The CO conversion obtained over the four catalyst packings is shown in Figure 5-1. In contrast to the other catalyst packings, the pellets showed a decrease in CO conversion with a decrease in space velocity. Note that CO conversion is expected to increase with decreasing space velocity if the reaction can be assumed to proceed with first order rate kinetics in terms of CO. The contrary trend shown by the catalyst pellets suggests that the reaction proceeded under severe mass transfer limitations. In an external mass transfer dominated regime, a higher gas flowrate may cause increased turbulence and a decrease in the thickness of the interface between the bulk gas and the external catalyst washcoat surface, resulting in improved mass transfer. Thus, an increase in gas flowrate would lead to an increase in the CO conversion achieved. It is believed that heat generated during the Fischer-Tropsch reaction is not removed efficiently from the pellet due to its larger diffusion distance when compared to the catalyst powder, resulting in exothermic temperature increase. Under these severe operating conditions, the temperature within the pellet could have become hotter than the surrounding gas, causing external mass transfer resistance to become rate limiting (Fogler, 2016; Levenspiel, 1993). Because high temperatures accelerate reaction rates (Fogler, 2016), the high internal temperature of the catalyst pellets were probably the most significant contributing factor to higher CO conversion achieved over the pellets when compared to the powder, foam and monolith.

It is evident that the catalyst powder outperforms the foams and monoliths considerably as the conversion achieved over these structured packings was roughly 30 percentage points lower than that obtained over the catalyst powder. The poorer performance of the foams and monoliths is thought to be a consequence of catalyst deactivation and poor transport properties when compared to the catalyst powder.

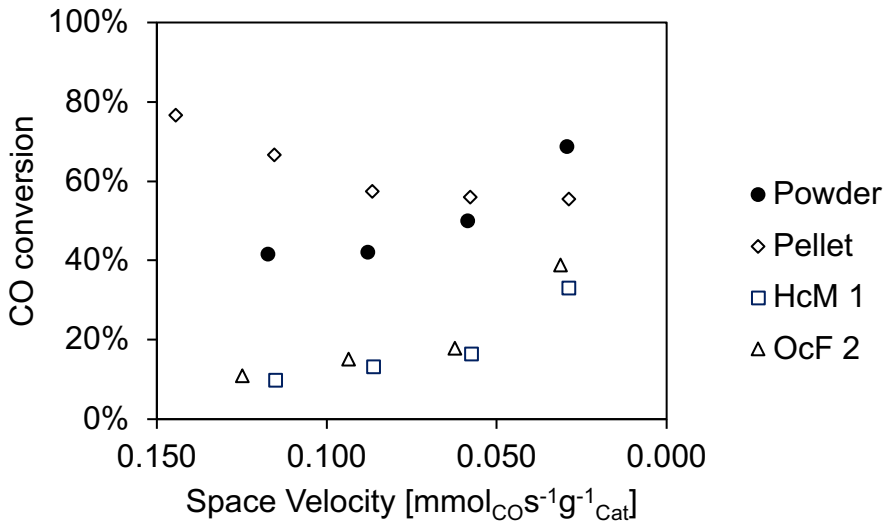

Figure 5-1: CO conversion over the powder, pellet, monolith and foam.

5.1.2. Reactor productivity

It is important to consider not just the conversion, but also the productivity of the catalyst. Because of the vastly different CO conversions achieved over the catalyst powder, the pellets and the structured packings, it is less useful to compare the catalyst performance purely on the merits of conversion and selectivity, but rather based on productivity, which is defined as the amount of carbon converted to a specific product fraction per mass of catalyst for a given flowrate of syngas feed. This comparison is useful because when assessing feasibility of each catalyst packing, the question will come down to maximising the amount and quality of revenue generating product that is produced per mass of catalyst loaded (a major operating expense) if the same amount of raw material is fed into the reactor. Furthermore, the global drive towards reduction in greenhouse gas emissions, it is also desirable to minimise CH_4 and CO_2 by-products. The productivities of the different catalyst packings is shown in Table 5-1.

It has already been established that under ordinary Fischer-Tropsch synthesis conditions, the product distribution is a function of conversion, and that CH_4 selectivity decreases with increasing CO conversion, while C_{5+} selectivity increases with increasing CO conversion (Bukur et al., 2012). The trend shown by the pellets was contradictory to this. In addition, the catalyst pellets exhibited significantly higher CH_4 and CO_2 selectivities at steady-state, despite achieving the highest conversions. Average CH_4 selectivities for the catalyst pellet were between 34 C-% to 42 C-%, while average CO_2 selectivities were between 4 C-% and 8 C-%. Note that CH_4 selectivities between 5-12 C-% and CO_2 selectivities lower than 2 C-% are typically reported for lab-scale packed bed Fischer-Tropsch synthesis reactors (Bukur *et al.*,

2012; Rytter *et al.*, 2016). It can be seen in Table 5-1 that the CH_4 productivity of the catalyst pellets was significantly higher than that of the catalysts. Moreover, the production of C_{5+} was remarkably low for the catalysts pellets, given the high levels of CO conversion that were achieved. Note that even when the powder achieved lower conversion than the pellet (at the same space velocities), it showed higher C_{5+} productivity, by approximately 50%. At the lowest space velocity, the C_{5+} productivity of the powder was nearly double that of the pellet. This is a clear indication of poor temperature control with respect to the pellet as CH_4 and CO_2 production are thermally favoured (Dry, 1982).

While it might appear as though the pellet is more productive than the structured packings when looking solely at the C_{5+} product fraction, the large amount of greenhouse gases (CH_4 and CO_2) produced over the pellets remains a major concern. Due to the lower CO conversion achieved over the monolith (HcM 1) and foam (OcF 2), productivity of all product compounds was lower than the catalyst powder and catalyst pellets. Both the foam and monolith reported insignificant production of CO_2 at steady state. CH_4 productivities for the foam (OcF 2) were generally between 2 to 3 times higher than the monolith (HcM 1). Furthermore, the foam also showed slightly lower C_{5+} productivity than the monolith. It is thought that the difference in the performance of the foam and monolith is a consequence of potentially more a significant level of deactivation of the foam, which experienced exothermic temperature increase up to 331°C while that of the monolith rose to 250°C.

Table 5-1: Productivity of catalysts at similar catalyst loadings (~0.5 g_{cat})

	Powder				Pellet			
Space velocity [$mmol_{CO} \cdot s^{-1} \cdot g^{-1}_{Cat}$]	0.11	0.08	0.06	0.03	0.11	0.08	0.06	0.03
X_{CO}	42%	42%	50%	69%	67%	57%	56%	56%
Productivity [$\mu mol_C \cdot s^{-1} \cdot g^{-1}_{Cat}$]								
CH_4	7.9	7.4	5.6	3.4	31	20	13	5
CO_2	0.2	0.3	0.3	0.3	5.7	2.5	1.3	0.6
C_2-C_4	5.3	5.0	4.0	2.6	18	11	6.6	3.1
C_{5+}	33	23	18	13	19	15	10	7
	Monolith 1 (HcM 1)				**Foam 2 (OcF 2)**			
Space velocity [$mmol_{CO} \cdot s^{-1} \cdot g^{-1}_{Cat}$]	0.11	0.08	0.05	0.03	0.12	0.09	0.06	0.03
X_{CO}	10%	13%	16%	33%	11%	15%	18%	39%
Productivity [$\mu mol_C \cdot s^{-1} \cdot g^{-1}_{Cat}$]								
CH_4	1.0	1.2	1.7	1.2	3.6	3.5	2.8	3.7
CO_2	-	-	-	-	-	-	-	-
C_2-C_4	0.75	0.89	1.2	0.9	2.8	3.0	2.6	3.4
C_{5+}	8.8	8.6	5.9	6.8	6.5	6.8	5.1	4.4

5.2. Catalyst deactivation

The thermal runaway temperatures observed after reaction startup, with temperatures rising well above 220°C during when testing the pellets, honeycomb monoliths and open-cell foams bring into question the reliability of the results obtained over these catalysts. It is likely that the structure of the catalyst surface was significantly altered, and severe catalyst deactivation had occurred (Bartholomew, 2001; Tsakoumis *et al.*, 2010; Moodley *et al.*, 2020). Thus, consideration of the deactivation is critical to assessing the performance of this catalyst. However, since multiple deactivation mechanisms can occur simultaneously and even transition with time on stream and/or changing reactor conditions, retroactive assessment of catalyst deactivation is not trivial (Bartholomew, 2001v; Fogler, 2016; Moodley *et al.*, 2020). In the case of Fischer-Tropsch synthesis, this is further complicated by the fact that reaction conditions exist in intricate interplay with the CO conversion levels, the multiple parallel reactions, concurrent transport phenomena and are to different extents based on already existing conditions (Rytter & Holmen, 2015).

For all the catalysts tested, the Fischer-Tropsch synthesis was started at 200°C and 20 bar. It was intended to subsequently ramp up the temperature to the reactor operating temperature of 220°C at a rate of 1°C/min. However, for some of the catalysts, rapid exothermic temperature increase was observed even before the temperature ramping programme was initiated, with reactor temperatures exceeding 220°C. Table 5-2 shows what temperature each catalyst reached above 220°C. Amongst the catalyst tested, it was only the reactor temperatures for the catalyst powder and the foam with the lowest catalyst loading (OcF1) that did not exceed 220°C after startup.

Table 5-2: Extent of exothermic temperature increase and catalyst wt.% in catalyst bed

Catalyst	Temperature reached above 220°C	Catalyst wt.% in catalyst bed
Catalyst powder	-	11%
Catalyst pellets	250	7.4%
HcM 1	250	33%
HcM 2	251	19%
OcF 1	-	15%
OcF 2	331	30%
OcF 3	246	22%

The Hüttig temperature of [bulk] metallic cobalt is ca. 257°C, that is the temperature at which surface atoms become mobile and may lead to particle growth (Argyle *et al.*, 2014). It can be seen in Table 5-2 that the catalyst pellets, monoliths, and two of the foams reached temperatures near or exceeding 250°C after startup. It is emphasised again that the reactor temperature could only be measured ca. 5 mm above the catalyst bed for these catalysts. Based on the expectation that an axial temperature gradient exists within the reactor (Jess & Kern, 2012), the temperature within the catalyst bed is likely to have been higher. Most worrying was the temperature measured for OcF 2, which was 331°C, which exceeds the Hüttig temperature by 74°C. The likelihood of sintering, which is a common cause of deactivation for cobalt Fischer-Tropsch synthesis catalysts and is a thermodynamically activated process, is quite high for these catalysts (Tsakoumis *et al.*, 2010; Moodley *et al.*, 2020). It is also noted that the CO conversions of up to ca. 100% were observed during the periods of high temperature operation. This is likely to have resulted in elevated H_2O partial pressures, which is a major by-product of FTS. Claeys et al. (2015) have shown using in situ Magnetometer studies of a 20 wt.% Co/Al_2O catalyst promoted with 0.05 wt.% Pt that a high ratio of H_2O to syngas resulted in a dramatic increase in particle growth.

EFTEM was performed on the unreacted catalyst powder and the spent catalysts, elemental mapping was carried out to determine whether sintering occurred as is suspected and the resulting images are shown in Figure 5-2. It is known that drying of the catalyst during preparation forms cobalt nitrate droplets, which result in the formation of Co_3O_4 clusters during calcination (Feller *et al.*, 1999). Thus, the presence of cobalt clusters in the calcined catalyst powder (image ‘a’) is not surprising. However, it is also known that reduction leads to a decrease in clustering and crystallite size, as well as improved cobalt dispersion. As such, the presence of large clusters in the spent catalyst pellet (image ‘b’) suggests that coalescence was at least underway. This is not surprising, as internal diffusion limitations caused by the larger particle diameter of the pellets probably caused the internal temperature of the pellets to be higher than the surrounding gas temperature, leading to increased particle migration.

Images ‘c’ to ‘e’ show the cobalt maps of spent catalyst from OcF 1, HcM 1 and OcF 2. In contrast to that of the pellets, visual inspection of these images suggests that the cobalt particle sizes in the spent structured catalysts was comparable to that of the fresh, calcined catalyst powder. These results are contradictory to what was expected, especially with regards to OcF 2, which exhibited the most severe temperature increase. However, this may not be viewed as conclusive evidence that sintering did not occur. As stated by Moodley *et al.* (2020), the fact that areas are randomly selected for TEM observation imaging prevents the possibility of observing the same area before and after reaction, making it difficult to ascertain whether

particles have grown in size or remained the same. Furthermore, spent Fischer-Tropsch catalysts are typically covered in wax, such that the image may not reflect the true size of crystallites (Moodley *et al.*, 2020).

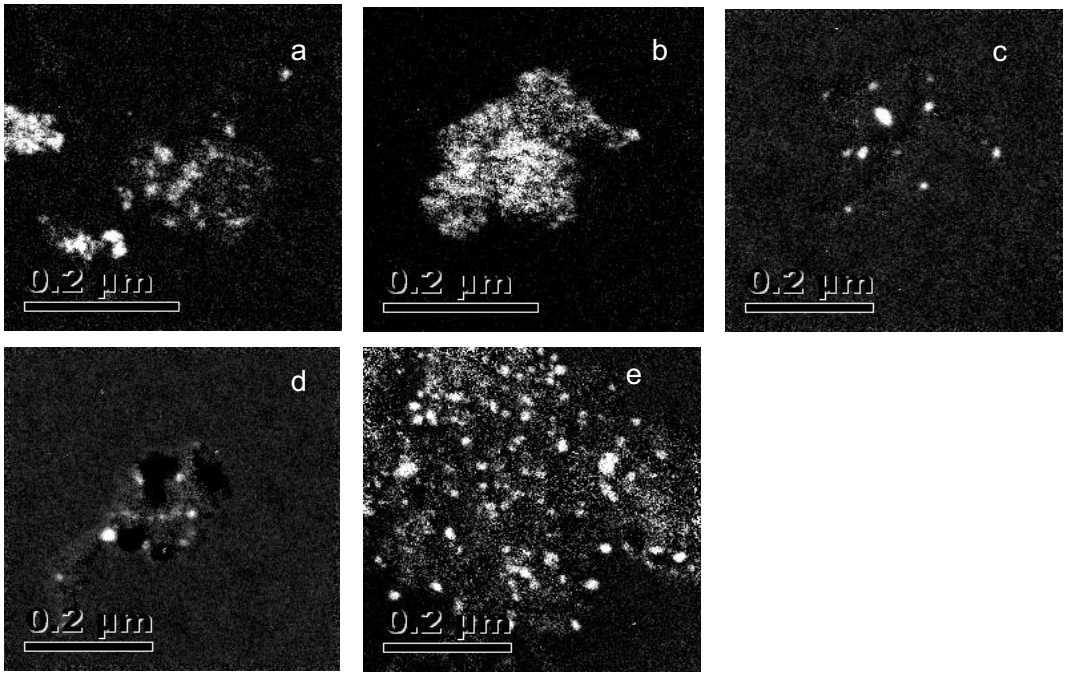

Figure 5-2: EFTEM images of (a) unreacted catalyst powder and the (b) spent pellet (c) spent OcF 1 (d) spent HcM 1 and (e) spent OcF 2.

It was also observed that CO_2 selectivities during the periods of high temperature operation were high, reaching 25 C-% for OcF 2 & HcM 2. This was attributed to a high extent of the water-gas shift (WGS) reaction. A high extent of the WGS reaction is typically associated with the presence of oxidic species (i.e., CoO), which are formed at high H_2O partial pressures (Ma *et al.*, 2011). Thus, re-oxidation is also likely to have contributed significantly to catalyst deactivation, especially during the initial periods after startup. It has also been said that high H_2O partial pressures can result in the formation of metal support species $CoAl_2O_4$ which catalyse side reactions such as the WGS reaction (Ma *et al.*, 2011). However, it was observed that CO_2 selectivities decreased to near zero when space velocity was decreased. Since $CoAl_2O_4$ is an irreducible species, the decrease in CO_2 selectivity discounts that claim for this catalyst (Saib *et al.*, 2006; Tucker & van Steen, 2020). Given the high reactor temperatures, high CO_2 selectivities may also be partially due to an increase in the Boudouard reaction, causing deactivation by carbon deposition. However, the amount of carbon deactivated may possibly plateau and quickly decrease with time-on-stream since carbon formed on the catalyst is likely to be hydrogenated to $-CH_2-$ species (Dry, 2004), especially as high WGS activity increases the availability of H_2.

Apart from the unsteady-state period after startup, other instances of carbon deposition were suspected. It has been stated within the experimental methodology and results chapters (3.3 and 4.4) that when the synthesis gas flowrate was decreased, H_2 was typically decreased first. This may have led to a momentary decrease in the H_2/CO ratio that the catalyst was exposed to. It is thought that this interruption of the reaction environment may have caused changes to the catalyst structure. In instances where this effect is thought to have been significant, little to no increase in CO conversion was observed when decreasing the space velocity. A study by Moodley (2008) revealed that very low H_2/CO ratios may lead to the formation unreactive carbon species on the catalyst surface. Low H_2 partial pressures cause oxygen to be removed from the catalyst surface, creating vacancies for CO dissociation. However, dissociated CO is not sufficiently removed by hydrogenation due to the low quantities of H_2. The overall consequence is reduced catalyst activity and poor product selectivity. Even when the H_2/CO ratio was returned to normal, the supply rate of H_2 may have remained greater than the rate of CO dissociation due to decreased number of available sites. This may have led to increased preference for hydrogenation than chain propagation (Moodley *et al.*, 2009). This was also evidenced by uncharacteristically high CH_4 selectivities and low C_{5+} selectivities. Unfortunately, the presence of hydrocarbon products on the spent catalyst surface makes it difficult to distinguish between unreactive carbon species on the surface and reactor products. Nonetheless, some evidence points to the formation of hard to remove carbon species on the catalyst surface being a relevant deactivation mechanism over the Co-Pt/Al_2O_3 catalyst with increasing time on stream (Moodley *et al.*, 2009).

Although deactivation in Fischer-Tropsch synthesis is inherent (Van Steen & Claeys, 2008), it still is an important consideration in the context of this study as the cost and life-span of the catalyst used for small-scale Fischer-Tropsch synthesis will ultimately determine economic feasibility. Since the catalyst deactivation thought to have occurred is linked to high reactor temperatures, preventing temperature runaway might be an important way of mitigating severe catalyst deactivation.

Although structured reactor packings have been said to offer enhanced heat transfer properties (Pangarkar *et al.*, 2008), it was observed that insufficient temperature control remained a major drawback for the structured packings tested in this study. However, this temperature increase may not be so unprecedented as Merino *et al.* (2017) observed exothermic temperature increase up to 300°C during LT-FTS over a FeCralloy® monolith washcoated with 20%Co-0.5%Re/Al_2O_3 catalyst and concomitant CO conversion of 100%. This thermal runaway was attributed to high catalyst loading since similar catalyst loaded with less catalyst did not exhibit high exothermic temperature increase (Merino *et al.*, 2017).

It is thought that the inert substrate can act as a heat sink, conducting heat away from the catalyst (Fratalocchi *et al.*, 2018). Thus, a link can also be made between the amount of catalyst coated on the substrate surface relative to the mass of the structured substrate. Table 5-2 also shows the amount of catalyst loaded as a fraction of the total catalyst bed mass, which included inert solid material, that is the mass of the 300 µm SiC particles for the catalyst powder and the pellets, the mass of the cordierite monolith substrate for HcM 1 and HcM 2, and the mass of the SiC foam substrate for OcF 1, OcF 2 and OcF 3. Of the catalyst tested in this study, the two catalysts for which no exothermic temperature increase was observed had the lowest amount of catalyst loaded as a fraction of the total catalyst bed mass, that is, 11 wt.% for the powder and 15 wt.% for OcF 1.

Since the catalyst bed was located in an externally heated and insulated isothermal zone with no means of heat removal through the reactor wall, the supposed radial heat removal benefits of the structured catalysts could not be realised.

5.3. Mass transfer considerations

An important justification for using structured reactor packings for intensification of LT-FTS has been the claim that they offer enhanced heat and mass transport properties when compared to catalyst pellets typically used in fixed bed reactors (Hilmen *et al.*, 2001; Hooshyar *et al.*, 2012; Pangarkar *et al.*, 2008), which can potentially increase reactor productivity. However, the results of this study did not reveal superior reactor productivity when structured catalysts were used. This may imply that the transport properties of the structured packings may not have been as enhanced as anticipated. Thus, the heat and mass transfer properties of the catalyst packings was characterised using known correlations in Appendix B to D.

Internal mass transfer limitations are a function of the particle diameter or catalyst layer thickness in the case of the structured packings, pore dimensions, and fluid properties. While external transport limitations are affected by gas flowrates, catalyst bed geometry and fluid properties.

Since the catalyst powder behaved most ideally for all the catalyst tested, it is believed that it did not suffer from heat and mass transfer limitations. To confirm this, the extent of internal mass transfer resistance in the catalyst powder was estimated using the Weisz modulus (Φ) and effectiveness factor (η). However, it is emphasized that the correlations used here do not account for other concurrent transport resistances or deactivation. The Weisz modulus found to be less than 0.08 at all space velocities, and since the value of Φ was small ($6.6 – 2.7 \cdot 10^{-4}$) for the powder, η can be assumed to be 1 (Froment, 2011). Thus, the Weisz-Prater criterion can be satisfied and internal mass transport limitations can be assumed to be negligible (Froment, 2011). It was also necessary to establish whether external mass transfer limitations were significant. Thus, the Carberry number (Ca) was calculated and shown to be less than 0.05 at all space velocities, which confirmed that external mass limitations can be ignored.

With regards to the structured catalyst packings, it is believed that external mass transfer resistance still played a significant role in the performance. It is speculated that an interfacial layer may have developed due to liquid/wax products formed during Fischer-Tropsch synthesis. In fact, when the catalysts were unloaded, the catalysts appeared to be covered by a thin layer of wax. Since the diffusion through a liquid film can be three to five times lower than diffusion through a gaseous medium (Hilmen *et al.*, 2001; Liu *et al.*, 2009), the slow diffusion rate of reactants and products through this liquid film would results in a reduced reaction rate and lower overall reactor efficiency. Furthermore, the enrichment of H_2 with

increasing depth within the catalyst layer would have resulted in increased preference for hydrogenation reactions, leading to lower chain growth probability.

Furthermore, the flow profile in liquid film is likely to be laminar due to the flat surface of the square channel walls, resulting in relatively poor mixing. On the other hand, while the tortuous structure of the foam was thought to greatly improve external mass transfer performance due to constant disturbance of the interfacial layer (Richardson *et al.*, 2003), it is more likely that the flow pattern is still laminar at the reactor conditions used in this study. This is supported by Seguin *et al.* (1998), who reported that flow profile in foam packings is more laminar than in packed bed reactors. Hall & Hiatt (1996) studied pore scale turbulence in ceramic foams with pore diameters between 0.85 mm and 2.5 mm and reported that the flow profile of 30 PPI ceramic foams was laminar in a range of pore Reynolds numbers between 20 and 200.

The mass transfer coefficients (k_m) of the powder, monolith and foam were estimated using correlations for Sherwood number (Sh), Schmidt number (Sc) and Reynold's number. The k_m values obtained are plotted as a function of superficial linear velocity in Figure 5-3. Details of the calculations can be found in Appendices B, C and D. The results indicate that the mass transfer coefficients of foams lie between those of powders and monoliths (i.e., powder ≫ foams ≫ monoliths. This trend is in agreement with that reported by Patcas *et al.* (2007).

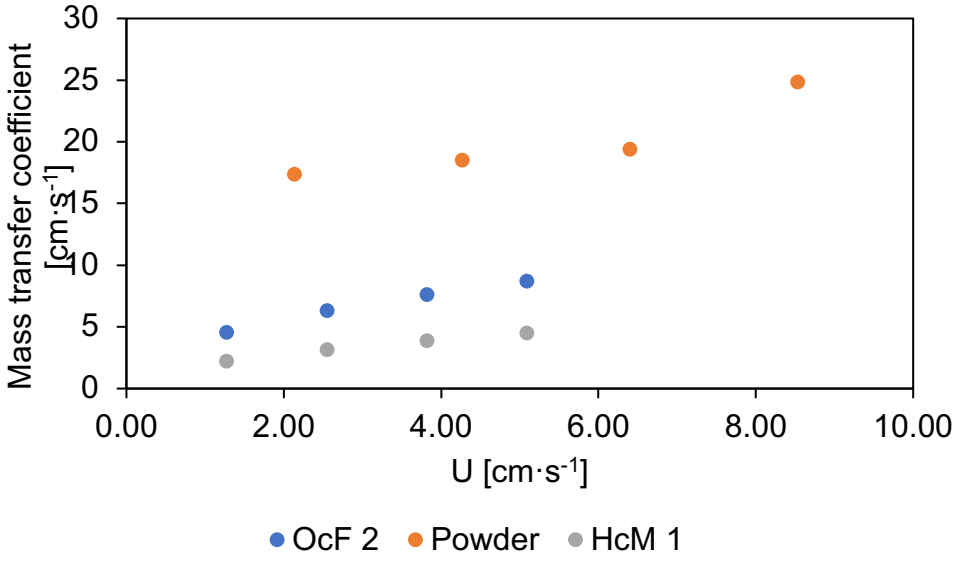

Figure 5-3: Mass transfer coefficients of foams loaded with ca 0.5 g Co-Pt/Al_2O_3

5.3.1. Effect of catalyst layer thickness

The amount of catalyst was coated on the foams and monoliths was varied to show the effect of catalyst layer thickness on internal mass transfer, conversion and product distributions.

5.3.1. (A) **Honeycomb monoliths**

As can be seen from Table 5-3, it appears that a lower catalyst layer thickness results in increased catalyst activity. HcM 2, which has an average catalyst layer thickness of ca. 22 µm, appears to be more than 275% more active than HcM 1, which has about double the catalyst layer thickness. In addition, the CH_4 and C_{5+} selectivities are improved with decreasing catalyst layer thickness. This suggests the presence of internal mass transfer limitations. It is noted that increasing the catalyst layer thickness may also reduce the pore size, which would change the linear gas velocity and result in increased external mass transfer resistance. Thus, both resistances may be responsible for the observed results.

Table 5-3: Performance of honeycomb monoliths at different catalyst layer thickness

	HcM 1		HcM 2	
Catalyst layer thickness [µm]	45		22	
Space velocity [$mmol_{CO} \cdot s^{-1} \cdot g^{-1}_{Cat}$]	0.11	0.055	0.11	0.055
Average X_{CO}	9.8%	16%	27%	46%
CH_4 selectivity	23%	25%	25%	19%
CO_2 selectivity	0%	0%	0.72%	1.1%
C_2-C_4 selectivity	27%	15%	19%	11%
C_{5+} selectivity	50%	51%	55%	70%

5.3.1. (B) **Open-cell Foams**

The same analysis was performed over the washcoated foams. A comparison of the catalytic performance of the foams at different washcoat layer thicknesses is presented in Table 5-4.
It appears that decreasing the catalyst layer thickness has a varied effect on CO conversion. At the higher space velocity (0.12 $mmol_{CO} \cdot s^{-1} \cdot g^{-1}_{Cat}$), the CO conversion decreased with a decrease in catalyst layer thickness while the opposite is observed at the lower space velocity (0.058 $mmol_{CO} \cdot s^{-1} \cdot g^{-1}_{Cat}$). However, it can be seen that for the lower catalyst layer thickness, small gains in CO conversion led to dramatic increase in C_{5+} selectivity. This dramatic

difference may be an artefact of catalyst deactivation in the case of the thicker catalyst (OcF 2). On the other hand, OcF 1 greatly outperformed OcF 3 at similar space velocities even despite having similar catalyst loadings/thicknesses. However, it is noted that no exothermic temperature increase was observed for OcF 1, which implies that any thermally activated deactivation may have been avoided. Although further repetition is required to confirm this, it appears that a washcoat loading of 15% may result in the absence of exothermic temperature increase, and this, prevent deactivation.

Thus, it can be argued that decreasing the catalyst layer thickness improves catalyst performance. Firstly, a decreased catalyst layer thickness may lead to increased internal heat and mass transfer rates, allowing better CO conversion, reduced production of light gases and higher selectivity towards liquid products. Secondly, lower catalyst layer thicknesses decrease the exothermic temperature increase as shown in chapter 5.2, which may then prevent catalyst deactivation.

Note that the catalyst layer thicknesses observed over the foam varied widely. Thus, it is likely that each foam was likely characterised by regions experiencing different extents of internal and external transport properties. Furthermore, since the observed catalyst layer thicknesses were vastly different from those estimated by assuming a uniform washcoat layer, no valid arguments can be made about a maximum catalyst layer thickness at which internal mass transfer limitations can be said to be negligible.

Table 5-4: Performance of washcoated SiC foams at different catalyst layer thicknesses

	OcF 2		OcF 3		OcF 1	OcF 3
Catalyst mass [g]	0.47		0.24		0.18	0.24
Estimated catalyst layer thickness [µm]	54		28		21	28
Space velocity [$mmol_{CO} \cdot s^{-1} \cdot g^{-1}_{Cat}$]	0.12	0.059	0.12	0.058	0.23	0.23
Average X_{CO}	11%	18%	11%	24%	13%	6%
CH_4 selectivity	26%	32%	20%	16%	11%	26%
CO_2 selectivity	0%	0%	0.0%	0.4%	0%	0.2%
C_2-C_4 selectivity	22%	30%	16%	14%	8%	22%
C_{5+} selectivity	51%	38%	64%	70%	81%	52%

5.4. Hydrodynamics

5.4.1. Pressure drop

Since one of the primary motivations for structured packings is the potential for a dramatic reduction in pressure drop when compared to conventional packed beds, pressure drop along the particle, monolith and foam packed beds was estimated. The estimated pressure drops are shown in Figure 5-4. The Ergun equation was used to estimate pressure drops along the particle packed catalyst bed, while the Darcy correlation was used for monoliths and the Forscheimer equation was used to estimate pressure drop for the open cell foams. Calculations can be found in the appendix section for each type packing.

The pressure drop in the particle packed catalyst bed was calculated using the diameter of the 300 μm SiC particles used to dilute the catalyst bed, as these take up a majority of the catalyst bed volume. The pressure drop over the monolith and foam bed was calculated using the hydraulic diameter of the uncoated substrates because the washcoat layer thickness is 10^4 magnitudes lower than the size of the monolith channels and the foam cells and does not cause a significant decrease in channel/pore size. It can be seen that the pressure drop along the particle packed catalyst bed is much higher than that in the structured packings. The pressure drop in the foam is slightly higher than that of the monolith due to the irregular surface of the foam and larger bed porosity in the monolith.

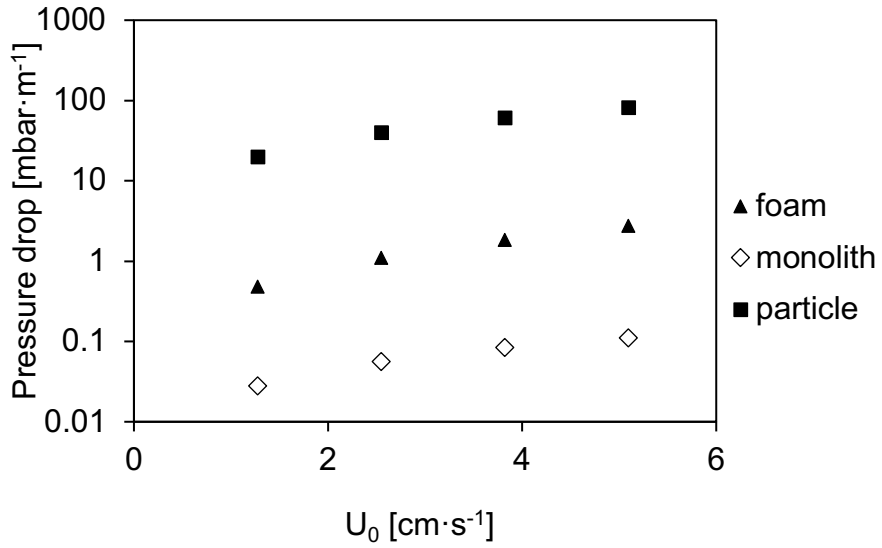

Figure 5-4: Pressure drop estimates for a catalyst bed comprising of catalyst particles, catalyst coated on 30 PPI SiC foam and catalyst coated on 230 CPSI cordierite monolith

6. Conclusions and recommendations

Fischer-Tropsch synthesis is a process for converting synthesis gas to a wide range of hydrocarbon products. Small-scale Fischer-Tropsch synthesis (LT-FTS) may go a long way in helping economies meet rising fuel demand and to tap locally available fuel sources such as biomass waste and stranded gas. However, because of the high cost associated with synthesis gas generation, significant improvements in LT-FTS reactor performance must be realised for small-scale Fischer-Tropsch synthesis to be economically viable. This includes increasing single-pass conversion and improving product selectivity. Reactor structuring has been proposed as a means of intensifying reactor performance (Pangarkar *et al.*, 2008; Almeida *et al.*, 2011; Hooshyar *et al.*, 2012; Delparish & Avci, 2016; Fratalocchi *et al.*, 2018). Thus, the aim of this study was to compare the performance of different catalyst packings, namely, catalyst powder, pellets, square channel honeycomb monoliths cordierite and open-cell SiC foams in low-temperature Fischer-Tropsch.

The different catalyst packings were tested with a 22wt.%Co-0.05wt.%/Al_2O_3 catalyst. The catalyst was prepared using vacuum evaporation as specified by van Berge et al. (2005). A portion of the catalyst was wet-milled to an average particle size (d_{50}) of 3.15 µm. Cylindrical pellets with a diameter and height of 5 mm and an average mass of 0.14 g were formed by placing the dense slurry of the wet-milled catalyst in a mould and drying it for ~12 hours at 120°C. Monoliths and foams were washcoated by dipping them in a slurry containing 30 wt.% wet-milled catalyst, water and HNO_3 as a dispersing agent. The mass of catalyst coated on the foams and monoliths was varied to compare the effect of catalyst layer thickness on catalyst performance, i.e., to test the impact of internal heat and mass transfer limitations. Homogenous washcoating was achieved over the monoliths, as SEM imaging indicated a uniform catalyst layer thickness. On the other hand, the washcoat over the foams showed a large variation in washcoat layer thickness, with the measured thicknesses differing widely to that estimated based on geometric surface area. However, washcoat adherence on both the foams and monoliths was promising, being at least 93% and increasing with a decrease in the mass of the washcoat.

Fischer-Tropsch catalyst performance tests were carried out at 220°C and 20 bar over the catalyst powder, pellets, monoliths and foams. The space velocity was varied to determine the effect of gas flowrate on transport properties, and ultimately, catalyst performance. The performance of the different catalyst packings was compared in terms of the CO conversion achieved, product selectivities and inferences on their heat and mass transfer properties.

The catalyst powder behaved predictably and showed high CO conversion compared to the structured catalyst packings, as well as the highest C_{5+} selectivities among all the catalyst packings at similar catalyst loadings. It is believed that catalyst deactivation, likely via oxidation as well as carbon deposition may have negatively affected catalyst activity. Evidence of this was that when the space velocity was decreased from 0.11 to 0.083 $mmol_{CO} \cdot s^{-1} \cdot g^{-1}_{Cat}$, CO conversion remained virtually unchanged at ca. 42 ± 0.5% while C_{5+} selectivity decreased from 72 C-% to 65 C-%.

The performance of the pellets indicated severe heat and mass transfer resistance, with poor temperature control, as expected. After reactor startup, the temperature measured ca. 5 mm above the catalyst bed rose from 200°C to 250°C within minutes. It is thought that even after the recorded temperature cooled to the operating temperature of 220°C, the internal temperature of the catalyst remained high, causing it to maintain high reaction rates: CO conversion ranged from 77 ± 3% to 56 ± 3% for space velocities of 0.14 to 0.028 $mmol_{CO} \cdot s^{-1} \cdot g^{-1}_{Cat}$. Furthermore, CO conversion decrease, instead of increasing, with decreasing space velocity, this is characteristic of reactions controlled by severe external mass transfer resistance. This was possible because the internal temperature of the pellet likely exceeded the surrounding bulk gas temperature to the point where the surface reaction was fast enough for external mass transfer to become rate limiting (Levenspiel, 1993). The high internal temperature of the pellet also led to high CH_4 and CO_2 selectivities, and low C_{5+} production, making the pellet unsuitable for small-scale Fischer-Tropsch synthesis unless small pellet diameters are used. However, high pressure drop resulting from small pellet diameters will drastically increase gas compression costs.

The structured catalyst packings performance was disappointing: they showed CO conversion about 40% lower than that of the catalyst powder. The structured catalyst packings also failed to regulate reactor temperature at the operating temperature of 220°C. Instead, temperatures after startup reached 250°C. At these elevated temperatures, CO conversion was excessively high, starting at 100%, and the main carbon containing products were CO_2 and CH_4. However, the structured packings showed better transport properties than the pellet once the catalyst cooled down, as CO conversion dropped and increased with decreasing space velocities, as expected for first order reactions in a fixed bed reactor. The performance of the foams was similar to that of the monoliths in terms of CO conversion and product distribution, contrary to assertions that the tortuous flow channels of foams would result in improved external mass transfer limitations, and consequently, better catalyst performance. It is likely that the flow pattern under the reaction conditions and the pore density of the foams (30 PPI) used in this study may have still been laminar, resulting in poor external mass transfer rates.

More importantly, the exposure to high temperatures and high CO conversion is likely to have facilitated catalyst deactivation via sintering and oxidation of Co to CoO. This is evidenced by high CO_2 production observed over the pellet at all space velocities tested, and the structured catalysts during their high temperature operation after startup, as this signals increased water-gas shift activity for cobalt-based Fischer-Tropsch catalysts. Deactivation by oxidation occurs due to high water partial pressure, resulting from high CO conversion (Moodley *et al.*, 2009; Ma *et al.*, 2011; Bukur *et al.*, 2012).

Furthermore, it was shown that a decrease in catalyst layer thickness resulted in better catalyst performance in terms of CO conversion and product selectivity, this result was more pronounced in the monoliths than in the foams due to more uniform catalyst layer thickness. For the foams, OcF 1, which has the catalyst lowest loading (0.18 g of catalyst), experienced no exothermic temperature increase after startup. These results are similar to those presented by Hilmen *et al.* (2001)., Kapteijn *et al.* (2005) and Merino et al. (2017); but contrary to those studies, it was seen that internal mass transfer limitations affected catalyst performance at catalyst layer thicknesses below 50 µm. The results of this study revealed that the foams and monoliths tested in this study do not intensify reactor performance.

It is important to acknowledge that the poor temperature control presents a major limitation and calls in to question the reliability of the results from this study, as well as the conclusions that can be drawn from it. It may be beneficial to determine the optimal temperature that will help prevent temperature runaway, for example, by starting the reaction at a temperature as low as 175°C, and gradually ramping it up over an extended period of time (e.g., hours or days). Alternatively, diluting the syngas at startup, e.g., with argon gas, and gradually increasing partial pressure of the reactants may also help to prevent temperature runaway.

Also important are the channel or pore dimensions required to achieve desired enhancement in performance. In this study, the catalyst layer thickness was varied by changing the mass of catalyst loaded on the foams. However, it may be beneficial to compare catalyst layer thicknesses while keeping the volumetric catalyst loading the same by using substrates with higher geometric surface areas (i.e., changing pore count). It is also possible that the washcoating procedure in itself prevents optimisation of the diffusion distance. In this study, the same batch of catalyst was used to test the catalyst powder as well as washcoat the monoliths and the foams to ensure that differences in catalytic performance could be attributed to the packings' structure rather than variances during catalyst preparation. However, it may

be possible to reduce the effect of internal mass transfer limitations by first coating the secondary support (Al_2O_3) on the catalyst surface and then depositing the metal components on the coated substrate, thus ensuring that the active metal concentration is higher near the bulk gas than it is near the substrate surface. Bakhtiari *et al.* (2008) showed better catalytic performance when monolith coated with alumina and then impregnated with Co. Higher pore densities may be required in foams to achieve a level of turbulence required to eliminate external mass transfer limitations. Although this may result in reduced porosity of the foams, the pressure drop may still be significantly lower than what is typically observed in conventional fixed-bed reactors. Additionally, the smaller pore diameters might make it more difficult to washcoat the catalyst without pore blockages. The cross-sectional area available for flow was greater for the structured packings and the pellets than it was for the catalyst powder due to the difference in the positioning of thermowell with respect to the catalyst bed. The consequence is that the linear gas velocity was higher for the catalyst powder. This may account for the difference in the extent of external mass transfer limitations for the catalyst powder and the structured packings and monoliths. Thus, testing all catalysts under similar linear gas velocities may make the results more comparable.

Although it is acknowledged that the results obtained in this work may still be improved by choosing more advantageous geometric features in monoliths and foams, trying different catalyst preparation methods, improving reactor packing to allow better heat transfer, the results of this study imply that a switch in reactor packing technology to the structured packings considered in this study may not help realise wide-spread commercialisation of small-scale Fischer-Tropsch synthesis as envisioned.

Reference List

Adesina, A.A. 1996. Hydrocarbon synthesis via Fischer-Tropsch reaction: travails and triumphs. *Applied Catalysis A, General.* 138(2):345-367.

Agrafiotis, C. & Tsetsekou, A. 2000. The effect of processing parameters on the properties of γ-alumina washcoats deposited on ceramic honeycombs. *Journal of Materials Science.* 35(4):951-960.

Almeida, L.C., Echave, F.J., Sanz, O., Centeno, M.A., Arzamendi, G., Gandía, L.M., Sousa-Aguiar, E.F., Odriozola, J.A. & Montes, M. 2011. Fischer–Tropsch synthesis in microchannels. *Chemical Engineering Journal.* 167(2):536-544.

Argyle, M.D., Frost, T.S. & Bartholomew, C.H. 2014. Cobalt Fischer–Tropsch catalyst deactivation modeled using generalized power law expressions. *Topics in Catalysis.* 57(6):415-429.

Bakhtiari, M., Khorasheh, F., Zamanian, A., Nakhaeuipour, A. Irani, M. 2008. Preparation, evaluaton and characterization of monolithic catalysts for Fischer-Tropsch synthesis. *Petroleum & Coal*. 50(2):56-61.

Bartholomew, C.H. 2001. Mechanisms of catalyst deactivation. *Applied Catalysis A: General.* 212(1):17-60.

Bercic, G. & Pintar, A. 1997. The role of gas bubbles and liquid slug lengths on mass transport in the Taylor flow through capillaries. *Chemical Engineering Science.* 52(21-22):3709-3719.

Binner, J. 2005. Ceramic foams. In *Cellular ceramics: structure, manufacturing, properties and applications.* P. Colombo and M. Scheffler, Eds. Weinheim: Wiley-VCH.p. 33-56.

Biquiza, L.D., Claeys, M. & van Steen, E. 2010. Thermodynamic and experimental aspects of 'supercritical' Fischer–Tropsch synthesis. *Fuel Processing Technology.* 91(10):1250-1255.

Blachou, V., Goula, D. & Philippopoulos, C. 1992. Wet milling of alumina and preparation of slurries for monolithic structures impregnation. *Industrial & Engineering Chemistry Research.* 31(1):364-369.

Botes, F.G. 2009. Influences of water and syngas partial pressure on the kinetics of a commercial alumina-supported cobalt Fischer-Tropsch catalyst. *Industrial and Engineering Chemistry Research.* 48(4):1859-1865.

Botes, F.G., van Dyk, B. & McGregor, C. 2009. The development of a macro kinetic model for a commercial $Co/Pt/Al_2O_3$ Fischer−Tropsch catalyst. *Industrial & Engineering Chemistry Research.* 48(23):10439-10447.

BP. 2018. *BP Energy Outlook.*

Breitkopf, C. 2008. *Diffusion in porous media.* TU Bergakademie Freiberg.

Bukur, D., Pan, Z., Ma, W., Jacobs, G. & Davis, B. 2012. Effect of CO conversion on the product distribution of a Co/Al_2O_3 Fischer–Tropsch synthesis catalyst using a fixed bed reactor. *Catalysis Letters.* 142(11):1382-1387.

Callesen, I., Keck, H. & Andersen, T.J. 2018. Particle size distribution in soils and marine sediments by laser diffraction using Malvern Mastersizer 2000—method uncertainty including the effect of hydrogen peroxide pretreatment. *Journal of Soils and Sediments.* 18(7):2500-2510.

Chu, W., Chernavskii, P.A., Gengembre, L., Pankina, G.A., Fongarland, P. & Khodakov, A.Y. 2007. Cobalt species in promoted cobalt alumina-supported Fischer–Tropsch catalysts. *Journal of Catalysis.* 252(2):215-230.

Ciambelli, P., Palma, V. & Palo, E. 2010. Comparison of ceramic honeycomb monolith and foam as Ni catalyst carrier for methane autothermal reforming. *Catalysis Today.* 155(1-2):92-100.

Claeys, M. & Van Steen, E. 2004. Basic studies. In *Fischer-Tropsch Technology.* A. Steynberg and M. Dry, Eds. Elsevier. *Studies in Surface Science and Catalysts*. 152: 601-680.

Claeys, M. & van Steen, E. 2005. *Die Fischer-Tropsch Synthese.* In *Winnacker-Küchler Chemische Technik: Prozesse und Produkte*, 5th ed. R. Dittmeyer, W. Keim, G. Kreysa, A. Oberholz, Eds. Vol. 4: „Energieträger, organische Grundstoffe“, Wiley-VCH Verlag, Weinheim, p. 823-845.

Claeys, M., Dry, M.E., van Steen, E., van Berge, P.J., Booyens, S., Crous, R., van Helden, P., Labuschagne, J., Moodley, D.J. & Saib, A.M. 2015. Impact of process conditions on the sintering behavior of an alumina-supported cobalt Fischer-Tropsch catalyst studied with an in situ magnetometer. *ACS Catalysis.* 5(2):841-852.

Das, T., Conner, W., Li, J., Jacobs, G., Dry, M.E. & Davis, B. 2005. Fischer-Tropsch synthesis: Kinetics and effect of water for a CO/SiO_2 catalyst. *Energy & Fuels.* 19(4):1430-1439.

Delparish, A. & Avci, A.K. 2016. Intensified catalytic reactors for Fischer-Tropsch synthesis and for reforming of renewable fuels to hydrogen and synthesis gas. *Fuel Processing Technology.* 151:72-100.

Department of Energy, T.S.A. 2018. *South African yearbook 2017/2018: Energy.* South Africa.

Dry, M.E. 1982. Catalytic aspects of industrial Fischer-Tropsch synthesis. *Journal of Molecular Catalysis.* 17(2):133-144.

Dry, M.E. 2002a. High quality diesel via the Fischer–Tropsch process – a review. *Journal of Chemical Technology & Biotechnology.* 77(1):43-50.

Dry, M.E. 2002b. The Fischer–Tropsch process: 1950–2000. *Catalysis Today.* 71(3):227-241.

Dry, M. 2004. Chemical concepts for used for engineering processes. In *Fischer-Tropsch Technology.* A. Steynberg and M. Dry, Eds. Elsevier. *Studies in Surface Science and Catalysts*. 152: 196-258.

Feller, A., Claeys, M. & van Steen, E 1999. Cobalt cluster effects in zirconium promoted Co/SiO_2 Fischer–Tropsch catalysts. *Journal of Catalysis.* 185(1):120-130.

Fletcher, J.V. 2009. *The effect of temperature on the Fischer-Tropsch selectivity and further mechanistic insights.* MSc-dissertation. University of Cape Town.

Fogler, H.S. 2016. *Elements of chemical reaction engineering.* Fifth edition. Boston: Prentice Hall

Förtsch, D., Pabst, K. & Groß-Hardt, E. 2015. The product distribution in Fischer–Tropsch synthesis: An extension of the ASF model to describe common deviations. *Chemical Engineering Science.* 138:333-346.

Fratalocchi, L., Visconti, C.G., Groppi, G., Lietti, L. & Tronconi, E. 2018. Intensifying heat transfer in Fischer-Tropsch tubular reactors through the adoption of conductive packed foams. *Chemical Engineering Journal.* 349:829-837.

Froment, G.F. 2011. *Chemical reactor analysis and design.* 3rd ed. Hoboken, N.J: Wiley

Frötsch, D., Pabst, K., Groβ-Hardt, E. 2015. The product distribution in Fischer-Tropsch synthesis: An extension of the ASF model to describe common deviations. Chemical Engineering Science. 138:333-348.

Fuller, E.N., Schettler, P.D. & Giddings, J.C. 1966. A new method for prediction of binary gas-phase diffusion coefficients. *Industrial and Engineering Chemistry.* 58(5):18-27.

Giani, L., Cristiani, C., Groppi, G. & Tronconi, E. 2006. Washcoating method for Pd/γ-Al_2O_3 deposition on metallic foams. *Applied Catalysis B: Environmental.* 62(1):121-131.

González-Velasco, J.R., Gutiérrez-Ortiz, M.A., Marc, J.L., Botas, J.A., González-Marcos, M.P. & Blanchard, G. 2003. Pt/$Ce_{0.68}Zr_{0.32}O_2$ Washcoated monoliths for automotive emission control. *Industrial & Engineering Chemistry Research.* 42(2):311-317.

Grobler, T., Claeys, M., van Steen, E. & Janse van Vuuren, M.J. 2009. GC×GC: A novel technique for investigating selectivity in the Fischer–Tropsch synthesis. *Catalysis Communications.* 10(13):1674-1680.

Groppi, G., Giani, L. & Tronconi, E. 2007. Generalized correlation for gas/solid mass-transfer coefficients in metallic and ceramic foams. *Industrial and Engineering Chemistry Research.* 46(12):3955-3958.

Guettel, R. & Turek, T. 2009. Comparison of different reactor types for low temperature Fischer–Tropsch synthesis: A simulation study. *Chemical Engineering Science.* 64(5):955-964.

Guettel, R., Kunz, U. & Turek, T. 2008. Reactors for Fischer-Tropsch synthesis. *Chemical Engineering & Technology.* 31(5):746-754.

Hall, M. & Hiatt, J. 1996. Measurements of pore scale flows within and exiting ceramic foams. *Experiments in Fluids.* 20(6):433-440.

Heibel, A.K., Vergeldt, F.J., Van As, H., Kapteijn, F., Moulijn, J. & Boger, T. 2003. Gas and liquid distribution in the monolith film flow reactor. *AIChE Journal.* 49(12):3007-3017.

Heiszwolf, J., Kreutzer, M., van Den Eijnden, M.G., Kapteijn, F. & Moulijn, J. 2001. Gas-liquid mass transfer of aqueous Taylor flow in monoliths. *Catalysis Today.* 69(1-4):51-55.

Hilmen, A.M., Bergene, E., Lindvåg, O.A., Schanke, D., Eri, S. & Holmen, A. 2001. Fischer–Tropsch synthesis on monolithic catalysts of different materials. *Catalysis Today.* 69(1):227-232.

Hilmen, A.M., Bergene, E., Lindvåg, O.A., Schanke, D., Eri, S. & Holmen, A. 2005. Fischer–Tropsch synthesis on monolithic catalysts with oil circulation. *Catalysis Today.* 105(3):357-361.

Hooshyar, N., Vervloet, D., Kapteijn, F., Hamersma, P.J., Mudde, R.F. & van Ommen, J.R. 2012. Intensifying the Fischer–Tropsch Synthesis by reactor structuring – A model study. *Chemical Engineering Journal.* 207-208:865-870.

Iglesia, E. 1997. Design, synthesis, and use of cobalt-based Fischer-Tropsch synthesis catalysts. *Applied Catalysis A: General.* 161(1):59-78.

Iglesia, E., Reyes, S.C. & Madon, R.J. 1991. Transport-enhanced α-olefin readsorption pathways in Ru-catalyzed hydrocarbon synthesis. *Journal of Catalysis.* 129(1):238-256.

Ilsen Önsan, Z. & Avci, A.K. 2011. Reactor design for fuel processing. In *Fuel cells: Technologies for fuel processing.* D. Shekhawat, J.J. Spivey and D.A. Berry, Eds.: Elsevier. 451-516.

Incera Garrido, G., Patcas, F.C., Lang, S. & Kraushaar-Czarnetzki, B. 2008. Mass transfer and pressure drop in ceramic foams: A description for different pore sizes and porosities. *Chemical Engineering Science.* 63(21):5202-5217.

Jacobs, G., Ma, W. & Davis, B. 2014. Influence of reduction promoters on stability of cobalt/γ-alumina Fischer-Tropsch synthesis catalysts. *Catalysts.* 4(1):49-76.

Jess, A. & Kern, C. 2012. Influence of particle size and single-tube diameter on thermal behavior of Fischer-Tropsch reactors. Part II. Eggshell catalysts and optimal reactor performance. *Chemical Engineering & Technology.* 35(2):379-386.

Kapteijn, F., de Deugd, R.M. & Moulijn, J.A. 2005. Fischer–Tropsch synthesis using monolithic catalysts. *Catalysis Today.* 105(3):350-356.

Khodakov, A.Y., Griboval-Constant, A., Bechara, R. & Zholobenko, V.L. 2002. Pore size effects in Fischer Tropsch synthesis over cobalt-supported mesoporous silicas. *Journal of Catalysis.* 206(2):230-241.

Kreutzer, M.T., Du, P., Heiszwolf, J.J., Kapteijn, F. & Moulijn, J.A. 2001. Mass transfer characteristics of three-phase monolith reactors. *Chemical Engineering Science.* 56(21):6015-6023.

Kuipers, E.W., Vinkenburg, I.H. & Oosterbeek, H. 1995. Chain length dependence of α-olefin readsorption in Fischer-Tropsch synthesis. *Journal of Catalysis.* 152(1):137-146.

Lacroix, M., Dreibine, L., de Tymowski, B., Vigneron, F., Edouard, D., Bégin, D., Nguyen, P., Pham, C., Savin-Poncet, S., Luck, F., Ledoux, M.-J. & Pham-Huu, C. 2011. Silicon carbide foam composite containing cobalt as a highly selective and re-usable Fischer–Tropsch synthesis catalyst. *Applied Catalysis A: General.* 397(1):62-72.

Lebens, P.J.M., Heiszwolf, J.J., Kapteijn, F., Sie, S.T. & Moulijn, J.A. 1999. Gas-liquid mass transfer in an internally finned monolith operated countercurrently in the film flow regime. *Chemical Engineering Science.* 54(21):5119-5125.

Levenspiel, O. 1993. *The Chemical Reactor Omnibook.* Corvallis, Or.: Distributed by OSU Book Stores

Liu, W., Hu, J. & Wang, Y. 2009. Fischer–Tropsch synthesis on ceramic monolith-structured catalysts. *Catalysis Today.* 140(3):142-148.

Liu, Y., Edouard, D., Nguyen, L.D., Begin, D., Nguyen, P., Pham, C. & Pham-Huu, C. 2013. High performance structured platelet milli-reactor filled with supported cobalt open cell SiC foam catalyst for the Fischer–Tropsch synthesis. *Chemical Engineering Journal.* 222:265-273.

LMNO-Engineering. 2013. *Gas Viscosity Calculator*. LMNO Engineering, Research, and Software, Ltd.: Athens, Ohio, USA Available: Gas Viscosity Calculator [2019].

Loffe-Institute. *Properties of Silicon Carbide (SiC)*. Available: http://www.ioffe.ru/SVA/NSM/Semicond/SiC/ [2019, 10 September].

Ma, W., Jacobs, G., Ji, Y., Bhatelia, T., Bukur, D.B., Khalid, S. & Davis, B.H. 2011. Fischer–Tropsch synthesis: Influence of CO conversion on selectivities, H_2/CO usage ratios, and catalyst stability for a Ru promoted Co/Al_2O_3 catalyst using a slurry phase reactor. *Topics in Catalysis.* 54(13):757.

Mears, D.E. 1971. Diagnostic criteria for heat transport limitations in fixed bed reactors. *Journal of Catalysis.* 20(2):127-131.

Merino, D., Sanz, O. & Montes, M. 2017. Effect of the thermal conductivity and catalyst layer thickness on the Fischer-Tropsch synthesis selectivity using structured catalysts. *Chemical Engineering Journal.* 327:1033-1042.

Mohajerani, S., Kumar, A. & Oni, A.O. 2018. A techno-economic assessment of gas-to-liquid and coal-to-liquid plants through the development of scale factors. *Energy.* 150:681-693.

Moodley, D.J. 2008. On the deactivation of cobalt-based Fischer-Tropsch synthesis catalysts. PhD thesis. Technische Universiteit Eindhoven.

Moodley, D.J., van de Loosdrecht, J., Saib, A.M., Overett, M.J., Datye, A.K. & Niemantsverdriet, J.W. 2009. Carbon deposition as a deactivation mechanism of cobalt-based Fischer–Tropsch synthesis catalysts under realistic conditions. *Applied Catalysis A: General.* 354(1):102-110.

Moodley, D., Claeys, M., van Steen, E., van Helden, P., Kistamurthy, D., Weststrate, K.-J., Niemantsverdriet, H., Saib, A., Erasmus, W. & van de Loosdrecht, J. 2020. Sintering of cobalt during FTS: Insights from industrial and model systems. *Catalysis Today.* 342:59-70.

Nabaho, D., Niemantsverdriet, J.W., Claeys, M. & van Steen, E. 2016. Hydrogen spillover in the Fischer–Tropsch synthesis: An analysis of platinum as a promoter for cobalt–alumina catalysts. *Catalysis Today.* 261:17-27.

N.N. A new world: The geopolitics of the energy transformation. IRENA - International renewable Energy Agency (2019) http://geopoliticsofrenewables.org/

assets/geopolitics/Reports/wp-content/uploads/2019/01/
Global_commission_renewable_energy_2019.pdf.

Nijhuis, T.A., Beers, A.E.W., Vergunst, T., Hoek, I., Kapteijn, F. & Moulijn, J.A. 2001. Preparation of monolithic catalysts. *Catalysis Reviews.* 43(4):345-380.

Önsan, Z.I. & Avci, A.K. 2016. Fixed-bed Reactors. In *Multiphase Catalytic Reactors - Theory, Design, Manufacturing, and Applications.* John Wiley & Sons.

Ou, X., Zhang, X., Lowe, T., Blanc, R., Rad, M.N., Wang, Y., Batail, N., Pham, C., Shokri, N., Garforth, A.A., Withers, P.J. & Fan, X. 2017. X-ray micro computed tomography characterization of cellular SiC foams for their applications in chemical engineering. *Materials Characterization.* 123:20-28.

Pangarkar, K., Schildhauer, T.J., van Ommen, J.R., Nijenhuis, J., Kapteijn, F. & Moulijn, J.A. 2008. Structured packings for multiphase catalytic reactors. *Industrial & Engineering Chemistry Research.* 47(10):3720-3751.

Park, J.C., Roh, N.S., Chun, D.H., Jung, H. & Yang, J., II. 2014. Cobalt catalyst coated metallic foam and heat-exchanger type reactor for Fischer–Tropsch synthesis. *Fuel Processing Technology.* 119:60-66.

Patcas, F.C., Garrido, G.I. & Kraushaar-Czarnetzki, B. 2007. CO oxidation over structured carriers: A comparison of ceramic foams, honeycombs and beads. *Chemical Engineering Science.* 62(15):3984-3990.

Polyanskiy, M.N. 2018. Refractive index database.

Post, M.F.M., Van' T Hoog, A.C., Minderhoud, J.K. & Sie, S.T. 1989. Diffusion limitations in Fischer-Tropsch catalysts. *AIChE Journal.* 35(7):1107-1114.

Richardson, J.T., Peng, Y. & Remue, D. 2000. Properties of ceramic foam catalyst supports: pressure drop. *Applied Catalysis A: General.* 204(1):19-32.

Richardson, J.T., Remue, D. & Hung, J.K. 2003. Properties of ceramic foam catalyst supports: mass and heat transfer. *Applied Catalysis A: General.* 250(2):319-329.

Rytter, E. & Holmen, A. 2015. Deactivation and regeneration of commercial type Fischer-Tropsch Co-catalysts — A mini review. *Catalysts.* 5(2):478-499.

Rytter, E. & Holmen, A. 2016. On the support in cobalt Fischer–Tropsch synthesis—Emphasis on alumina and aluminates. *Catalysis Today.* 275:11-19.

Rytter, E., Tsakoumis, N.E. & Holmen, A. 2016. On the selectivity to higher hydrocarbons in Co-based Fischer–Tropsch synthesis. *Catalysis Today.* 261:3-16.

Saib, A.M., Borgna, A., van de Loosdrecht, J., van Berge, P.J. & Niemantsverdriet, J.W. 2006. XANES study of the susceptibility of nano-sized cobalt crystallites to oxidation during realistic Fischer–Tropsch synthesis. *Applied Catalysis A: General.* 312:12-19.

Schulz, H. 1999. Short history and present trends of Fischer–Tropsch synthesis. *Applied Catalysis A: General.* 186(1):3-12.

Schulz, H., Steen, E. & Claeys, M. 1995. Specific inhibition as the kinetic principle of the Fischer-Tropsch synthesis. *Topics in Catalysis.* 2(1-4):223-234.

Schulz, H., Claeys, M. & Harms, S. 1997. Effect of water partial pressure on steady state Fischer-Tropsch activity and selectivity of a promoted cobalt catalyst. In *Natural Gas Conversion IV*. M. de Pontes, R.L. Espinoza, C.P. Nicolaides, J.H. Scholtz and M.S. Scurrell, Eds.: Elsevier. *Studies in Surface Science and Catalysis.* 107:193-200.

Seguin, D., Montillet, A., Comiti, J. & Huet, F. 1998. Experimental characterization of flow regimes in various porous media—II: Transition to turbulent regime. *Chemical Engineering Science.* 53(22):3897-3909.

Shafer, D.W., Gnanamani, K.M., Graham, M.U., Yang, J., Masuku, M.C., Jacobs, G. & Davis, H.B. 2019. Fischer–Tropsch: Product selectivity – the fingerprint of synthetic fuels. *Catalysts.* 9(3):259 - 315.

Stern, D., T. Bell, A. & Heinemann, H. 1983. Effects of mass transfer on the performance of slurry reactors used for Fischer-Tropsch synthesis. *Chemical Engineering Science.* 38(4):597-605.

Steynberg, A.P., Dry, M.E., Davis, B.H. & Breman, B.B. 2004. Fischer-Tropsch reactors. In *Fischer-Tropsch Technology.* A. Steynberg and M. Dry, Eds. Elsevier. *Studies in Surface Science and Catalysts*. 152: 64-196.

Sun, S., Tsubaki, N. & Fujimoto, K. 2000. The reaction performances and characterization of Fischer–Tropsch synthesis Co/SiO_2 catalysts prepared from mixed cobalt salts. *Applied Catalysis A, General.* 202(1):121-131.

Sweeting, T.B., Norris, D.A., Strom, L.A. & Morris, J.R. 1994. Reticulated ceramics for catalyst support applications. *MRS Online Proceedings Library Archive.* 368:309.

Tarì, G., Ferreira, J.M.F., Fonseca, A.T. & Lyckfeldt, O. 1998. Influence of particle size distribution on colloidal processing of alumina. *Journal of the European Ceramic Society.* 18(3):249-253.

Tijmensen, M.J.A., Faaij, A.P.C., Hamelinck, C.N. & van Hardeveld, M.R.M. 2002. Exploration of the possibilities for production of Fischer Tropsch liquids and power via biomass gasification. *Biomass and Bioenergy.* 23(2):129-152.

Tsakoumis, N.E., Rønning, M., Borg, Ø., Rytter, E. & Holmen, A. 2010. Deactivation of cobalt based Fischer–Tropsch catalysts: A review. *Catalysis Today.* 154(3):162-182.

Tucker, C.L. & van Steen, E. 2020. Activity and selectivity of a cobalt-based Fischer-Tropsch catalyst operating at high conversion for once-through biomass-to-liquid operation. *Catalysis Today.* 342:115-123.

Twigg, M.V. & Richardson, J.T. 2007. Fundamentals and applications of structured ceramic foam catalysts. *Industrial & Engineering Chemistry Research.* 46(12):4166-4177.

Valentini, M., Groppi, G., Cristiani, C., Levi, M., Tronconi, E. & Forzatti, P. 2001. The deposition of γ-Al_2O_3 layers on ceramic and metallic supports for the preparation of structured catalysts. *Catalysis Today.* 69(1):307-314.

Van Berge, P.J. & Everson, R.C. 1997. Cobalt as an alternative Fischer-Tropsch catalyst to iron for the production of middle distillates. In *Natural Gas Conversion IV*. M. de Pontes, R.L. Espinoza, C.P. Nicolaides, J.H. Scholtz and M.S. Scurrell, Eds.: Elsevier. *Studies in Surface Science and Catalysis.* 107:207-212.

Van Berge, P.J., van de Loosdrecht, J., Caricato, E.A., Barradas, S. & Sigwebela, B.H. 2002. *Impregnation process for catalysts.* US 6,455,462 B2 (assigned to Sasol Technology Ltd.).

Van der Laan, G.P. & Beenackers, A.A.C.M. 1999. Kinetics and Selectivity of the Fischer–Tropsch Synthesis: A Literature Review. *Catalysis Reviews.* 41(3-4):255-318.

Van Steen, E. & Schulz, H. 1999. Polymerisation kinetics of the Fischer–Tropsch CO hydrogenation using iron and cobalt based catalysts. *Applied Catalysis A, General.* 186(1):309-320.

Van Steen, E. & Claeys, M. 2008. Fischer-Tropsch catalysts for the Biomass-to-Liquid (BTL)-process. *Chemical Engineering & Technology.* 31(5):655-666.

Van Steen, E., Claeys, M., Möller, K.P. & Nabaho, D. 2018. Comparing a cobalt-based catalyst with iron-based catalysts for the Fischer-Tropsch XTL-process operating at high conversion. *Applied Catalysis A, General.* 549:51-59.

Van Steen, E., Claeys, M., Dry, M.E., van de Loosdrecht, J., Viljoen, E.L. & Visagie, J.L. 2005. Stability of nanocrystals: Thermodynamic analysis of oxidation and re-reduction of cobalt in water/hydrogen mixtures. *The Journal of Physical Chemistry B.* 109(8):3575-3577.

Visconti, C.G., Tronconi, E., Groppi, G., Lietti, L., Iovane, M., Rossini, S. & Zennaro, R. 2011. Monolithic catalysts with high thermal conductivity for the Fischer–Tropsch synthesis in tubular reactors. *Chemical Engineering Journal.* 171(3):1294-1307.

Wakao, N., Kaguei, S. & Funazkri, T. 1979. Effect of fluid dispersion coefficients on particle-to-fluid heat transfer coefficients in packed beds: Correlation of nusselt numbers. *Chemical Engineering Science.* 34(3):325-336.

Wallard, A., Sené, M., Craston, D., Williams, J. & Milton, M. 2017. *Kaye & Laby Table of Physical and Chemical Constants*. Available: http://www.kayelaby.npl.co.uk/general_physics/2_3/2_3_7.html [2018, 15 April 2018].

Wang, W.-J. & Chen, Y.-W. 1991. Influence of metal loading on the reducibility and hydrogenation activity of cobalt/alumina catalysts. *Applied Catalysis.* 77(2):223-233.

Wood, D.A., Nwaoha, C. & Towler, B.F. 2012. Gas-to-Liquids (GTL): A review of an industry offering several routes for monetizing natural gas. *Journal of Natural Gas Science and Engineering.* 9:196-208.

Yang, J.-I., Yang, J.H., Kim, H.-J., Jung, H., Chun, D.H. & Lee, H.-T. 2010a. Highly effective cobalt catalyst for wax production in Fischer–Tropsch synthesis. *Fuel.* 89(1):237-243.

Yang, J.H., Kim, H.-J., Chun, D.H., Lee, H.-T., Hong, J.-C., Jung, H. & Yang, J.-I. 2010b. Mass transfer limitations on fixed-bed reactor for Fischer–Tropsch synthesis. *Fuel Processing Technology.* 91(3):285-289.

Yates, I.C. & Satterfield, C.N. 1991. Intrinsic kinetics of the Fischer-Tropsch synthesis on a cobalt catalyst. *Energy and Fuels.* 5(1):168-173.

Appendix A: Reactor testing and product analysis

A.1. Reactor temperature profile

Table 0-1: Temperature profile measured over a bed of 300 µm SiC particles in Argon

Height above the reactor outlet	Thermowell imbedded in the catalyst bed	Thermowell above catalyst bed
70	213.8	-
80	216.6	-
90	219.9	-
100	220.5	-
110	220.6	-
120	220.4	-
130	219.8	-
140	219.0	-
145	-	214.5
150	213.0	213.0
160	208.6	206.7
170	202.5	202.0
180	196.0	195.0
190	119.0	119.1

A.2. Reactor leak testing

The reactor was leak tested after each reloading of the catalyst. This was done to ensure that the reactor could maintain pressure at 20 bar and that reactants and products were not escaping through loose fittings or openings during the reaction.

The leak test was carried out at ambient temperature by filling the reactor with argon until the pressure indicator read 20 bar. The input and exit valves were closed to isolate the pressurised section of the reactor. Possible leaks were detected by spraying Snoop® Liquid Leak detector on fittings, where bubbling of the soap-based liquid would indicate a gas leak. Alternatively, the leak was also sought by using a handheld mini gas leak detector. Loose fittings were tightened while worn fittings were replaced. The valves remained closed for about 12 hours, such that the leak rate could be determined as shown below:

$$\dot{V}_{leak(NTP)} = \frac{V_{reactor}}{\Delta T} \cdot \frac{\Delta P}{20\ bar} \quad \text{0-1}$$

A.3. Calibration of the GC-TCD

The GC-TCD was calibrated using a gas cylinder with known concentrations of analytes that are similar to those contained in the reactor tail gas. On a 100 mol·s^{-1} basis, a relative response factor for each component 'i ' in the gas stream was estimated as shown:

$$RR_{f,i} = \left(\frac{A_i}{A_{N_2} \cdot V_i}\right) V_{N_2} \quad \text{0-2}$$

Table 0-2: Peak areas obtained during the calibration of the CG-TCD

Gas	Analyte amount (V_i)	Sample 1	Sample 2	Sample 3	Average relative response factors $RR_{f,i}$
H_2	39.8	221192163	221540864	228289232	8.98
CO_2	10.1	7872939	7870711	7213948	1.34
N_2	5.8	3770741	3769747	4358623	1
CH_4	15.9	35883926	35947333	35555616	4.04
CO	18.5	11579502	11589098	10809580	1.03
Ar	balance	-			

A.4. Feed flowrate and composition confirmation

GC-TCD data was collected through the bypass for each syngas flowrate used, this was done to determine the deviation of the feed flowrate as detected by the GC-TCD from the set values. Below, a sample is provided for syngas flowrate of 180 ml·min^{-1}. It can be seen that the measured flowrates deviate slightly from the set flowrates. Analysis of gas products (X_{co} and S_i) was done using the deviated flowrates

Compound	Setpoint	Area			Average flowrate [ml·min^{-1}] $F_i = \left.v_{N_2}\left(\frac{A_i}{A_{N_2}}\right)\right/ RR_{f,i}$
H_2	120	342906223	342535180	342404961	126
CO_2	-	-	-	-	-
N_2	20	6160642	6149346	6143576	20
CH_4	-	-	-	-	-
CO	60	17942270	17916465	17907585	57

Appendix B: Hydrodynamic and transport properties of catalysts

B.1. Evaluation of gas properties at reaction conditions

B.1.1. Synthesis gas density

The density of synthesis gas was estimated by taking the volume averaged density of CO and H_2 calculated using the ideal gas law as shown below:

$$\rho_i = \frac{P \cdot M_i}{R \cdot T} \qquad \text{0-3}$$

	Molar mass [g·mol^{-1}]	Density [g·ml^{-1}]
CO	28.01	$1.37 \cdot 10^{-2}$
H_2	2.016	$9.83 \cdot 10^{-4}$
Syngas	$\frac{1}{3} \cdot (1.37 \cdot 10^{-2}) + \frac{2}{3} \cdot (9.83 \cdot 10^{-4}) = 5.21 \cdot 10^{-3}$	

B.1.2. Synthesis gas viscosity

As with the density, the gas viscosity was taken as the volume averaged viscosity of CO and H_2 in the feed. The Sutherland formula (Crane, 1988) was used to estimate viscosity of each gas based on reactor temperature.

$$\mu = \mu_0 \left(\frac{0.555 \cdot T_0 + C}{0.555 \cdot T + C}\right)\left(\frac{T}{T_0}\right)^{\frac{3}{2}} \qquad \text{0-4}$$

In equation 0-4 above, μ_0 is the viscosity of the gas at a reference temperature (T_0), T is the gas temperature, and C is the Sutherland constant. The (LMNO-Engineering, 2013)

	μ_0 [centipoise]	T_0 [°R]	C	Calculated viscosity [cm^2·s^{-1}]
CO	0.01720	518.67	118	$2.56 \cdot 10^{-5}$
H_2	0.0876	528.93	72	$1.23 \cdot 10^{-5}$
Volume fraction averaged viscosity [cm^2·s^{-1}]				$1.68 \cdot 10^{-5}$

B.1.3. Gas diffusivity

An empirical correlation developed by Fuller et al. (1966) was used to estimate the diffusivity of syngas.

$$D_{AB} = \frac{10^{-3} \cdot T^{1.75} \sqrt{\left(\frac{1}{M_A} + \frac{1}{M_B}\right)}}{P \cdot \left[(\sum_i V_{i1})^{\frac{1}{3}} + (\sum_i V_{i2})^{\frac{1}{3}}\right]^2} \quad \text{0-5}$$

Where T is the gas temperature in K, P is the total pressure in atm, M_A and M_B are the molar masses of CO and H_2 respectively in g·mol^{-1}, and $\sum V_{i1}$ and $\sum V_{i2}$ are the atomic diffusion volumes for simple molecules. The diffusion volumes used for CO were H_2 were 18.9 and 7.07 respectively.

$D_{CO,H_2} = 9.10 \cdot 10^{-2}\ cm^2 \cdot s^{-1}$

B.2. Transport properties in the catalyst powder

B.2.1. External mass transfer limitations

The extent of external mass transfer limitations was estimated using the Carberry number:

$$a = \frac{-r_A{}^{obs}}{k_m \cdot a_v \cdot C_{CO,bulk}}$$

The external mass transfer coefficient (k_m) was estimated by solving dimensionless correlations for the Sherwood number.

$Sh = 2 + 1.1 \cdot Re^{0.6} \cdot Sc^{\frac{1}{3}}$ and $Sh = \frac{k_m \cdot d_p}{D_{CO,H_2}}$

Reynolds (Re) and Schmidt (Sc) numbers were calculated using the fluid properties in appendix B.1. The concentration of CO in the bulk gas was calculated from the Ideal gas law based on feed flowrate and reactor conditions. It is noted that above estimation does not account for the presence of product species in the bulk gas. Below is a summary of the estimates obtained:

Table 0-3: Summary of values used to assess the extent of external mass transfer limitations

Space velocity [$mmol_{CO} \cdot s^{-1} \cdot g^{-1}_{Cat}$]	0.11	0.083	0.055	0.028
Linear gas velocity [$cm \cdot s^{-1}$]	8.53	6.40	4.27	2.13
$Re = \frac{U_o \cdot D_p}{v}$	3.3	2.5	1.66	0.83
$Sc = \frac{v}{D_{A,B}}$	0.354			
$Sh = 2 + 1.1 \cdot Re^{0.6} \cdot Sc^{\frac{1}{3}}$	3.42	2.67	2.55	2.39
Integral reaction rate $(-r_A{}^{obs})$ [$mmol_{CO} \cdot s^{-1} \cdot g^{-1}_{Cat}$]	$3.8 \cdot 10^{-3}$	$2.9 \cdot 10^{-3}$	$2.3 \cdot 10^{-3}$	$1.6 \cdot 10^{-3}$
Carberry number	$9.7 \cdot 10^{-5}$	$9.4 \cdot 10^{-5}$	$7.8 \cdot 10^{-5}$	$5.8 \cdot 10^{-5}$
Mass transfer coefficient (k_m) [$cm \cdot s^{-1}$]	25	19	18	17

B.2.2. Internal mass transfer limitations

The Weisz-Prater criterion was used to assess whether internal mass transfer limitations could be neglected.

As data for surface concentration of CO is not available, the Carberry number was used to determine $C_{CO,s}$ as per the equation below, these were found to be identical due to absence of external mass transfer limitations.

$$Ca = \frac{C_{A,b} - C_{A,s}}{C_{A,b}}$$

$\frac{\varepsilon}{\tau}$ was assumed to be 0.1 (Breitkopf, 2008) while L was taken as the characteristic diffusion length for spherical catalyst particles $\left(\frac{d_p}{6}\right)$. The reaction rate was adapted using specific surface area and density as the Weisz modulus is calculated over a single catalyst particle.

Table 0-4: Summary of parameters used to assess the extent of internal mass transfer limitations over the powder catalyst

$C_{CO,bulk}$ [mmol·cm^{-3}]	0.014			
$C_{CO,s}$ [mmol·cm^{-3}]	0.014			
$D_{CO}^{Eff} = \frac{\varepsilon}{\tau} D_{CO,H_2}$ [cm·s^{-1}]	0.34			
Weisz modulus $\left(\Phi = \frac{-r_A{}^{obs}}{D_{CO,eff} \cdot C_{CO,s}} L^2\right)$	$6.6 \cdot 10^{-4}$	$5 \cdot 10^{-4}$	$3.9 \cdot 10^{-4}$	$2.7 \cdot 10^{-4}$

Appendix C: Hydrodynamic, geometric and transport properties of 230 CPSI cordierite monoliths

Hydrodynamic modelling of monoliths was done using correlation for square channels.

C.1. Catalyst layer thickness

The geometric surface area of the monolith reactor was estimated based on the total surface area of the 16 square channel monolith pieces loaded in a 50 mm catalyst bed.

$$Volume = height * (total\ width)^2 = 2.48\ \text{ml}$$

Catalyst layer thickness is calculated based on a washcoat density of 2.23 g·cm^{-3} and assuming a uniform coating over the total surface area of the monoliths

$$Catalyst\ layer\ thickness = \frac{m_{catalyst}}{\rho_{catalyst} \cdot total\ surface\ area}$$

Monolith 1	44.9 µm
Monolith 2	22.2 µm

C.2. Pressure drop

Pressure drop of the monolith was estimated using the following correlation (Ilsen Önsan & Avci, 2011):

$$\frac{\Delta P}{L} = \frac{2 * f \cdot \mu \cdot u^2}{{d_h}^2}$$

The fanning friction factor (f), was taken as the standard value for square monolith channels, 14.23. The hydraulic diameter (d_h), fluid viscosity (μ), and superficial gas velocity (u), were previously estimated.

C.3. Estimation of mass transfer coefficients

Reynolds number was estimated using the hydraulic diameter

Linear gas velocity [cm·s^{-1}]	5.1	3.8	2.5	1.3
$Sh = 0.664 \cdot \mathrm{Re}^{0.5} \cdot Sc^{1/3}$	7.2	6.2	5.1	3.6
K_m	4.5	3.9	3.2	2.2

Appendix D: Hydrodynamic, geometric and transport properties of 30 PPI SiC foams

D.1. Specific surface area

The following properties of the 30 PPI foams were measured/estimated:

Table 0-5: Estimated/Measured properties of 30 PPI SiC foams

Property	Value
Solid density (ρ_s) [g/cm^3]	3.21 (Loffe-Institute)
Average bulk density (ρ_B) [g/cm^3]	0.295 (estimate)
Bulk porosity $\left(\epsilon = 1 - \frac{\rho_B}{\rho_{SiC}}\right)$	90.8%
Strut porosity$\left(\epsilon_{strut} = \frac{BJH\ pore\ volume}{\rho_{SiC}}\right)$	44.3%

A simplified tetrakaidehedral model was also used to estimate the specific surface area of the foams for comparison, the following equations were used to estimate the geometric constants of tetrakaidehedral cells obtained by Gibson & Ashby (1988)

The specific surface area of the foams can be estimated using solid porosity and pore diameter alone. The bulk density of the foams was used to convert the volumetric specific surface area to a mass-normalised specific surface area (S_m), a value of cm^2·g^{-1}

$$S_v = \frac{4.82}{D_p}\sqrt{1 - \epsilon_{strut}}$$

1.51 mm^2·mm^{-3}

51.2 cm^2·g^{-1}

D.2. Catalyst layer thickness

D.3. Pressure drop

The pressure drop per unit length of the uncoated 30 PPI ceramic foams was estimated using the Forcheimer equation.

α	7.72			
β	0.0838			
a_0 [g·cm^{-3}·s]	3.40			
a_1 [g·cm^{-4}]	0.435			
Flowrate [cm^3·s^{-1}]	4	3	2	1
Superficial linear velocity [cm/·s^{-1}]	5.09	3.82	2.55	1.27
Pressure drop (mbar·m^{-1})	2.86	1.93	1.15	0.50

D.3.1. Estimation of external mass transfer coefficients

The external mass transfer of the foams were calculated using the modified Sherwood number (Sh)

In F_g,0.58 and 0.44 are dimensionless fitting constants and were taken (Incera Garrido et al., 2008). ϵ_h is the hydrodynamically relevant porosity (i.e., open cell porosity)

Table 0-6: Mass transfer coefficients of in 30 PPI SiC foams

$F_g = \left(\frac{D_p\ [mm]}{0.58}\right)^{0.58} \cdot \epsilon_h^{0.44}$	1.55			
Superficial linear gas velocity [cm·s^{-1}]	5.09	3.82	2.55	1.27
$Re = \frac{U_o \cdot D_p}{v}$	234	176	117	58.6
$Sc = \frac{v}{D_{A,B}}$	0.354	0.354	0.354	0.354
$Sh = Re^{0.45} Sc^{\frac{1}{3}} F_g$	14.23	12.43	10.27	7.41
K_m	8.74	7.64	6.31	4.56

Appendix E: Post-run catalyst EFTEM catalyst support images

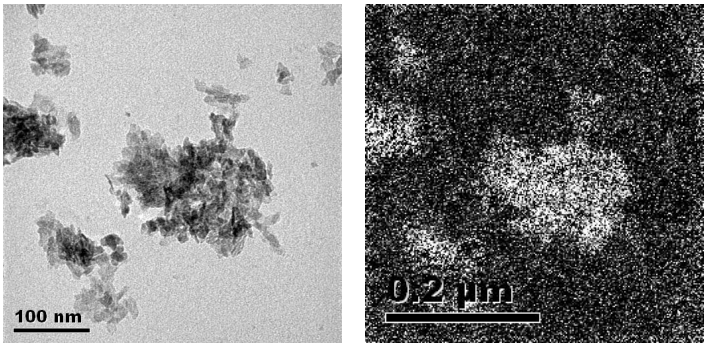

Figure 0-1: TEM image of unreacted catalyst powder and aluminium map (right)

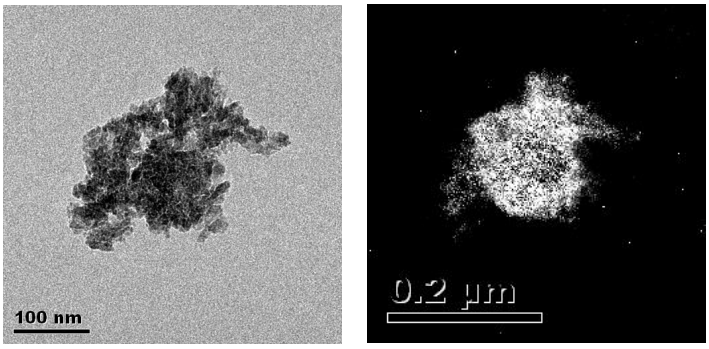

Figure 0-2: TEM image of spent catalyst pellet and aluminium map (right)

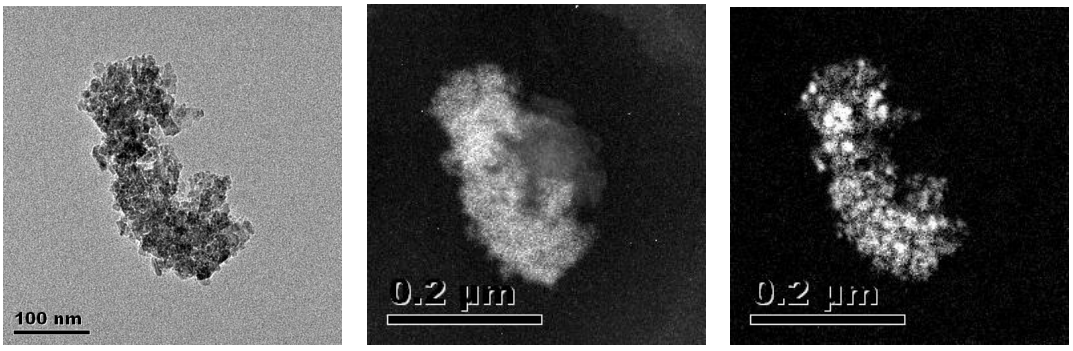

Figure 0-3: TEM image of spent catalyst pellet, aluminium map (middle) and cobalt map (right)

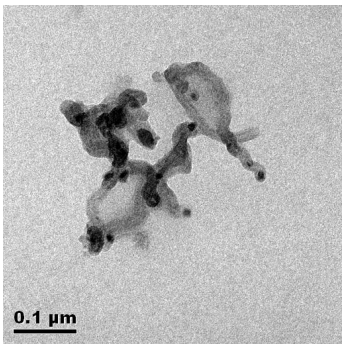

Figure 0-4: TEM image of spent monolith coating (HcM 1)

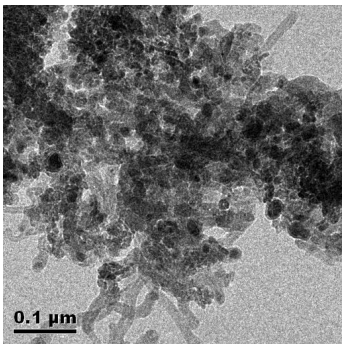

Figure 0-5: TEM image of spent foam coating (OcF 2)

Appendix F: Miscellaneous

Specifications of type-1 water used in ICP-OES analysis:

Table 0-7: Standard specifications for type 1 de-ionised water

Minimum resistivity at 25°C	18 MΩ·cm
Maximum electrical conductivity at 25°C	0.056 μS·cm^{-1}
Maximum particulate matter size	0.2 μm
Maximum total organic carbon (TOC)	100 μg·l^{-1}
Maximum sodium content	1 μg·l^{-1}
Maximum silica content	3 μg·l^{-1}
Maximum chloride content	1 μg·l^{-1}

* The water quality standard was established by the American Society for Testing Materials (ASTM)

Appendix G: Ethics in research form

Application for Approval of Ethics in Research (EIR) Projects
Faculty of Engineering and the Built Environment, University of Cape Town

APPLICATION FORM

Please Note:
Any person planning to undertake research in the Faculty of Engineering and the Built Environment (EBE) at the University of Cape Town is required to complete this form **before** collecting or analysing data. The objective of submitting this application *prior* to embarking on research is to ensure that the highest ethical standards in research, conducted under the auspices of the EBE Faculty, are met. Please ensure that you have read, and understood the **EBE Ethics in Research Handbook** (available from the UCT EBE, Research Ethics website) prior to completing this application form: http://www.ebe.uct.ac.za/ebe/research/ethics1

APPLICANT'S DETAILS		
Name of principal researcher, student or external applicant		Masana Mhinga
Department		Chemical Engineering
Preferred email address of applicant:		Mhnmas002@myuct.ac.za
If Student	Your Degree: e.g., MSc, PhD, etc.	MSc
	Credit Value of Research: e.g., 60/120/180/360 etc.	120
	Name of Supervisor (if supervised):	Eric Van Steen
If this is a researchcontract, indicate the source of funding/sponsorship		
Project Title		Development of foam reactors for Fischer-Tropsch Synthesis

I hereby undertake to carry out my research in such a way that:

- there is no apparent legal objection to the nature or the method of research; and
- the research will not compromise staff or students or the other responsibilities of the University;
- the stated objective will be achieved, and the findings will have a high degree of validity;
- limitations and alternative interpretations will be considered;
- the findings could be subject to peer review and publicly available; and
- I will comply with the conventions of copyright and avoid any practice that would constitute plagiarism.

SIGNED BY	Full name	Signature	Date
Principal Researcher/ Student/External applicant	Masana Mhinga		24 Apr 2018

APPLICATION APPROVED BY	Full name	Signature	Date
Supervisor (where applicable)	Eric Van Steen		25/04/18
HOD (or delegated nominee) Final authority for all applicants who have answered NO to all questions in Section1; and for all Undergraduateresearch (Including Honours).	Mary Seaton		26-4-18
Chair : Faculty EIR Committee For applicants other than uncergraduate students who have answered YES to any of the above questions.			

Signatures Removed